Ing. S.P. Haanappel

Non-Crimp Fabric Permeability Modelling

University of Twente
Faculty of Engineering Technology
Chair of Production Technology

Enschede, June 23, 2008

Examination committee:
Prof. dr. ir. R. Akkerman
Dr. ir. R. Loendersloot
Dr. ir. T. Bor
Ir. W. Grouve

CTW-PT-08-54
Student number: 0100633
s.p.haanappel@student.utwente.nl

Summary

A qualitative study was performed on the in-plane permeability modelling of Non-Crimp Fabrics (NCFs). A network flow model was developed to describe flow through inter bundle channels (meso level). These inter bundle channels are referred to as Stitch Yarn induced Fibre Distortions (SYDs) and have a wedge shaped geometry.

The stitch yarn penetration points are the origins of the SYDs. Since a piece of NCF exhibits many stitch yarn penetration points, there are many SYDs that intersect each other. An intersection search algorithm was developed to identify the intersection points. Nodes were defined at these points and 1D elements were created in between. These 1D elements represent the flow channels through the NCF and were assembled in a system of equations.

Initially, the model predicted a highly anisotropic permeability, which is unrealistic. To improve this model, it was extended with details that consider stitch yarn influenced regions. External channels are created by the stitch yarns, running from one stitch yarn penetration point to the other. These were described by 1D elements and added to the network. The regions in the SYDs with the penetrating stitch yarns (stitch yarn penetration point) were added as well. These regions were described by a small assembly of 1D elements. The properties of the elements that describe these details were obtained by performing parametric studies with flow simulation software.

Finally, a network of elements that represent the flow domain of the NCF was created and the model was made suitable to generate solutions for both steady state and transient (fill simulation) situations. For the steady state model configuration, all flow channels are filled with a liquid initially (resin). After applying incompressibility and pressure boundary conditions to the nodes, the system of equations will be solved to obtain a pressure field solution. The resulting nodal nett fluxes will be processed in Darcy's law to obtain an effective permeability for the modelled piece of NCF. The added details gave an $\approx 10\%$ lower permeability prediction in the machine direction, whereas they did not influence the permeability perpendicular to the machine direction. Also, the added details did affect the anisotropy of the permeability by $\approx 8\%$ (more isotropic).

For the transient model configuration, all flow channels are empty initially (air). The system matrix will be assembled, in which the averaged element viscosities are processed. Solving leads to element fluxes finally. The developed filling scheme uses these fluxes to process the transport of substances (e.g. resin and air) through the flow domain. For each time step, a new pressure field solution and its associated element fluxes result. The transient solutions give a better understanding of flow processes at the meso scale, but the filling scheme has not been developed that far to simulate a real infusion process, e.g. to imitate the situation during validation experiments.

Infusion experiments were executed to validate the network flow model. Due to a varying cavity height (fabric's thickness) during the experiments, measurements resulted in an initial and final cavity related permeability determination. The results showed good agreement with the predicted permeability in the machine direction of the fabric. However, the predicted anisotropy of the permeability did not correspond with the experimental results, which suggest a close to isotropic permeability of the NCF. Due to a high dependency of the SYD length on the effective permeability perpendicular to the machine direction, flow through fibre filaments (micro level) is expected to be significant near the SYD intersection regions.

Samenvatting

Een kwalitatieve studie naar de in-plane permeabiliteitsmodellering van Non-Crimp Fabrics (NCFs) is uitgevoerd. Een netwerk stromingsmodel was ontwikkeld om stromingen door inter bundel kanalen te beschrijven (op meso niveau). Deze inter bundel kanalen worden ook wel Stitch Yarn induced Fibre Distortions (SYDs) genoemd en hebben een wigvormige geometrie.

De stikdraad penetratiepunten zijn de beginpunten van de SYDs. Omdat een stukje NCF veel stikdraad penetratiepunten heeft, zijn er veel SYDs die elkaar kruisen. Een algoritme was ontwikkeld om deze kruispunten te zoeken. Nodes werden gedefiniëerd op deze kruispunten en 1D elementen werden tussen deze nodes gecreëerd. Deze 1D elementen representeren de stromingskanalen door het NCF en werden geassembleerd in een stelsel van vergelijkingen.

Het model voorspelde een hoge anisotrope permeabiliteit en is niet realistisch. Om dit model te verbeteren, was het uitgebreid met details die de stikdraad-beïnvloede gebieden beschouwen. Externe kanalen die gemaakt worden door stikdraden die van het ene stikdraad penetratiepunt naar het andere lopen. Deze werden beschreven door 1D elementen en toegevoegd aan het netwerk. Het gebied in de SYDs met de penetrerende stikdraad werd ook beschouwd. Dit gebied werd beschreven door een assemblage van enkele 1D elementen. De eigenschappen van deze toegevoegde elementen zijn verkregen door het uitvoeren van parametrische studies met behulp van stromingsimulatie software.

Uiteindelijk is een netwerk van elementen gecreëerd die het stromingsdomein in een NCF representeerd en dit model was geschikt gemaakt om oplossingen te genereren voor steady state en transiënte (vulsimulatie) situaties. In de steady state configuratie zijn alle stromingskanalen in het begin gevuld (met hars). Na het aanbrengen van randvoorwaarden voor incompressibiliteit en druk op de nodes, kan het stelsel van vergelijkingen worden opgelost om een drukveld oplossing te krijgen. De resulterende netto fluxen op de nodes worden verwerkt in de wet van Darcy om een effectieve permeabiliteit van het gemodelleerde stukje NCF te verkrijgen. De toegevoegde details gaven een $\approx 10\%$ lagere permeabiliteitsvoorspelling in the fabricagerichting, terwijl deze de permeabiliteit loodrecht op de fabricagerichting niet beinvloedde. De toegevoegde details beïnvloedde ook de anisotropie van de permeabiliteit met $\approx 8\%$ (meer isotroop).

Voor de transiënte model configuratie zijn de stromingskanalen in het begin van de simulatie leeg (lucht). De systeem matrix wordt geassembleerd waarin de gemiddelde viscositeiten van de elementen verwerkt worden. Het oplossen geeft uiteindelijk fluxen in de elementen. Het ontwikkelde vulschema gebruikt deze fluxen om het transport van de substanties (hars en lucht) door het stromingsdomein te verwerken. Iedere tijdstap resulteert in een nieuwe drukveldoplossing met de geassociëerde element fluxen. De transiënte oplossingen verbeteren het inzicht en begrip in bepaalde stromingsprocessen, maar het vulschema is nog niet zo ver ontwikkeld om werkelijke infusie processen te simuleren, bijvoorbeeld om de situatie tijdens validatie experimenten na te bootsen.

Infusie experimenten waren uitgevoerd om het network flow model te valideren. Vanwege een variërende hoogte van de holte (dikte van het NCF), resulteerde de metingen in een “initiële” en een “uiteindelijke” holte gerelateerde permeabiliteitsbepaling. De resultaten waren in overéénstemming met de voorspelde permeabiliteit in de fabricagerichting van het NCF. De voorspelde anisotropie van de permeabiliteit correspondeerde niet met de experimentele resultaten die een nagenoeg isotrope permeabiliteit suggereerden. Het is verwacht dat stroming door de vezelfilamenten (op micro niveau)

significant zijn rondom de kruispunten van de SYDs, vanwege de grote afhankelijkheid van de SYD lengte op de effectieve permeabiliteit, loodrecht op de fabricagerichting.

Contents

1

Introduction

Composite materials have been used, probably since the existence of the *homo faber* (Man the Maker). In the context of this thesis, the definition of *composite materials* (also referred to as *composites*) is:

Definition 1. *A composite material is a material that consists of two or more constituent materials with significantly different physical and/or chemical properties and which remain separate and distinct on a macroscopic level within the finished structure.*

One of the most primitive combinations of materials is the combination of straw and mud in order to create walls. Nowadays, a well known and widely used combination of materials is steel reinforced concrete.

The idea of producing composite materials on an industrial scale came much later. A story tells the accidental discovery of the potential of composite materials. During his work, someone accidently dropped some bakelite on his clothes. Being home, removing the bakelite was impossible. It had cured completely and there was a hard piece of impregnated textile. The idea for industrial application of composite materials was born. Bakelite was invented around 1908 by Leo Baekeland. This means that the incident described above, happened later. The first applications on an industrial scale were circuit boards made of linen weaves, impregnated with bakelite.

Nowadays, Continuous Fibre Reinforced Polymers (CFRPs) are used in automotive and aerospace engineering. The main reasons to use these materials are their high specific strengths and stiffnesses, which could lead to a strong, stiff and lightweight product. In this way a lightweight racing car or aircraft could reach higher speeds and/or save fuel and emissions.

Most times, costly trial and error process developments are needed to create a product that fulfils the requirements. Encountered problems are non-uniform impregnation, formation of dry spots, void inclusions and lengthy impregnation cycles. Redesign of products and process tools are often needed, but are costly. As a result, there is a lot of interest in models. Such models should be able to predict different mechanisms that occur during a particular production process. Models finally serve as tools to reduce product development times, production cycle times and should also lead to better reproducibility.

To serve the call for knowledge about CFRP production, many researchers are working on models to describe and predict the production processes. The contents of this thesis form just a small piece of knowledge that could be used in other models again, namely “Non-Crimp Fabric Permeability Modelling”.

1.1 CFRPs and Production Methods

A CFRP consists globally of two components, namely fibres and a polymer matrix. The axial direction of the fibres serves for the strength and stiffness of the composite. The polymer matrix serves for the absorption of shear stresses and the formation of an entity, called the composite. The polymer matrix can be shaped arbitrarily. The polymer matrix could be a thermoset or a thermoplastic. Thermosets can be cured only once while thermoplastics can be reheated after curing, in order to be reused.

The fibre filaments are generally made of glass, carbon or aramid. A fibre yarn is a compacted bundle of fibre filaments. Those yarns or filaments could somehow form an entity or textile. See figure 1.1 for some examples. As can be observed from this figure, most textiles appear in sheet form. However, filament winding is a process that winds filaments around a mandrel in order to directly obtain an entity in its final geometry.

Woven fabrics exhibit an excellent integrity of the textile. However, deformability is limited due to the commingled configuration of the yarns. Moreover, the properties of the fibres are not used to their full extent due to the undulation of the yarns. Undulation is hardly present in unidirectional textiles, but their integrity in dry form is weak. Moreover, the resistance of unidirectional composites against delamination is less than for woven composites.

Composite products are mostly thin walled and curved to exploit the high membrane stiffness. There are three main strategies to create such a product:

- **Single heated driving process**
  Manual lay up of prepreg material to define the final geometry. The prepreg contains a thermoset matrix that will be melted and cured only once during an autoclave cycle.
- **Multiple heated driving process**
  First a pre-consolidated flat laminate is created by a heat and pressure driven process to impregnate the fibre filaments with a thermoplastic matrix. This laminate is reheated and when the thermoplastic is melted and viscosity is at the right level, the laminate will be formed in its final geometry. This strategy is used in production methods like thermo-folding, diaphragm forming and rubber pressing.
- **Non-heated driving process**
  A textile, containing dry fibres like a braid or a fabric, will be placed in a mould to define the final geometry. This process is referred to as draping. This draped textile is also referred to as a preform. The preform will be injected with a thermoset resin in order to impregnate the spaces between the fibre filaments, after which the resin will cure. The curing of the resin proceeds by the formation of cross links. Increasing the temperature will increase speed of curing, but this is not the main parameter that drives the production process, as is the case in the abovementioned strategies. This strategy is used in production methods like hand lay-up and Liquid Composite Moulding (LCM) methods.

The abbreviation LCM represents a collection of many production processes related to impregnation methods to produce fibre reinforced products. Examples are Resin Transfer Moulding (RTM), Resin Infusion under Flexible Tooling (RIFT), Resin Film Infusion (RFI), Vacuum Assisted RTM (VARTM), Seeman Composite Resin Infusion Moulding Process (SCRIMP) and Advanced RTM (ARTM). RTM is a frequently used production method in aerospace and automotive engineering and has proven to be a cost effective production method for near-net shaped products with a high accuracy and a high reproducibility.

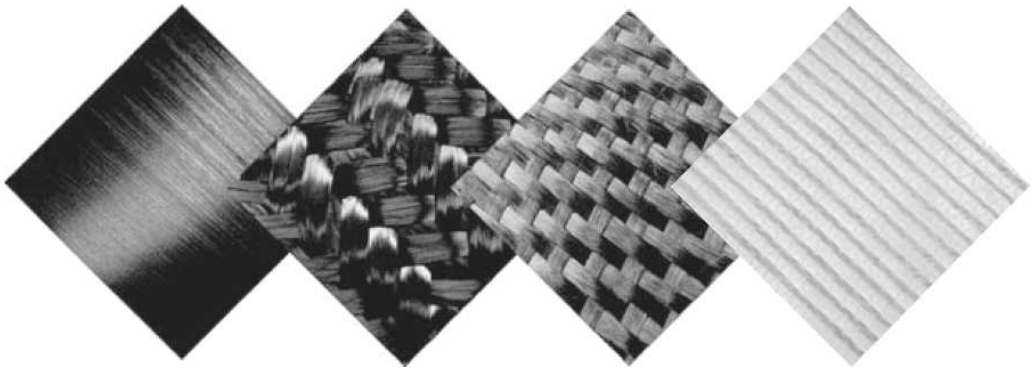

Fig. 1.1. Several types of continuous fibre reinforcements. From left to right a unidirectional prepreg, a braid, a woven fabric and a non-crimp fabric.

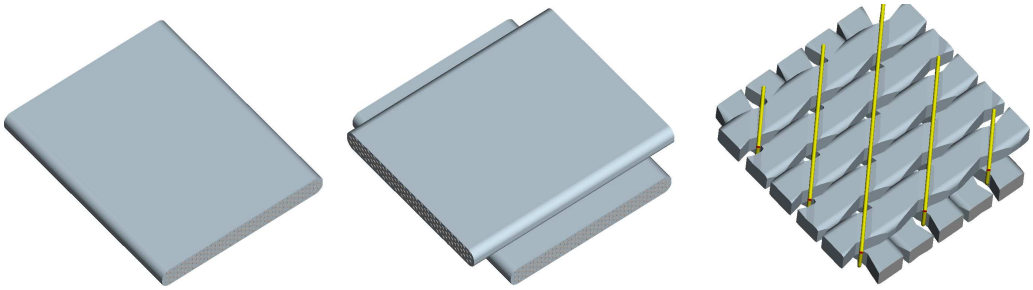

Fig. 1.2. Two stacked unidirectional plies, which are stitched together. The resulting entity is a bi-axial NCF.

A disadvantage in LCM methods is the limited deformability of woven fabrics. Because of the good deformability of an unidirectional textile, draping proceeds well. As mentioned, the integrity of a unidirectional textile is weak. The call for good draping properties of a fabric in LCM methods and the weak integrity of unidirectional textiles led to the development of Non-Crimp Fabrics (NCFs)[1]. An NCF consists of a number of stacked unidirectional plies that are stitched together in order to create the integrity of the fabric, see figure 1.2.

1.2 Motivation and Objective

Common problems that are encountered in Liquid Composite Moulding (LCM) processes are non-uniform impregnation, formation of dry spots, void inclusions and lengthy impregnation cycles. Accurate flow simulations are essential in finding the optimal process parameters. The infusion behaviour is strongly influenced by the fabrics permeability, which is inhomogeneous in case of a draped fabric. An explanation of the permeability will be given in the last part of this chapter (section 1.3). The permeability depends on the fabrics geometry, which is determined by positions and directions of fibres and yarns. This research focuses on the in-plane permeability prediction of NCFs.

The question arises, why not obtain permeability values from experiments, which were done for the particular textile of interest and using these results in flow simulations. Actually, this could be done for a preform without any curvature. But consider a product with curvature, which was created by draping the preform (figure 1.3(a)), to obtain the desired product shape. During this draping, the preform has a developing shear field and ends with a shear distribution over the entire product shape (figure 1.3(b), note that the shear field is not symmetrical in case of an NCF), as can be predicted by proposed models of TEN THIJE [1] or LAMERS [2].

Shear influences the dimensions of flow channels inside the fabric, which subsequently influences the channels' permeabilities. As a consequence, a shear distribution leads to a permeability distribution, and once the draped preform is being infused by a resin, non-uniform infusion behaviour could result at a global scale. Since each product could have different curvatures, a limited number of infusion experiments with particular shear distributions of the textile are not sufficient to predict infusion behaviour of any arbitrarily shaped (draped) product.

LOENDERSLOOT [3] and NORDLUND [4] developed a network flow model independently. Both assumed that the flow through an NCF is mainly governed by flow through the inter bundle channels and that these channels mainly determine the effective permeability of the fabric. A geometric and fluidic description of these channels will be given in the first part of chapter 2 and 3 respectively. NORDLUND analysed the flow in inter bundle channels by using a 3D flow model in ANSYS CFX. The results served as an input for a network model. LOENDERSLOOT represented the inter bundle channels by 1D finite elements (FE), to be assembled in a network model as well.

Model results and experiments [3] did not correspond well. The model predicted a highly anisotropic permeability, whereas experiments suggested an isotropic permeability. Details of stitch yarn influenced regions that are expected to be important, were not incorporated yet. Therefore, this model will be

[1] The material is also referred to as "Non-Crimp stitched (bonded) Fabric" or as Multi-axial Multiply stitched Fabric (MMF)

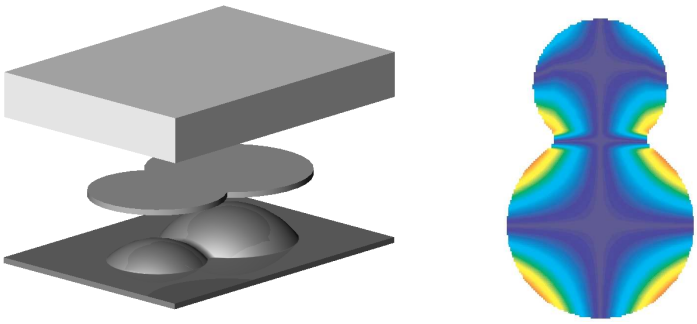

(a) Closing the upper and lower mould, results in draping of the initially flat preform.

(b) Shear distribution after draping.

Fig. 1.3. Draping of an arbitrarily shaped (double dome) product and its resulting shear distribution. Note that the shear field is not symmetrical in case of an NCF.

extended with elements that describe these regions for which the parameterisation will be done in the last part of chapter 2. Flow modelling of these regions will be done in the last part of chapter 3. Herewith the source of the anisotropic permeability could result in a better understanding.

The elements that represent all the features that were described in chapter 2 and 3 will be assembled in a network flow model in chapter 4, for which a numerical program in MATLAB was written (section 4.1). A steady state solution may be found to determine the effective permeability of a piece of NCF (section 4.2). Beside a steady state solution, the network model will also be extended in order to give transient solutions that represent a fill simulation (section 4.3). By doing this, the potential of a fill simulation tool that is based on the inter bundle channels may be judged.

Qualitative infusion experiments have to be executed in order to validate the network flow model, as will be described in chapter 5. The experimental situation will be imitated by the network flow model in the first part of chapter 6, after which the results that follow will be discussed and compared with the experimentally obtained results from chapter 5. The isotropy of the network flow model will be discussed as well. The last part of chapter 6 gives a recapitulation and recommendations for future work. General conclusions will be made in chapter 7.

1.3 Permeability

This section shortly describes the origin and application of the term permeability. Inspector General Of Bridges and Highways called HENRY DARCY [5] was the first in 1856 to give an empirically determined relation between pressure drop Δp over a length L and flow rate Φ:

$$\Phi = \frac{\mathcal{A}K}{\mu}\frac{|\Delta p|}{L}, \tag{1.1}$$

in which $\mathcal{A}$ is the cross-sectional flow area, K the permeability and μ the dynamic viscosity. Experiments were executed by transporting water through sand, in order to describe water flow of the public fountains of Dijon. This relation is analogous to Ohm's, Fourier's and Fick's law. Darcy's law is generally accepted as the macroscopic equation of motion for Newtonian fluids in porous media at small Reynold numbers (Stokes flow (1.14)). The Reynolds number is defined as the ratio between inertial and viscous forces:

$$\mathrm{Re} \equiv \frac{\rho U^2 L^{-1}}{\mu U L^{-2}} = \frac{\rho U L}{\mu}, \tag{1.2}$$

where ρ is the volumetric density, U the mean velocity and L a characteristic length.

In some cases it is not possible to identify a cross-sectional area $\mathcal{A}$, as described in the first item of the domain properties enumeration (for example in section C and 3.4.2). Therefore, equation (1.1) will also be used in a slightly different form:

$$\Phi = \frac{K^A}{\mu}\frac{|\Delta p|}{L}, \tag{1.3}$$

in which K^A is the area included permeability. Generalisation of equation (1.1) gives the following homogeneous linear relationship:

$$\mathbf{\Phi} = -\frac{\mathcal{A}}{\mu}\underline{\mathbf{K}} \cdot \frac{\mathrm{d}p}{\mathrm{d}\mathbf{x}} \tag{1.4}$$

In the literature, Darcy's law appears in the following form as well:

$$\mathbf{v} = -\frac{\underline{\mathbf{K}}}{\mu} \cdot \frac{\mathrm{d}p}{\mathrm{d}\mathbf{x}}, \tag{1.5}$$

in which $\mathbf{v}$ is the superficial velocity. To convert these equations into one of the other forms, the cross-sectional area $\mathcal{A}$ that has to be used is the area through which the fluid flows. This means that in a particular cross-section perpendicular to the flow, the area represented by solid particles has to be excluded!

Referring to the analogy with Ohm's law, electric resistances could be connected in parallel and in serial configurations. An effective resistance can be determined according to the well-known relations. Because permeability K is inversely proportional to the electric resistance $\mathcal{R}$, an effective permeability for flow channels with permeability K_n that are serially connected, could be determined according to [3, 6]:

$$K^A_{\underset{s}{E}} = L\left(\sum_{n=1}^{N}\frac{L_n}{K^A_n}\right)^{-1}, \tag{1.6}$$

in which L is the shortest length between the highest and lowest pressure regions, i.e. in the pressure gradient direction. The summation will be done for N serial connected channels with permeability K^A_n and channel length L_n. A parallel configuration could be handled as:

$$K^A_{\underset{p}{E}} = L\sum_{n=1}^{N}\frac{K^A_n}{L_n}, \tag{1.7}$$

in which the summation will be done for N parallel connected channels with permeability K^A_n and channel length L_n.

Darcy's law was derived by experimental observation, but in a later stage it was shown by Neuman [7] that it can be derived from the Navier-Stokes equation. Details of this derivation will not be mentioned, but some assumptions that have to be satisfied, and their effects, will be shown in next subsection.

1.3.1 Theoretical Assumptions to Obtain Darcy's Law

The continuity equation in the Partial Differential Equation (PDE) conservation form is:

$$\frac{\partial \rho}{\partial t} + \boldsymbol{\nabla} \cdot \rho\mathbf{u} = 0, \tag{1.8}$$

where ρ is the fluid's density and t represents time. By assuming incompressibility of the fluid and a steady state situation, the first term on the left hand side disappears which results in a continuity condition that has to be satisfied:

$$\boldsymbol{\nabla} \cdot \mathbf{u} = 0 \tag{1.9}$$

The momentum equation in its PDE-conservation form reads:

$$\frac{\partial}{\partial t}\rho\mathbf{u} + \boldsymbol{\nabla} \cdot \rho\mathbf{u}\mathbf{u} = \rho\mathbf{g} - \boldsymbol{\nabla}p + \boldsymbol{\nabla} \cdot \underline{\boldsymbol{\tau}}, \tag{1.10}$$

which is also known as the famous Navier-Stokes equation. The body forces are represented by the first term on the right hand side. Surface forces are represented by the second term and traction forces by the last term. The first term on the right hand side will disappear by neglecting body forces and inertia effects. The first term on the left hand side disappears as well by assuming a steady state situation $\frac{\partial}{\partial t} = 0$. The slow viscous flow (Re $<<$ 1) assumption makes non-linear velocity terms disappear, i.e. the second term on the left hand side. Equation (1.10) becomes:

$$\boldsymbol{\nabla} \cdot \underline{\boldsymbol{\tau}} = \boldsymbol{\nabla} p \tag{1.11}$$

The viscous stress tensor $\underline{\boldsymbol{\tau}}$ can be expressed as:

$$\underline{\boldsymbol{\tau}} = \mu(\mathbf{u}\boldsymbol{\nabla} + \boldsymbol{\nabla}\mathbf{u}) - \frac{2}{3}\mu\underline{\mathbf{I}}\boldsymbol{\nabla} \cdot \mathbf{u}, \tag{1.12}$$

where $\underline{\mathbf{I}}$ is the identity tensor. Taking the divergence of this equation and using the continuity relation in (1.9) gives:

$$\boldsymbol{\nabla} \cdot \underline{\boldsymbol{\tau}} = \mu\nabla^2\mathbf{u} \tag{1.13}$$

Substituting this result in (1.11) gives the Stokes flow equation:

$$\mu\nabla^2\mathbf{u} = \boldsymbol{\nabla} p \tag{1.14}$$

This equation has been integrated over a porous space by Neuman [7]. By applying the Slattery-Whitaker averaging theorem and the given proof that the permeability tensor $\underline{\mathbf{K}}$ is symmetric and an unique macroscopic property of the porous medium, Darcy's law (1.4) finally had its mathematical derivation.

Darcy's law must be viewed merely as a constitutive relation which does not yield much information about the properties of the permeability tensor itself. The permeability was shown to be a valid constitutive property by assuming that the flow is a slow viscous flow. Non-linear velocity terms are not present in the Stokes equation. Because Darcy's law could theoretically be derived from the Stokes equations, it means that once non-linear velocity terms (second term on the left hand side of (1.10)) are incorporated and become significant, permeability is more or less meaningless. Then the domain is characterised by a permeability under invalid conditions. The permeability concept is only valid under the conditions for which it was derived. If the invalid conditions are present, like including non-linear velocity terms, permeability would not only be influenced by the geometry, but by the fluid as well. This happens because permeability can only be derived from a known pressure and velocity field, i.e. permeability is a constitutive property like elasticity in solid mechanics.

1.3.2 Practical Permeability Usage

Traditionally the practical Kozeny-Carman relation has been used to compute the effective permeability. The effective permeability K_E could also be interpreted as the global permeability of a particular domain, see figure 1.4. It is a relation between the fibre content of the reinforcement and its permeability:

$$K_E = \frac{r_f^2}{8Z}\frac{(1 - V_f)^3}{V_f^2}, \tag{1.15}$$

where Z is an empirical constant, r_f the radius of the fibre filament and V_f the overall fibre content. This relation was originally derived for homogeneous isotropic porous media, hence the effective permeability K_E is a scalar. Therefore this relation seems to work best for porous media made up of spherical or small aspect ratio particles such as soil. However, a textile's permeability is often not isotropic which forced several researchers [8–13] to modify the Kozeny-Carman relation (1.15). They made a distinction between Z for axial and transverse flow, see table 1.1. Figure 1.5 clarifies the difference between isotropic and anisotropic permeability.

A more realistic flow equation for porous media has been proposed by Brinkman [14], known as Brinkman's equation:

Table 1.1. Values of the Kozeny constant Z as found in the literature for axial and transverse flow

Reference		$Z_{\|\|}$	$Z_\perp$	V_f
Williams	[8]	$0.1 - 0.8$	$0.8 - 6$	$0.2 - 0.65$
Gebart	[9]	$1.66 - 1.78$	8	
Lam and Kardos	[10]	$0.35 - 0.68$	11	$0.57 - 0.75$
Batch	[11]	1.06	8	
Muzzy	[12]	$3 - 7$	7.6	< 0.8
Gutowski	[13]	0.7	17.9	$0.4 - 0.8$

$$\boldsymbol{\nabla} p = -\frac{\mu}{\underline{\mathbf{K}}} \cdot \mathbf{u} + \mu \nabla^2 \mathbf{u}, \tag{1.16}$$

where $\mathbf{u}$ represents the mean fluid velocity through the porous medium. This equation is frequently used to describe flow behaviour inside fibre yarns [4, 15–18]. Then $\underline{\mathbf{K}}$ is the yarn's permeability which can be constructed by using the principle permeabilities $Z_{||}$ and $Z_\perp$ in table 1.1. This equation transfers momentum by shear at the boundaries and reduces to Darcy's law (1.4) away from the boundary.

1.4 Brief Overview of this Research Area

In general, during an infusion process, a textile exhibits two fluid phenomena caused by dual scale porosity. One is flow at meso scale, another is flow at micro scale (figure 2.1). Permeability prediction models that incorporate the dual-scale porosity have been developed by many. This section briefly describes a very small amount of work that has been done in this research area, in order to indicate approaches for permeability modelling.

Cai and Berdichevsky [19] and Pillai and Advani [15] analysed permeability of a bunch of porous circular cylinders, which were aligned perpendicular to the flow direction. Flow at meso scale was described by Stokes' equation. Cai and Berdichevsky [19] described flow at micro scale with Darcy's law (1.4). Pillai and Advani [15] used Brinkman's equation for this micro scale, which re-

(a) Structure with different permeabilities K_n with $n = 1, 2, .., 5$.

(b) Effective permeability K_E, which represents the parallel connected permeabilities in figure 1.4(a), see equation (1.7).

Fig. 1.4. Schematic representation of the effective permeability K_E (not on scale).

(a) Isotropic permeability tensor $\underline{\mathbf{K}}$: $K_{11} = K_{22} = K_{33}$.

(b) Anisotropic permeability tensor $\underline{\mathbf{K}}$: $K_{11} \neq K_{22}$, $K_{22} = K_{33}$.

Fig. 1.5. Direction dependent permeabilities K_{11}, K_{22} and K_{33}.

duces to Darcy's law (1.4) away from the micro domain's boundary. They related effective permeability K_E to total flow rate Φ_t and mean pressure drop $\Delta\bar{p}$ over a unit cell.

Yu and Lee [17] used a unit cell approach as well. A unit cell is the smallest piece of a textile that repeats itself, as is schematically represented in figure 1.6. The aim of using unit cells is to solve the flow problem for one unit cell, such that the resulting flow solution can be extrapolated to a flow solution for a whole textile. In this unit cell the one-dimensional (1D) stokes equation was used to model flow at meso scale and the 1D Brinkman equation was used to model flow at micro scale. They found that permeability of their investigated textiles was mainly determined by flow in the meso scale domain and therefore the effects of micro structures at micro scale may be neglected, when one fulfills their assumptions. Ngo and Tamma [18] used the Stokes and Brinkman equations as well, but in three-dimensional (3D) form. The FE method was used to solve their equations.

Ranganathan [16] also modelled dual-scale porosity by using Stokes' equation at meso scale and Brinkman's equation at micro scale. They developed a semi-analytical solution for flow across arrays of aligned cylinders with elliptical cross-sections that represent the textile. They found that upon increasing the overall fibre volume fraction V_f, effects at micro scale become more important. These effects are most critical for cases in which fibre yarns touch each other. In this case, a model based on solid yarns predicts a very low permeability at meso scale and is therefore not reliable. Aspect ratio of a yarns' cross-section has a proportional effect on micro scale importance as well.

Lekakou and Bader [20] proposed a mathematical model based on Darcy's law for both meso and micro scale domains. They analysed three modes of infiltration of resin. They are: flow through the textile while fibre yarns are not yet radially impregnated by resin, flow through the textile while yarns are already fully impregnated and a third mode where yarns are fully impregnated only where the flow front in that particular yarn is far ahead. This model accounts for mechanical, capillary and vacuum pressures.

Nordlund and Lundström [21] modelled the effect of micro scale domains artificially by applying a slip condition at the boundary of the meso scale domains, i.e. at the fluid-porous medium interfaces. They compared the results with a computationally expensive model, i.e. modelling the meso and micro scale domains individually. They concluded that the slip model is a good approximation for low fibre volume fractions V_f inside the fibre yarns, i.e. in the micro scale domain.

So far, all the researchers found that predicting permeability of a textile, containing a relatively high fibre volume fraction V_f inside the yarns, could be done by excluding the porous effects in the micro scale domains. For a textile containing a relative low fibre volume fraction V_f inside the yarns, the porous micro scale domains will influence the effective permeability significantly.

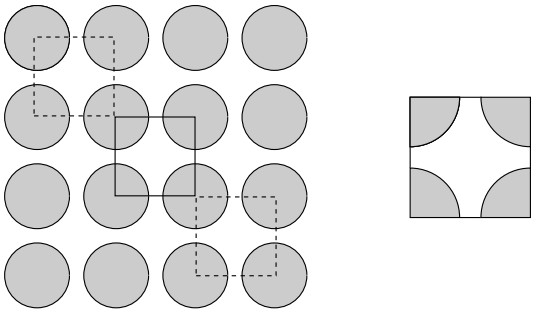

Fig. 1.6. Schematic representation of a unit cell. The right block shows up repeatedly in the entity on the left.

2

Geometry Modelling

To identify problems related to textiles, it is useful to identify the length scale of the domain, to which the problem is related. The domain scales macro, meso and micro are clarified in figure 2.1. The geometric and fluidic domains in this thesis are mainly based on the meso scale. The geometry of the NCF at the meso scale is the result of the manufacturing process, as will be described in section 2.1. In summary, the following geometries will be described in this chapter:

- the wedge shaped channels (SYDs) and their intersections as described in section 2.2;
- the region next to the stitch yarn which runs from one stitch yarn penetration point, to the other stitch yarn penetration point, as indicated with I in figure 2.1 and described in section 2.3.1;
- the region where the stitch yarn penetrates the fabric as in indicated by II in figure 2.1 and described in section 2.3.2.

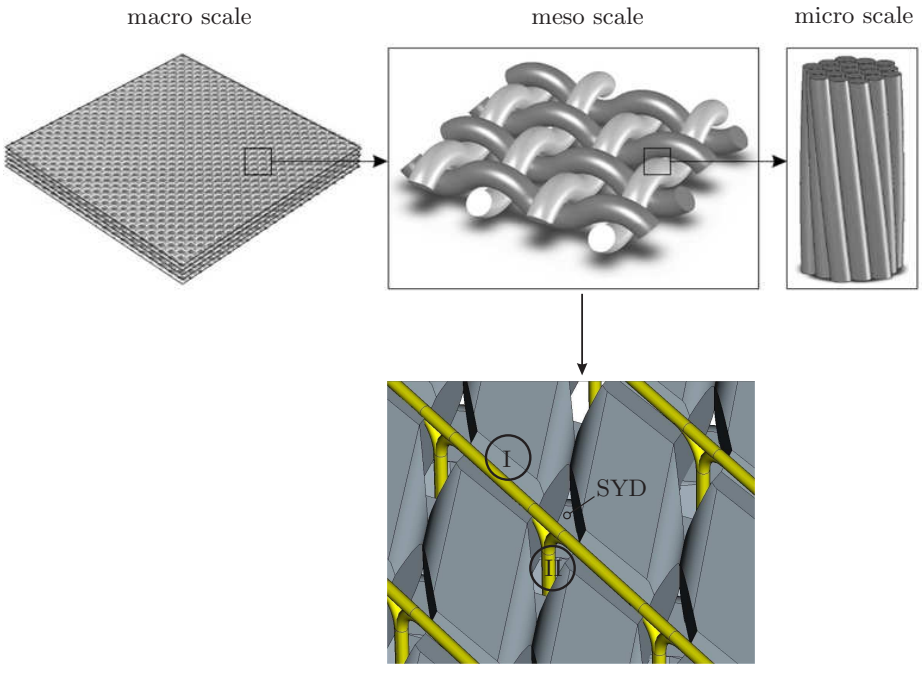

Fig. 2.1. Three length scales. Geometries at the meso scale will be analysed.

2.1 Manufacturing and Resulting Structure of NCFs

Non-Crimp Fabrics consist of unidirectional plies of fibres that are stitched together by a stitch yarn. The stitching provides the fabric sufficient stability in dry form for preforming. NCFs can therefore be used in LCM processes, just as woven fabrics. Other unidirectional reinforcements cannot be used in LCM and are generally available as prepreg materials only.

A single layer NCF is manufactured from a stack of unidirectional plies of fibres. The unidirectional plies are positioned on the machine bed after which they are stitched together to obtain a single layer of NCF material [22]. An NCF production machine is shown in figure 2.2. The orientation of the fibres on the machine bed is defined as the angle between the fibres and the manufacturing direction (θ in figure 2.2(b)). In practice, the angles of the unidirectional plies are limited to 0°, 90°and ±45°, combined as 0°/90° or ∓45°fabrics (bi-axial NCF), −45°/90°/45° fabrics (tri-axial) and −45°/0°/45°/90° fabrics (quadri-axial). The sequence of orientation angles are from the upper ply, passing the intermediate plies till the lower ply of the NCF. This means that in a −45°/90°/45° fabric, the -45°ply will be the upper ply, the 90°the intermediate ply and the 45°the lower ply. Other configurations for tri-axial and quadri-axial fabrics can be used as well. Additional chopped fibres or random mat layers may be placed under, between or on top of the fibrous plies.

The basic production parameters of an NCF are depicted in figure 2.2(b): the orientation of the fibres θ and the stitch distances A and B. Stitch distance A depends on the needle spacing. Stitch distance B, the distance between subsequent needle penetrations in machine direction, depends on

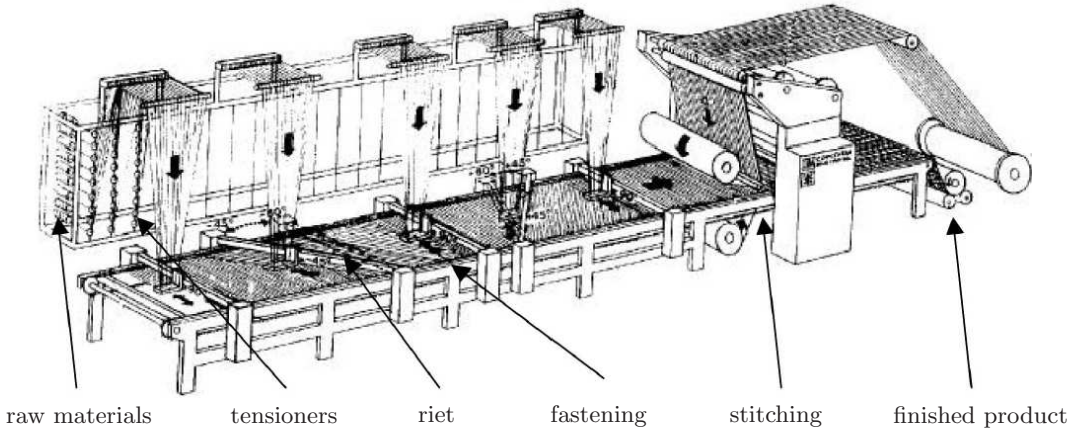

(a) Machine layout.

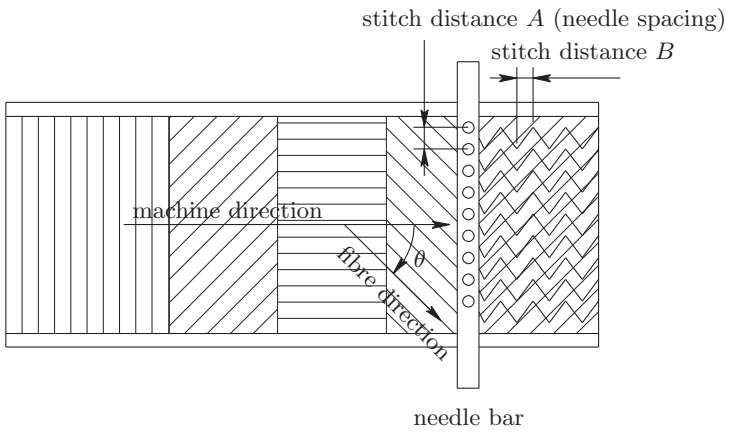

(b) Machine parameters.

Fig. 2.2. LIBA machine for the production of an NCF [22].

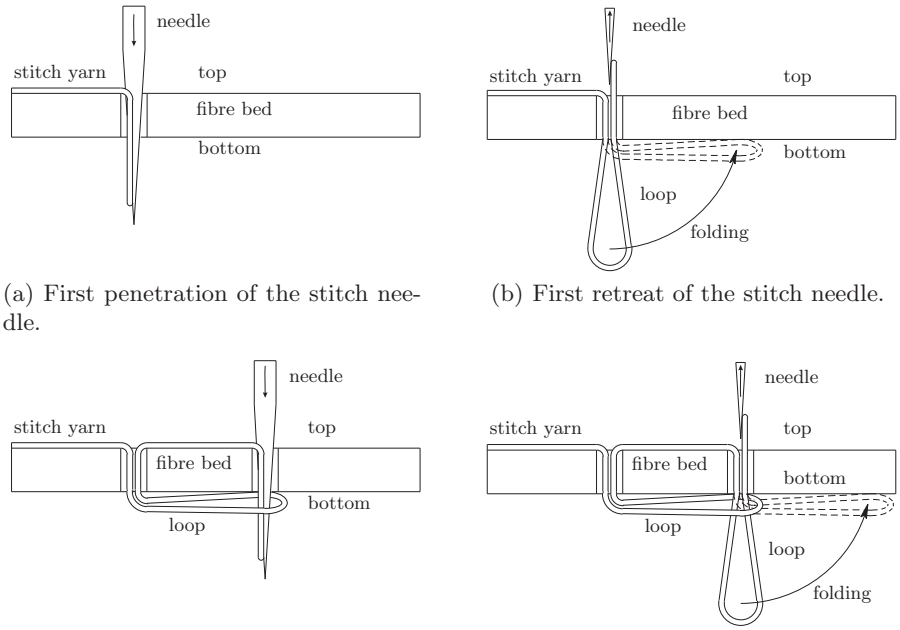

(a) First penetration of the stitch needle.

(b) First retreat of the stitch needle.

(c) Second penetration of the stitch needle.

(d) Second retreat of the stitch needle.

Fig. 2.3. Schematic of the warp knitting process of a chain knit pattern in four steps. The arrows in the needle indicates the direction of motion of the needle.

the speed of the loom and the frequency of knitting actions. A rectangular grid of needle penetrations results, since the stitch distances are constant during the manufacturing process.

The warp knitting process of a chain knit stitch pattern is schematically shown in figure 2.3. Other patterns are made in a similar way. The fibre yarns are spread on the machine bed during production. By reducing the distinction between fibre yarns, a more or less continuous bed of fibres is formed. The needle subsequently penetrates this fibre bed and the fibres are forced aside by the needle and the stitch yarn will be pulled through the individual layers, see figure 2.3(a). Subsequently the needle retreats, while pulling the yarn back through the fabric such that a loop of the stitch yarn is left at the bottom face, figure 2.3(b). The loop is folded onto the fabric's bottom face by the machine. The stitch yarn is pushed through the loop during the next knitting action (figure 2.3(c)). Again the needle is retreated and the new loop is folded onto the fabric's bottom face, fixing the position of the previous loop (figure 2.3(d)). The loops at the bottom face can be considered as oriented in the manufacturing direction, inherent to the stitching process.

Stitch patterns are formed by moving the needles in the transverse direction, in addition to the relative movement in machine direction. Three different stitch patterns are shown in figure 2.4: a tricot, a tricot/chain and a chain warp knit. In this research, only the chain warp knit stitching type will be accounted for, but extension to other stitching types is pretty straightforward. Note that the pattern at the top face differs for each fabric, but the loops at the bottom face are identical for all stitch patterns. Different types of stitch yarns as well as different stitch tensions are applied. Mechanical properties [23], drape properties [24, 25] and consequently infusion properties are affected by these stitching parameters.

Mouritz [26] stated that the needle hardly damages the fibres when penetrating the fabric. Less than 0.5% of the fibres are damaged during the stitching process of dry fabrics. However, the fibre filament paths are distorted due to the stitch yarn, which is left behind by the needle. A double wedge shaped distortion in the plane of the fibres in each layer is formed, as can be seen in figure 2.5. Moreover, the loops, which are formed on the bottom face of the fabric (see figure 2.3), are forced between the fibres of the lower layers, leading to differences between the distortions on the top face and the bottom face of the fabric.

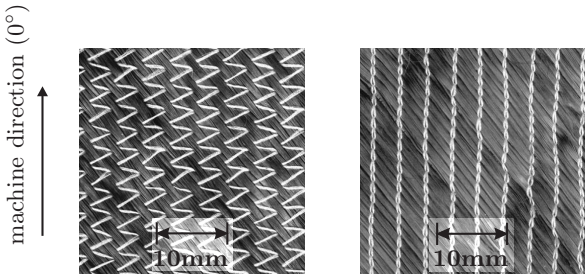

(a) Tricot (left top, right bottom).

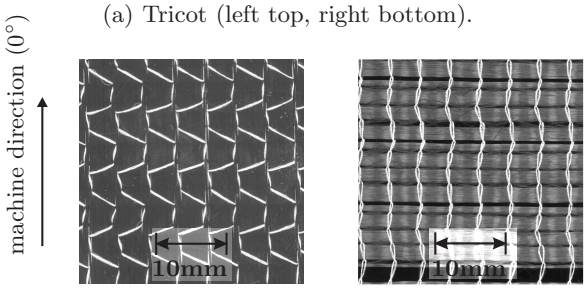

(b) Tricot/Chain (left top, right bottom).

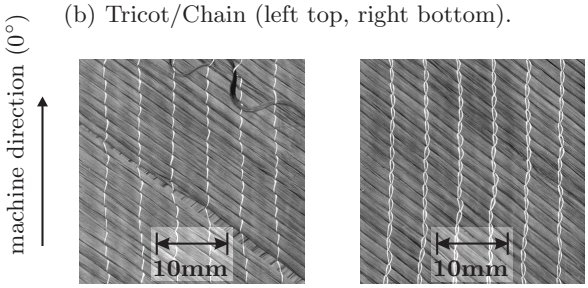

(c) Chain (left top, right bottom).

Fig. 2.4. Three different stitch patterns. Note: the pattern on the top face differs, whereas the loops at the bottom face are identical for all patterns.

Weimer and Mitschang [27] refer to the wedge shaped distortions as "stitch holes". The definition of the distortions for modelling purposes was first presented by Lomov [28], who referred to them as "cracks"and "channels". Here the term Stitch Yarn induced fibre Distortion (SYD) is used to comprise both these terms. Lekakou [29] and Schneider [30] describe these distortions as well and refer them to as "fish eyes". Note that the distortions are not continuous in the direction of the fibres, as can be seen in figure 2.5. The model of Lundström [31] assumes continuous channels formed by the stitches. Recent modifications in this model account for these so-called fibre crossings [32, 33], which implies a similar limitation to the channels as implicitly accounted for in the wedge shaped geometrical description using the SYDs, see section 3.2.

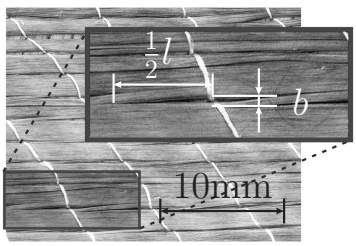

(a) Top face.

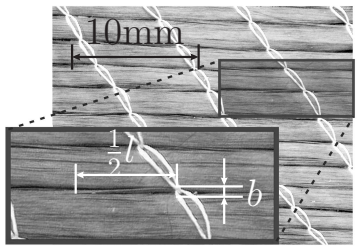

(b) Bottom face.

Fig. 2.5. Stitch Yarn Distortions (SYD) on the top and the bottom face of a bi-axial ±45° NCF (chain knit pattern) with b, the width of the SYD and l, the length.

In the subsequent text, the wedge shaped distortions in NCFs will also be referred to as "inter bundle channels" to pronounce the difference between spaces between fibre filaments ("intra bundle" spaces) and larger spaces between cluttered fibre filaments. Actually the term "inter bundle" is not valid for NCFs because during production, just before the stitching proceeds, the fibre bed has a continuous distribution of the fibre filaments. After stitching, a dual scale porosity has been created, i.e. spaces between the fibre filaments that were already present, and the spaces between regions with a higher fibre volume fractions, now referred to as inter bundle channels or SYDs.

2.2 Stitch Yarn induced fibre Distortions

As can be seen in figure 2.6(a), the SYDs are somehow connected to each other. A SYD in the upper ply can be connected by a SYD in the lower ply. Consider the SYD pair in figure 2.6(b) for which the SYD arms are numbered $1-4$ (six arms in case of a tri-axial NCF). Loendersloot [3, 34] proposed a relation that related the length of a SYD to the fibre filament directions θ and stitch distances A and B. An additional factor was empirically determined by visual analyses of the fabric. In this thesis, the dimensions l^u and l^l will be used to describe the upper and lower SYD lengths respectively.

Loendersloot proposed a relation for the SYD width as well. This relation was related to the penetrating stitch yarn diameter d_c and an additional factor, to be determined empirically as well. The dimensions b^u and b^l will be used in this thesis to describe the upper and lower SYD widths respectively. The compacted diameter d_c of the stitch yarn [28] is given by

$$d_c = \sqrt{\frac{4\rho_L}{\pi\rho\mathcal{L}}}, \tag{2.1}$$

with ρ_L and ρ, the linear and volumetric density of the yarn respectively and $\mathcal{L}$, the packing coefficient, which is 0.907 for a perfect hexagonal packing. Also a shear dependent relation for the SYD width was proposed by Loendersloot [3, 34, 35]. A transition shear angle was recognised. From this point, an increasing shear angle yields a constant SYD width due to the positioning of the penetrating stitch yarns.

The reference angle $\theta = 0$ is defined at the vertical and increases when rotating clockwise and decreases when rotating counter-clockwise, see figure 2.6(b). If θ denotes the upper ply fibre angle, then $\theta^u \leq 0$ and if θ denotes the lower ply angle, then $\theta^l \geq 0$. The situation

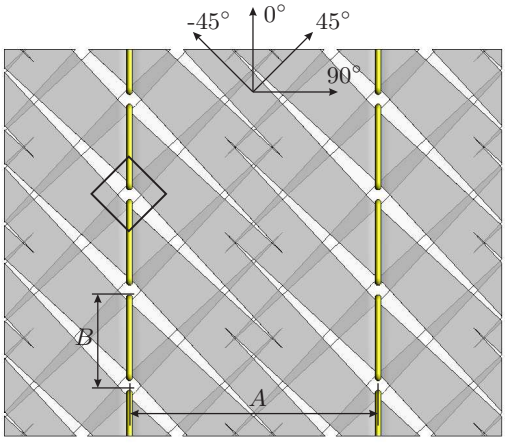

(a)

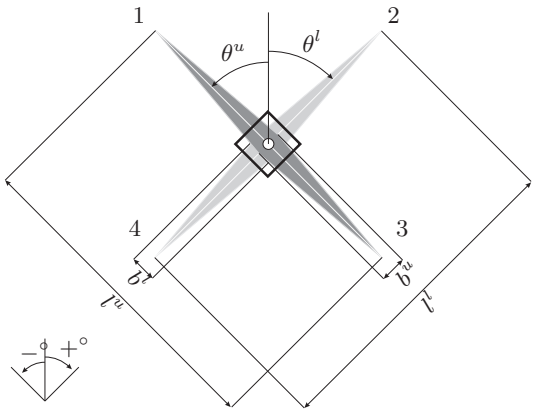

(b) One SYD pair for which the numbers $1-4$ refer to the arms, which will intersect other SYD arms when assembling these SYD pairs as in figure 2.7.

Fig. 2.6. Transparent view of a bi-axial NCF. Stitch yarn penetrations push the fibres aside, such that the SYDs are arising. The SYDs intersect each other at particular positions, such that a network of channels results.

$$\theta^l = 180 - |\theta^u| \qquad \begin{matrix} \theta^u \leq 0 \\ \theta^l \geq 0 \end{matrix},$$

can not be dealt with, because the SYDs are aligned in the same direction in both plies then. This case should be treated as one ply with a thickness of two plies.

2.2.1 Intersection Search

The stitch distances A and B determine the stitch yarn penetration positions at $(\hat{x},\hat{y})$. The intersection distances D of intersecting SYDs depend on stitch yarn penetration positions. The following properties of SYD pairs are related to each stitch yarn penetration point

- SYD lengths l^l and l^u,
- the fibre filament directions θ^l and θ^u.

For an unsheared piece of NCF, the stitch distances are equal everywhere and the itemised properties are equal for each stitch yarn penetration position, as shown in figure 2.7 and 2.6. However, they do vary for a draped piece of NCF, since the stitch yarn penetration positions will change and a shear distribution results (for example in figure 1.3). Now, the stitch distances differ over the piece of NCF and the itemised properties differ per stitch yarn penetration point. As a consequence, the intersection distances D will differ per SYD as well.

To account for the different intersection distances in case of a draped NCF, generalised geometrical relations have to be derived. Loendersloot [3] referred to the intersection distances as projected distances. They were directly related to the stitch distances A and B and the fibre filament directions θ^l and θ^u. However, these relations did not consider the consequence of draping. To deal with these different configurations and to use a generalised relation to calculate the intersection distances D, a definition of a pair of two points is needed:

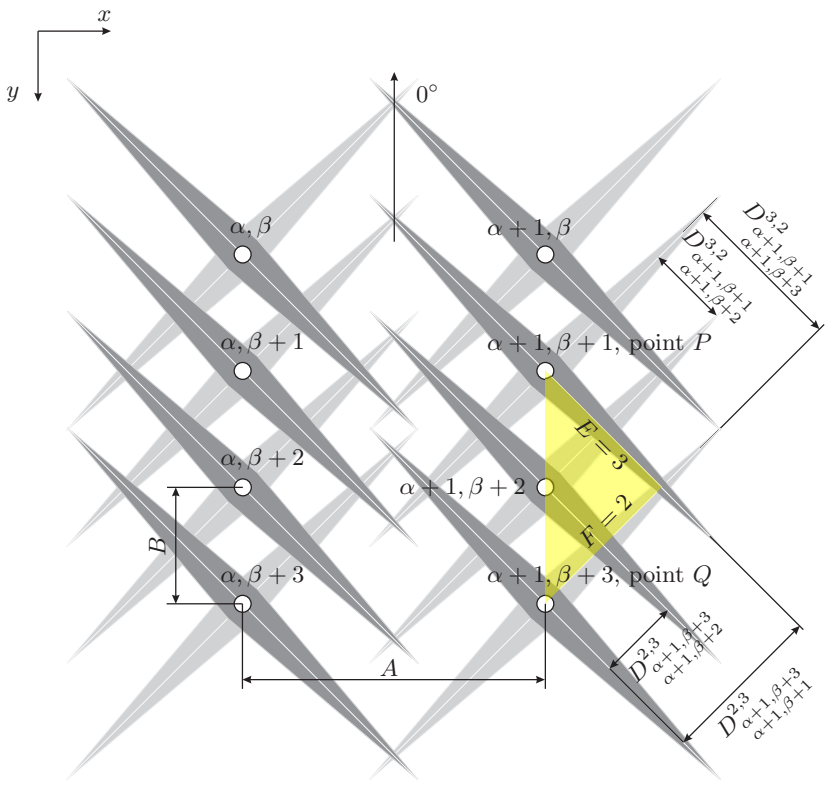

Fig. 2.7. Stitch yarn penetration points at $(\alpha + j, \beta + k)$, in which $j = 0, 1$ and $k = 0, 1, .., 3$. See definition 2 and equation (2.2) for the explanations of all sub- and superscripts. Point P and Q will be used in the example.

Definition 2. *The stitch yarn penetration point pair are two stitch yarn penetration points* $P(\hat{x},\hat{y})^{u}_{\alpha+j,\beta+k}$ *and* $Q(\hat{x},\hat{y})^{l}_{\alpha+j+m,\beta+k+n}$ *for which point* P *is the root for the SYD in the upper ply with negative fibre orientation angle* θ^{u}_{P}*. Point* Q *represents the root of the SYD in the lower ply with positive fibre orientation angle* θ^{l}_{Q}*.*

The position integers j and k and tracing integers m and n may all be zero, positive or negative as long as the indicated stitch penetration points exists. The tracing integer m indicates the penetration point, tracing m number of penetration points from point P in the x-direction, with respect to the undeformed piece of NCF in figure 2.7. The tracing integer n indicates the penetration point, tracing n number of penetration points from point P in the y-direction, with respect to the undeformed piece of NCF in figure 2.7.

Intersection Distance

A local coordinate system will be defined with its origin in point Q. The new positions of the stitch yarn penetration points will be:

$$\begin{aligned} P'(\hat{x}',\hat{y}') &= P'(P_x - Q_x, P_y - Q_y) \\ Q'(\hat{x}',\hat{y}') &= Q'(0,0), \end{aligned}$$

where the subscripts x and y indicate the x- and y-components of the particular point respectively. The components of the intersection point $S(x',y')$ in the local coordinate system are:

$$\begin{aligned} S_x &= \frac{-\frac{P'_x}{\tan|\theta^{u}_{P}|} - P'_y}{\left(\frac{\cos|\theta^{u}_{P}|}{\sin\theta^{u}_{P}} - \frac{\cos|\theta^{l}_{Q}|}{\sin\theta^{l}_{Q}}\right)} \\ S_y &= \frac{\cos|\theta^{l}_{Q}|}{\sin\theta^{l}_{Q}} S_x \end{aligned}$$

See appendix A for more details of this derivation. Now the distance between the roots of the SYDs (stitch yarn penetration points) and the intersection point S can easily be calculated as:

$$\begin{aligned} D^{E,F}_{P,Q} &= \sqrt{(P'_x - S_x)^2 + (P'_y - S_y)^2} \\ D^{F,E}_{Q,P} &= \sqrt{(S_x)^2 + (S_y)^2}, \end{aligned} \tag{2.2}$$

where E and F refer to an arm of a SYD ($1-4$, see figure 2.6(b)) in point P in the upper ply and point Q in the lower ply respectively, see figure 2.7. The subscripts P and Q indicate the points P and Q defined in definition 2, to indicate the roots of the intersection distance. This information will be needed for the intersection search algorithm, to be used in the numerical program that configures a network flow model as will be described later in chapter 4.

Intersection Point Presence

The intersection point S only exists if the intersection distances are smaller than or equal to half the length of their corresponding SYD. This means that the following statements have to be satisfied both:

$$D^{E,F}_{P,Q} \leq \frac{l^{u}_{P}}{2} \tag{2.3a}$$

$$D^{F,E}_{Q,P} \leq \frac{l^{l}_{Q}}{2} \tag{2.3b}$$

Considering definition 2: for a particular point P, the tracing integers m and n may be varied independently in order to trace the stitch yarn penetration points Q in the x- and y-direction of the piece

Table 2.1. SYD intersection configurations. Once the SYD-arm from point P does not reach the calculated intersection point, no further intersections with this arm will be found when continuing with tracing stitch penetration points Q in a particular direction. This situation will be indicated by the combination $m = 0$ and $n = 0$. Increasing an integer by 1, means replacing the point Q in order to find a new intersection point with the arm from point P.

equation (2.3a) satisfied	✓	✓	×	×
equation (2.3b) satisfied	✓	×	✓	×
y-direction	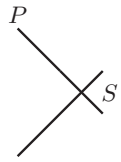	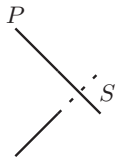	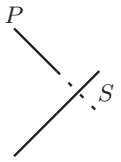	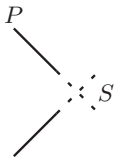
next point Q	$n = n + 1$ $m = 0$	$n = n + 1$ $m = 0$	$n = 0$ $m = 0$	$n = 0$ $m = 0$
x-direction	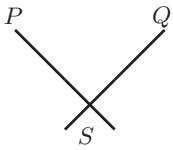	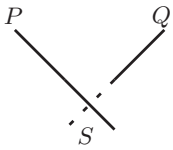	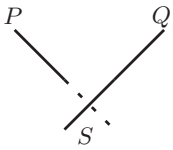	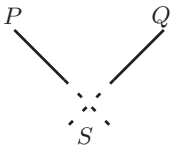
next point Q	$n = 0$ $m = m + 1$	$n = 0$ $m = m + 1$	$n = 0$ $m = 0$	$n = 0$ $m = 0$

of NCF to find the intersection points. This will be done by abovementioned algorithm, to be used in the numerical program.

Visual inspection of the NCF was leading to the restriction that intersection points, characterised by $m > 0$ and $n > 0$ are not likely to occur. Consider for example figure 2.7, in which connections between points (α, β) and $(\alpha + 1, \beta)$ or (α, β) and $(\alpha, \beta + 1)$ will be sought for. However, processing the restriction in the search algorithm to minimise its computational work results for example in the absence of a connection search between the points (α, β) and $(\alpha + 1, \beta + 1)$.

Table 2.1 shows schematically the treatment of the tracing integers m and n. The lines represent the lengths of the SYD-arms. According to the specific situation, it will be determined if more intersections of the arm in point P with the arm in a next replaced point Q are possible. When both tracing integers m and n are zero, no intersection will be searched for and point P should be replaced to another stitch yarn penetration point. Then again points Q will be determined by varying tracing integers m and n in order to detect other intersections with the SYD arm that is associated with the replaced point P. This process will continue until both tracing integers m and n are, according to table 2.1, zero again.

Example

An example of a pair of points according to definition 2 and its associated intersection distance and possible presence will be done with help of the shaded area in figure 2.7. The possibility of a connection of the third arm ($E = 3$) in point $P^u_{\alpha+1,\beta+1}$ with the second arm in a lower located point, will be examined. Tracing integers are set to:

$$m = 0 \qquad n = 2,$$

such that the point Q becomes:

$$Q^l_{\alpha+1+0,\beta+1+2} = Q^l_{\alpha+1,\beta+3}$$

A local coordinate system will be defined with its origin in point $Q^l_{\alpha+1,\beta+3}$, the position of the intersection point S may be calculated and the intersection distances:

$$D^{3,2}_{\substack{\alpha+1,\beta+1\\ \alpha+1,\beta+3}} \qquad D^{2,3}_{\substack{\alpha+1,\beta+3\\ \alpha+1,\beta+1}}$$

results by using (2.2). According to table 2.1 the presence of the intersection will be validated, which is the first case in the y-direction for this example.

2.3 Model Extensions

2.3.1 External Channels

As can be seen near region I in figure 2.1, compression caused by a closing mould pushes the stitch yarns into the fibrous ply. Actually, the drawn stitch yarn that creates the external channels consists of two stitch yarns at the bottom face, as can be seen by watching figure 2.4(c) closely. Since these yarns are close together, it is unlikely that the fluid flows massively in between these stitch yarns. Therefore, these two stitch yarns are assumed to be one stitch yarn that travels from one stitch yarn penetration point to another stitch yarn penetration point.

Due to the compression mechanism, a channel will be created on both sides of the stitch yarn. The cross-sectional geometry of the channel has been idealised in order to do a parametric study, see figure 2.8. It has been assumed that the cross-sectional area is constant over the channel's length and that pushing the stitch yarn in the fibrous ply could lead to deformation of the stitch yarn's cross-section. This leads to an elliptical cross-section with major axis $2e$ and minor axis $2f$. The maximum height of the channel is characterised by the minor axis of the stitch yarn's cross-section. The elliptical cross-section results in a varying radius, which is a part of the boundary of the flow channel. This varying radius is related to the ratio between the major and minor axes. This ratio is characterised by the assumption that the cross-sectional area of the stitch yarn remains constant during the compression, such that:

$$\frac{f}{e} = \frac{1}{4}\left(\frac{d_c}{e}\right)^2, \tag{2.4}$$

in which d_c is the compacted diameter of the stitch yarn, see equation (2.1). Microscopic research is needed to determine the actual cross-sectional dimensions of these channels, see section H.5.

2.3.2 SYD Domain Obstacles

Objects in a flow channel generally influence the flow behaviour. It has been shown by Hu and Liu [36] and Nordlund and Lundström [37] that solid cylinders, representing the stitch yarns in flow channels, influence the permeability of these channels significantly.

Figure 2.1 shows a sketch of the region where the stitch yarns with diameter d_c penetrate the NCF, as indicated by region II in figure 2.1. This region is also indicated by the rotated squares in figure 2.6 and can be described by the domain in figure 2.9. The four opening surfaces are numbered $1-4$. Each opening represents the connection with the SYD-arms, as they were numbered for the SYD pair in figure 2.6(b).

The width $b = b^u = b^l$ and height h of the SYD dimensions are directly related to this flow domain around the penetrating stitch yarns with a compacted diameter d_c. The penetrating stitch yarns could

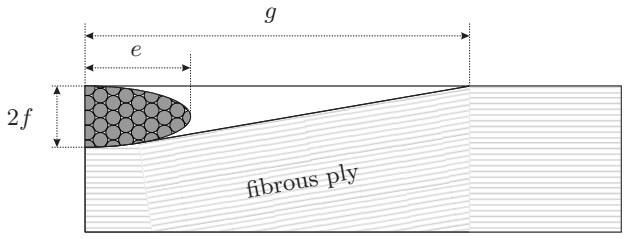

Fig. 2.8. The flow channel (unfilled area), created by pushing the stitch yarn in the fabric.

be positioned arbitrary in reality. For this geometry description, the yarns are positioned as in figure 2.9(b), such that the widths of the upper and lower SYDs of one SYD pair are equal.

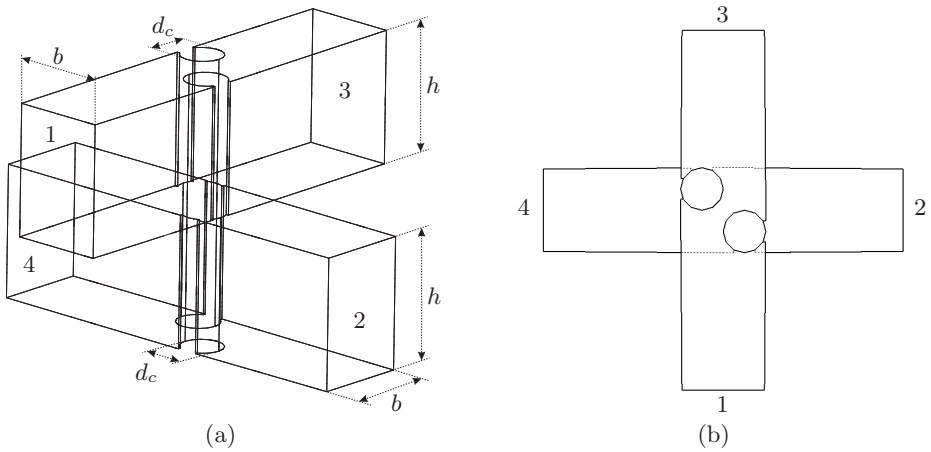

Fig. 2.9. Flow domain around the penetrating stitch yarns and its characteristics.

3

Flow Modelling

The pressure-driven steady state flow of a liquid through long, straight and rigid channels of any constant cross-sectional shape (Hagen-Poiseuille flow), is often characterised by the hydraulic resistance:

$$R = \frac{\Delta p}{\Phi}, \tag{3.1}$$

in which Δp is the pressure drop over the channel and Φ the volume flow through the channel. A natural unit for the hydraulic resistance is given by dimensional analysis as:

$$R^* \equiv \frac{\mu L}{\mathcal{A}^2}, \tag{3.2}$$

in which $\mathcal{A}$ is the cross-sectional surface, μ the viscosity and L the channel's length. The shape of a cross-section is characterised by its compactness:

$$\mathcal{C} \equiv \frac{\mathcal{P}^2}{\mathcal{A}}, \tag{3.3}$$

in which $\mathcal{P}$ is the cross-section's perimeter. Flow channels to be dealt with in this thesis, exhibit a rectangular cross-section approximately. The compactness for a rectangular cross-section with dimensions b and h is:

$$\mathcal{C} = 4\frac{h}{b} + 4\frac{b}{h} + 8 \qquad \text{with} \qquad b < h \tag{3.4}$$

Since the hydraulic resistance depends on the the compactness, this dependence may be included by defining a dimensionless geometrical correction factor:

$$\alpha \equiv \frac{R}{R^*} \tag{3.5}$$

Additionally, comparison with Darcy's law in (1.1) and (1.3) gives:

$$\alpha = \frac{\mathcal{A}}{K} = \frac{\mathcal{A}^2}{K^A} \tag{3.6}$$

There are different ways to determine the hydraulic resistance and the geometrical correction factor of a rectangular channel for which some of them are shown in section 3.1. Section 3.2 shows different ways to model the flow domains of an NCF. One of these will be used in this thesis for which permeability relations for the geometries of SYDs (section 2.2), region I in figure 2.1 (section 2.3.1) and region II in figure 2.1 (section 2.3.2) need to be derived and determined to serve as an input. This will be done in sections 3.3, 3.4.1 and 3.4.2 respectively. The results may be explained by using the equations (3.1)-(3.6) and its derivations in section 3.1.

3.1 Channel Flow

Consider fully developed, steady and incompressible laminar flow (Poiseuille flow) between horizontal infinite plates as shown in figure 3.1. The plates are separated by a distance b and are considered infinite in z-direction. To find an expression for the hydraulic resistance R for this configuration, a control volume formulation for the momentum equation (1.10) (Newton's second law) will be used:

$$\mathbf{F} = \mathbf{F}_S + \mathbf{F}_B = \frac{\partial}{\partial t}\int_{CV} \rho \mathbf{u} \mathrm{d}\mathcal{V} + \int_{CS} \rho \mathbf{u}\mathbf{u} \cdot \mathrm{d}\mathbf{n}, \tag{3.7}$$

where $\mathbf{F}_S$ and $\mathbf{F}_B$ are the surface and body forces respectively and $\mathrm{d}\mathbf{n}$ is the differential Cartesian component of the outward normal surface vector. The first integral will be taken over the control volume, whereas the second integral will be taken over the control surface. For this analysis, a control volume of size $\mathrm{d}\mathcal{V} = \mathrm{d}x\mathrm{d}y\mathrm{d}z$ as in figure 3.1 will be selected. Evaluation of the x-component of the control volume based momentum equation (3.7) and processing the absence of body forces, gives:

$$F_{Sx} = \cancelto{0,\,\text{steady state}}{\frac{\partial}{\partial t}}\int_{CV} \rho u \mathrm{d}\mathcal{V} + \cancelto{0,\,\text{fully developed}}{\int_{CS} \rho u \mathbf{u} \cdot \mathrm{d}\mathbf{n}} \tag{3.8}$$

Due to the fully developed (no net momentum flux through control surface) and steady state situation, the right hand side equals zero.

Pressure and shear forces in the x-direction act on the control volume surfaces as shown in figure 3.1. The surface forces will be described by using a Taylor series expansion about the centre of the element. Summing them leads to:

$$F_{Sx} = \left(p - \frac{\partial p}{\partial x}\frac{\mathrm{d}x}{2}\right)\mathrm{d}y\mathrm{d}z - \left(p + \frac{\partial p}{\partial x}\frac{\mathrm{d}x}{2}\right)\mathrm{d}y\mathrm{d}z - \left(\tau_{yx} - \frac{\mathrm{d}\tau_{yx}}{\mathrm{d}y}\frac{\mathrm{d}y}{2}\right)\mathrm{d}x\mathrm{d}z + \left(\tau_{yx} + \frac{\mathrm{d}\tau_{yx}}{\mathrm{d}y}\frac{\mathrm{d}y}{2}\right)\mathrm{d}x\mathrm{d}z,$$

with τ_{yx} a component of the viscous stress tensor. The total derivative for the Taylor series expansion of τ_{yx} may be used since $u = u(y)$. Substitution in (3.8) gives:

$$\frac{\mathrm{d}\tau_{yx}}{\mathrm{d}y} = \frac{\partial p}{\partial x},$$

in which the left and right hand side are equal to a constant, since p and τ_{yx} are dependent on different Cartesian coordinates. Assuming a Newtonian fluid:

$$\tau_{yx} = \mu\frac{\mathrm{d}u}{\mathrm{d}y},$$

and integrating twice gives:

$$u = \frac{1}{2\mu}\left(\frac{\partial p}{\partial x}\right)y^2 + \frac{c_1}{\mu}y + c_2 \tag{3.9}$$

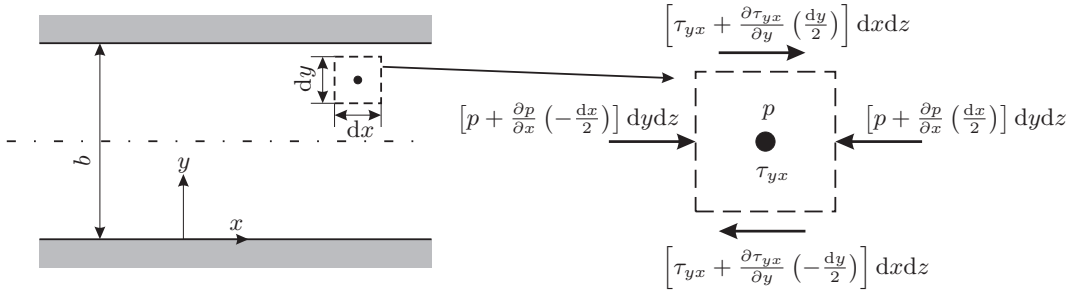

Fig. 3.1. Control volume for laminar flow between stationary infinite plates. On the right: forces acting on the control volume.

Actually, simplifying the Stokes flow equation (1.14) followed by the integration steps above, leads to the velocity profile (3.9) as well. Using the boundary conditions:

$$\begin{aligned} u &= 0 \qquad \text{at} \qquad y = 0 \\ u &= 0 \qquad \text{at} \qquad y = b, \end{aligned}$$

to solve the unknown coefficients c_1 and c_2 finally gives the following velocity profile:

$$u = \frac{b^2}{2\mu}\left(\frac{\partial p}{\partial x}\right)\left[\left(\frac{y}{b}\right)^2 - \left(\frac{y}{b}\right)\right] \tag{3.10}$$

For a particular depth h in the z-direction, the volume flow rate per unit depth may be calculated as:

$$\frac{\Phi}{h} = \int_0^b u \mathrm{d}y \tag{3.11}$$

Substitution of (3.10) in (3.11), solving the integral and assuming a linear varying pressure over a length L:

$$\frac{\partial p}{\partial x} = -\frac{\Delta p}{L},$$

finally gives:

$$\frac{\Phi}{h} = \frac{b^3 \Delta p}{12 \mu L} \tag{3.12}$$

Comparing this result with equation (3.1) gives a relation for the hydraulic resistance of a channel with a constant rectangular cross-section and length L:

$$R = \frac{12\mu L}{b^3 h}$$

Using (3.2) and (3.5) results in an expression for α, dependent on b and h that are related to the compactness according to (3.4):

$$\alpha = 12\frac{h}{b} \tag{3.13}$$

Relating this result to equation (3.6), gives an expression for the area included permeability:

$$K^A = \frac{b^3 h}{12} \qquad \text{with} \qquad b < h \tag{3.14}$$

In the literature [3, 38, 39], other relations for the hydraulic resistance of a tube with a constant rectangular cross-section can be found. Mortensen *et al.* [38] related the compactness $\mathcal{C}$ to the geometrical correction factor α, by using an analytical solution for the velocity field over a rectangular cross-section (Hagen-Poiseuille flow). The resulting relation is:

$$\alpha(\mathcal{C}) \approx \frac{22}{7}\mathcal{C} - \frac{65}{3} + \mathcal{O}([\mathcal{C} - 18]^2), \tag{3.15}$$

in which the compactness (3.4) for a rectangular cross-section was used.

The hydraulic radius of an arbitrarily shaped cross-section is often used as well [3]. This radius is defined as the radius of a circular cross-section, for which the flow resistance equals the flow resistance of the arbitrarily shaped cross-section. It is defined as:

$$r_H \equiv \frac{2\mathcal{A}}{\mathcal{P}} \tag{3.16}$$

Table 3.1. Laminar friction factors for a rectangular cross-section with height h and width b. The graph of (3.19) in figure 3.2 was constructed by using a sixth order polynomial fit, constructed with these data.

b/h	0	0.05	0.1	0.125	0.167	0.25	0.4	0.5	0.75	1
$\mathcal{F}$Re	96	89.91	84.86	82.34	78.81	72.93	65.47	62.19	57.89	56.91

Actually, this concept was developed for turbulent flows, i.e. flows in which secondary flows are present [39, 40]. The permeability of a circular cross-section is:

$$K = \frac{r_H^2}{8} \tag{3.17}$$

Using this concept to derive the hydraulic resistance for a rectangular cross-section by using (3.6) and (3.17) gives:

$$\alpha = \frac{8(2b + 2h)^2}{bh} \tag{3.18}$$

The hydraulic radius concept could be corrected for laminar flow and the cross-sectional shape. Related to the laminar area in the Moody-diagram for pipe flow, the radius of a tube with a flow resistance that corresponds with the flow resistance of a rectangular cross-section is:

$$r = \frac{64}{\mathcal{F}\mathrm{Re}} r_H,$$

with the empirically determined term $\mathcal{F}$Re in table 3.1, as can be found in classical fluid mechanics books like White [39]. The factor $\mathcal{F}$ is the Darcy-Weisbach friction factor. Expanding equation (3.18) with this correction term gives:

$$\alpha = \frac{(\mathcal{F}\mathrm{Re})^2}{2048} \frac{(2b + 2h)^2}{bh} \tag{3.19}$$

Figure 3.2 shows the geometrical correction factors α according to equations (3.15), (3.13), (3.18) and (3.19). Applying the hydraulic radius concept as in (3.18) on a slow viscous flow situation, gives probably an underestimation of the permeability (see equation (3.6)).

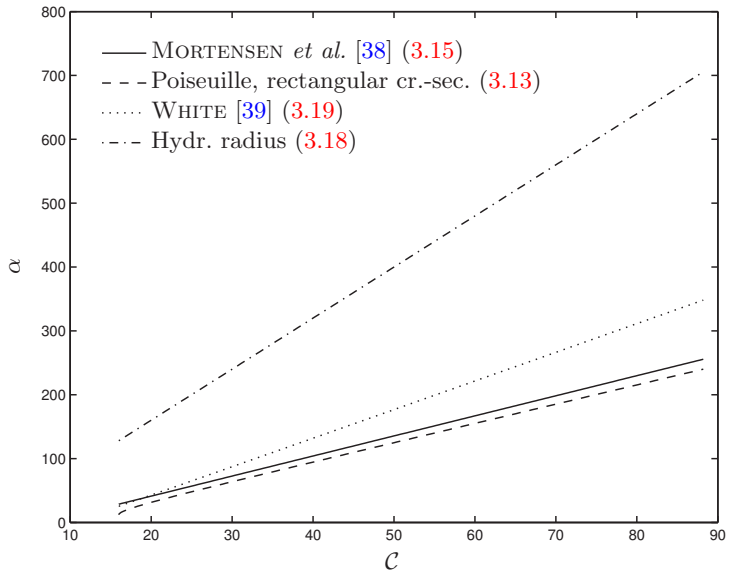

Fig. 3.2. Geometrical correction factors according to different approximations to laminar flow in a tube or duct with an uniform rectangular cross-section.

3.2 NCF Meso Level based Flow Models

Lomov [28, 41–43] describes the geometry of fibre yarns by using the developed textile geometry software package WiseTex. It can be used to model different types of textiles like weaves and NCFs. Belov [44] is mainly using unit cells, generated by WiseTex [28, 41, 43], which serve as the geometrical domain. A lattice Boltzmann method was used, developed and tested by Spaid [45], to solve the flow problem. A lattice Boltzmann method is equivalent to a hybrid method like combinations of Stokes (1.14) and Brinkman (1.16) equations and is a numerical scheme, which allows flows through complex geometry like a textile, to be dealt with. Nordlund and Lundström [4, 21, 33, 37, 46] use Computer Aided Design (CAD) tools to model the flow domain. The solutions were obtained by using the Computational Fluid Dynamics (CFD) software ansys cfx-5.

Nordlund [4] and Loendersloot [3] developed NCF specified permeability models independently, which will be described sections 3.2.1 and 3.2.2 respectively. These permeability models could be used for any type of NCF. Only small modifications in the model will be needed to include type dependent features of the particular NCF type.

3.2.1 Multidimensional Flow Domain

The first attempt of Nordlund to model the geometrical domain of an NCF was done by assuming the distorted regions as continuous channels [46]. The unit cell approach was used (figure 1.6), and therefore only one small piece of the NCF served as the geometrical domain, see figure 3.3(a) and 3.3(b). The solids are the inter bundle domains and are assumed to dominate the flow by setting the no-slip boundary condition at the fluid-fibre yarn interface. This unit cell was modelled using CAD tools. The domain was discretised using cfx-5 meshing tools to obtain triangular elements on the

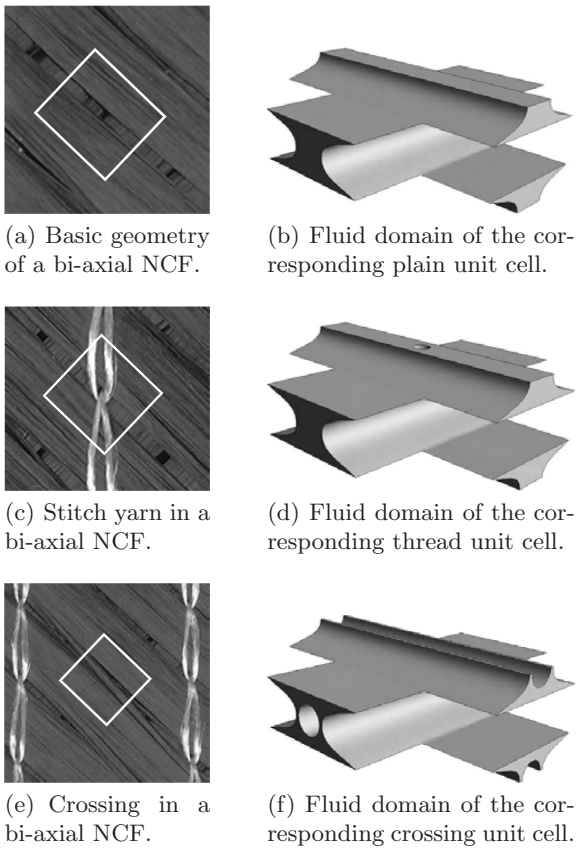

(a) Basic geometry of a bi-axial NCF.

(b) Fluid domain of the corresponding plain unit cell.

(c) Stitch yarn in a bi-axial NCF.

(d) Fluid domain of the corresponding thread unit cell.

(e) Crossing in a bi-axial NCF.

(f) Fluid domain of the corresponding crossing unit cell.

Fig. 3.3. Three different unit cells, identified by Nordlund. A network was created, containing these different unit cells [33].

surface, after which the tetrahedral element containing volume mesh was generated. The flow problem was solved by CFX-5, using a slow flow (Re << 1, i.e. laminar) that is incompressible, see appendix B and [47] for more details. The HRS difference scheme was used for the advection term in equation (1.8) and (1.10). A stitch yarn interrupting domain (figure 3.3(c) and 3.3(d)) was modelled as well and showed the decrease in permeability. The simulation results were an overestimation of the permeability compared to the experiments, mainly caused by the assumption of continuous channels throughout the fabric.

Because of the differences in permeability, NORDLUND [37] kept the unit cell approach, but now three different basic unit cells were used to model the fabric, i.e. the plain, the stitch yarn containing and the crossing containing unit cell, see figure 3.3(a)-3.3(f). Again, no-slip boundary conditions were applied at the fluid-fibre yarn interface. A parametric study had been carried out in order to indicate the dependence of the permeability on the channel dimensions. It came out that the stitch yarn could reduce the local permeability by around 5.5% and the crossings could reduce it up to 75%, compared to unit cells without these features. These features did influence the permeability of the wider channels more than the narrow channels. The main conclusion was that a model to predict the global permeability of an NCF, should account for statistical variations in the channel dimensions in order to obtain realistic permeability predictions.

Later, NORDLUND [33] proposed a model to predict the effective permeability of a piece of NCF at the macro level. This model consists of a network of the three different unit cells in figure 3.3. Statistical variations were accounted for and the model predictions were approaching the experimental results (see section 6.1.5 for values).

Also, the assumption of no-slip at the boundaries was investigated by NORDLUND [21]. To incorporate the porous effect of the bundle, slip conditions were applied at the fluid-fibre yarn interface. The amount of slip was determined by using Brinkman's equation (1.16) to describe the flow inside the fibre yarns. Permeability of the fibre yarn was determined by equation (1.15) and the use of $K_{0,||}$ and $K_{0,\perp}$ according to GEBART [9]. It came out that using the no-slip boundary condition for fibre yarns with a high fibre volume fraction V_f is reasonable. In case of a low V_f in the fibre yarns, the slip condition have to be applied in order to obtain a reasonable permeability prediction.

3.2.2 One-Dimensional Flow Domain

Since the NCF permeability modelling approach that uses difference and finite element schemes, requires a lot of computational work (especially when statistical variations have to be accounted for), LOENDERSLOOT [3, 34, 35, 48–50] approximated the inter bundle channels by Stitch Yarn induced fibre Distortions (SYDs), which can be represented by 1D elements. This model assumes that the flow in an NCF is mainly governed by flow through the SYDs, thus at the meso-level (figure 2.1). A coupled network of SYDs with statistical variations in their dimensions could serve as a representation for a whole, or at least a part of the textile. Because solving the fluid problem in a SYD is computationally efficient, a whole network of SYDs with statistical variations in their dimensions can be solved with relative ease.

Imagine the NCF is approximated by a network of connected channels (SYDs), which are filled by an incompressible fluid. The fluid in the channels is at rest. When pushing the fluid in a single channel, the flow will move. It will not only move in this particular channel, but it will move in the subsequent connected channels as well, due to the incompressibility. So an action at one side of the domain, results directly in an action at the other side of the domain. It is very convenient to solve differential equations related to such characteristics by the finite element method.

In first instance, predicting the filling behaviour in NCF's does not require detailed knowledge about the velocity profiles in each channel. Unlike many other flow problems, the momentum (Navier-Stokes) equations (1.10) will not be used as the governing equations to describe the flow. Instead, the continuity equation (1.8) will be used to describe the macroscopic behaviour of the channels, i.e. the flow rates in the channels. Globally, a channel exhibits flow in one direction, such that this one-dimensional (1D) appearance will be maintained by averaging the fluidic and geometrical properties of a channel over its length. This means these properties are constant over the length of the channel and thus these channels can be treated as 1D. The incompressibility condition, which means a constant density, leads to the following simplified continuity equation as in (1.9), but for one dimension:

$$\frac{\mathrm{d}u}{\mathrm{d}x} = 0,$$

where u is the velocity component in x-direction. The channel's flow rate Φ can be obtained by integrating the velocity distribution over the cross-sectional area $\mathcal{A}$:

$$\Phi = \int_{\mathcal{A}} u \mathrm{d}\mathcal{A}$$

Because velocity is constant in a 1D channel, flow rate Φ will be constant as well and leads to the governing equation for this flow problem:

$$\frac{\mathrm{d}\Phi}{\mathrm{d}x} = 0 \tag{3.20}$$

This equation has to be satisfied at every point in the domain, i.e. in the 1D channel of length L and is called the strong form formulation. The weak form of (3.20) is:

$$\int_L \omega \frac{\mathrm{d}\Phi}{\mathrm{d}x} \mathrm{d}x = 0,$$

which is valid for all arbitrarily finite functions ω, which are not allowed to contain singular terms. As a consequence of the integral formulation, the restriction in (3.20) will be met in an averaged sense. Applying the chain rule of differentiation results in:

$$\int_L \frac{\mathrm{d}}{\mathrm{d}x}(\omega\Phi)\mathrm{d}x - \int_L \frac{\mathrm{d}\omega}{\mathrm{d}x}\Phi \mathrm{d}x = 0,$$

and subsequently:

$$\int_L \frac{\mathrm{d}\omega}{\mathrm{d}x}\Phi \mathrm{d}x = \omega\Phi,$$

where one integral has been left in order to incorporate a constitutive relation and finally obtain some kind of element matrix (stiffness matrix in solid mechanics problems). In solid mechanics problems a constitutive relation like Hooke's law can be used to relate stresses to strains by using properties of the conducting continuum. Here, we use the 1D formulation of Darcy's law (1.3) with the area included permeability as a constitutive relation, to relate flow rates and pressures:

$$\int_L \frac{\mathrm{d}\omega}{\mathrm{d}x} \frac{K^A}{\mu} \frac{\mathrm{d}p}{\mathrm{d}x} \mathrm{d}x = \omega\Phi \tag{3.21}$$

A 1D element is defined by two nodes, see figure 3.4. If pressure p is known at the nodes, one can interpolate the pressure to obtain pressure at a particular position x in the element. Due to the nature of this 1D formulation, element properties are given in an averaged way. Therefore a linear

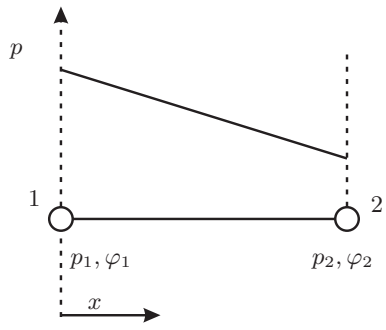

Fig. 3.4. Assuming a linear pressure profile over a 1D element.

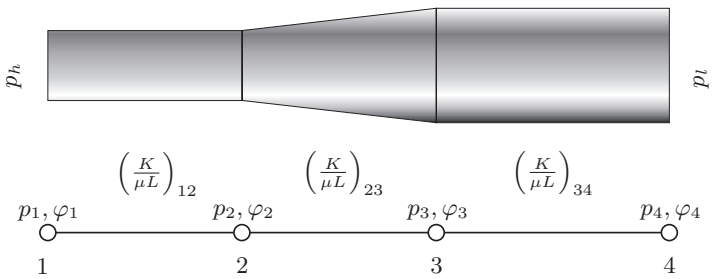

Fig. 3.5. A tube consisting of three parts with different permeabilities and lengths. Viscosity will be constant for all elements for steady state situations and variable for transient situations (fill simulation, see section 4.3).

pressure profile over the element is assumed. Suppose we store the nodal pressures p_1 and p_2 in a nodal pressure vector $\mathbf{p}$, then pressure along the element can be expressed as:

$$p = \mathbf{N} \cdot \mathbf{p} = \begin{Bmatrix} 1 - \frac{x}{L} \\ \frac{x}{L} \end{Bmatrix} \cdot \begin{Bmatrix} p_1 \\ p_2 \end{Bmatrix},$$

where $\mathbf{N}(x)$ is the linear interpolation function (or shape function). Taking the derivative of this expression with respect to x gives:

$$\frac{\mathrm{d}p}{\mathrm{d}x} = \frac{\mathrm{d}\mathbf{N}}{\mathrm{d}x} \cdot \mathbf{p} = \begin{Bmatrix} -\frac{1}{L} \\ \frac{1}{L} \end{Bmatrix} \cdot \begin{Bmatrix} p_1 \\ p_2 \end{Bmatrix} \tag{3.22}$$

Applying the method of Galerkin [51] by choosing the interpolation function $\mathbf{N}$ for the weighting function ω and substitution of (3.22) in (3.21) and noting that $\mathbf{p}$ represents nodal values and thus can be taken out of the integral, gives:

$$\int_L \frac{\mathrm{d}\mathbf{N}}{\mathrm{d}x} \frac{K^A}{\mu} \frac{\mathrm{d}\mathbf{N}}{\mathrm{d}x} \mathrm{d}x \cdot \mathbf{p} = \boldsymbol{\varphi},$$

where $\boldsymbol{\varphi}$ are the nodal nett fluxes and are known only at the nodes (compare with the force vector in solid mechanics problems). Working out the dyadic product of the interpolation functions $\mathbf{N}$:

$$\int_L \frac{K^A}{\mu L^2} \begin{bmatrix} 1 & -1 \\ -1 & 1 \end{bmatrix} \mathrm{d}x \cdot \mathbf{p} = \boldsymbol{\varphi}$$

Processing the integral finally yields the FE formulation for a 1D element:

$$\frac{K^A}{\mu L} \begin{bmatrix} 1 & -1 \\ -1 & 1 \end{bmatrix} \cdot \mathbf{p} = \boldsymbol{\varphi}$$

Now a network can be created by connecting 1D elements. A global system of equations follows:

$$\mathbf{M} \cdot \mathbf{p} = \boldsymbol{\varphi}, \tag{3.23}$$

where $\mathbf{p}$ contains all nodal pressures, $\boldsymbol{\varphi}$ contains all the nodal nett fluxes and $\mathbf{M}$ is the system matrix, in which all element properties are stored. The elements contain one degree of freedom (DOF) n_d. A network of elements contains n number of nodes. Assembling all elements result in an $n \cdot n_d \times n \cdot n_d$ system matrix $\mathbf{M}$. Consider for example the tube in figure 3.5, in which a medium will flow because of the difference in pressure between p_h and p_l. The three unique parts of the tube will be described by three 1D elements that are connected by their nodes. For this configuration, equation (3.23) becomes:

$$\begin{bmatrix} \frac{K_{12}^A}{\mu_{12} L_{12}} & -\frac{K_{12}^A}{\mu_{12} L_{12}} & 0 & 0 \\ -\frac{K_{12}^A}{\mu_{12} L_{12}} & \frac{K_{12}^A}{\mu_{12} L_{12}} + \frac{K_{23}^A}{\mu_{23} L_{23}} & -\frac{K_{23}^A}{\mu_{23} L_{23}} & 0 \\ 0 & -\frac{K_{23}^A}{\mu_{23} L_{23}} & \frac{K_{23}^A}{\mu_{23} L_{23}} + \frac{K_{34}^A}{\mu_{34} L_{34}} & -\frac{K_{34}^A}{\mu_{34} L_{34}} \\ 0 & 0 & -\frac{K_{34}^A}{\mu_{34} L_{34}} & \frac{K_{34}^A}{\mu_{34} L_{34}} \end{bmatrix} \cdot \begin{Bmatrix} p_1 \\ p_2 \\ p_3 \\ p_4 \end{Bmatrix} = \begin{Bmatrix} \varphi_1 \\ \varphi_2 \\ \varphi_3 \\ \varphi_4 \end{Bmatrix}, \tag{3.24}$$

where the single subscript indicate the corresponding node and the double subscripts refer to a property of an element between the two nodes indicated by these subscripts. Because in this example there is only one DOF (i.e. the pressure) and there are 4 nodes, the system matrix becomes a 4×4 matrix.

Applying boundary conditions will complete the problem description. The pressures at nodes 1 and 4 should correspond to the pressures p_h and p_l at the openings of the tube respectively. Pressures at nodes 2 and 3 are in the interior domain of the tube and are unknown, but it is assumed that the pressure varies linearly over the element. Since it is unknown how much fluid will flow through the tube, the nett fluxes at nodes 1 and 4 are unknown as well. But since we have an incompressible fluid, the amount of flow that enters an element will leave the element as well, within a particular time interval. This means that the nett fluxes at the internal nodes 2 and 3 will be zero. Now we have two unknown pressures and two unknown nett fluxes and the system matrix in (3.24) represents four independent equations; hence the problem can be solved.

3.3 Stitch Yarn induced fibre Distortions

At points where SYDs intersect each other, nodes have to be assigned. Continuous regions in SYDs between those nodes can be described by 1D elements, derived in section 3.2.2. The characteristic property L of the element is the length of the continuous channel in a SYD between those nodes. This length can be determined with the intersection distances. Their determination is explained in section 2.2.1. The SYD is assumed to be a channel with constant height h and a linearly varying width b, see figure 3.6.

The linearly varying width b, cross-sectional area $\mathcal{A}$ and perimeter $\mathcal{P}$ of the channel in figure 3.6 can be described respectively by:

$$b(x) = \frac{b_2 - b_1}{L} x + b_1 \tag{3.25}$$

$$\mathcal{A}(x) = hb(x) \tag{3.26}$$

$$\mathcal{P}(x) = 2h + 2b(x)$$

The compactness according to (3.3) becomes:

$$\mathcal{C}(x) = 4\frac{h}{b(x)} + 4\frac{b(x)}{h} + 8, \tag{3.27}$$

which shows for a decreasing width b a more than linearly increasing compactness $\mathcal{C}$.

It was shown in section 1.3 that the 1D formulation of Darcy's law requires the cross-sectional area $\mathcal{A}$, perpendicular to the flow. So far, only straight channels with a uniform cross-section were considered. But a SYD has a linearly varying cross-sectional area $\mathcal{A}$ over its length, that is perpendicular to

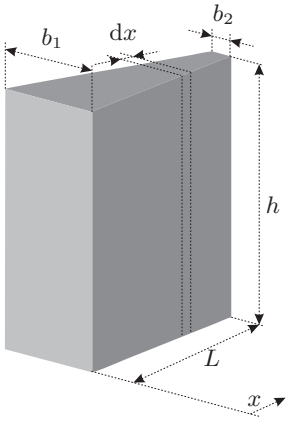

Fig. 3.6. Flow domain of a channel with a linear varying width.

the flow. If we take a slice of an infinite small length dx as in figure 3.6, its cross-sectional area $\mathcal{A}$ may be considered as being uniform over its length dx. This slice has a permeability that is dependent on its perimeter $\mathcal{P}(x)$ and cross-sectional area $\mathcal{A}(x)$. The whole channel can now be considered as serially connected sections of length dx. According to equation (1.6) in section 1.3, the effective permeability K_E can now be determined as:

$$K_E = L\left(\int_0^L \frac{1}{K(x)}\mathrm{d}x\right)^{-1},$$

or in case of the area included permeability:

$$K_E^A = L\left(\int_0^L \frac{1}{K(x)\mathcal{A}(x)}\mathrm{d}x\right)^{-1}$$

To find a relation for the permeability $K(x)$, a relation for the geometric correction factor $\alpha(\mathcal{C})$ is needed in equation (3.6). Different relations for $\alpha(\mathcal{C})$ were plotted in figure 3.2. The results of Mortensen *et al.* [38] (equation (3.15)) will be used, since those were obtained directly from the rectangular cross-sectional geometry (unlike converting to a circular cross-section with a hydraulic radius) and showed good agreement between their analytical and numerical results. Substitution of (3.25), (3.26), (3.27) and (3.15) in (3.6) gives:

$$K(x) \approx \frac{hb(x)}{\frac{22}{7}\left(4\frac{h}{b(x)} + 4\frac{b(x)}{h} + 8\right) - \frac{65}{3}}$$

Solving the integrals results in the following effective permeabilities:

$$K_E = \frac{21h^2b_2b_1(b_2 - b_1)}{264\left\{b_2^2b_1 - b_2b_1^2 - h^2b_1 + h^2b_2\right\} + 73hb_1b_2\ln\left(\frac{b_2}{b_1}\right)} \tag{3.28}$$

$$K_E^A = \frac{21h^3b_2^2b_1^2(b_2 - b_1)}{73\left\{b_2^2b_1h - b_2b_1^2h\right\} + 132\left\{b_2^2h^2 - b_1^2h^2\right\} + 264b_1^2b_2^2\ln\left(\frac{b_2}{b_1}\right)}, \tag{3.29}$$

where b_1 and b_2 refer to the widths of the channel in figure 3.6. These results were validated by using a finite element model in ANSYS CFX-5.

3.4 Model Extensions

This section describes the flow modelling within the domains that were parameterised in section 2.3, i.e. the external channels (region I in figure 2.1) and the region in the SYD with the penetrating stitch yarns (region II in figure 2.1). For convenience, just as was done by Hu and Liu [36], a dimensionless permeability $\mathcal{K}$ is defined as:

$$\mathcal{K} \equiv \frac{K^A}{K_0^A}, \tag{3.30}$$

where subscript 0 indicates the domain's permeability without the object. In this thesis, K_0^A will be referred to as the nominal area included permeability. The $\mathcal{K}$ is a useful measure to indicate the object's influence on the permeability directly.

Appendix C considers a domain for which a slow viscous flow problem (Re<< 1) was solved by Hu and Liu [36]. To validate the correct usage of ANSYS CFX-5, it's code has been subjected to this problem. Appendix C shows the results and good agreement was found. This validation was done, since the flow problems in section 3.4.1 and 3.4.2 will be solved by using ANSYS CFX-5.

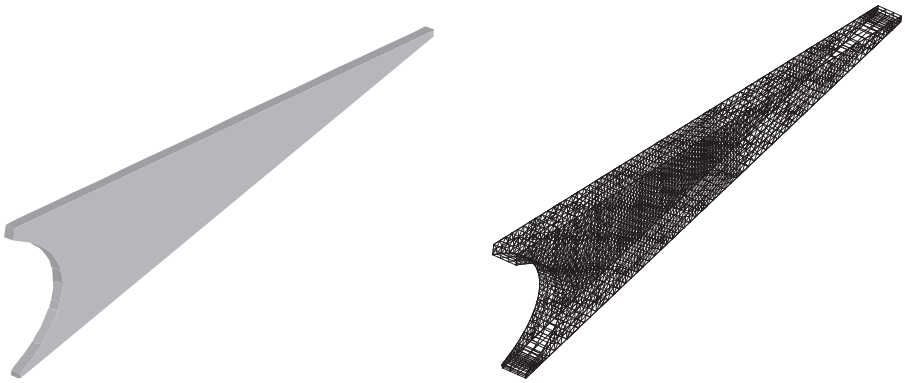

(a) Flow domain, to be meshed.

(b) 2D surface mesh, extruded to 3 layers.

Fig. 3.7. The flow domain which describes the channel, created by the stitch yarns. The number of plotted elements were insufficient to obtain an accurate approximation to the solution. However, they have been depicted like this to avoid a too high density of lines.

3.4.1 External Channels

The parameterisation for the external channels was done in section 2.3.1. These channels can be described by a 1D element, as described in section 3.2.2. It is likely that the channel dimensions show some distribution over a draped textile. The results of a parametric study, obtained by varying the cross-sectional dimensions independently, can be used easily to allocate an individual permeability to the elements that describe these external channels.

A parametric study to the domain in figure 2.8 was performed. The dimensions g and f have been varied independently in order to describe the permeabilities $K = K(g, 2f)$ and $K_0 = K_0(g, 2f)$. The dimension e is related to f by (2.4). During the simulations, sufficient fine meshes were created with the information obtained from the accuracy analyses in appendix D.2. The cross-sectional surface was meshed by using the `extruded 2D` mesh option in CFX-MESH. Figure 3.7(b) shows a typical mesh that was used. The surface mesh was extruded to three layers of equal length (see appendix D.1). As a result, the surfaces were meshed by triangular and quadrilateral elements. The volume mesh contains wedge elements (also referred to as triangular prisms).

The solution was obtained by assuming a laminar flow, a steady state situation and an incompressible fluid. Automatic time-stepping and the HRS difference scheme for the advection term were used, see appendix B. A pressure difference was created such that $1 \cdot 10^{-2} > \mathrm{Re} > 5 \cdot 10^{-6}$, which gives reliable results according to the accuracy analyses in appendix D.3. Low Reynolds numbers result in lower velocity gradients, which results in an increasing speed of convergence and a gain in computational time.

Results

Figure 3.8 shows the results of the channel's permeability K^A and its nominal permeability K_0^A. The nominal permeabilities were obtained by modelling and meshing the domain in figure 2.8 without the stitch yarn. A response surface through the obtained permeability values was created by a two-dimensional polynomial of the sixth order in the form of:

$$\tilde{K}^A_{(0)}(g, 2f) = \sum_{j=0}^{6} \sum_{k=0}^{6-j} a_{\underset{(0)}{jk}} g^j (2f)^k, \tag{3.31}$$

where a_{jk} are the fit coefficients, which are listed in appendix D.4. At least 28 evaluation points were needed to solve the coefficients for this sixth order polynomial fit. Even more points were needed to obtain a smooth fit. The huge number of points that were needed, were caused by the region of small

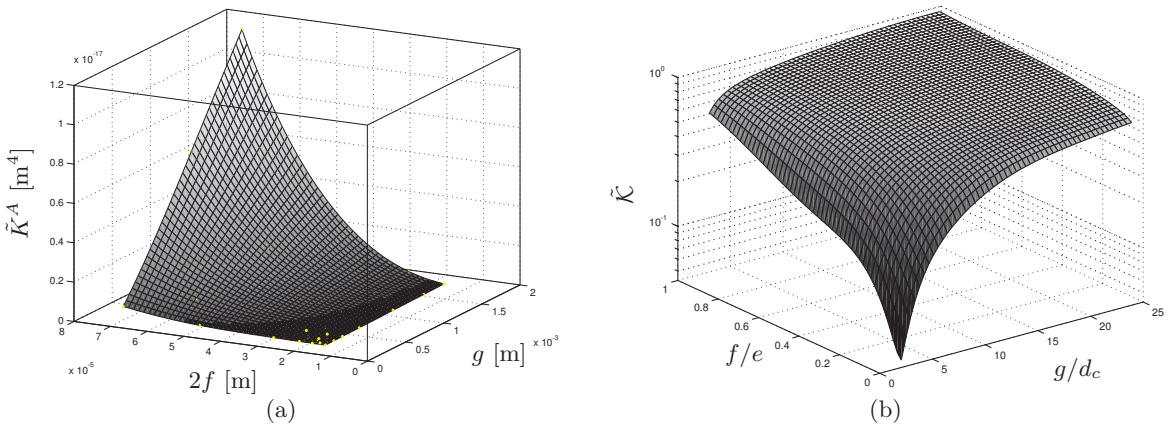

Fig. 3.8. See table D.1 for the fit data of the response surface. The dots are the evaluations points. In the area of small dimensions, a lot of points were needed to obtain a smooth fit. This explains the high density of evaluation points in this area.

dimensions of g and f. Therefore, density of the evaluation points have been increased in this region (see the tiny spheres in figure 3.8).

Figure 3.8(a) shows the result of $\tilde{K}^A(g, 2f)$. Increasing the greatest dimensions leads to a linear increasing permeability, whereas the smallest dimension $2f$ leads to a more than linear increasing permeability. Consider the relations in section 3.1 for flow through a rectangular cross-section. The external channel could be approximated by a rectangular channel with $2f < g$. Comparison with expression (3.14) for the area included permeability, gives:

$$K^A \sim \frac{(2f)^3 g}{12} \qquad \text{with} \qquad 2f < g \tag{3.32}$$

which explains the observed behaviour in figure 3.8(a).

The dimensionless permeability according to (3.30) was determined as:

$$\mathcal{K}\left(\frac{g}{d_c}, \frac{f}{e}\right) = \frac{\tilde{K}^A(g, 2f)}{\tilde{K}_0^A(g, 2f)}, \tag{3.33}$$

and is shown in figure 3.8(b). The dimensions g and $2f$ are made dimensionless as g/d_c and $2f/2e$ respectively.

As can be seen in figure 3.8(b), an increasing width of the channel and a constant volume assumption of the stitch yarn, will have a decreasing influence on the nominal permeability. At scales where the channel's width g is smaller than approximately fifteen times the stitch yarn diameter, the nominal permeability will be influenced significantly. In this region, the influence of the compression of the stitch yarn and its associated deformation (characterised by f/e) will be significant as well and shows a decreasing influence when g/d_c increases.

3.4.2 SYD Domain Obstacles

The parameterisation for the region in the SYDs with the penetrating stitch yarn was done in section 2.3.2. It is not possible to assign a single permeability to this region. The fluid in this domain could flow towards many openings, depending on the pressure condition and the different permeabilities in different directions. This means that flow paths between the openings are somehow commingled.

Considering the implementation of this direction dependent permeability in the NCF network model, it is not possible to describe this region with a single 1D element as described in section 3.2.2. However, a small assembly of 1D elements as in figure 3.9(b) can be used to describe this region's permeability with, such that the 1D element formulation from section 3.2.2 can still be used. The nodes $1-4$ represent the openings $1-4$ in figure 2.9. The elements describe all possible connections between the openings and contain a unique permeability.

Assembling the elements in figure 3.9(b) in a system matrix as was done in equation (3.24), gives:

$$\frac{1}{\mu}\begin{bmatrix} \frac{K_{12}^A}{L_{12}}+\frac{K_{13}^A}{L_{13}}+\frac{K_{14}^A}{L_{12}} & -\frac{K_{12}^A}{L_{12}} & -\frac{K_{13}^A}{L_{13}} & -\frac{K_{14}^A}{L_{12}} \\ -\frac{K_{12}^A}{L_{12}} & \frac{K_{12}^A}{L_{12}}+\frac{K_{13}^A}{L_{13}}+\frac{K_{14}^A}{L_{12}} & -\frac{K_{14}^A}{L_{12}} & -\frac{K_{13}^A}{L_{13}} \\ -\frac{K_{13}^A}{L_{13}} & -\frac{K_{14}^A}{L_{12}} & \frac{K_{12}^A}{L_{12}}+\frac{K_{13}^A}{L_{13}}+\frac{K_{14}^A}{L_{12}} & -\frac{K_{12}^A}{L_{12}} \\ -\frac{K_{14}^A}{L_{12}} & -\frac{K_{13}^A}{L_{13}} & -\frac{K_{12}^A}{L_{12}} & \frac{K_{12}^A}{L_{12}}+\frac{K_{13}^A}{L_{13}}+\frac{K_{14}^A}{L_{12}} \end{bmatrix} \cdot \begin{Bmatrix} p_1 \\ p_2 \\ p_3 \\ p_4 \end{Bmatrix} = \begin{Bmatrix} \varphi_1 \\ \varphi_2 \\ \varphi_3 \\ \varphi_4 \end{Bmatrix}, \tag{3.34}$$

for which it was assumed that all elements were filled with the same fluid with viscosity μ. Since the domain has some symmetry, the system matrix in (3.34) was constructed by using the following assumptions for the permeabilities and lengths, respectively:

$$\begin{aligned} K_{12}^A = K_{34}^A \qquad K_{13}^A = K_{24}^A \qquad K_{14}^A = K_{23}^A \\ L_{12} = L_{23} = L_{34} = L_{14} \qquad L_{13} = L_{24} \end{aligned} \tag{3.35}$$

The lengths are defined as:

$$\begin{aligned} L_{12} &\equiv \sqrt{\left(\frac{b}{2}\right)^2 + h^2} \\ L_{13} &\equiv b, \end{aligned}$$

where b and h are the lower and upper SYD dimensions.

Processing a load case like:

$$\mathbf{p} = \begin{Bmatrix} p_1 \\ p_2 \\ p_3 \\ p_4 \end{Bmatrix} = \begin{Bmatrix} 1 \\ 0 \\ 0 \\ 0 \end{Bmatrix} \text{ or } \begin{Bmatrix} 0 \\ 1 \\ 0 \\ 0 \end{Bmatrix} \text{ or } \begin{Bmatrix} 0 \\ 0 \\ 1 \\ 0 \end{Bmatrix} \text{ or } \begin{Bmatrix} 0 \\ 0 \\ 0 \\ 1 \end{Bmatrix} [\mathrm{Nm}^{-2}], \tag{3.36}$$

in the system matrix (3.34) results in three independent equations. The flow domain will be modelled and meshed as in figure 3.9(a). Applying one load case (3.36) and solving the momentum equations by using ANSYS CFX-5 finally gives the fluxes $\boldsymbol{\varphi}$ at the openings, after which the three independent

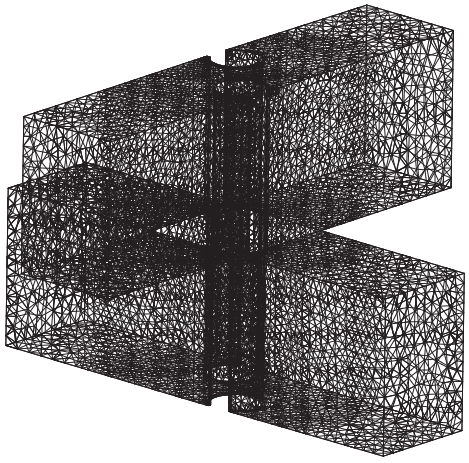

(a) Typical mesh of the flow domain in figure 2.9, as it has been used throughout the parametric study.

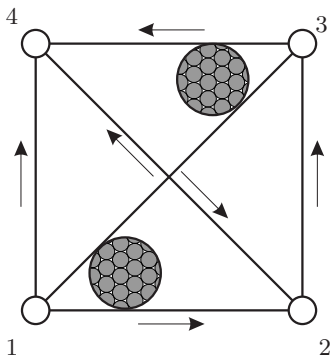

(b) The arrows indicate the local (element) positive coordinate direction.

Fig. 3.9. Flow domain near the SYD domain obstacles. The upper channel represents the upper SYD and the lower channel represents the lower SYD.

relations in (3.34) may be solved for K^A_{12}, K^A_{13} and K^A_{14}. The reliability of this method was shown by applying all different load cases in (3.36), as shown in appendix E.3.

The domain in figure 2.9 has been modelled without the stitch yarns as well, to obtain the nominal permeabilities. In this case, the domain contains even more symmetry, such that:

$$K^A_{\substack{0\\12}} = K^A_{\substack{0\\34}} = K^A_{\substack{0\\14}} = K^A_{\substack{0\\23}}$$
$$K^A_{\substack{0\\13}} = K^A_{\substack{0\\24}}$$

Then, the system matrix (3.34) reduces to two independent relations, which may be solved for $K^A_{0,12}$ and $K^A_{0,13}$ by using the flow solutions from ANSYS CFX-5 for the nominal flow domain. Subsequently, the results for the normal and nominal permeabilities will be processed in equation (3.30) to obtain the behaviour of the dimensionless permeability $\mathcal{K}$.

A parametric study on the domain in figure 2.9 was performed. The SYD dimensions h and b have been varied independently in order to describe the permeabilities $K = K(h,b)$ and $K_0 = K_0(h,b)$. The stitch yarn diameter was constant for all model configurations $d_c = 0.071$[mm]. The nominal permeabilities were obtained as well by meshing the domain in figure 2.9 without the stitch yarns. For the simulations, sufficiently fine meshes were used as they were determined with the accuracy analyses in appendix E.2. Triangular elements were used to mesh the surfaces and tetrahedral elements to mesh the volume. The domain around the stitch yarns was refined by using some layers of prismatic elements, over the length of the original elements that were located there (see figure 3.9(a)). Pressure boundary conditions were applied by using a load case as in (3.36), such that the Reynolds number was small enough to obtain a reliable solution (appendix E.1). The solution was obtained by assuming a laminar flow, a steady state situation and an incompressible fluid. Automatic time-stepping and the HRS difference scheme for the advection term were used (see appendix B).

Results

A response surface through the obtained permeability values was created by a two-dimensional polynomial of the third order in the form of:

$$\tilde{K}^A_{\substack{12\\13\\14}}(h,b) = \sum_{j=0}^{3}\sum_{k=0}^{3-j} a_{jk}\,h^j b^k \qquad (3.37)$$

$$\tilde{K}^A_{\substack{0\\12\\13}}(h,b) = \sum_{j=0}^{3}\sum_{k=0}^{3-j} a_{jk}\,h^j b^k, \qquad (3.38)$$

for the normal and nominal permeabilities respectively. At least ten evaluation points were needed to solve the coefficients for the third order polynomial fit. The fit coefficients a_{jk} are listed in appendix E.4. Appendix E.4 shows the plotted results of the permeabilities K^A_{12}, K^A_{13} and K^A_{14} as well. Unlike the explanation for the results of external channels in section 3.4.1, it is hard to relate these results ((non)-linearity) to the results (3.14) in section 3.1 that were found for Poiseuille flow through a rectangular channel, since this problem deals with flow through commingled paths. Globally, increasing dimensions h and b results in an increasing permeability, due to a decreasing compactness.

The dimensionless permeabilities according to (3.30) were determined as:

$$\mathcal{K}_{\substack{12\\13\\14}}\left(\frac{h}{b},\frac{b}{d_c}\right) = \left(\frac{\tilde{K}^A(h,b)}{\tilde{K}^A_0(h,b)}\right)_{\substack{12\\13\\(14)}}, \qquad (3.39)$$

for which the dimensions h and b were made dimensionless as h/b and b/d_c respectively. The results are depicted in figure 3.10 and show that all permeabilities K^A are increasingly being influenced by the stitch yarns, as the SYD width b decreases (for a constant stitch yarn diameter d_c). The connections

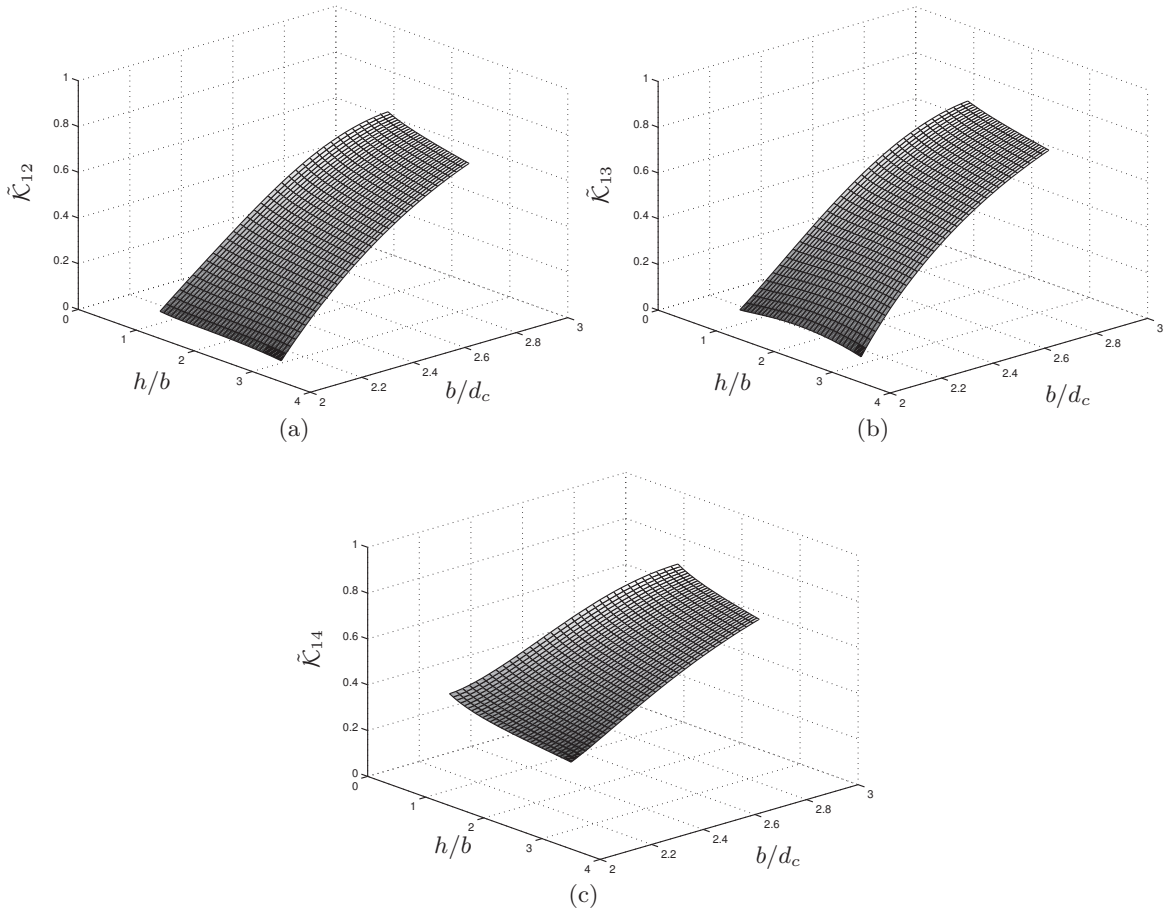

Fig. 3.10. Third order polynomial fitted response surface, which describes the dimensionless permeabilities $\mathcal{K}_{12}$, $\mathcal{K}_{13}$ and $\mathcal{K}_{14}$ for the three unique elements in figure 3.9(b).

between openings 1 and 2 and openings 3 and 4 are characterised by the fact that the fluid always has to flow around a stitch yarn. The connections between openings 1 and 4 and openings 2 and 3 do not have such an obstruction. Instead, the passage will only be smaller. These events show up in figures 3.10(a) and 3.10(c) in which the stitch yarns have more influence on the permeability K_{12}^A than on permeability K_{14}^A, when the SYD width decreases and the stitch yarn diameter remains constant. Globally (all results in figure 3.10), the effect of the presence of the stitch yarn on the permeabilities is highly dependent on the width of the channel, and weakly dependent on the height to width ratio of the channel.

4

Network Flow Model

In this chapter, relations from chapters 1, 2 and 3 have been assembled to obtain a network flow model, representing a piece of an NCF. In the future, the network flow model should somehow serve as a fill prediction tool, to predict infusion behaviour of products during the LCM process.

To obtain the permeability of a piece of NCF, a steady state solution of the pressure field has to be obtained. From this solution, an effective permeability of this piece of NCF can be determined, as will be explained in section 4.2. Additionally, a filling scheme was developed based on the network of 1D elements as described in section 4.3. It is a tool to simulate the infusion behaviour at the local scale (meso level) and gives more understanding of local flow processes during infusion, see section 4.3.2. However, the method and the principle of this filling scheme can be used to set up a filling scheme in the future based on global infusion behaviour (at macro level), as discussed in section 6.2.2.

The program, which handles the steady state problem and the transient problem, was written in the MATLAB syntax. The main structure of the program will be explained in section 4.1. The treatment and storage of the NCF variables will be explained as well.

4.1 Numerical Program

The network flow model was implemented in MATLAB by LOENDERSLOOT [3], and was able to solve a steady state situation of the problem, including statistical variations of the SYD dimensions. However, the program has been rewritten in order to incorporate different types of elements, related to the stitch yarns and inter ply connections, and to store properties at particular positions in the fabric more easily. To be more flexible in assigning permeabilities to elements, making the program structure suitable for a transient solution and improving the pre- and post-processing, were also the reasons to rewrite the program.

Each stitch yarn penetration point in the NCF has an associated pair of SYDs (two for a biaxial NCF, see figure 2.6(b)). This pair has properties like SYD lengths l^u and l^l, SYD widths b^u and b^l, SYD height h and orientation angles θ^u and θ^l. From drape simulation results (for example, using proposed models like TEN THIJE [1] and LAMERS [2]), new positions of stitch yarn penetration points and the shear angle at those positions, can be determined. All this information will be stored in a cell array [52], for each stitch yarn penetration point. Cell arrays are used, since they store data in an organised manner and are efficient in terms of memory usage. The program code has some annotations, which describe extensively where properties are stored.

The structure of the program is schematically shown in figure 4.2. The bounded area (dashed line) will be excluded when solving the steady state problem and will be executed when solving the transient problem. More details of the processes in this flow chart will be described in sections 4.2 and 4.3, while here some processes will be explained briefly.

Considering the first process in the flow chart, stitch yarn penetration point locations may be delivered from drape simulation results, or may be user specified by setting the number of stitch distances A and B. Subsequently, the abovementioned properties will be stored in the associated position in the cell array. Then, pre-processing may be continued by the SYD intersection search, as described in section 2.2.1. The results of the intersection search will be stored at the associated

positions of the cell array, in a multi-dimensional manner (see annotations in the code). Nodes are assigned to the intersections and elements will be created (third process in figure 4.2). Nodes can be numbered in two different directions. The direction may be specified by the user and determines the bandwidth of the coefficient matrix. This is useful for domains with a large aspect ratio, considering their in-plane dimensions.

Figure 4.1 shows a piece of an NCF and its resulting network of elements. Elements, representing the features described in section 3.3 and 3.4, i.e. SYDs and stitch yarn related regions, can be recognised. Blue and red elements represent the flow channels in the upper and lower ply respectively. The black elements represent the inter ply flow channels, i.e. channels that connect the lower ply to the upper ply and vice versa. A relation for the permeability of these elements has not been developed yet. These elements are set to be highly permeable to ignore their presence. Nodes are represented by the tiny spheres. The information of nodes are stored in an array called `nodes`. Elements and their associated nodes are stored in the array `Connect`. For each element, this array has additional information like its type. Different types of elements are:

- SYD elements.
- Elements, related to the stitch yarn that runs over the fibre bed, see region I in figure 2.1 (permeability of these elements will be referred to as K_{est}).
- Elements that represent the region in SYDs with the stitch yarn obstruction, see region II in figure 2.1 (permeability of these elements will be referred to as K_{ist}).
- Inter ply elements, which connect a SYD in the upper ply with the SYD in the lower ply.

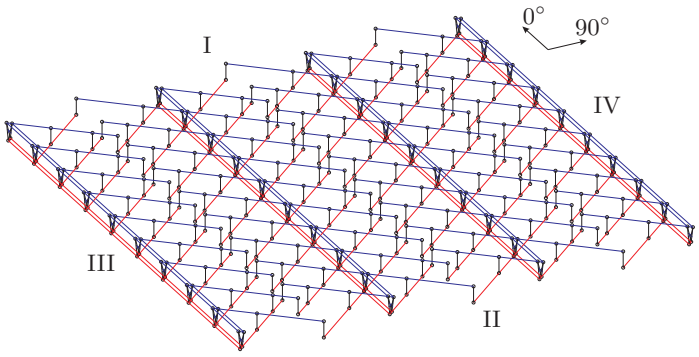

(a) Representation of a piece of NCF by elements, as sketched in figure 4.1(b). The Roman numbers indicate the textile's sides, at which pressure boundary conditions may be applied.

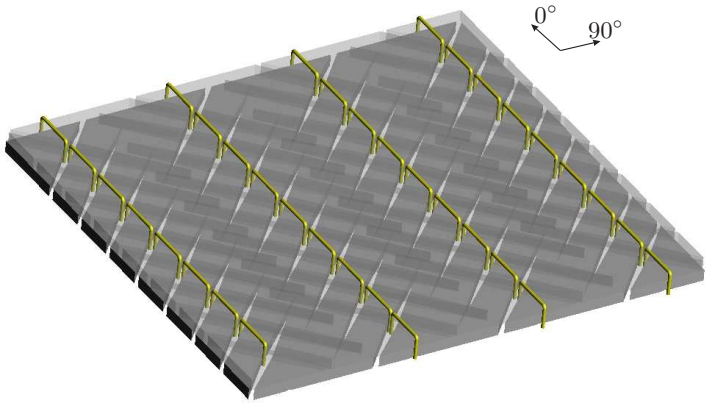

(b) One layer NCF, consisting of 2 plies. The upper ply is transparent, such that the intersections of SYDs in the upper ply with the lower ply can be seen.

Fig. 4.1. Piece of an undeformed (unsheared) biaxial NCF, characterised by stitch distances $3A$ and $9B$.

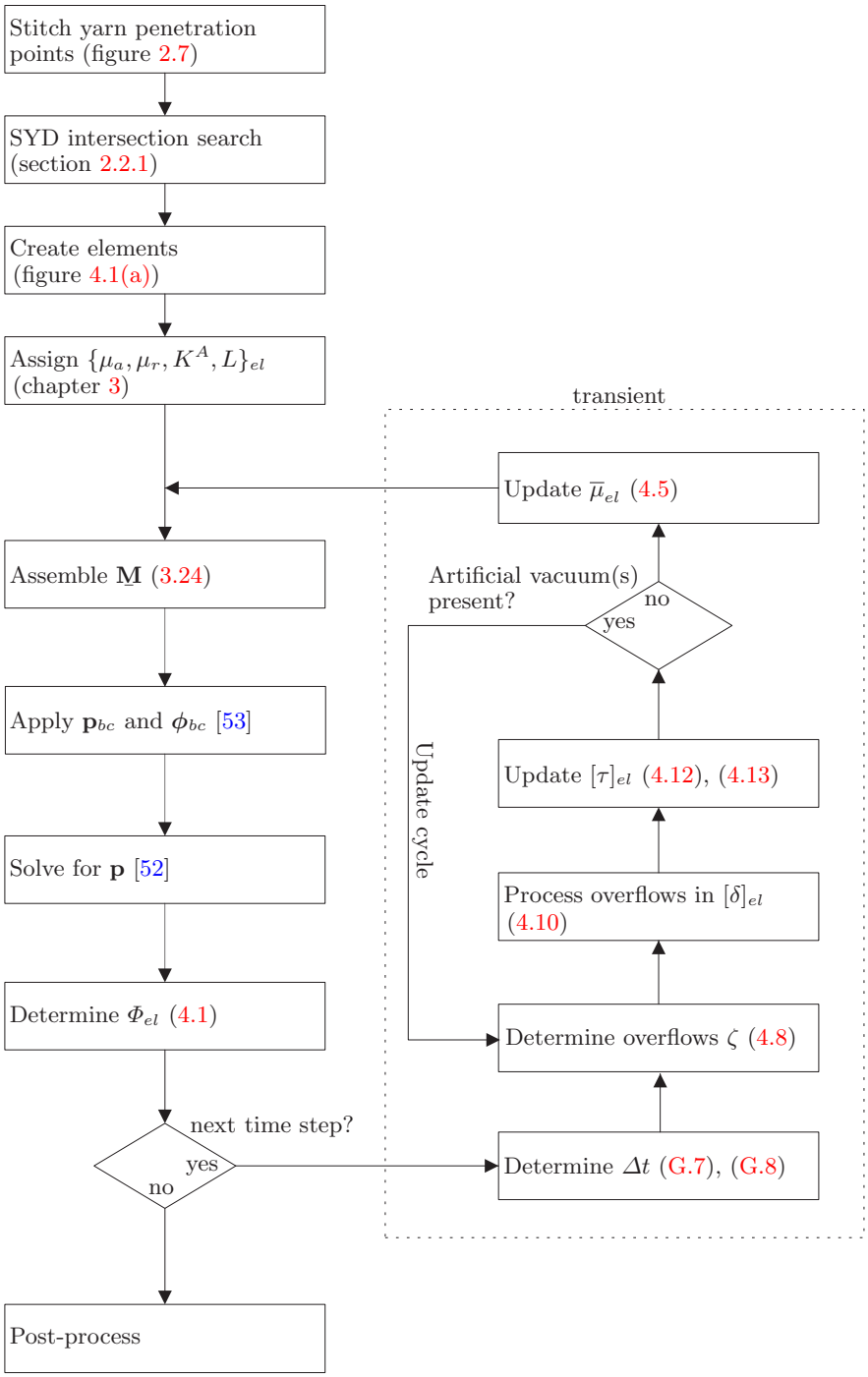

Fig. 4.2. MATLAB program structure. The subscript *el* indicates an element quantity. The symbol $[\tau]$ is a fill factor array and $[\delta]$ is the donation array. Both of them contain element volume fractions and their associated viscosities. The square brackets indicate a numerical array, used in many computational languages [52]. Subscripts a and r refer to air and resin respectively, but could represent other immiscible substances as well. The processes, which are bounded by the dashed lines, will be incorporated when a fill simulation runs (transient solution, section 4.3). The program without these processes represents a steady state solution of the problem (section 4.2).

4.2 Steady State Solution

Considering the flow chart in figure 4.2, a steady state solution will be obtained by excluding the processes that are bounded by the dashed line. The steady state situation implies that all elements are filled with the substance with viscosity μ_r (resin). Once an element network as in figure 4.1(a) has been created, the system matrix $\underline{\mathbf{M}}$ can be assembled, just as was done for the tube in figure 3.5 with the result in equation (3.24).

Pressure boundary conditions have to be applied to particular nodes, in order to obtain a flow through the domain. For example, high pressures $\mathbf{p}_h$ (containing pressures p_h) may be applied at side I or III, and low pressures $\mathbf{p}_l$ (containing pressures p_l) at side II or IV respectively, see figure 4.1(a). These boundary conditions will be processed in the system of equations (3.23), according to a method described by Cook [53, sect. 2.7]. Boundary conditions, concerning the nodal nett fluxes ($\varphi = 0$, continuity), have to be applied to nodes without pressure boundary conditions. These nodal nett fluxes could directly be processed in the right hand side vector $\boldsymbol{\varphi}$ of the system of equations (3.23).

The system will be solved for the unknown nodal pressures $\mathbf{p}$. The direct solver (invoked by the `mldivide` \ command) from Matlab will be used. The selection of an appropriate algorithm to solve the system of equations was based on the structure of the coefficient matrix [52]. The structure of the coefficient matrix is important, since element properties differ up to four orders of magnitude.

Once the nodal pressures are known, the element fluxes will be calculated, by using equation (1.3):

$$\Phi_{el} = \frac{K^A_{el}}{\mu_r} \frac{|\Delta p_{el}|}{L_{el}} \tag{4.1}$$

An effective permeability of the modelled piece of textile can be calculated according to:

$$K^A_E = \frac{\mu_r \overline{L}}{|p_h - p_l|} \sum |\varphi_h| \qquad \text{or} \qquad K^A_E = \frac{\mu_r \overline{L}}{|p_h - p_l|} \sum |\varphi_l|, \tag{4.2}$$

The term μ_r refers to the viscosity of the fluid (resin) and $\overline{L}$, to the averaged length between the nodes with pressure boundary conditions p_h and p_l. The summation of φ_h or φ_l means summation of the resulting nodal nett fluxes at the nodes, at which pressure boundary conditions p_h or p_l were applied respectively.

So far, above relations used the effective area included permeability K^A_E only. The permeability K_E is much more interesting and will be determined by $K_E = K^A_E / \mathcal{A}_E$. The effective cross-sectional flow area $\mathcal{A}_E$ will be determined by using the total volume of the inter bundle channels (total volume of the elements):

$$\mathcal{A}_E = \frac{\sum_{j=1}^{N} \mathcal{V}_j}{\overline{L}}, \tag{4.3}$$

To obtain the in-plane permeability tensor for the modelled piece of NCF, pressure boundary conditions have to be applied in at least three directions. In this way, permeabilities in three directions can be determined with equation (4.2) and the in-plane permeability tensor can be determined, as explained in Loendersloot [3, appendix F].

Appendix F.2 shows an example of results that were produced by the numerical program in its steady state configuration. The following properties of the modelled piece of NCF were used:

- Piece of fabric characterised by a number of stitch distances $10A$ and $25B$ ($A = 5.71$[mm], $B = 2.20$[mm]).
- Modelling a bi-axial NCF, which means a lower and an upper ply with their associated SYDs.
- Permeability of SYDs ($1{\cdot}10^{-17} > K^A_{SYD} > 1{\cdot}10^{-18}$) determined with the results from Mortensen [38], see section 3.3.
- Permeability of the region in the SYD with the stitch yarn obstruction, determined with the results from section 3.4.2 ($d_c = 0.071$[mm], $K^A_{ist} \approx 1 \cdot 10^{-18}$ [m^4]).
- Permeability of the external channels determined with the results from section 3.4.1, combined with the results of the microscopy analyses in appendix H.5 ($K^A_{est} = 7.85 \cdot 10^{-19}$ [m^4]).

- Permeability of the inter ply elements set to be highly porous compared to the other elements, since there is no relation for their permeabilities yet.
- Constant SYD dimensions $l = l^u = l^l = 10[\text{mm}]$, $h = 0.4[\text{mm}]$ and $b = b^u = b^l = 0.142[\text{mm}]$.

Pressure boundary conditions were applied along the sides I and II in figure 4.1(a). Solving led to a solution for the nodal pressures, as shown in figure 4.3(a). The global pressure field varies linearly over this piece of NCF. The pressure differences vary at the local scale (at the element level), since these elements have different permeabilities, as shown in appendix F.2.

Using the solved pressure field in equation (4.1), leads to the element fluxes in figure 4.3(b). As was expected from the element permeability distribution (as shown in appendix F.2), element flows differ and are dominating in elements that represent the widest part of the SYDs. Also, these elements show some boundary effects along the left and right sides of the flow domain (figure 4.3(a) shows these effects as well). These effects disappear when periodic boundary conditions are applied along these sides, but is not yet an option in the program. However, these boundary effects are expected to influence the permeability determination minimally, certainly when a considerable amount of unit cells are modelled. This has been shown in the unit cell sensitivity analysis in appendix F.1.

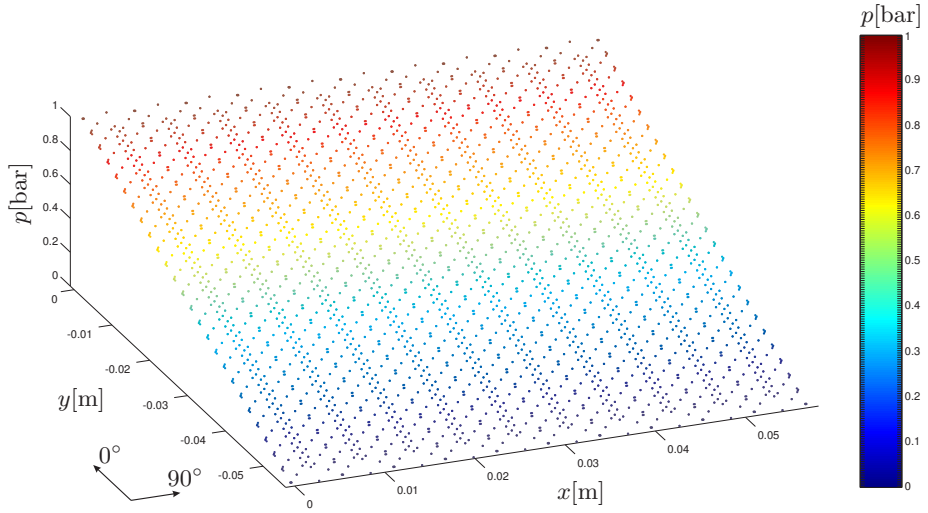

(a) Solution for the nodal pressures.

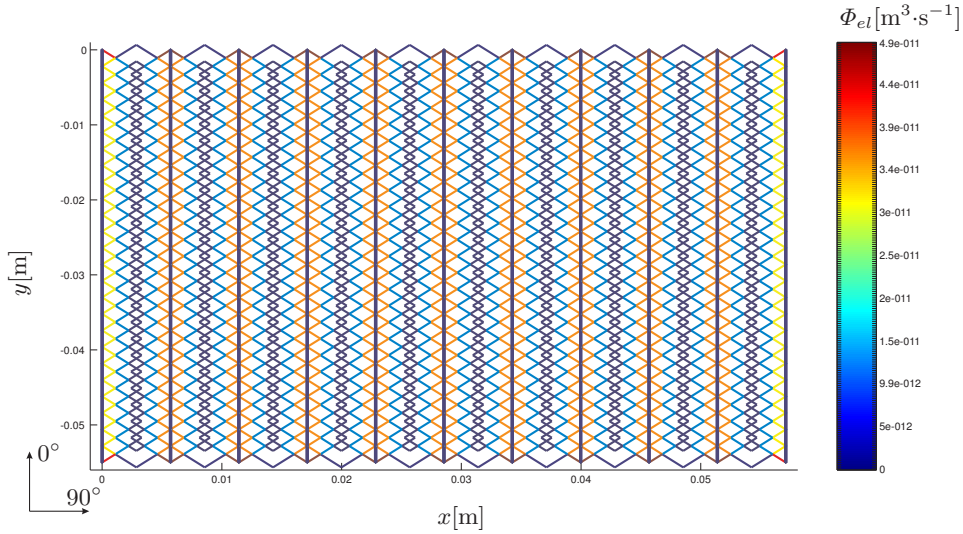

(b) Element fluxes Φ_{el} (4.1).

Fig. 4.3. Solutions for the network as was used in appendix F.2.

4.2.1 Sensitivity Analyses

The effect of the number of unit cells to built the element network with, was investigated and the results are shown in appendix F.1. It came out that using an element network with a size of $10A \times 25B$, was sufficient for permeability predictions. Other sensitivity analyses related to the permeability of the added stitch yarn related elements, were carried out as well and are shown below. The suggested network size was used.

Permeability of added Stitch Yarn related Elements

The effect of the permeabilities K_{ist} and K_{est} of the stitch yarn related elements (sections 3.4.2 and 3.4.1) on the effective permeability has been investigated. Several configurations were modelled, characterised by different values of K^A_{ist} and K^A_{est}, while the cross-sectional flow areas $\mathcal{A}$ were kept as a constant. For each configuration, all six elements (figure 3.9(b)) that are related to the stitch yarn obstruction in the SYD had the same value of K^A_{ist}. The effective permeabilities were determined in

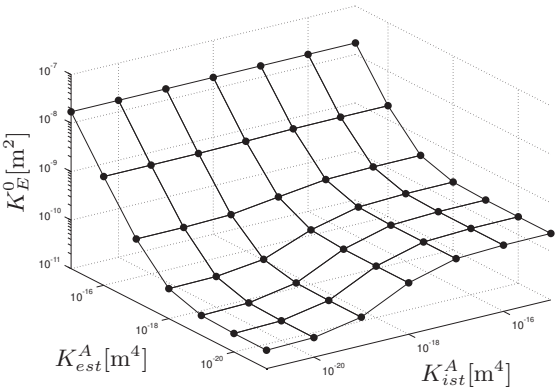

(a) Effective permeability in the 0°direction of the NCF.

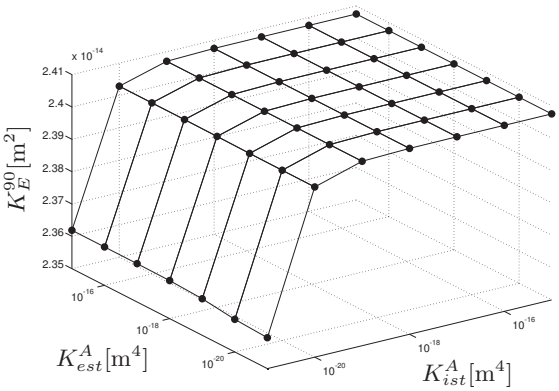

(b) Effective permeability in the 90°direction of the NCF (linear z-axis!).

Fig. 4.4. Permeabilities of the added elements that represent the external channels (section 3.4.1, K^A_{est}) and the SYD obstructing regions (section 3.4.2, K^A_{ist}) were varied in order to quantify their effect on the effective permeability of the fabric, with constant SYD lengths $l = 8.1$[mm]. Other parameter settings are listed on page 38.

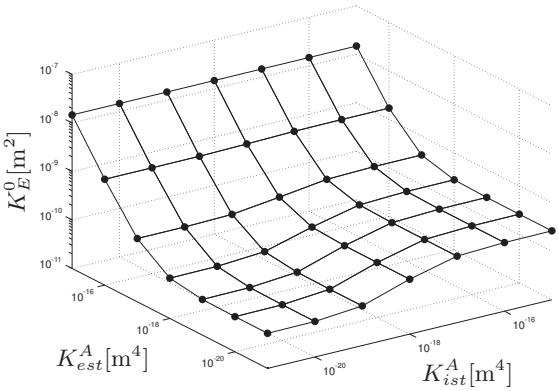

(a) Effective permeability in the 0°direction of the NCF.

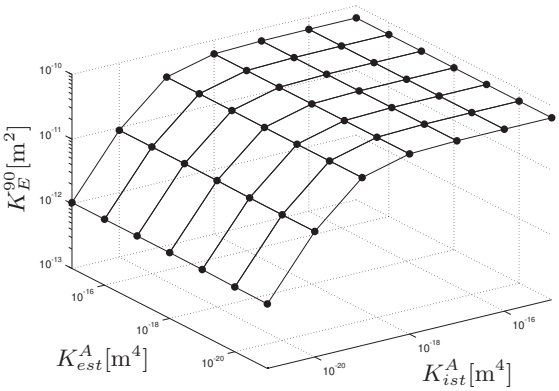

(b) Effective permeability in the 90°direction of the NCF.

Fig. 4.5. Permeabilities of the added elements that represent the external channels (section 3.4.1, K^A_{est}) and the SYD obstructing regions (section 3.4.2, K^A_{ist}) were varied in order to quantify their effect on the effective permeability of the fabric, with constant SYD lengths $l = 10$[mm]. Other parameter settings are listed on page 38.

the 0° and 90° direction with constant SYD lengths $l = 8.1$[mm] and $l = 10$[mm]. Other parameter settings of the network flow model are listed on page 38.

The results in figure 4.4 were obtained by using the SYD lengths $l = 8.1$[mm]. The effective permeability K_E^0 in the 0° direction (in the stitching direction) could strongly be influenced by the permeability K_{est} of the external channels (figure 4.4(a)). This behaviour is expected, since these channels are parallel to the pressure gradient direction. This reasoning can be used to explain the results for the effective permeability K_E^{90} in the 90° direction in figure 4.4(b). Here, the external channels do not influence the effective permeability of the piece of NCF at all. These effects for SYD lengths $l = 8.1$[mm] were also observed in figure 4.5, which shows the results that were obtained with SYD lengths $l = 10$[mm].

Consider the results for K_E^0 in figure 4.4(a) and 4.5(a). For the region in which K_{est}^A influences K_E^0 extremely ($1 \cdot 10^{-18}$[m^4] $< K_{est}^A < 1 \cdot 10^{-15}$[m^4]), the permeability K_{ist}^A barely affects the value of K_E^0. The region in which K_{est}^A barely influences K_E^0 ($1 \cdot 10^{-21}$[m^4] $< K_{est}^A < 1 \cdot 10^{-18}$[m^4]), K_{ist}^A affects K_E^0 somewhat but not as much as the permeability K_{est}^A of the external channels. In the range of $1 \cdot 10^{-21}$[m^4] $< K_{ist}^A < 1 \cdot 10^{-15}$[m^4], the permeability of the elements related to the stitch yarn obstruction in the SYD influences the effective permeability K_E^0 one order of magnitude at most.

The results of K_E^{90} for SYD lengths $l = 8.1$[mm] in figure 4.4(b), are barely influenced by both permeabilities K_{ist}^A and K_{est}^A. For SYD lengths of $l = 8.1$[mm], the tips of the SYD arms hardly touch each other in the 90° direction. This means that there is almost no connection of the elements in this direction, which explains the low permeability K_E^{90} ($\approx 2.4 \cdot 10^{-14}$[m^2]). For these SYD lengths, the elements that describe the tips of the SYDs are highly impermeable (permeability around $1 \cdot 10^{-22}$[m^4]). Additionally, these elements have a considerable length compared to the stitch related elements with K_{ist}^A and K_{est}^A, such that they dominate the effective permeability K_E^{90}. This phenomenon will be discussed further in chapter 6.

The results that were obtained with SYD lengths $l = 10$[mm] in figure 4.5(b) do show a dependence of K_E^{90} on K_{ist}^A. These results show much more influence of K_{ist}^A, since the tips of the SYDs overlap more in the 90° direction. As a result, the elements that describe the tip of the SYDs are much more permeable (permeability around $1 \cdot 10^{-19}$[m^4]) than those for SYD lengths $l = 8.1$[mm].

4.3 Transient Solution

This section describes the details that are associated with the processes within the bounded region in figure 4.2 that will be activated during a fill simulation. For the steady state situation (section 4.2), all elements were filled with resin. In case of a fill simulation, the initial situation is characterised by an air filled domain. The elements will be filled with resin after some simulation time. The domain is characterised by a high and low pressure side, just as in the described steady state situation. To start up the fill process in case of a fill simulation, another type of boundary condition has to be added that concerns the element fill factors, connected to the nodes with the high pressure boundary conditions. The initial amount of resin in these elements will be determined according to their element flows from the steady state solution. During the fill simulation, these elements will always be donated with resin. They supply the resin, to be transported through the whole element domain. These elements are referred to as *kick off* elements.

After determining time step Δt (see figure 4.2 and section G.3), it is possible to derive how resin will travel through the network of elements. For this, a filling scheme had to be developed, which should be compatible with the element domain description as was used in this thesis. This scheme has to process the immiscible flows of resin and air for a particular determined time step. This scheme will be described in section 4.3.1. Unlike other filling schemes [54–56], this scheme considers both resin and air transport through the domain. Some phenomena that occur due to this strategy will be explained in appendix G.2.

4.3.1 Filling Scheme

The resin and air fractions in an element are respectively:

$$\tau_r = \frac{\mathcal{V}_r}{\mathcal{V}_{el}} \qquad \tau_a = \frac{\mathcal{V}_a}{\mathcal{V}_{el}},$$

in which $\mathcal{V}_{el}$ is the total volume of the element. During the fill simulation, the amount of resin $\mathcal{V}_r$ and air $\mathcal{V}_a$ in an element have to be kept updated. Each element contains a fill factor array, in which these data will be stored. The array has the following structure:

$$[\tau]_{el} = \begin{bmatrix} \tau_v & - \\ \tau_r & \mu_r \\ \tau_a & \mu_a \end{bmatrix}_{el}, \tag{4.4}$$

with μ_r and μ_a referring to the viscosity of the two considered substances (resin and air respectively). These data and the assumption of a linearly varying pressure (figure 3.4) over the element, the following relation (lever rule) for the averaged viscosity in an element will be used:

$$\overline{\mu} = \tau_r \mu_r + \tau_a \mu_a \tag{4.5}$$

Incorporating this relation in the program (figure 4.2), and invoking it for every time step and every element, leads to an updated system of equations after reassembling the system matrix $\underline{\mathbf{M}}$.

For practical reasons (see appendix G.2), it is assumed that the amount of a substance in an element will stick together. This means, for an element that contains two substances, at most two regions in an element contain a different viscosity. An additional assumption is that the substance represented by the second row of the fill factor array (4.4), is always positioned at the high pressure side of the element. This means, in the scope of this thesis (LCM processes), the resin is always at the high pressure side and the air at the low pressure side of the element.

Considering the fill factor array (4.4) again, it should be noted that the first row has been added in order to process the element flows. The term τ_v contains the moved volume fraction of the element, resulting from the element flow Φ_{el}. It is a utility to be used by the filling scheme. Considering a physical analogy of this fraction, it will be referred to as an *artificial vacuum*. Note that this is just a tool and has nothing to do with physics.

Consider the assembly of elements in figure 4.6(a). All elements' permeabilities and cross-sectional areas are equal. Elements 1 and 2 are the *kick off* elements, thus they will always be supplied with resin and contain a user specified filled fraction ($\overline{\mu} > \mu_a$) at $t = 0$. The other elements are all filled with air ($\overline{\mu} = \mu_a$) initially at $t = 0$. After building the system matrix $\underline{\mathbf{M}}$, applying pressure and continuity boundary conditions and solving for the unknown nodal pressures, the following resulting pressure case is assumed:

$$p_1 > p_2 > p_4 \qquad \begin{matrix} p_1 = p_5 \\ p_4 = p_6 \end{matrix} \tag{4.6}$$

By using equation (4.1) and the known pressures, element fluxes Φ_{el} will be calculated. Assuming that the element flux is constant for a particular time step Δt (linearisation of $\mathcal{V}_r(t)$; appendix G.1 shows the analytical derivation for $\mathcal{V}_r(t)$), the moved volume fraction of an element (4.4) could be calculated as:

$$\tau_v = \Delta t \frac{\Phi_{el}}{\mathcal{V}_{el}} \tag{4.7}$$

This has been visualised in figure 4.8(b). The associated accuracy was investigated and is described in section 4.3.2. It came out that the order of accuracy reads $\mathcal{O}(\Delta t)$ and that the filled volume at a particular time could be over- or underestimated, depending on the curvature of $\Phi_{el}(t)$ and the size of Δt. To determine the size of the time step, an algorithm was developed that considers the criterion ψ, which indicates the number of time steps for which the resin-air interface travels along one element. This time step controlling is fully described in appendix G.3.

The *artificial vacuum* τ_v is positioned on the high pressure side of an element, as is shown in figure 4.6(a) (unfilled areas). Now, it is possible to calculate how much and which substance will leave the particular element. This will be referred to as an *overflow* ζ, and three cases for a single element were identified:

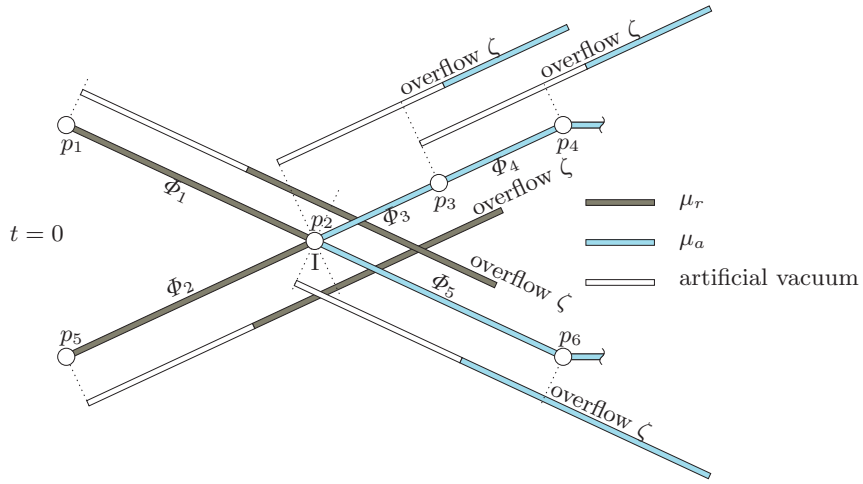

(a) Calculation of *artificial vacuums* by using the element fluxes Φ_{el}.

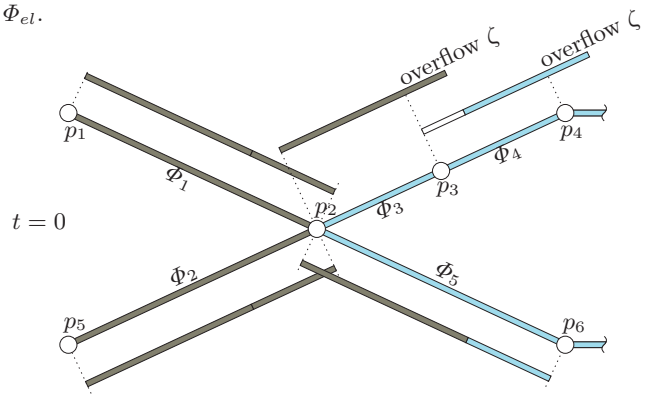

(b) End of the first update cycle.

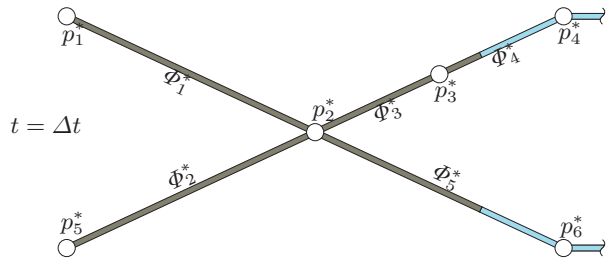

(c) End of the second update cycle. No *artificial vacuums* are left. The stars as superscripts indicate that the variables need to be derived again, and will follow from the solution of the updated system matrix.

Fig. 4.6. Graphical explanation of the filling scheme. The most left elements 1 and 2 are the *kick off* elements.

$$
\left.\begin{aligned}
\zeta_v &= (\tau_v - 1)\mathcal{V}_{el} \\
\zeta_r &= \tau_r \mathcal{V}_{el} \\
\zeta_a &= \tau_a \mathcal{V}_{el}
\end{aligned}\right\} \quad \text{if} \quad \tau_v > 1
$$

$$
\left.\begin{aligned}
\zeta_v &= 0 \\
\zeta_r &= (\tau_v + \tau_r - 1)\mathcal{V}_{el} \\
\zeta_a &= \tau_a \mathcal{V}_{el}
\end{aligned}\right\} \quad \text{if} \quad \begin{aligned} \tau_v &< 1 \\ \tau_v + \tau_r &> 1 \end{aligned} \tag{4.8}
$$

$$
\left.\begin{aligned}
\zeta_v &= 0 \\
\zeta_r &= 0 \\
\zeta_a &= (\tau_v + \tau_r + \tau_a - 1)\mathcal{V}_{el}
\end{aligned}\right\} \quad \text{if} \quad \begin{aligned} \tau_v + \tau_r &< 1 \\ \tau_v + \tau_r + \tau_a &> 1 \end{aligned}
$$

where the subscripts v, r and a refer to the vacuum, resin and air respectively. It is possible that one substance is not present, while it is still incorporated in the cases above. This will be accounted for implicitly, by having a zero fill factor for that particular substance.

After deriving the *overflows* ζ, they have to be shared over the elements on the low pressure side of this *donating* element. The *overflow* of element 1 in figure 4.6(a) need to be processed at node I with pressure p_2, because $p_1 > p_2$ (see equation (4.6)). Knowing all the elements connected to node I, a filter procedure has to be applied in order to obtain a set of so-called *receiving* elements. To be a *receiving* element, node I has to be on the high pressure side of that *receiving* element. If this condition has not been met, the flow direction is not aligned with the *donating* element 1 and it will not receive any substance of this *donating* element. For example, element 2 in figure 4.6(a) does not meet this condition for the *donating* element 1. The filter procedure results in a set of *receiving* elements 3 and 5, in which the *overflow* of element 1 has to be processed. The *overflow* will be donated in the donation array $[\delta]_{el}$ of the *receiving* elements. It has the same structure as the fill factor array in (4.4):

$$[\delta]_{el} = \begin{bmatrix} \delta_v & - \\ \delta_r & \mu_r \\ \delta_a & \mu_a \end{bmatrix}_{el} \tag{4.9}$$

The *overflow* has to be shared by accounting for the difference in fluxes Φ_{el} of the *receiving* elements, such that the following relations will be used by processing the *overflow* of an element in a *receiving* element:

$$\begin{aligned} \delta_{\underset{j}{v}} &= \delta_{\underset{j}{v}} + \frac{\zeta_v}{\mathcal{V}_j} \frac{\Phi_j}{\sum^N \Phi_j} \\ \delta_{\underset{j}{r}} &= \delta_{\underset{j}{r}} + \frac{\zeta_r}{\mathcal{V}_j} \frac{\Phi_j}{\sum^N \Phi_j} \\ \delta_{\underset{j}{a}} &= \delta_{\underset{j}{a}} + \frac{\zeta_a}{\mathcal{V}_j} \frac{\Phi_j}{\sum^N \Phi_j} \end{aligned} \tag{4.10}$$

in which subscript j represents a unique element from the set of *receiving* elements. Summation of element fluxes will be done for the total number of elements N in the *receiving* elements set. These relations will be applied individually for all elements j in the *receiving* elements set. The volume $\mathcal{V}_j$ is the volume of the *receiving* element and ζ the *overflow* of the *donating* element.

The donation array (4.9) of an element could be filled several times during one update cycle. For example, element 3 in figure 4.6(a) will receive *overflows* from element 1 and 2. This explains the incorporated donation in (4.10) (first term on the right hand side). At the end of an update cycle, the sum of donations in an element's donation array equals the element's moved volume fraction τ_v:

$$\tau_v = \delta_v + \delta_r + \delta_a$$

After processing all overflows during one update cycle, the element's fill factors will be reset, such that the sum of fill factors in the fill factor array (4.4) equals 1 again. This will be done according to the case (as in (4.8)), for which the element is eligible:

$$\left.\begin{aligned} \tau_v^* &= 1 \\ \tau_r^* &= 0 \\ \tau_a^* &= 0 \end{aligned}\right\} \quad \text{if} \quad \tau_v > 1$$

$$\left.\begin{aligned} \tau_v^* &= \tau_v \\ \tau_r^* &= 1 - \tau_v \\ \tau_a^* &= 0 \end{aligned}\right\} \quad \text{if} \quad \begin{aligned} &\tau_v < 1 \\ &\tau_v + \tau_r > 1 \end{aligned} \tag{4.11}$$

$$\left.\begin{aligned} \tau_v^* &= \tau_v \\ \tau_r^* &= \tau_r \\ \tau_a^* &= 1 - \tau_v - \tau_r \end{aligned}\right\} \quad \text{if} \quad \begin{aligned} &\tau_v + \tau_r < 1 \\ &\tau_v + \tau_r + \tau_a > 1 \end{aligned}$$

where the asterisk superscripts indicate the new fill factors.

The element donation arrays (4.9) could now be processed in the associated element fill factor array (4.4). Two cases will be treated differently, i.e. :

- processing the donations $[\delta]_{el}$ in the element's fill factor array $[\tau]_{el}$ for which the sum of the element donations are smaller than or equal to 1 (see element 5 in figure 4.6(a), $\tau_v < 1$):

$$\left.\begin{aligned} \tau_v^{**} &= \delta_v \\ \tau_r^{**} &= \tau_r^{*} + \delta_r \\ \tau_a^{**} &= \tau_a^{*} + \delta_a \end{aligned}\right\} \qquad \text{if} \qquad \delta_v + \delta_r + \delta_a \leq 1 \tag{4.12}$$

- processing the donations $[\delta]_{el}$ in the element's fill factor array $[\tau]_{el}$ for which the sum of the element donations are greater than 1 (see elements 3 and 4 in figure 4.6(a), $\tau_v > 1$):

$$\left.\begin{aligned} \tau_v^{**} &= \delta_v \\ \tau_r^{**} &= \delta_r \\ \tau_a^{**} &= \delta_a \end{aligned}\right\} \qquad \text{if} \qquad \delta_v + \delta_r + \delta_a > 1 \tag{4.13}$$

When these operations have been done, the end of an update cycle has been reached (see the cycle in the enclosed transient part in figure 4.2). Donations of *artificial vacuums* were noticed, when they were present during these operations. In that case, a new update cycle will be activated to repeat the steps from equation (4.8) again. Then, overflows will be calculated again for elements that contain an *artificial vacuum*. For example, processing the donations that were calculated from the case in figure 4.6(a), resulted in the intermediate state in figure 4.6(b). A vacuum was donated by element 3 to *receiving* element 4, such that another update cycle was needed with the final result in figure 4.6(c) for this time step.

4.3.2 Results

The following results show some characteristics of the filling scheme. For this, comparison with analytical solutions of the flow front position is straightforward. However, a flow front position is sometimes hard to define (non-uniform infusion). Therefore, instead of flow front positions, filled volumes $\mathcal{V}_r$ will be used to indicate the fill progression. Consider the tube with a constant permeability K and cross-sectional area $\mathcal{A}$ in figure 4.7. Making use of Darcy's law separately in both the resin and air filled parts of the tube, and using the continuity equation (1.8) with the incompressibility condition $\partial\rho/\partial t = 0$, results in the following expression:

$$t(\mathcal{V}_r) = t_r = \frac{\mu_a \mathcal{V}_r \mathcal{V}_{el} + \frac{1}{2}\mathcal{V}_r^2(\mu_r - \mu_a)}{\mathcal{A}K^A(p_h - p_l)}, \tag{4.14}$$

in which t_r is the time, which was needed to obtain the substances' (resin-air) interface at $\mathcal{V} = \mathcal{V}_r$ (see figure 4.7). Solving for $\mathcal{V}_r$ gives two roots for which the following is a physical realistic one:

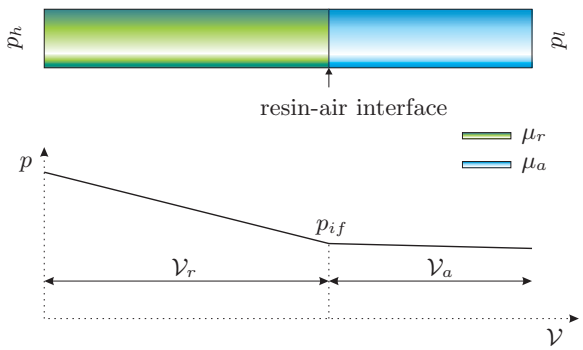

Fig. 4.7. A tube with volume $\mathcal{V}_{el}$, a constant permeability K, a constant cross-sectional area $\mathcal{A}$ and a variable pressure gradient $\mathrm{d}p/\mathrm{d}\mathcal{V}$ over its length. Two substances are present, characterised by their viscosities μ_r and μ_a.

$$\mathcal{V}_r(t_r) = \frac{\sqrt{\mu_a^2 \mathcal{V}_{el}^2 + 2\mathcal{A}K^A(p_h - p_l)(\mu_r - \mu_a)t_r} - \mu_a \mathcal{V}_{el}}{\mu_r - \mu_a} \tag{4.15}$$

See appendix G.1 for the derivation of these relations.

Accuracy

The accuracy of the filling scheme will be investigated for an assembly of two elements as in figure 4.8(a). Constant inlet and outlet pressures ($p_h = 1[\mathrm{Nm}^{-2}]$ and $p_l = 0[\mathrm{Nm}^{-2}]$ respectively) are applied. Element 1 is initially filled (resin), while element 2 is empty (air). Further element properties are:

$$\begin{array}{lll} L_1 = L_2 = 0.5[\mathrm{m}] & K_1^A = K_2^A = 1[\mathrm{m}^4] & \mathcal{A}_1 = \mathcal{A}_2 = 1[\mathrm{m}^2] \\ \mathcal{V}_1 = \mathcal{V}_2 = 0.5[\mathrm{m}^3] & \mu_r = 1[\mathrm{Nsm}^{-2}] & \mu_a = 1 \cdot 10^{-5}[\mathrm{Nsm}^{-2}] \end{array}$$

The time to fill half of element 2 will be referred to as $t_{0.5}$ and follows analytically from equation (4.14) as:

$$t_{0.5} \equiv t(\mathcal{V}_{r,1} + 0.5\mathcal{V}_{r,2}) - t(\mathcal{V}_{r,1})$$

With the filling scheme, numerical solutions were found for different time steps $\Delta t = t_{0.5}/j$; in which j is an integer. An error is defined as the difference between the analytically filled volume $\mathcal{V}_{r2}(t_{0.5})$ and the numerically filled volume $\tilde{\mathcal{V}}_{r2}(t_{0.5})$:

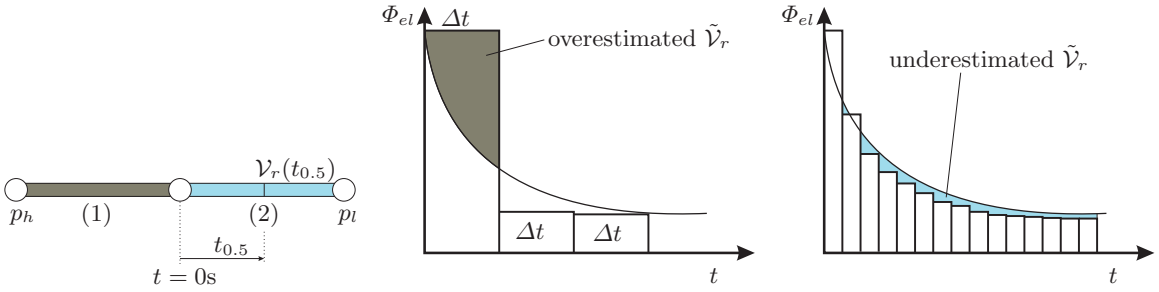

(a) Assembly of two elements. (b) Large Δt. (c) Small Δt.

Fig. 4.8. Comparing analytical and numerical (indicated by ˜) behaviour of the assembly.

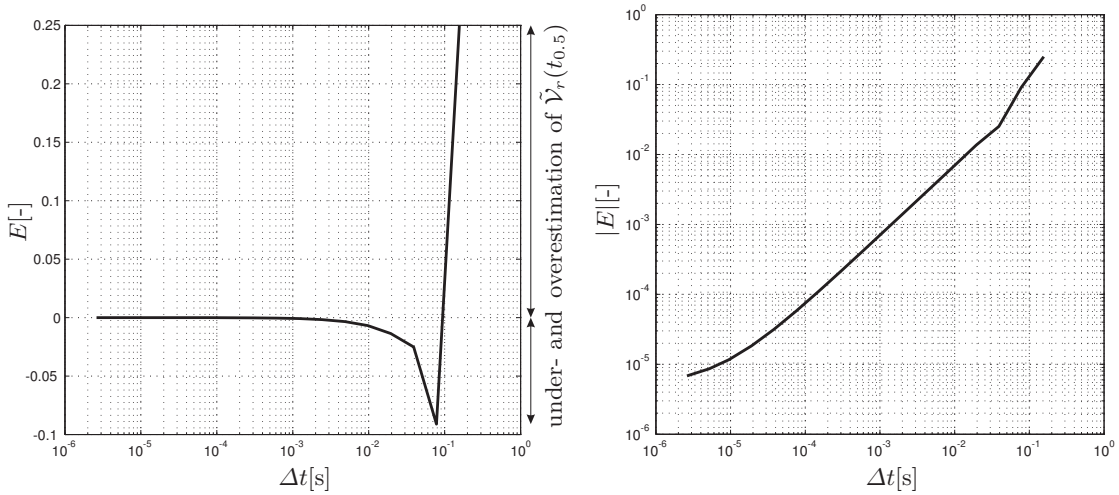

Fig. 4.9. Error of the filled volume $\tilde{\mathcal{V}}_r(t_{0.5})$. The behaviour of the absolute error (figure 4.9(b)) indicates an accuracy of $\mathcal{O}(\Delta t)$.

$$E = \frac{\tilde{\mathcal{V}}_{r2}(t_{0.5}) - \mathcal{V}_{r2}(t_{0.5})}{\mathcal{V}_{r2}(t_{0.5})},$$

and has been visualised in figure 4.9(a). Its behaviour will be explained with help of figure 4.8(b) and 4.8(c). The first time step always overestimates the filled volume $\tilde{\mathcal{V}}_r(\Delta t)$ due to the linearisation of $\mathcal{V}_r(t)$, which is equivalent to the assumption of a constant flow Φ within Δt. Updating the system matrix $\underline{\mathbf{M}}$ and solving leads thus to:

$$\boldsymbol{\nabla}\tilde{p} < \boldsymbol{\nabla}p \qquad \text{such that} \qquad \tilde{\Phi}_{el} < \Phi_{el},$$

in which $\tilde{}$ indicates the numerically obtained variable. This has been shown in figure 4.8(b) and 4.8(c), in which the beginning of the second time step starts at a lower volume flow than the analytical volume flow at that moment. Depending on the curvature of $\Phi_{el}(t)$ and the size of the time steps Δt, the numerically filled volume at a particular time could be over- or underestimated. This has been visualised by the dark and light shaded areas in figure 4.8(b) and 4.8(c) respectively. The absolute error has been depicted in figure 4.9 and shows a first order of accuracy $\mathcal{O}(\Delta t)$.

Test case

A test configuration as in figure 4.10, has been used to validate the filling scheme and to show some phenomena, which will only occur in the transient solutions. This configuration and its node as well as element numbering are visualised in figure 4.10(a). A high (1 bar) and a low (0 bar) pressure have been applied to nodes 1 and 4 respectively. A steady state situation, in which all elements have viscosity μ_r, was solved first. By using equation (4.2), an effective permeability K_E^A for this network was determined. The solid line in the graph has been obtained by using this effective permeability, while evaluating equation (4.15) at different times, and using the cross-sectional area $\mathcal{A}_E$ according to equation (4.3).

The case in figure 4.10(a), considers that all element permeabilities are equal. Applying the filling scheme for different values of ψ (appendix G.3 explains the usage and meaning of this parameter), results in the plotted fill progressions (broken lines). It can be seen that more time steps Δt during the fill simulation results in a fill time, which is closer to the fill time that was determined with the effective permeability and equation (4.15). This converging behaviour was expected and shown in the accuracy analysis.

The graphs related to the fill simulation start with a more descent slope, compared to the steady state predicted fill progression. After this, a stage will follow with a steeper slope. The last stage has a decreasing slope again. The difference of this behaviour, compared to the steady state behaviour, follows from the fill progression determination with the effective permeability K_E^A and its associated cross-sectional area $\mathcal{A}$. This area was determined in an averaged sense (4.3) and will be greater than the cross-sectional area of element 1 and lower than the averaged cross-sectional area in the parallel region (elements 2 and 3, elements 4 and 5). The colour plots show the fill progression at different times. The colours are related to the averaged element viscosity $\overline{\mu}$, according to (4.5). Elements 2 till 5 are filled simultaneously, due to equal element permeabilities.

The results in figure 4.10(b) were obtained by using a low permeability value for element 3, while the other element permeabilities were remaining. In this way, elements 2 and 4 were filled quicker than elements 3 and 5. While elements 3 and 5 were not filled, resin already reached element 6 via elements 2 and 4 (see the fill progressions in the colour plots). As a result, the pressure at node 3 was increasing, in such a way that the pressure gradient over elements 3 and 5 was decreasing, while these elements were not filled yet. The fill progression for these elements will therefore be slower and influences the overall fill progression. This situation, in which some elements are insulated, will be referred to as inclusion behaviour. This reasoning and the reasoning in the previous paragraph (related to the averaged cross-sectional area), explain the more descent slope in the graph for the fill progressions, compared to the steady state predicted fill progressions. The sudden decreasing slope in the end of the fill simulation (from $t = 0.6 \cdot 10^{-5}$s) was caused by the arriving of resin at the end of the domain (node 4). From this point, fill progression of only element 5 was taken into account, while the steady state based fill prediction does not account for a limited domain. Also, the converging behaviour can be related to the accuracy analysis in the previous subsection.

Another phenomenon was observed for a low permeability value K_5^A, while all other element permeabilities were higher and equal. Considering the colour plots in figure 4.10(c), elements 2 and 3 were almost simultaneously filled due to the low viscosity of air of the downstream elements. Once these elements were filled, element 4 was filled quicker than element 5, due to the difference in their permeabilities. As can be seen from the graphs, the time to fill the total volume convergences to a lower time, compared to the steady state based fill time prediction. Somehow, the pressure field development results in a quicker filling (boost behaviour). However, this behaviour was only observed for a very limited range of K_5^A. Indeed, in this configuration, values of $K_5^A << 0.2K_j^A$ results in the observed inclusion behaviour in figure 4.10(b). Again, this behaviour could partly be related to the accuracy analysis as well, which indicated that both under- and overestimation of the filling time are possible, depending on the time step and the curvature of $\Phi(t)$.

Example

At this moment, transient solutions (fill simulation) can be obtained for a piece of modelled NCF. However, only the behaviour as shown in the test cases in section 4.3.2 can be observed and argued. Further conclusions about the fabric's isotropy or permeability values will not be done, since the steady state model is more suited for such analyses. Section 6.1 will show and discuss those results. However, it is interesting to show what kind of flow progressions could be shown by the filling scheme. These impressions may be help to plan the following steps towards a fill simulation tool.

The fill simulation tool was applied for a piece of NCF with the following properties:

- Piece of fabric characterised by a number of stitch distances $2A$ and $5B$ ($A = 5.71$[mm], $B = 2.20$[mm]).
- Modelling a bi-axial NCF, which means a lower and an upper ply with their associated SYDs.
- Permeability of SYDs ($1{\cdot}10^{-17} > K_{SYD}^A > 1{\cdot}10^{-18}$) determined with the results from Mortensen [38], see section 3.3.
- Permeability of the region in the SYD with the stitch yarn obstruction, determined with the results from section 3.4.2 ($d_c = 0.071$[mm], $K_{ist}^A \approx 1 \cdot 10^{-18}$ [m^4]).
- Permeability of the external channels determined with the results from section 3.4.1, combined with the results of the microscopy analyses in appendix H.5 ($K_{est}^A = 7.85 \cdot 10^{-19}$ [m^4]).
- Permeability of the inter ply elements set to be highly porous compared to the other elements, since there is no relation for their permeabilities yet.
- Constant SYD dimensions $l = l^u = l^l = 8.1, 12.4$[mm], $h = 0.4$[mm] and $b = b^u = b^l = 0.142$[mm].
- Infusion in the 0° direction of the fabric.

Some snapshots of the flow front propagation are depicted in figure 4.11. All figures on the left are the results for model configurations with constant SYD lengths $l = 8.1$[mm] and all figures on the right are the results for model configurations with constant SYD lengths $l = 12.4$[mm]. It is clear that the regions between the stitch yarn penetrations points in the 90° direction are impermeable for the configuration with SYD lengths $l = 8.1$[mm], since they are hardly filled. Effects like inclusions occur in these regions, as was identified during the test cases in the previous subsection. This behaviour is also observed in figure 4.11(g). The transient solutions converge to a longer filling time, compared to the predicted filling time that used the steady state determined effective permeability K_E. The sudden change in the slopes of the transient solutions occur, since the flows with μ_r (for example resin) run to the end of the flow domain. The plotted time dependent filled volume will not consider the flow outside the domain. The flat slope is almost only related to the elements in the impermeable region.

Filling proceeds more uniformly for the configuration with SYD lengths $l = 12.4$[mm]. This has been visualised in figure 4.11(h), where the fill progression graphs do not show a sudden change in the slopes. The transient solutions converge to a somewhat longer infusion time. This can be argued by some effects introduced by the pressure boundary conditions, which introduce a zero pressure gradient over some elements at the inlet side of the domain (see unfilled elements on top of each snapshot for the results with $l = 12.4$[mm]). The differences between the effective permeabilities with SYD lengths $l = 8.1$[mm] and $l = 12.4$[mm] will be discussed in section 6.1.

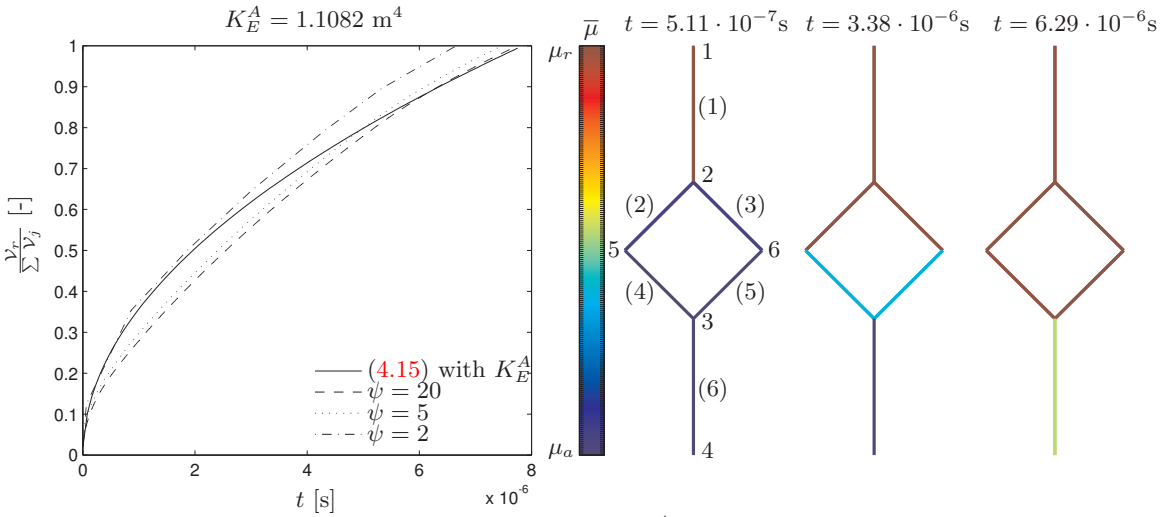

(a) All element permeabilities K_j^A are equal to 1.

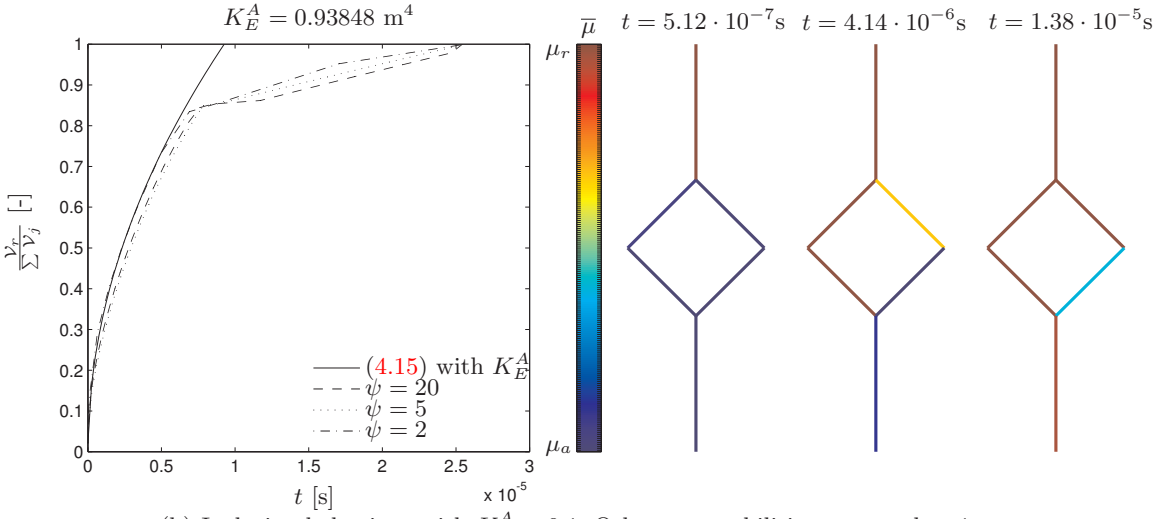

(b) Inclusion behaviour with $K_3^A = 0.1$. Other permeabilities are equal to 1.

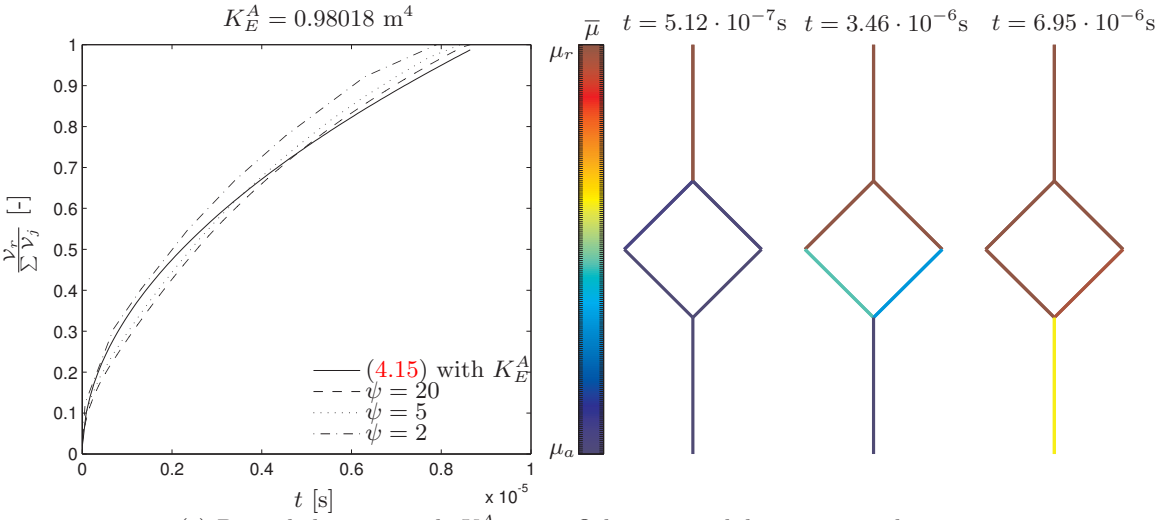

(c) Boost behaviour with $K_5^A = 0.2$. Other permeabilities are equal to 1.

Fig. 4.10. Test cases in which the permeability of some elements will be varied to show observed phenomena. All elements have an equal cross-sectional area $\mathcal{A}_j$. Element volumes $\mathcal{V}_j$ are proportional to their lengths. The resin filled volume is referred to with $\mathcal{V}_r$. $\mu_r = 0.03[\text{Nsm}^{-2}]$; $\mu_a = 1.78 \cdot 10^{-5}[\text{Nsm}^{-2}]$.

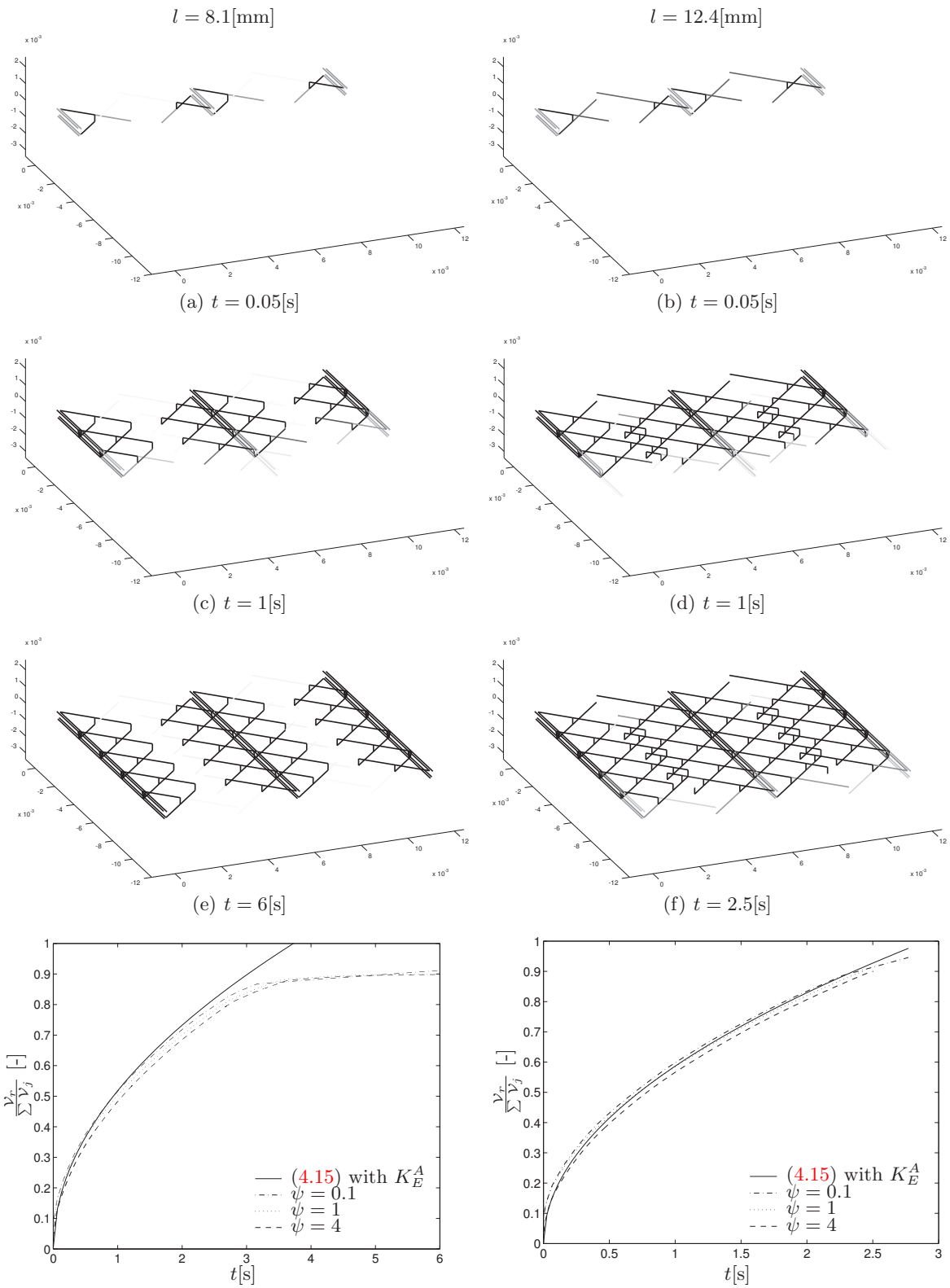

(a) $t = 0.05$[s]

(b) $t = 0.05$[s]

(c) $t = 1$[s]

(d) $t = 1$[s]

(e) $t = 6$[s]

(f) $t = 2.5$[s]

(g) Fill progression for time steps, characterised by different values of ψ.

(h) Fill progression for time steps, characterised by different values of ψ.

Fig. 4.11. The left and right columns of the subfigures show the fill progression for a piece of NCF with constant SYD lengths 8.1[mm] and 12.4[mm] respectively. The colours of the elements in the snapshots refer to the elements' fill factors. Black and white coloured elements, refer to filled ($\tau_r = 1; \tau_a = 0$) and unfilled ($\tau_r = 0; \tau_a = 1$) respectively. Intermediate colours refer to partly filled elements ($1 > \tau_r > 0; 1 > \tau_a > 0$).

5

Experiments

To validate the network flow model presented in chapter 4, liquid infusion experiments were executed. A simple infusion set-up has been developed, which could be compared with a Vacuum Assisted Resin Transfer Moulding (VARTM) method with rigid tooling (infusion between two glass plates). This set-up is described in section 5.1. Due to some characteristics of the infusion set-up, deformation of the rigid tooling occurs and has to be accounted for, since permeability is heavily dependent on the fibre volume fraction (determined by the cavity height/preform's thickness). These mechanisms were identified (appendix H.1) and acquired. A permeability determination method that accounts for a varying cavity height has been developed in section 5.2. Results of the experiments were processed and the associated permeabilities were determined, by using both acquired data and visually obtained information, as described in section 5.3. Comparison of the experimentally obtained results with the network flow model model results will be done in chapter 6.

5.1 Experimental Set-Up

Roughly, the experimental set-up consists of two glass plates, the fabric to be infused with a viscous, Newtonian and incompressible liquid lying within. The lower glass plate was clamped on an aluminium frame, as is shown in figure 5.1. A fabric was positioned on the lower glass plate and it was covered by the upper glass plate, such that the fabric was surrounded by rigid tooling. To seal the sides of the fabric, tacky tape was positioned around the infusion domain. A transparent foil was trimmed over this domain, such that it sticked to the tacky tape, see figure 5.1(b). As can be seen in the figures, a part of the tacky tape covers the fabric in order to obtain a higher fibre volume fraction V_f locally. This was done to avoid race tracking, such that a straight flow front resulted during the experiments. Pieces of gauze were positioned at the inlet and outlet side of the fabric. Because the liquid experiences the presence of the gauze at the inlet side, the liquid will be spread uniformly over the width of the infusion domain, before it runs through the fabric.

To determine the permeability of a textile, the variables in Darcy's law (1.1) need to be known. These are cross-sectional area $\mathcal{A}$, volume flow Φ_r and viscosity μ_r of the infusion liquid, pressure difference Δp over the saturated region of the fabric and the length L_r, over which the pressure gradient is significant (saturated region) at a particular infusion time t.

Figure 5.1(a) shows all sensors that were used during the infusion experiments. Data from these sensors were acquired by using an acquisition tool in MATLAB, via a 16[bit] (15[bit] effective by using a differential reference setting) NATIONAL INSTRUMENTS data acquisition box (NI USB-6210). The cavity height between the lower and upper glass plates (determines the cross-sectional area $\mathcal{A}$) is very important for the permeability determination. Therefore, a height measurement sensor has been placed on a guidance rail. This guidance rail is attached to the aluminium frame. Then, at each position on the guidance rail, the associated height that is measured by the upper height measurement sensor, is known.

Before setting up the infusion experiment, a height reference will be created by using the lower glass plate. Since the thicknesses of the upper glass plate ($H_{up} = 5,25$[mm]) and the transparent foil ($H_{foil} = 4,5 \cdot 10^{-2}$[mm]) are known, the cavity height $2h(x)$ (twice the SYD height in case of a biaxial

NCF) during the infusion process can be acquired several times. The lower height measurement sensor was only used to determine the deflection of the lower glass plate during the infusion process. More details that consider the acquisition of the height measurements and the resulting position dependent cavity height $2h(x)$, are described in appendix H.1.

The volume flow Φ_r can be acquired by using the liquid's volumetric density ($\rho_r = 1,4{\cdot}10^3[\mathrm{kg{\cdot}m^{-3}}]$) and measuring the weight of the bucket (load cell with a maximum load of 1[kg]) in which the infusion liquid was stored. Viscosity measurements were executed to obtain the liquid's viscosity μ_r (appendix

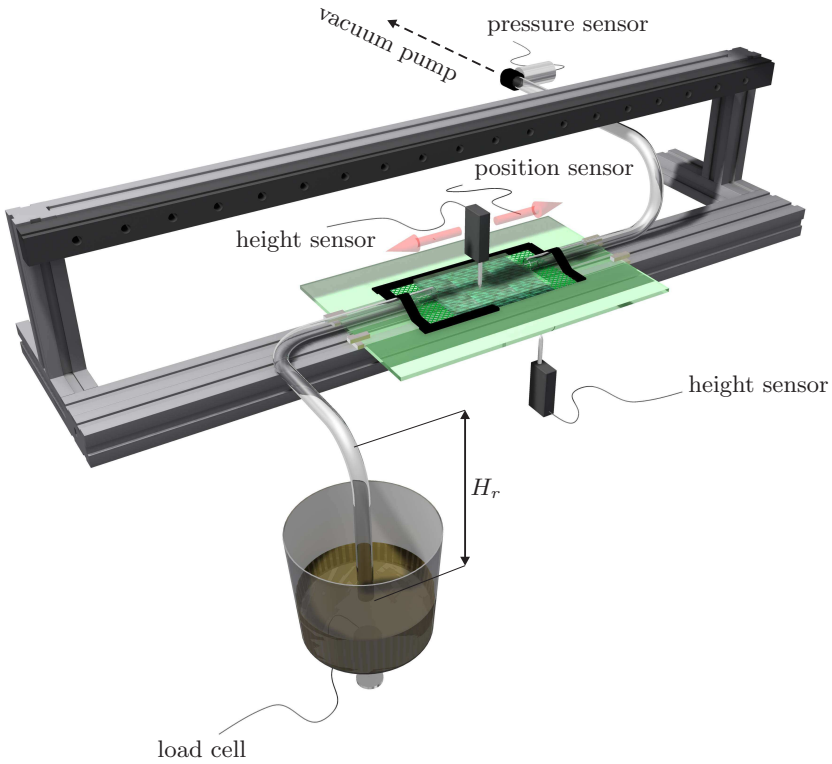

(a) Experimental set-up for infusion experiments. Signals of objects with a wire are acquired with acquisition software during the experiments (except the lower height sensor). The height H_r is the height, to be climbed by the liquid ($H_r = 20 \cdot 10^{-2}[\mathrm{m}]$).

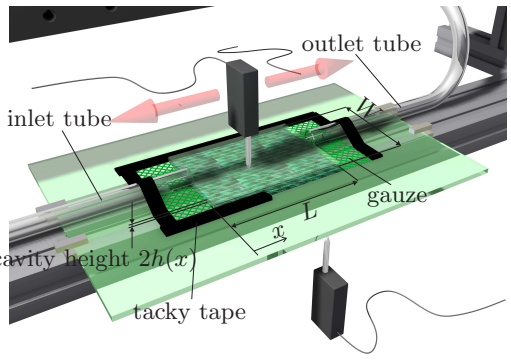

(b) Close-up of figure 5.1(a). Dimensions of the region, to be infused: W=9,6·10^{-2}[m] L=13,4·10^{-2}[m].

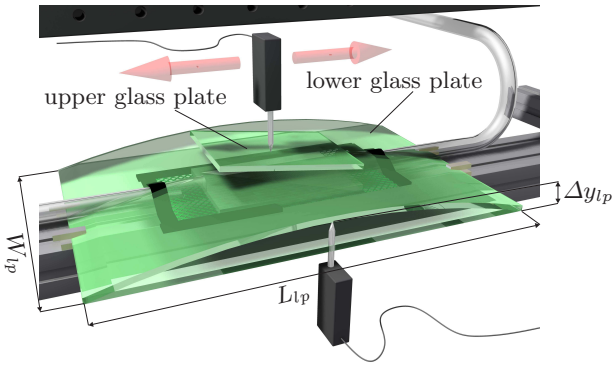

(c) Deformation mechanisms during the infusion process, i.e. tilting of the upper glass plate and bending of the lower glass plate, Δy_{lp}=60·10^{-6}[m], $L_{lp} = 36,8 \cdot 10^{-2}$[m], $W_{lp} = 23,9 \cdot 10^{-2}$[m].

Fig. 5.1. Experimental set-up.

H.3). The infusion liquid that was used, was a mixture of VAN GILSE SCHENKSTROOP (some kind of maple syrup) and water with the volume ratio 6:1, respectively.

A pressure difference over the fabric was created by attaching a vacuum pump to the outlet tube. Here, the pressure will be measured by a pressure sensor, which was attached in front of the inlet of the vacuum pump, see figure 5.1(a). It has been assumed that this pressure equals the pressure at the flow front, since the viscosity of air is much lower than the viscosity of the infusion liquid ($\mu_r >> \mu_a$). This means that pressure drop over the air filled part of the fabric and the air filled outlet tube is negligible, compared to the pressure drop in the liquid filled part of the fabric and the liquid filled inlet tube. Atmospheric pressure was assumed to be present at the inlet side of the inlet tube.

The properties of the fabric that was used, are summarised in table 5.1.

Table 5.1. Properties of the biaxial NCF that was used for the infusion experiments.

manufacturer		DEVOLD
areal density ρ_A	[kg·m^{-2}]	0.541
fibre		TENAX HTS 5631
fibre count in tow	[-]	12K
fibre material		carbon
fibre density ρ_f	[kg·m^{-3}]	1750
orientation	[°]	$\mp$45
stitch		PES
linear density	[tex]	5
stitch yarn diameter d_c (2.1)	[mm]	0.071
knit pattern		chain
gauge	[needles/inch]	5
stitch length (B)	[mm]	2.5
stitch distance A according to LOENDERSLOOT [3]	[mm]	5.71± 0.04
stitch distance B according to LOENDERSLOOT [3]	[mm]	2.20± 0.02
SYD width $b = b^u = b^l$ according to LOENDERSLOOT [3]	[mm]	0.21
SYD length $l = l^u = l^l$ according to LOENDERSLOOT [3]	[mm]	7.5

5.2 Permeability Determination

Since the fabric's thickness $2h(x)$ is known during the infusion experiments, the position dependent fibre volume fraction is known as well:

$$\tilde{V}_f(x) = \frac{\rho_A}{2\tilde{h}(x)\rho_f} \tag{5.1}$$

in which $2\tilde{h}(x)$ is twice the SYD height (see section 2.2) in case of a biaxial NCF. The areal density ρ_A is a fabric's property and ρ_f represents the volumetric density of the fibre material. The tilde $\tilde{}$ indicates that the function was obtained by a fit through acquired data points. In this case, these points are the measured heights during an infusion experiment, as described in appendix H.1. Now, the fabric's flow area $\tilde{\mathcal{A}}(x)$ can be determined according to:

$$\tilde{\mathcal{A}}(x) = W\left(2\tilde{h}(x) - \frac{\rho_A}{\rho_f}\right), \tag{5.2}$$

with W the width of the infusion domain as indicated in figure 5.1(b).

In case of a variable cross-sectional area along the pressure gradient direction (which was experienced during infusion experiments), it is practical to know the volume of the porous space in the fabric at a particular Cartesian position. Such a relation can be found by evaluating:

$$\tilde{\mathcal{V}}(x) = \int_0^x \tilde{\mathcal{A}}(x)\mathrm{d}x, \tag{5.3}$$

in which x is the Cartesian coordinate in the pressure gradient direction. Then, the position of the resin-air interface (flow front) could be related to the filled volume $\mathcal{V}_r = \tilde{\mathcal{V}}(x = L_r)$. This only holds when it is assumed that there is a straight flow front and that air filled inclusions or dry spots are absent.

Now consider that for a piece of $L_r - \Delta x$ infused NCF, the effective permeability is known, as is shown in figure 5.2. Within an incremental time step, the flow front was propagated to L_r over an incremental distance Δx. At that position, acquired variables like pressure difference Δp and volume flow Φ are known. This means that at this moment, the serially connected effective permeability of the piece of NCF $L_r - \Delta x$ and the permeability of the piece Δx, can be related to the acquired variables such that the permeability of the piece Δx can be extracted. Applying the formulation (1.6) for N serially connected permeabilities with a pressure gradient over length L:

$$\mathcal{A}_E K_E = L \left(\sum_{n=1}^{N} \frac{L_n}{\mathcal{A}_{E,n} K_{E,n}} \right)^{-1},$$

to the situation in figure 5.2, gives for the effective permeability at the flow front position $x = L_r$ in figure 5.2:

$$\mathcal{A}_E K_E \Big|_{x=L_r} = L_r \left(\frac{L_r - \Delta x}{\mathcal{A}_E K_E \Big|_{x=L_r-\Delta x}} + \frac{\Delta x}{\mathcal{A}_E^{\Delta x} K_E^{\Delta x}} \right)^{-1}, \tag{5.4}$$

with the assumption that $\mu_r >> \mu_a$, such that the permeability of the region with μ_a can be neglected, while evaluating this equation. The effective (or averaged) cross-sectional areas $\mathcal{A}_E$ will be determined in an averaged sense:

$$\begin{aligned} \mathcal{A}_E(L_r) &= \frac{1}{L_r} \int_0^{L_r} \tilde{\mathcal{A}}(x) \mathrm{d}x \\ \mathcal{A}_E(L_r - \Delta x) &= \frac{1}{L_r - \Delta x} \int_0^{L_r - \Delta x} \tilde{\mathcal{A}}(x) \mathrm{d}x \\ \mathcal{A}_E^{\Delta x} &= \frac{1}{\Delta x} \int_{L_r - \Delta x}^{L_r} \tilde{\mathcal{A}}(x) \mathrm{d}x \end{aligned} \tag{5.5}$$

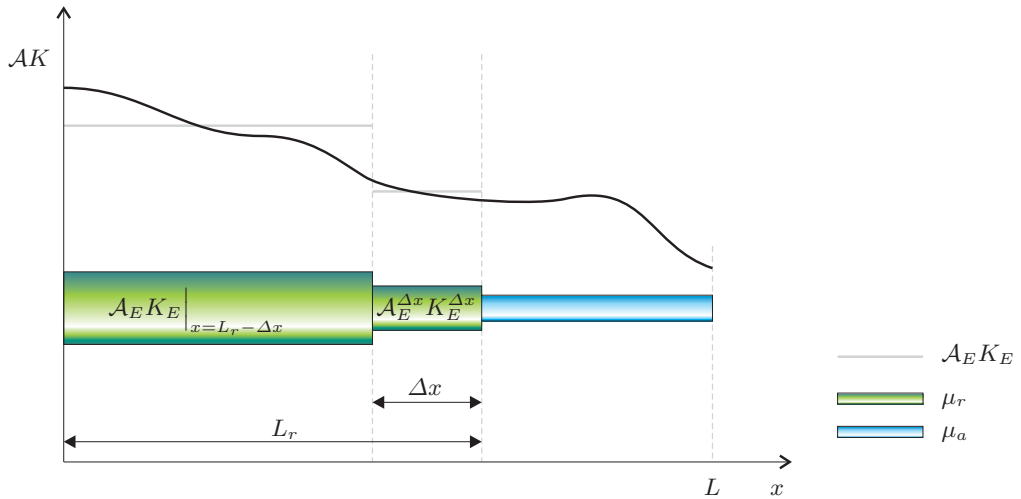

Fig. 5.2. Schematic representation of the permeability calculation method, based on serially connected layers with a unique permeability. A small piece Δx of the NCF will successively be added to the effective permeability, such that the permeability $K_E^{\Delta x}$ of one particular cross-sectional area $\mathcal{A}_E^{\Delta x}$ (or fibre volume fraction) is known.

Repeatedly applying equation (5.4) for every flow front position L_r with a resolution that is determined by Δx, starting from $L_r = \Delta x$ and ending with $L_r = L$ (L is the the dimension of the textile in the pressure gradient direction), results in a spatial dependent permeability distribution. This distribution can be related to the position dependent fibre volume fraction. Several relations for $K_E(x = L_r)$ on the left hand side of equation (5.4) can be used, in which the experimentally acquired data will be processed. These are shown in the subsequent sections.

Note that these permeabilities are related to the unsaturated (dry) fabric. The saturated permeability could be obtained by evaluating the acquired variables when the infusion process is steady, which occurs for a totally filled fabric. In this way, the method of serially connected permeabilities can not be used. To determine the saturated permeability, the varying height over the fabric's length has to be incorporated such that this saturated permeability could only be related to some kind of averaged thickness $\overline{2h}$ or fibre volume fraction $\overline{V_f}$. Since the infusion experiments were coping with a strongly varying cavity height, the saturated permeability has not been determined.

5.2.1 Quasi-Steady State Based

For a quasi-steady state permeability determination, it is assumed that a steady state situation for each flow front position L_r (with a spatial resolution determined by Δx) has been obtained. For all these situations, it is assumed that the textile's length L is equal to L_r. Using the time t that is associated with the flow front position L_r, the volume flow Φ_r of the resin and the pressure difference Δp over L_r at that moment can be extracted from the acquired data. Finally, the effective cross-sectional area $\mathcal{A}_E$ may be determined with (5.5), and Darcy's law (1.1) can be used to determine the effective permeability:

$$K_E(L_r) = \left.\frac{\Phi_r \mu_r L_r}{\mathcal{A}_E \Delta p}\right|_{x=L_r}, \tag{5.6}$$

which could be substituted in the left hand side of equation (5.4) to obtain the permeability at several positions of the fabric. The term $\Phi_r/\mathcal{A}_E$ can be seen as the actual speed of the flow front, but treated as constant in time and based on an averaged constant cavity height $\tilde{h}(x) = h$. But since $\tilde{h}(0) > \tilde{h}(L_r)$, this results in an underestimation of the actual speed at $x = L_r$. The pressure difference Δp will be determined by:

$$\Delta p = p_{atm} - \Delta p_{inlet} - p_{pump}, \tag{5.7}$$

in which p_{atm}, represents the atmospheric pressure and p_{pump}, represents the pressure that is measured by the pressure sensor. The term Δp_{inlet} represents the pressure drop over the filled inlet tube, which depends on the volume flow Φ_r and the hydraulic resistance of the tube:

$$\Delta p_{inlet} = \frac{8\mu_r L_{tube}}{\pi r_{tube}^4}\Phi_r(L_r) + \rho_r \mathcal{G} H_r, \tag{5.8}$$

in which the last term represents the pressure loss that is caused by gravity $\mathcal{G}$ and the height H_r to be climbed by the liquid, as is shown in figure 5.1(a). The flow resistance of the inlet tube has been processed in the first term on the right hand side ($r_{tube} = 3.85 \cdot 10^{-3}$[m], $L_{tube} = 58 \cdot 10^{-2}$[m]). The pressure drop over the outlet tube will not be considered, since it is only filled by air during the infusion experiment.

5.2.2 Flow Front Position Based

Using the expression (4.15) in section 4.3.2, which was derived in appendix G.1, substituting $\mathcal{V}_r = \mathcal{A}_E L_r$ and assuming $\mu_r >> \mu_a$ gives:

$$L_r = \left.\sqrt{\frac{2tK_E\Delta p}{\mu_r}}\right|_{x=L_r} \tag{5.9}$$

Rearranging gives:

$$K_E(L_r) = \frac{\mu_r}{2t\Delta p} L_r^2 \Big|_{x=L_r}, \tag{5.10}$$

such that the infusion time t is directly related to the flow front position L_r. This relation could be substituted in the left hand side of equation (5.4) to obtain the permeability at several positions of the fabric. Again, the pressure drop Δp will be determined with (5.7).

5.2.3 Flow Front Speed Based

Differentiating equation (5.9) with respect to time and rearranging gives:

$$K_E(L_r) = \frac{2t\mu_r}{\Delta p} \left(\frac{\mathrm{d}L_r}{\mathrm{d}t} \right)^2 \Big|_{x=L_r}, \tag{5.11}$$

such that the infusion time t is directly related to the flow front speed $\mathrm{d}L_r/\mathrm{d}t$. This relation could be substituted in the left hand side of equation (5.4) to obtain the permeability at several positions of the fabric. Again, the pressure drop Δp will be determined with (5.7). Another way in which this equation can be obtained, is differentiating equation (G.3) to time, after which the obtained relation can be solved for K^A. Then $\mu_r >> \mu_a$ may be assumed and $\mathcal{V}_r = \mathcal{A}_E L_r$ may be used to obtain (5.11). The difference between relation (5.11) and the quasi-steady state based relation (5.6) is the usage of the real flow front speed and the averaged (based on a constant cavity height $\tilde{h}(x) = \tilde{h}$) flow front speed respectively.

5.3 Results

Six valid infusion experiments were executed. Three experiments dealt with infusion in the 0° direction (see figure 2.2(b)) and the other three experiments dealt with infusion in 90° direction of the fabric. The experiments are numbered as ISD# and PSD#, respectively. The subsections show how acquired data was processed to obtain permeability values finally. The determination of the infusion liquid's viscosity is described in appendix H.3.

5.3.1 Data Analyses

In this section, acquired data for one experiment (ISD2) will be shown. All data from other experiments were processed similarly. These data will be processed in relations (generally using MATLAB and MAPLE), which have to be derived in order to describe the variables that are needed for the permeability determination, as described in section 5.2.

The captions of figure 5.3, 5.4 and 5.5 explain the origins of the relations. Data that was used to derive the relations in figure 5.3 was obtained from the position and the upper height sensor (figure 5.1(a)). These relations are all position dependent. However, due to a time dependent cavity height as explained in appendix H.1, these relations are time dependent as well. Since it is hard to process this time dependency in the permeability determination method from section 5.2, this determination will only be applied to the initial (at $t = T1$) and final cavity (at $t = T2$) per experiment. Therefore, a distinction between the relations in figure 5.3, 5.4 and 5.5 was made, related to the initial and final situation (solid and dashed lines respectively). The initial and final cavities are then assumed to be constant in time. In this way, an initial and final cavity related permeability estimation follows.

Figure 5.4 shows relations, which are time dependent and will directly be used in the permeability determination. Data from figures 5.4(a) and 5.4(c) were obtained from the load cell and the pressure sensor, respectively (figure 5.1(a)). The relation $\tilde{\mathcal{V}}_{r,sc}(t)$ in figure 5.4(b) was obtained by scaling relation $\tilde{\mathcal{V}}_r(t)$ in figure 5.4(a), since the original acquired data from the load cell overestimated the amount of liquid that was infused in the fabric. This volume flow complication and the associated corrections are described in appendix H.2. The relation in figure 5.4(d) was obtained by taking the derivative of $\tilde{\mathcal{V}}_{r,sc}$ with respect to time, such that the volume flow $\Phi_r(t)$ of the liquid is known.

Figure 5.5(a) shows the relation $t(L_r)$ which was solved from $\mathcal{V}(x) = \tilde{\mathcal{V}}_{r,sc}(t)$ for t. This relation is the most important for the permeability determination, since the steps Δx propagate the position

L_r in equation (5.4). This position is related to an infusion time t, which is related to all variables in figure 5.4.

No analytical expression was obtained for the relation in figure 5.5(b), which was to complex to solve from $t(L_r)$. Therefore, this relation was constructed by using sample points L_r, and using the analytical relations $t(L_r)$, $\Phi_r(t)$ and $\tilde{\mathcal{A}}(x)$, such that:

$$\frac{\mathrm{d}L_r}{\mathrm{d}t} = \frac{\Phi_r(t(L_r))}{\tilde{\mathcal{A}}(x)} \tag{5.12}$$

which is the flow front's speed, to be used in equation (5.11).

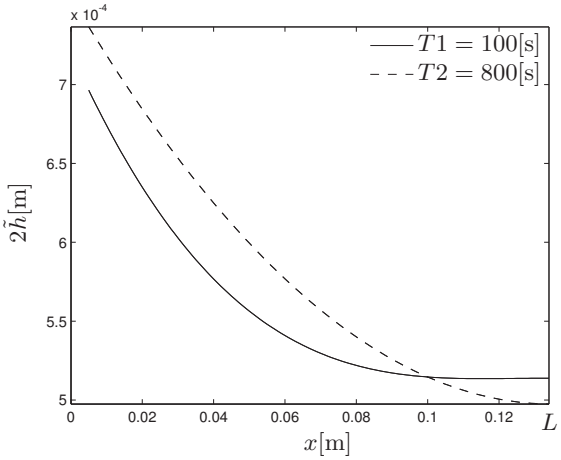

(a) Analytical fitted expression for the position dependent cavity height (H.1).

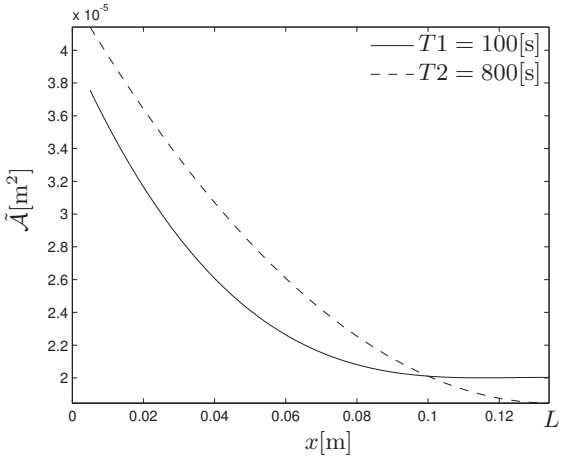

(b) Analytical fitted expression for the position dependent flow area (5.2).

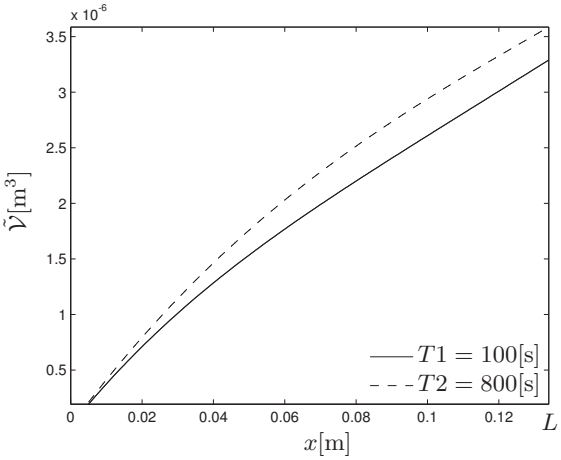

(c) Analytical fitted expression for the position dependent fibreless volume (5.3).

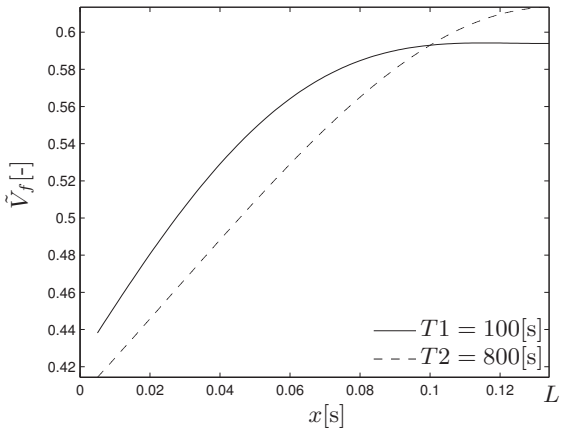

(d) Analytical fitted expression for the position dependent fibre volume fraction (5.1).

Fig. 5.3. Properties of the infused fabric from experiment ISD2.

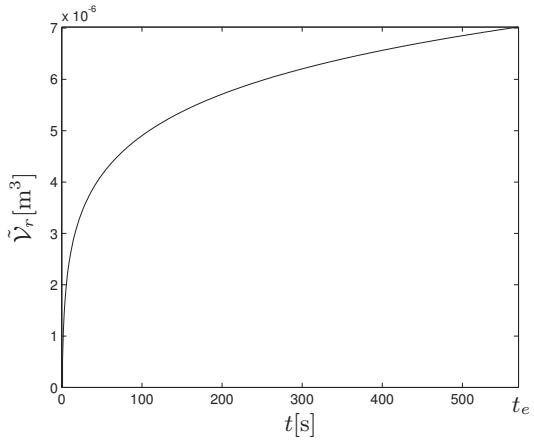

(a) Analytical fitted expression for the time dependent filled volume (H.2), directly from acquired data.

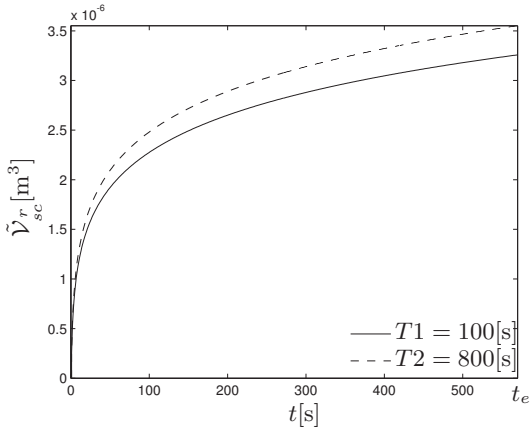

(b) Analytical fitted expression for the time dependent filled volume (H.3), from scaled acquired data.

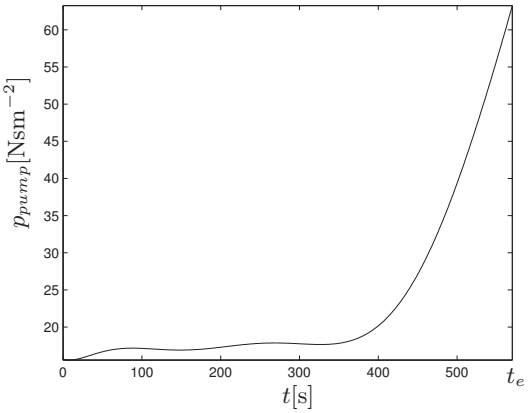

(c) Analytical fitted expression for the time dependent pressure on the pump side, to be used in (5.7).

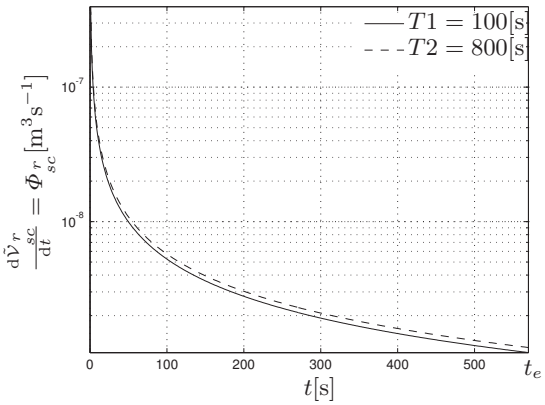

(d) Analytical expression for the time dependent volume flow, obtained from the derivative of (H.3).

Fig. 5.4. Acquired data from the infusion experiment ISD2.

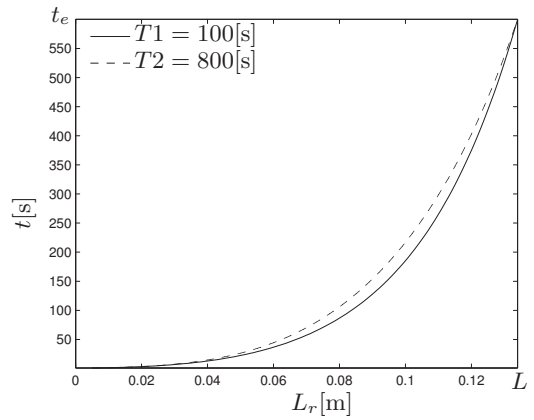

(a) Analytical expression for the time dependent flow front position, obtained by solving $\mathcal{V}(x) = \tilde{\mathcal{V}}_{r,sc}(t)$ for t, (H.3) (5.3).

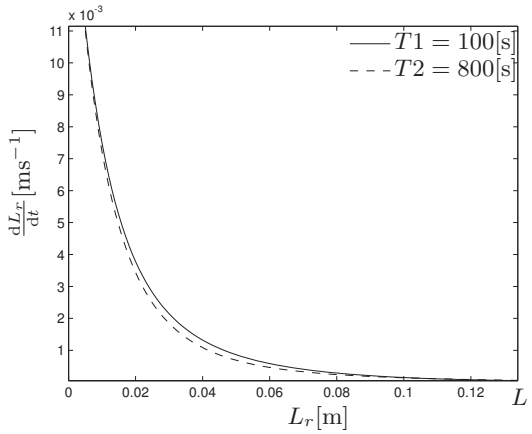

(b) Obtained by combining the relations $t(L_r)$, $\Phi_{r,sc}(t)$ and $\tilde{\mathcal{A}}(x)$ to yield in a flow front position dependent flow front speed. See figures 5.5(a), 5.4(d) and 5.3(b) respectively.

Fig. 5.5. Indirect properties of the infusion experiment ISD2.

Permeability

An algorithm to determine the permeability was based on serially connected permeabilities, as described by equations (5.4) and (5.5) and further information that was given in section 5.2. Repeatedly applying equation (5.4) for every flow front position $x = L_r$ with a resolution that is determined by Δx, results in a position dependent permeability $K_E^{\Delta x}(x)$. This process was applied twice for each experiment, in which the initial ($t = T1$) and final ($t = T2$) cavity height were assumed to be constant in time. Combining $K_E^{\Delta x}(x)$ and the partly constant or non-monotonic:

- cavity height $2\tilde{h}(x)$,
- or its associated cross-sectional flow area $\mathcal{A}(x)$,
- or its associated fibre volume fraction $V_f(x)$,

results in data sets:

$$\{(K_E^{\Delta x}, 2h_E^{\Delta x})_1, (K_E^{\Delta x}, 2h_E^{\Delta x})_2, \ldots, (K_E^{\Delta x}, 2h_E^{\Delta x})_N\}, \tag{5.13}$$

or

$$\{(K_E^{\Delta x}, \mathcal{A}_E^{\Delta x})_1, (K_E^{\Delta x}, \mathcal{A}_E^{\Delta x})_2, \ldots, (K_E^{\Delta x}, \mathcal{A}_E^{\Delta x})_N\}, \tag{5.14}$$

or

$$\{(K_E^{\Delta x}, V_{f,E}^{\Delta x})_1, (K_E^{\Delta x}, V_{f,E}^{\Delta x})_2, \ldots, (K_E^{\Delta x}, V_{f,E}^{\Delta x})_N\}, \tag{5.15}$$

respectively, with $N = L/\Delta x$ number of sample points over the infusion length. Figure 5.6 contains only the data from data set (5.13). This will be done to make comparison between the model predictions and the experimental results straightforward. Results that are related to the data sets (5.14) and (5.15) can be found on the included DVD. In summary, the objects in figure 5.6:

- the markers indicate the evaluated positions L_r, with a resolution determined by Δx, as was explained in the preamble of section 5.2;
- the unique shape of the marker refers to results that were obtained from one unique experiment;
- the open markers indicate the results that were obtained by using the first cavity measurement at $t = T1$ during the infusion experiment;
- the filled markers indicate the results that were obtained by using the last cavity measurement at $t = T2$ during the infusion experiment;
- the unique transparently and coloured areas indicate the tolerance on the determined permeabilities for a particular fabric thickness $2h$.

Scatter

The use of this method introduced some scatter, since the cavity height $2\tilde{h}(x)$ was partly constant or non-monotonic in some cases. As a result, cavity heights along the infusion direction x are not unique and could appear several times as is the case in figure 5.3(a) for $t = 100$[s]. A clear example of this type of scatter, can be observed in figure 5.6(c) at $K_E^{\Delta x,0}(2h_E^{\Delta x} = 5.15 \cdot 10^{-4}\text{[m]})$ for the ISD2 T1 data set.

Another source of scatter in the data sets (5.13)-(5.15) is the result of the time dependent cavity height (appendix H.1). The permeability was determined for the initial and final cavity heights $2\tilde{h}(x)$ such that the permeability $K_E^{\Delta x}$ could have two estimations at one position x. As already mentioned, this scatter is indicated by the coloured areas in figure 5.6. Finally, scatter due to the inconsistency between the experiments is observed. Each unique marker shape or coloured area refers to one experiment.

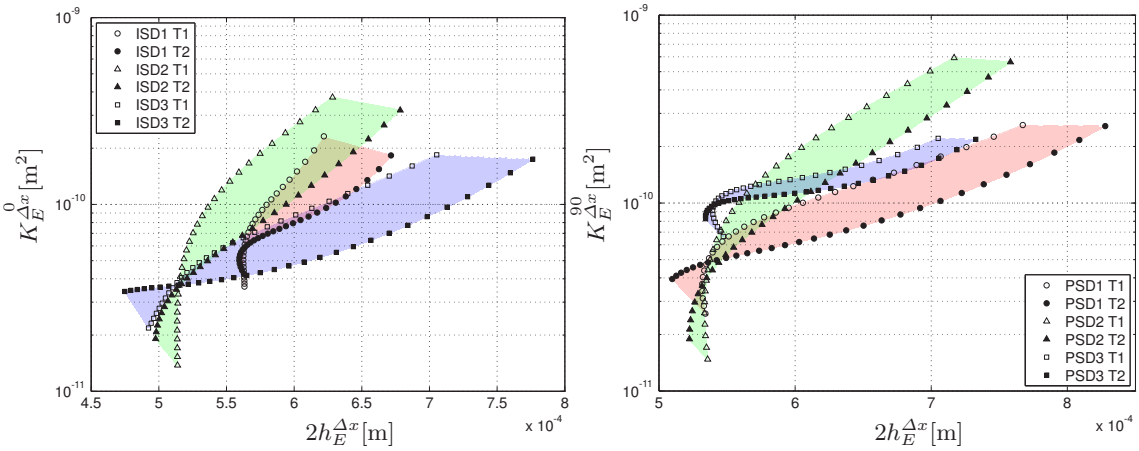

(a) Quasi-steady state based for ISD#.

(b) Quasi-steady state based for PSD#.

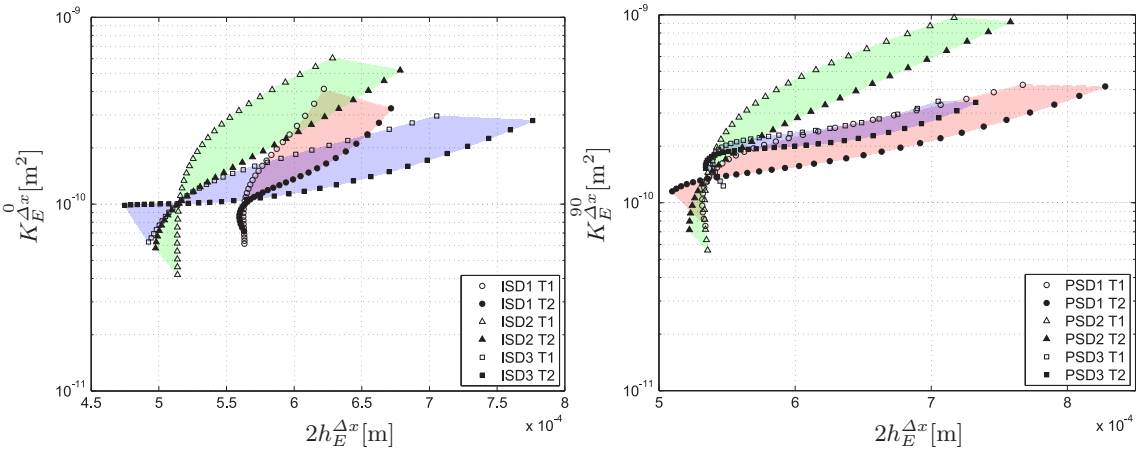

(c) Flow front position based for ISD#.

(d) Flow front position based for PSD#.

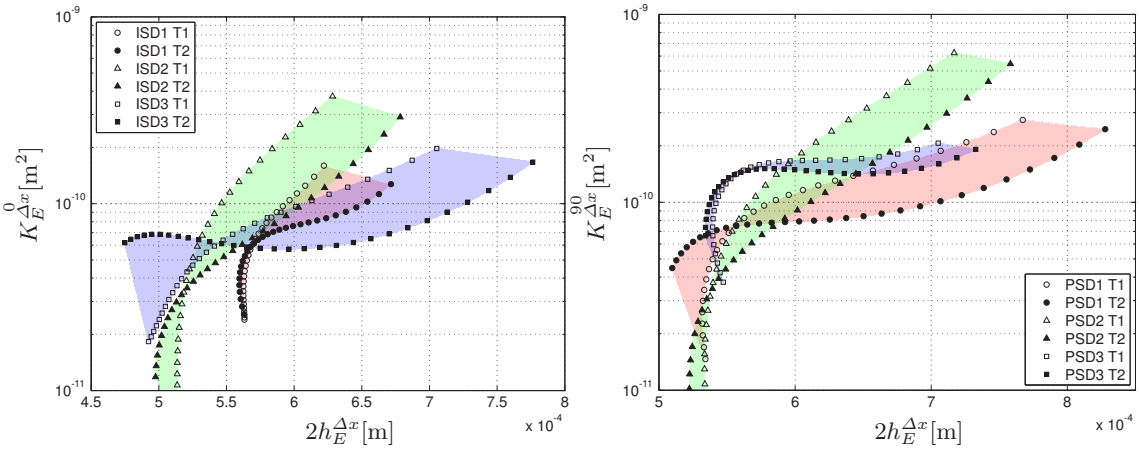

(e) Flow front speed based for ISD#.

(f) Flow front speed based for PSD#.

Fig. 5.6. Permeability determinations for experiments ISD# and PSD#, according to three different methods, described in section 5.2.

5.3.2 Visual Observations

Figure 5.7(b) and 5.7(d) show a typical flow front during an infusion experiment and is representative for all experiments that were analysed in this thesis. Appendix H.6 shows the typical propagation of the flow front for infusion in the 0° and 90° directions. As can be seen, there is a straight front without dry spots or any race tracking along the sides of the fabric. This observation justifies the assumptions that were made, based on the flow front's behaviour.

For each experiment in the series ISD# and PSD#, the position of the flow front at particular times was measured as is indicated by the markers in figure 5.7. This data can also be used to determine permeabilities according to the described methods in section 5.2. Since $L_r(t)$ is known from the visual observations, this relation will not be derived from the acquired data from the load cell. Therefore, this relation does not have a cavity height dependence, which means that there will not be an initial and final cavity related $L_r(t)$. A fit in the form of:

$$\tilde{L}_r(t) = a_{11} t^{a_{12}} \tag{5.16}$$

was created, with help of the visually observed flow front positions. Since equation (5.4) uses positions of the sample points (determined by Δx), the relation $t(L_r)$ is needed to link the positions to the variables in figure 5.4. Due to the simplicity of this relation, solving for t results in the relation $\tilde{t}(L_r)$ with ease. The flow front's speed is obtained by taking the derivative of $\tilde{L}_r(t)$ with respect to time.

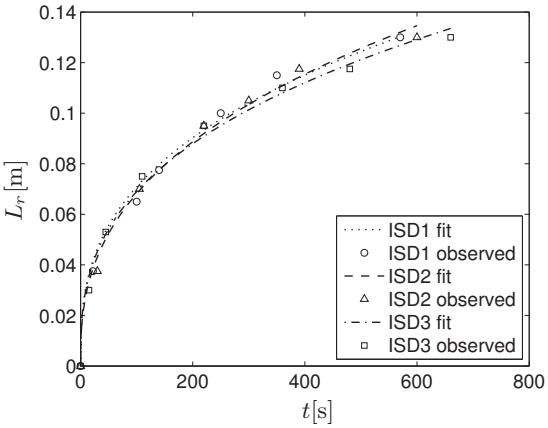

(a) ISD# experiments.

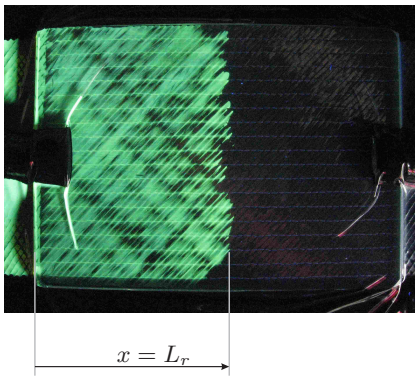

(b) Typical flow front at $t = 90$[s] for the ISD# experiments.

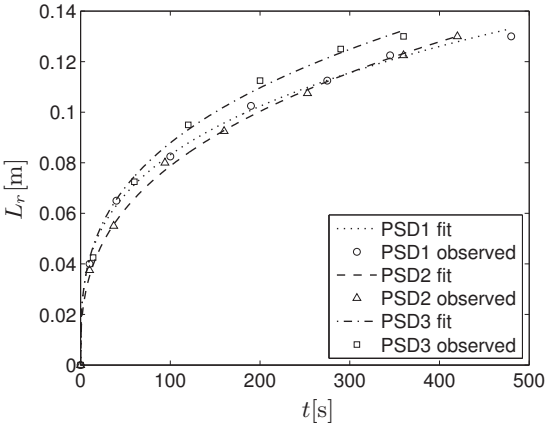

(c) PSD# experiments.

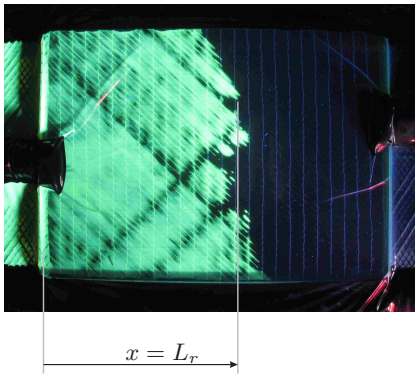

(d) Typical flow front at $t = 80$[s] for the PSD# experiments.

Fig. 5.7. Visually observed flow front positions, indicated by the markers. The lines show the obtained function fits, which were used in the permeability determinations.

The function $\tilde{\mathcal{V}}_r(t)$ will simply be obtained by substituting $\tilde{L}_r(t)$ in $\tilde{\mathcal{V}}_r(x)$. This $\tilde{\mathcal{V}}_r(x)$ is dependent on the cavity height and the cavity height is dependent on time, such that an initial and final cavity related $\tilde{\mathcal{V}}_r(x)$ results, just as in figure 5.3(c). The volume flow Φ_r is obtained by taking the derivative of $\tilde{\mathcal{V}}_r(t)$ with respect to time.

Permeability

Data sets like (5.13)-(5.15) were obtained by using equation (5.16) to obtain relations as in figure 5.4 and 5.5. Further information about these data sets and the plotted results in figure 5.8, can be found in the subsection "Permeability" on page 59.

Scatter

The relation $t(L_r)$was almost directly obtained, without using the time dependent cavity height or cross-sectional flow area, as was done in section 5.3.1. Therefore, less scatter resulted in figure 5.8 compared to the results in figure 5.6 (indicated by the coloured area). Other sources of scatter due to a non-monotonic cavity height and the inconsistency between experiments were already mentioned in the subsection "Scatter" on page 59.

5.4 Evaluation

Infusion experiments were executed and permeabilities of the bi-axial NCF were determined with three different relations. These relations served as an input in the developed relation (5.4), to extract more information from the acquired experimental data. The use of this method introduced some scatter, since the cavity height was partly constant or non-monotonic in some cases. Other sources of scatter were identified as well.

Scatter that was indicated by the coloured areas, was less for the data sets that were obtained by using the visually acquired flow front position, compared to the data sets that were obtained by using the indirect determined initial and final cavity related flow front position. Additionally, consistency between the experiments was better when the visually acquired flow front position was used.

The three different relations for permeability to be used in equation (5.4) resulted in somewhat different results. However, compared to the overall scatter, these differences are almost nil. Their mutual differences are consequent, i.e. the results obtained with the quasi-steady state relation (5.6) give the lowest permeabilities. The results obtained with the flow front speed based relation (5.11) lead to somewhat higher permeabilities and the results obtained with the flow front position based relation (5.10) give the highest permeability estimations.

Due to the large amount of scatter, it is hard to assign a permeability to a particular cavity height (thickness of the fabric) or fibre volume fraction. Since this is a qualitative study, it is convenient to know in which order the experimentally obtained permeabilities lie ($\approx 1 \cdot 10^{-10}[\mathrm{m}^2]$). Generally, scatter in the results of permeability determination of textiles is common. Comparison of the permeability in the 0°(experiments ISD#) and the 90°(experiments PSD#) direction of the fabric does not give obvious differences. The experiments suggest a close to isotropic permeability of the NCF.

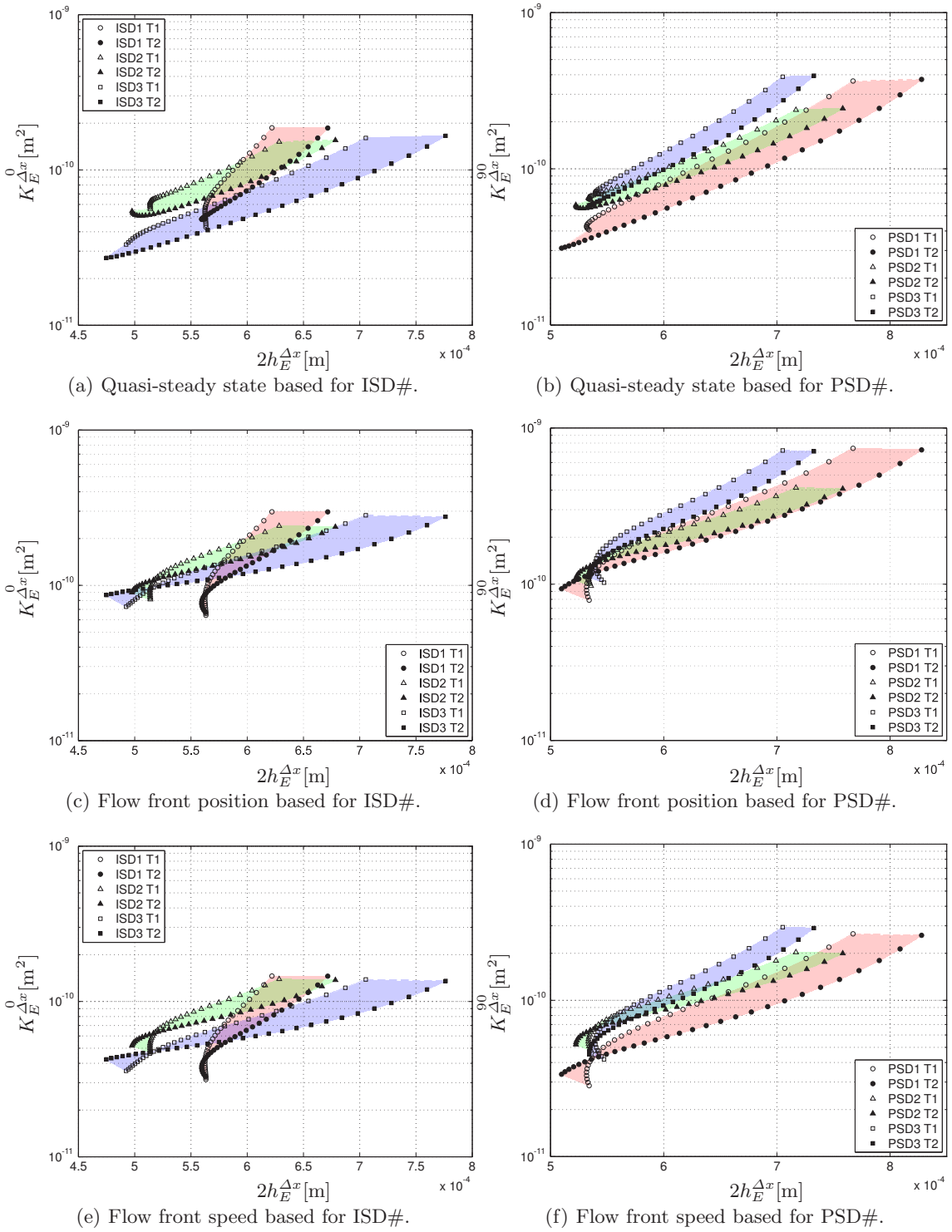

(a) Quasi-steady state based for ISD#.

(b) Quasi-steady state based for PSD#.

(c) Flow front position based for ISD#.

(d) Flow front position based for PSD#.

(e) Flow front speed based for ISD#.

(f) Flow front speed based for PSD#.

Fig. 5.8. Visual observation of the flow front tracking was used to determine the volume flow, flow front position and flow front speed, to be used in the permeability determinations for experiments ISD# and PSD#, according to three different methods, described in section 5.2.

6

Discussion

The situation during the experiments will partly be imitated by generating solutions with the network flow model in its steady state configuration (section 6.1) for several constant and uniformly distributed cavity heights. Then, experiment and model results will be compared and discussed.

Section 6.2 deals with recommendations and suggestions that partly follow from the steady state model results. The results of the developed filling scheme cannot directly be compared with the experiments, since modelling the whole domain with a varying cavity height is not yet possible. For this, the filling scheme has to be developed further. However, suggestions to modify and extend the filling scheme will be done in section 6.2.2.

To directly compare transient results of the experiments (flow front propagation) with the model, an idea to deal with the spatial and time dependent cavity height $h(x,t)$ with the steady state model results has been presented in section 6.2.3. This could lead to a conclusive model verification, which was not done in this thesis.

6.1 Steady State Model Results

The characteristics and the behaviour of the network flow model in its steady state configuration were analysed thoroughly in section 4.2.1. Now, the actual dimensions of the SYD lengths, external channels and the elements that describe the region with the stitch yarn obstruction in the SYDs and their permeabilities will be processed in the model.

The SYD lengths are determined with the averaged results from Loendersloot [3]. Actually, these SYD lengths were too short to create a connection between the elements in the 90° direction

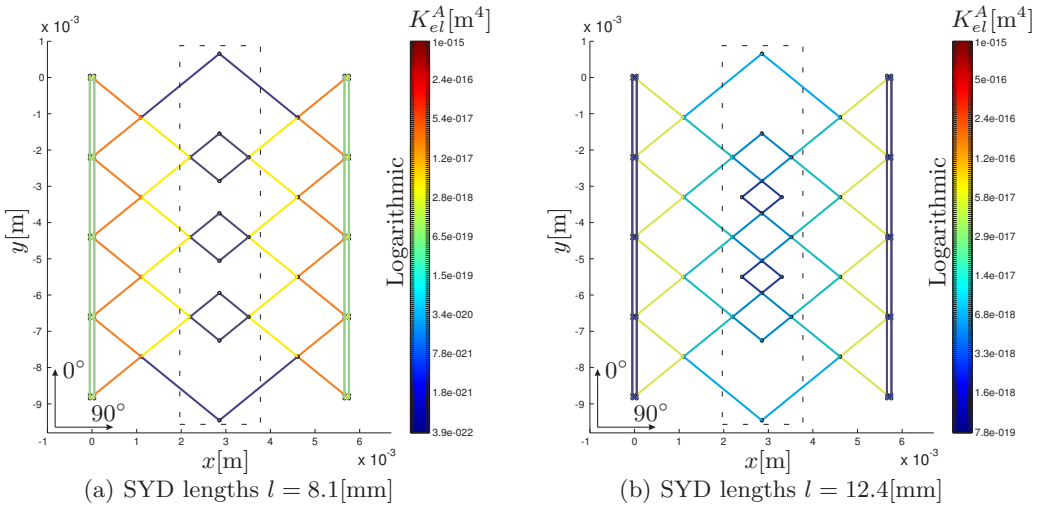

(a) SYD lengths $l = 8.1$[mm] (b) SYD lengths $l = 12.4$[mm]

Fig. 6.1. Element connections and permeabilities K_{el}^A for two different SYD lengths.

of the fabric. To ensure a connection, the SYD lengths were manipulated such that the SYDs just touched each other. These SYD lengths were $l = 8.1$[mm]. The associated element structure and permeabilities are visualised in figure 6.1(a). Furthermore, other SYD lengths till $l = 12.4$[mm] have been processed in the model to see their influence on the effective permeability. Figure 6.1(b) shows the structure and element permeabilities for SYD lengths $l = 12.4$[mm].

6.1.1 Variable SYD Lengths

The dimensions of the external channels were captured from the experimentally obtained results (appendix H.5) and processed in the model to imitate the situation during the experiments. The size of the domain was characterised by $10A \times 25B$ stitch distances, which gives reliable permeability predictions according to section 4.2.1. SYD dimensions h and b were taken constant ($h = 0.4$[mm], $b = 0.142$[mm]). To summarise, the following parameters were processed in the network flow model:

- Piece of fabric characterised by a number of stitch distances $10A$ and $25B$ ($A = 5.71$[mm], $B = 2.20$[mm]).
- Modelling a bi-axial NCF, which means a lower and an upper ply with their associated SYDs.
- Permeability of SYDs ($1{\cdot}10^{-17} > K^A_{SYD} > 1{\cdot}10^{-18}$) determined with the results from Mortensen [38], see section 3.3.
- Permeability of the region in the SYD with the stitch yarn obstruction, determined with the results from section 3.4.2 ($d_c = 0.071$[mm], $K^A_{ist} \approx 1 \cdot 10^{-18}$ [m^4]).
- Permeability of the external channels determined with the results from section 3.4.1, combined with the results of the microscopy analyses in section H.5 ($K^A_{est} = 7.85 \cdot 10^{-19}$ [m^4]).
- Permeability of the inter ply elements set to be highly porous compared to the other elements, since there is no relation for their permeabilities yet.
- Constant SYD dimensions $h = 0.4$[mm] and $b = b^u = b^l = 0.142$[mm].
- Different SYD lengths were taken ($l = l^u = l^l = 8.1, \ldots, 12.4$[mm]).

Results of these analyses are shown in figure 6.2. The effective permeability in both the 0° and 90° direction depends linearly on the SYD lengths l within the investigated range. Elongating the SYD lengths shows a great effect on permeability in the 90° direction of the fabric. The model predicts a highly anisotropic permeability in the small range of SYD lengths. As the SYD lengths increase, the difference between permeabilities K^0_E and K^{90}_E becomes smaller and the model predicts a more isotropic permeability.

The high dependence of the SYD lengths on the effective permeability in the 90° direction could be argued by using figure 6.1. The encircled regions show the elements that make the connection

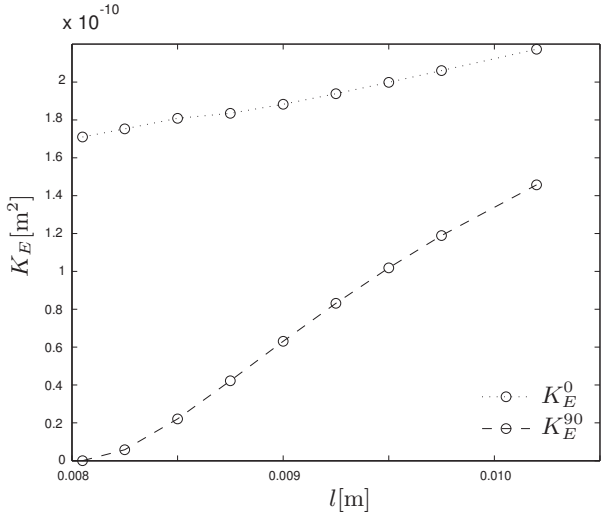

Fig. 6.2. Effective permeability K^0_E and K^{90}_E, as a function of the SYD lengths l. Parameter settings are listed on page 66.

between elements in the 90° direction. As the SYD lengths increase, the region in which the SYDs in the 90° direction intersect becomes wider. This leads to a higher permeability of the elements within the encircled region, as can be seen with help of the colour legend (logarithmic) in figure 6.1. This affects the effective permeability K_E^{90} a lot, since these elements are the only connections between two sides of the flow domain for flow in the 90° direction.

6.1.2 Variable SYD Heights and SYD Widths

Analyses in which the fabric's thickness $2h$ (twice the SYD height) and the SYD width b were varied, were done as well. Figures 6.3 and 6.4 show the results for constant SYD lengths $l = 8.1$[mm] and 12.4[mm] respectively. Further parameter settings are listed on page 66.

Figure 6.3 shows a highly anisotropic permeability prediction, while the results in figure 6.4 show less difference between K_E^0 and K_E^{90}. This behaviour was also observed in figure 6.2. Both dimensions b and $2h$ depend linearly on the effective permeability. For all graphs, increasing the SYD width b influences the effective permeability more than increasing the fabric's thickness $2h$.

Just as shown in the parametric study for the external channels in section 3.4.1, the effective permeability is mostly influenced by the smallest dimension of the channels that dominate the flow domain, which are the SYD widths b in this case. The linear dependency of the effective permeability on both the SYD dimensions $2h$ and b, does not correspond with the results from the channel flow

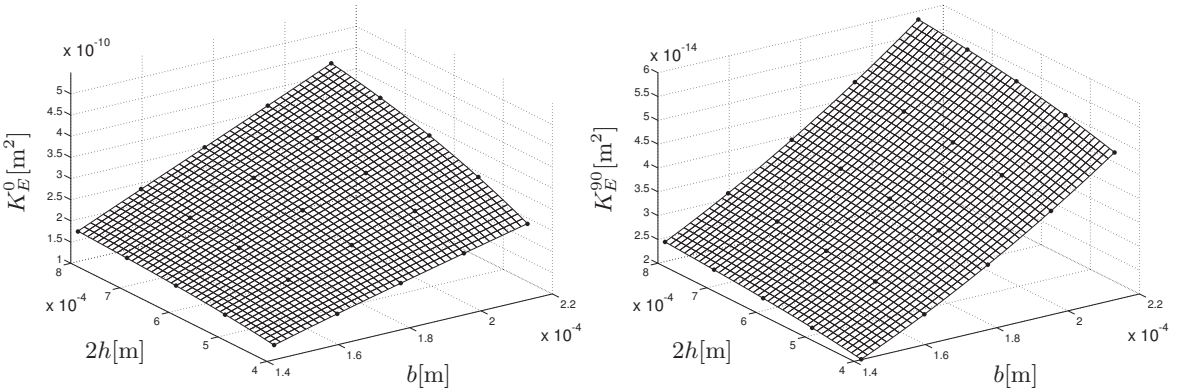

(a) Effective permeability in the 0° direction of the fabric.

(b) Effective permeability in the 90° direction of the fabric.

Fig. 6.3. Effective permeability K_E with constant SYD lengths $l = 8.1$[mm]. Other parameter settings are listed on page 66.

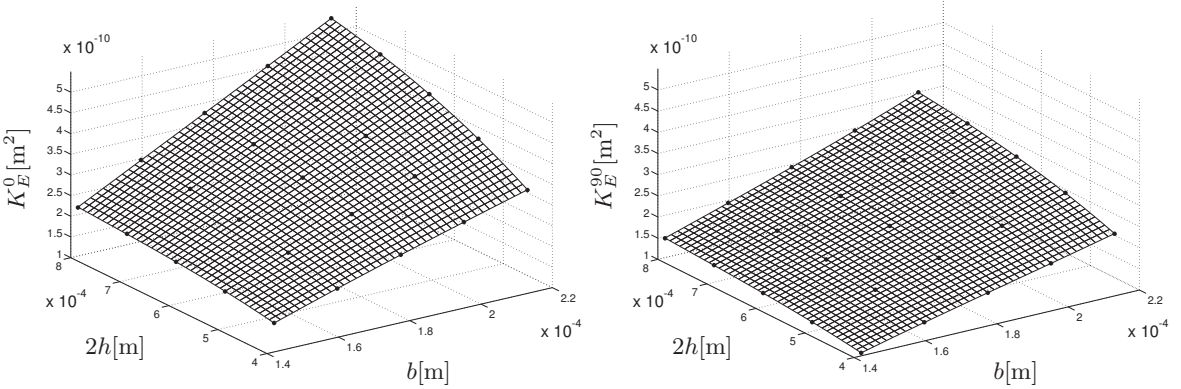

(a) Effective permeability in the 0° direction of the fabric.

(b) Effective permeability in the 90° direction of the fabric.

Fig. 6.4. Effective permeability K_E with constant SYD lengths $l = 12.4$[mm]. Other parameter settings are listed on page 66.

example in section 3.1, in which a non-linear behaviour of the smallest dimension was observed $\sim b^3$. However, the situation of the channel network cannot be compared directly with simple channel flow.

6.1.3 Isotropy of the Permeability (Model vs. Experiment)

Experiments did indicate a close to isotropic permeability of this biaxial NCF in the order range of $\approx 1 \cdot 10^{-10}[\mathrm{m}^2]$ (figure 5.8). Comparing these isotropic permeabilities with the partly anisotropic permeability predictions as discussed in section 6.1.1 and 6.1.2, it is expected that flows at micro level are significant. Micro channels can serve as additional connections between inter bundle channels (SYDs), such that the permeability in the 90° direction increases.

The source of the determined isotropy of the fabric during the experiments, could also be found by considering statistical variations in the inter bundle dimensions. SYD lengths and widths will vary over the fabric and since these dimensions influence the effective permeability much, the consideration of a statistical distribution of SYD lengths (with the averaged value around 8.1[mm] [3]) could predict a closer to isotropic permeability.

Loendersloot [3] did analyses with a statistical distribution of the SYD widths. Depending on the type of distribution, the effective permeability can be influenced significantly. When elaborating the Matlab program in section 4.1 with the option to consider a statistical distribution of channel dimensions, similar analyses could be done with a statistical distribution of the SYD lengths.

6.1.4 Influence of Added Details and SYD Dimensions

A sensitivity analysis has been executed to investigate the influence of several parameters on the effective permeability. These parameters are the SYD length l, the fabric's thickness $2h$ (twice the SYD height) and the SYD width b. An effective permeability was determined (for a piece of fabric with $10A \times 25B$) for which all abovementioned parameters were kept as a constant, except the parameter ϕ to be investigated. Each of the abovementioned parameters was treated as an investigation parameter once. Per investigated parameter, two configurations of the network were built. Namely, a configuration with a minimum value ϕ_{min} and a configuration with a maximum value ϕ_{max}, such that it fulfilled:

$$\gamma[\%] = \frac{\phi_{max} - \phi_{min}}{\phi_{min}} \cdot 100$$

in which γ is a predefined change of ϕ, which was set to 50%. These values are listed in table 6.1. While ϕ has a minimum and a maximum value, the other parameters were set to a constant intermediate value (fourth column in table 6.1) that lay within its own minimum and maximum value, which were used in another sensitivity analyses that considered this parameter to be investigated.

Subsequently, a minimum and maximum effective permeability was determined per sensitivity analysis, by using the steady state configuration of the network flow model. The change of permeability was determined as:

$$\kappa[\%] = \frac{K_E(\phi_{max}) - K_E(\phi_{min})}{K_E(\phi_{min})} \cdot 100$$

A configuration was used with the absence of the added details to yield κ_0 in figure 6.5(a). The absence configuration is obtained by setting the elements that describe the penetrating stitch yarns in the SYD to permeable (e.g. $K^A_{ist} = 1 \cdot 10^{-15}[\mathrm{m}^4]$), compared to the other elements. The external channels are then set as impermeable (e.g. $K^A_{est} = 1 \cdot 10^{-21}[\mathrm{m}^4]$), compared to the other elements.

Another configuration was used with the presence of the added details by considering:

Table 6.1. Minimum and maximum values of the investigation parameter ϕ and its intermediate value, which was used when it was treated as a constant in another sensitivity analysis.

ϕ	ϕ_{min}	ϕ_{max}	intermediate value
l[m]	$8.1 \cdot 10^{-3}$	$12.1 \cdot 10^{-3}$	$10.1 \cdot 10^{-3}$
$2h$[m]	$5 \cdot 10^{-4}$	$7.5 \cdot 10^{-4}$	$6.25 \cdot 10^{-4}$
b[m]	$1.42 \cdot 10^{-4}$	$2.13 \cdot 10^{-4}$	$1.78 \cdot 10^{-4}$

- the permeability for external channels ($K^A_{est} = 7.85 \cdot 10^{-19}$ [m^4], from external channel dimensions that were obtained with microscopy), to imitate the situation during the experiments;
- the permeability values ($K^A_{ist} \approx 1 \cdot 10^{-18}$ [m^4]) of the elements that describe the penetrating stitch yarns in the SYD, which are dependent on the SYD width b,

to yield κ in figure 6.5(b)

Similarly, the effect of the change of a parameter on the anisotropy λ:

$$\lambda = \frac{K_E^{90}}{K_E^0},$$

has been investigated. The change of anisotropy was determined as:

$$\Lambda[\%] = \frac{\lambda(\phi_{max}) - \lambda(\phi_{min})}{\lambda(\phi_{min})} \cdot 100$$

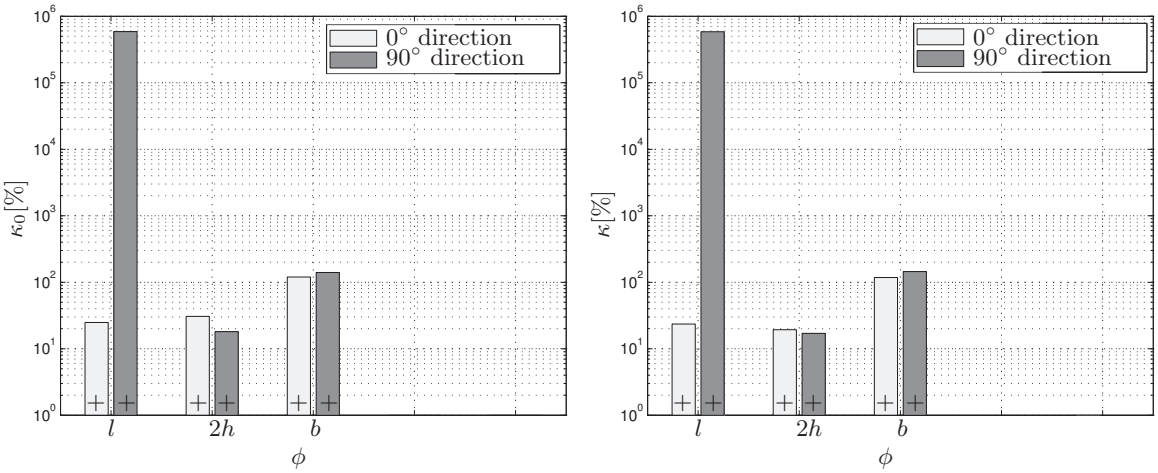

(a) $\gamma = 50\%$ (b) $\gamma = 50\%$

Fig. 6.5. The change of permeability κ_0 (without added details) and κ (with added details) by increasing the parameter ϕ with 50%. The plus signs indicate an increasing effective permeability.

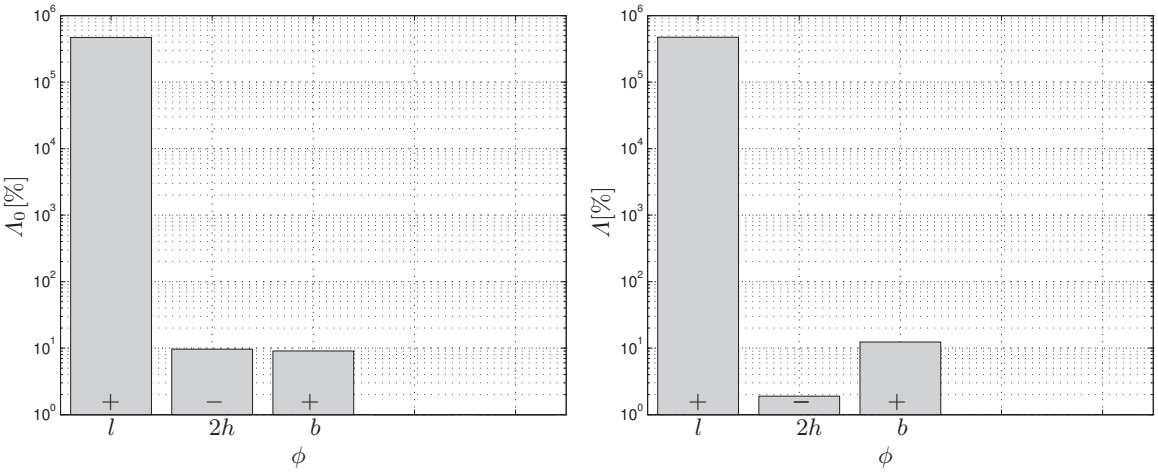

(a) $\gamma = 50\%$ (b) $\gamma = 50\%$

Fig. 6.6. The change of anisotropy Λ_0 (without added details) and Λ (with added details) by increasing the parameter ϕ with 50%. The plus and minus signs indicate a less anisotropic (more isotropic) and a more anisotropic (less isotropic) permeability.

Table 6.2. Overview of the values of the permeability and the anisotropy that were obtained by configuring the network flow model with the parameters as listed in table 6.1. The percentages indicate the difference of the permeability and the anisotropy between the configuration with and without the added details, with respect to the configuration without the added details.

investigation parameter		l	$2h$	b
without added details				
	$K^0_{E,min}$[m^2]	2.886e-010	2.7282e-010	2.0388e-010
	$K^{90}_{E,min}$[m^2]	3.3228e-014	8.2806e-011	5.5711e-011
	λ_{min}[-]	1.1514e-004	0.3035	0.2733
	$K^0_{E,max}$[m^2]	3.6045e-010	3.5649e-010	4.488e-010
	$K^{90}_{E,max}$[m^2]	1.954e-010	9.7754e-011	1.3375e-010
	λ_{max}[-]	0.5421	0.2742	0.2980
with added details				
	$K^0_{E,min}$[m^2]	2.6249e-010 (9.0%)	2.6313e-010 (3.6%)	1.8356e-010 (10%)
	$K^{90}_{E,min}$[m^2]	3.218e-014 (3.2%)	8.2273e-011 (0.6%)	5.3861e-011 (3.3%)
	λ_{min}[-]	1.2260e-004 (6.5%)	0.3127 (3.0%)	0.2934 (7.4%)
	$K^0_{E,max}$[m^2]	3.243e-010 (10%)	3.1393e-010 (12%)	4.0019e-010 (11%)
	$K^{90}_{E,max}$[m^2]	1.8852e-010 (3.5%)	9.6296e-011 (1.5%)	1.3191e-010 (1.4%)
	λ_{max}[-]	0.5813 (7.2%)	0.3067 (12%)	0.3296 (11%)

By assuming $K^0_E > K^{90}_E$ (which was the case for all analyses), a negative Λ means that an increasing value of the parameter leads to a more anisotropic (less isotropic) permeability of the fabric, whereas a positive Λ means that an increasing value of the parameter leads to a less anisotropic (more isotropic) permeability of the fabric. This is indicated in figure 6.6 by the minus and plus signs respectively.

The results are processed in table 6.2 and figure 6.5 and 6.6. These will be discussed in the subsequent subsections.

Effect of added details and SYD dimensions on the effective permeability (figure 6.5)

- Increasing the SYD length l by 50% shows an increase of 10% of the effective permeability in the 0° direction and an increase of many orders of magnitude for the effective permeability in the 90° direction (within the investigated range of SYD lengths $12.4 \geq l \geq 8.1$[mm]).
- Increasing the fabric's thickness $2h$ by 50% shows an increase of 10% of the effective permeability in the 0° and 90° direction.
- Increasing the SYD width b by 50% shows an increase of 100% of the effective permeability in the 0° and 90° direction.
- There is no difference for the dependency of l, $2h$ and b on the change of permeability κ, between the configuration of the model with the absence and the presence of the added details.
- Considering the values and percentages in table 6.2, the added details affect the permeability in the 0° direction by $\approx 10\%$. Their effect on the permeability in the 90° direction is almost nil.

Effect of added details and SYD dimensions on the isotropy of the effective permeability (figure 6.6)

- As the SYD length l increases, the difference between permeabilities K^0_E and K^{90}_E becomes smaller and the model predicts a more isotropic permeability (figure 6.2 and 6.6(b)). Increasing the SYD length by 50% shows a change of some orders of magnitude of the isotropy of the effective permeability (more isotropic).
- An increase of the SYD width b leads to a more isotropic prediction, but not as much as the effect of an increasing SYD length l. Increasing the SYD width by 50% shows a 10% more isotropic effective permeability prediction.
- There is no difference for the dependency of l and b on the change of anisotropy Λ, between the configuration of the model with the absence and the presence of the added details.

- Increasing the fabric's thickness $2h$ leads to a more anisotropic permeability of the fabric. For the configuration without the added details, increasing the SYD height by 50% shows a 10% more anisotropic effective permeability prediction. However, this change in isotropy is almost nothing when the added details are involved.
- Considering the values and percentages in table 6.2, the added details affect the anisotropy λ by $\approx 8\%$ (more isotropic).

6.1.5 Permeability Range Comparisons

Considering the experimentally obtained permeabilities, it is impossible to assign just one value for a particular NCF with a particular fibre volume fraction. In general, experiments show a lot of variation in the measurements of permeability. Considering the order of magnitude, this thesis shows permeabilities $\approx 1 \cdot 10^{-10}[\mathrm{m}^2]$ in the 0°and 90°direction of biaxial NCF's with the properties as listed in table 5.1. The permeability could vary half an order of magnitude up or down easily for both experimental and model results. For example, see the

- experimentally obtained graphs for permeability in the 0°and 90°direction in figure 5.6 and 5.8,
- the predicted results in figure 6.2 with the SYD length dependency,
- and the results from the sensitivity analyses in figure 4.4 and 4.5 with the dependency on the permeability of the model extensions, as they were described in section 2.3 and 3.4.

Experiments were done by Loendersloot [3] at the National Aerospace Laboratory (NLR) and the University of Twente (UT) for this type of NCF (table 5.1). The fibre volume fractions were 57%, which corresonds with a fabric height of $2h \approx 0.55 \cdot 10^{-3}[\mathrm{m}]$ (determined with (5.1)). Measurements at the NLR indicated an unsaturated permeability of $\approx 1 \cdot 10^{-10}[\mathrm{m}^2]$. The saturated permeability were just a fraction higher, but still $\approx 1 \cdot 10^{-10}[\mathrm{m}^2]$. Measurements at the UT resulted in higher unsaturated permeabilities $\approx 5 \cdot 10^{-10}[\mathrm{m}^2]$. The saturated permeabilities were even twice as big. However, the reliability of the used test rig at the UT during those measurements is debatable (race-tracking, cavity height controlling).

For the bi-axial NCF with its properties in table 5.1 and a fabric height of $2h = 0.6 \cdot 10^{-3}[\mathrm{m}]$, model predictions of Nordlund [4] resulted in values $\approx 1 \cdot 10^{-10}[\mathrm{m}^2]$ for the effective permeability for an unperturbed geometry and without considering the penetrating stitch yarns and fibre crossings (see figure 3.3). The permeability predictions gave lower values with a minimum of $4.5 \cdot 10^{-11}[\mathrm{m}^2]$ ($\approx 50\%$ lower), when those features were included. As discussed in section 6.1.4, the effect of the added details result in an $\approx 10\%$ lower effective permeability. However, the explicitly modelled fibre crossings by Nordlund are implicitly incorporated in this thesis by assuming the geometry of the SYDs. This means that it cannot be said exactly about Nordlund's investigation, what the influence of the penetrating stitch yarns was. Experiments were done as well (with $2h = 0.6 \cdot 10^{-3}[\mathrm{m}]$) and resulted in a saturated permeability between $2.5 \cdot 10^{-11}[\mathrm{m}^2]$ and $4.7 \cdot 10^{-11}[\mathrm{m}^2]$.

Lekakou [29] modelled bi-axial NCFs as well, but these fabrics were made from glass fibres. A fibre volume fraction of 55% was used. Experiments were done as well and both results (model and experimental) resulted in a permeability around $\approx 1 - 1.5 \cdot 10^{-11}[\mathrm{m}^2]$. This is 0.5-1 order of magnitude lower than the results from analyses with NCFs made of carbon fibres. These lower values may be argued, since the glass fibres have a greater diameter than carbon fibres. However, packing is assumed to be better for carbon fibres, since they have a smaller diameter.

6.2 Recapitulation and Recommendations

A qualitative study to the in-plane permeability modelling of Non-Crimp Fabrics has been carried out. A network flow model was developed by Loendersloot [3] to describe flow through inter bundle channels (meso level). To improve this model, it was extended with details that consider stitch yarn influenced regions. The hydraulic radius based permeability relation for the SYD arms was rejected and a more valid relation was developed, which uses a relation from Mortensen [38] that was based on Poiseuille flow. The program's code was rewritten to deal with the added elements that describe the stitch yarn influenced regions and to make it suitable for both steady state and transient (fill

simulation) solutions. A lot of suggestions were developing during this thesis to improve the model or to give a better understanding to some phenomena. These will be discussed in the subsequent sections.

6.2.1 Steady State Model

Isotropy of the Permeability

Several configurations of the model were built, for which SYD dimensions h, b and l were varied. The influence of these SYD dimensions on the effective permeability was investigated in section 6.1.1, 6.1.2 and 6.1.4. It was shown that the anisotropy of the effective permeability is highly dependent on the SYD length l.

Liquid infusion experiments were carried out to validate the network flow model. Since the cavity height and thus the fibre volume fraction varied along the infusion direction, the permeability of the NCF varied along the infusion direction as well. Therefore, a formulation based on serially connected permeabilities was developed to deal with this variable permeability. Comparison of the experimentally determined permeability with the predicted permeability of the NCF in the 0° direction showed good agreement. Furthermore, the experiments suggest an isotropic permeability, i.e. permeability in the 90° direction was in the same order of magnitude as the permeability in the 0° direction.

As indicated during the discussion about the model results in section 6.1.3 and abovementioned differences in the isotropy of the permeability, it is interesting to consider different statistical distributions of the channels' dimensions. Loendersloot [3] did consider such distributions for the SYDs' widths b. It is worth to reconsider statistical distributions of the variations of:

- SYD lengths $l = l^u = l^l$, since they highly affect the predicted isotropy of the bi-axial NCF;
- dimensions g and f of the external channels (section 3.4.1);
- SYD widths $b = b^u = b^l$, since they:
  - significantly influence the permeability of the elements that describe the SYD arms (3.3);
  - are related to the permeability of the elements that describe the stitch yarn obstructed region in the SYDs (section 3.4.2).

When considering variations of these dimensions and to give reliable solutions, the domain size is expected to be larger than the size that followed from the sensitivity analyses in section 4.2.1 (for uniformly distributed dimensions). Loendersloot [3] showed that a network of $40A \times 80B$ is sufficient.

If the abovementioned statistical distributions of SYD lengths do not lead to an isotropic permeability prediction, it is expected that:

- the measured averaged SYD lengths [3] are an underestimation or,
- flows at micro scale are significant, especially in the 90° direction of the fabric.

At this moment, the last option is expected. Especially micro flow around the tips of the SYD could influence the global flow behaviour. The flow in these regions can be described by the 1D elements. The permeability of these elements could for example be related to the Kozeny-Carman relation (1.15). In the neighbourhood of the SYD elements that describe the tip, connections between micro flow elements could be established (within the encircled region in figure 6.1). In this way, it is expected that the high dependency of the permeability's isotropy on the SYD lengths will decrease. This would be beneficial, since the experiments suggest a far from anisotropic permeability.

Extending the network flow model with elements that describe micro flow leads to an assembly of even more elements to describe the flow domain of a small piece of NCF. Considering the computational memory usage, it might be worthwhile to elongate the SYD lengths such that the connection of elements in the 90° direction of the fabric improves. As was shown in section 6.1, elongating the SYD lengths directly lead to a more isotropic permeability prediction. To reduce the number of elements and thus the size of the system of equations to solve, this option could be applied instead of adding elements that describe micro flow. However, it is still recommended to incorporate the elements that represent the micro flow. Comparison of these results with results of the network flow model for which the SYD lengths were elongated only, will highlight the best option.

Stitch Pattern

Extending the network flow model with the option to choose a particular stitch pattern is recommended. Different stitch patterns are visualised in figure 2.4. The external channels that are related to the chain stitch pattern were directed along the 0° direction of the fabric, such that the permeability in the 90° direction of the fabric will not be influenced by these channels. The external channels that are related to a tricot or a chain/tricot stitch pattern do influence the permeability in both the 0°and 90°direction, which could give interesting results.

Multiple Plies and Layers

So far, the model is developed for a bi-axial NCF that contains two uniquely orientated stacked plies. In practise, tri-axial and quadri-axial (three and four uniquely orientated stacked plies respectively) NCFs are used as well. Therefore, it is worthwhile to elaborate the model for these types of NCFs. The greatest modification that is needed will be the SYD intersection search algorithm (figure 4.2). Also, the relations to calculate the intersection distances (section 2.2) need to be modified or even be generalised for layers with an arbitrary number of plies.

Designs of composite products to be produced by using LCM techniques, usually require more than 1 layer of a fabric to be infused. Stacking multiple layers of NCFs results in different stacked grids of stitch yarn penetration points, which are the roots of the SYDs. These grids (1 layer has one grid of stitch yarn penetration points) are randomly shifted. As a consequence, the SYDs on top and at the bottom of the layers overlap each other at arbitrary positions. This randomness leads to a lower and upper bound for the permeability, related to an impermeable and permeable interaction of layers respectively. A second connection search algorithm should be needed to connect the different layers (figure 4.2). Therefore, relations have to be developed to relate two different grids of penetration points and their associated intersecting SYDs.

Inter Ply Elements

Relations for the permeability of inter ply elements (figure 4.1(a)) have not been developed yet and were set to be highly permeable during the analyses. These elements describe the connection between intersecting SYDs of interacting plies. These flow paths are not explicitly given, as was the case for the external channels. Instead these flow paths can be described by an assembly of six 1D elements, just as was done for the region in the SYD with the stitch yarn obstruction. Implementation of these elements means that the single inter ply elements need to be replaced by the assembly of six elements. Again, a parametric study needs to be done to describe the element permeabilities. For this, different flow domains have to be modelled for which the dimensions of the upper channel (piece of upper SYD arm) and interacting lower channel (piece of lower SYD arm) are different. This is needed to describe the many possibilities of intersections between lower and upper SYD arms, e.g. the intersection may be at positions where the lower and upper SYD arms are narrow and wide respectively.

However, it is expected that these regions do not influence the in-plane permeability a lot. The increasing number of elements is an additional reason to wait to process this model extension till above suggested extensions are processed. One might think that the suggested assembly of elements are important to determine the out-of-plane permeability of the NCF, but it is expected that flows in this direction are dominated by micro flows through the fibre filaments. This makes this meso flow based model not suitable and another model is needed to describe the out-of-plane permeability of NCFs.

Textile Deformations

Shear (Akkerman [57] and ten Thije [25]), stacking and compression (mould closing) of layers is related to nesting and compaction mechanisms. Relations for these mechanisms could be processed in the model. However, the suggested model extensions so far need to be applied and compared with experimental data first. The results of the comparisons may be used to deliberate the urge for incorporating these details. Once this is needed, it is possible that the SYD widths will be smaller than

twice the penetrating stitch yarn diameter d_c as in figure 6.7, due to compaction mechanisms. In that case, the parametric study about the SYD domain obstacles in section 3.4.2 needs to be elaborated, since the results for the permeability of this region dealt with a minimum SYD width of $2d_c$. A new response surface will be needed to describe the permeability, since the current response surface is described by a third order polynomial in two dimensions and could give an unreliable permeability outside the investigated domain.

It is also advised to obtain a response surface that is described by a rational fit, since these functions have a limit. As the channel dimensions tend to zero, permeability will tend to zero as well. This behaviour is not represented by a polynomial based fit, but rational based fits do.

6.2.2 Fill Simulation

A filling scheme was developed in section 4.3 and some interesting transient effects were identified in section 4.3.2. The developing transient solution could show non-uniform filling. As a result, the filling times that are estimated with the steady state obtained effective permeability could differ from filling times that are predicted with the transient solution. At the unit cell level, it is possible that micro flows undo this effect in reality. However, the identification of transient effects show that the filling scheme could also predict non-uniform infusion and dry spots when a fill simulation is applied to a macro scale based flow domain. An idea to model a macro scale based domain with meso level based information will be given. This will be done, since computational work and time need to be reduced to model real size products. Other suggestions to save computational work and to make the filling scheme more accurate will be done as well.

Macro Scale based Flow Domain

An example of a macro scale based flow domain is presented in figure 6.8(a). When modelling this product with its shear distribution and considering all inter bundle channels (SYDs) and stitch related regions, a huge number of elements is needed to create the whole flow domain. This results in a huge system of equations, which needs to be solved for every time step in the developed filling scheme. An alternative to model the flow domain, is to coarsen the shear distribution, as is schematically drawn in figure 6.8(b). This results in pieces of NCF with a uniform shear, represented by the single coloured squares. Each square could be represented by an assembly of 1D elements as sketched in figure 6.8(b), such that the 1D element based filling scheme could still be used. All squares could be represented by such assemblies, and these could again be assembled in a global system matrix that represents the whole product.

The effective permeability of a coloured square could be determined with the steady state model for different directions. The different directions are represented by the six elements in the assembly, which have an individual permeability. It is recommended to create a database in which results from the steady state model (direction dependent permeability) are stored for pieces of NCF with a particular shear angle. Assigning permeabilities to a global system matrix that represents the product could then be done quickly.

The alternative presented here could save a lot of computational work and time. However, the next section discusses the possibility of a modification on the filling scheme that could reduce the com-

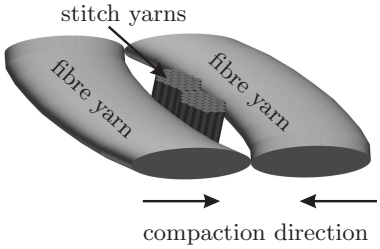

Fig. 6.7. Compacted, maximum space taken by the stitch yarn, $b \approx d_c$

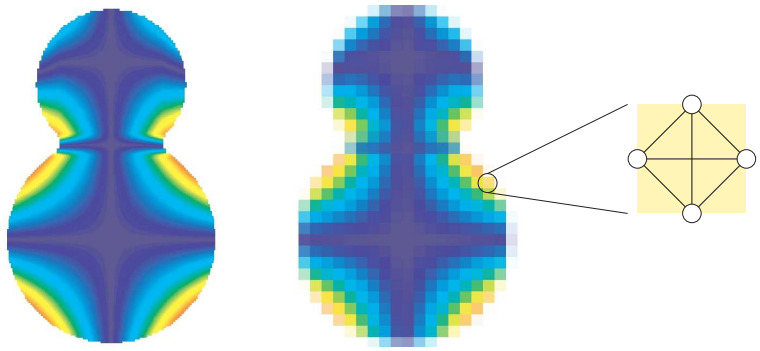

(a) Shear distribution after draping.

(b) A coarsened shear distribution.

Fig. 6.8. Draping of an arbitrarily shaped (double dome) product and its resulting shear distribution. Note that the shear field is not symmetrical in case of an NCF.

putational work dramatically and is another alternative to reduce simulation time. Both alternatives could also be combined and could result in a better modification.

Flow Front Tracking

Other developed fill simulation tools are mainly based on a Volume of Fluids (VOF) method (actually identical to a Galerkin FEM formulation on linear elements). An important difference is that VOF methods use fill factors that are associated to nodes, while in this thesis fill factors are associated to the 1D elements.

Koorevaar [54] uses the VOF method with control volumes for which its filling state is defined by a fill factor on the corresponding nodes. A pressure field solution need to be found by solving a system of equations, after which flow rates will be determined and a fill factor update will follow. These separated steps are needed, since there is no explicit relationship between the pressure and fill factor fields. In some respects, the lack of this explicit relationship is analogous to the lack of an explicit relationship between the pressure and velocity in solving the incompressible Navier-Stokes equations. However, if the infused liquid was compressible, then such a relationship would exist. A well-known means of solving the incompressible Navier-Stokes equations is to assume slight incompressibility, thereby introducing an equation of state that leads to an explicit pressure-velocity coupling in the continuity equation. Luoma and Voller [55] used this principle in the melting enthalpy method. Unlike the method proposed by Koorevaar, this method does not need a system of equations to be solved, since it is an explicit scheme. A disadvantage is that the restricted small time step is proportional to the grid spacing and the compressibility, which is set to a low value to approximate an incompressible fluid.

Koorevaar [54] had a time step restriction as well, i.e. only one node can be filled per time step, instead of subsequent connected nodes to be filled within one time step. In this thesis, the restriction that concerns one element to be filled in one time step was avoided by using update cycles. Similar update cycles were introduced by Mohan *et al.* [56]. Here, fill factors associated with nodes and the pressure field are solved in an iterative manner, based on finite element discrete equations (this is still a VOF method, while they do not refer to it in their article). During these iterations, corrections for under and over filled nodes will be applied until mass conservation at each time step is preserved. In this way, there is no time step restriction. Just as the filling scheme in this thesis, the time step does influence the accuracy of the transient pressure field solutions.

For the VOF method as proposed by Koorevaar and Mohan *et al.* , the system of equations needs to be built only once in case of an isothermal situation (temperature could influence the viscosity, which is processed in the system of equations), while the scheme that is developed in this thesis needs to rebuild the system of equations every time step. This was needed since the elements' effective viscosities were changing every time step. In the VOF methods used by Koorevaar and Mohan *et al.* the viscosity of the infused liquid was taken equal throughout the whole domain. They use a

flow front tracking method and use the assumption that there is a zero pressure gradient in the air filled part of the domain. As a consequence, pressure boundary conditions that are the same as the outlet boundary conditions may be added to the flow front (partly full elements). Solving the pressure field and determining the element flows lead to an update of the fill factors. Then at new partly filled nodes (i.e. the flow front), outlet pressure boundary conditions will be applied on the original system of equations again and solving leads to a new pressure field. In this way, new pressure boundary conditions need to be processed in the the original system of equations, which needs to be built only once.

The filling scheme developed here, could account for two different substances with unique viscosities. However, when the two unique viscosities differ around three orders of magnitude, which is the case for resin infusion in LCM processes, a zero pressure gradient may be assumed in the region with the originally located substance with the lowest viscosity. When applying flow front tracking and its associated outlet boundary conditions to this filling scheme:

- it is unnecessary to process overflows of the substance with the lowest viscosity. The assumptions lead to considering the movement of the substance with the highest viscosity only;
- the outlet pressure boundary condition needs to be applied at upstream or downstream node of a partly filled 1D element. Hence it is implicitly assumed that the partly filled element is unfilled or filled respectively and some accuracy will be lost.

The computational work that is associated with assembling the system of equations for every time step and the routine that processes all the overflows of two substances is quite time consuming. Because of the gain in simulation time and the consideration of the itemised consequences and associated accuracy loss, it is highly recommended to apply the flow front tracking method to this filling scheme. When these modifications are applied, the filling scheme could still predict problematic regions (non-uniform filling, dry spots) in a product, which is the most important to be predicted by fill simulation tools.

Above recommendations save a lot of computational work, such that it may be possible to construct a whole product with elements that describe the inter bundle channels and the added stitch yarn related details. Then, a product with its shear distribution as in figure 6.8(a) could be modelled with many details. However, the mentioned coarsening alternative in the previous section could be combined with the suggested modification here and is more realistic, considering the amount of elements.

Time Step Determination

If a serious attempt will be made to use the filling scheme for further developments, it is highly recommended to improve the time step controlling algorithm (section G.3), such that it obeys the criterion ψ better. The time step was determined by application of a filter procedure (appendix G.3) and gives an underestimation too often, compared to the given criteria ψ. This results in more solutions of the system of equations and thus computational time than expected.

6.2.3 Conclusive Model Verification

To validate the model in a decisive manner, the transient behaviour during the infusion experiments should be accounted for, since the experiments are the references. The experiments showed a varying cavity height in time and space, i.e. $h = h(x, t)$. The steady state configuration of the network flow model could not account for this, while the transient configuration has not been developed that far. However, a compromise between the steady state model and the developed filling scheme may do the job.

The flow chart in figure 4.2 from chapter 4 has been modified slightly to process the steady state model results from section 6.1.2 (e.g. figure 6.4) and to account for a varying cavity height and its associated porous volume in time. The cavity height was obtained by several measurements during the infusion experiments, which can be described by a two-dimensional polynomial fit to obtain $\tilde{h}(x, t)$. The flow chart has been depicted in figure 6.10. The developed filling scheme was processed as well.

The infused fabric during the experiments will be represented by serially connected 1D elements that were defined in section 3.2.2. A sufficient amount of elements with length Δx are needed to accurately represent the fabric with its varying thickness along the infusion direction, as is schematically

shown in figure 6.9. Creation of these elements will be done in the initialisation part of the flow chart. A *kick off* element will be used at the high pressure side, such that its fill factor will be $[\tau_r]_1 \neq 0$.

The next process in the flow chart considers the assignment of the element permeabilities. This will be based on the results from the steady state model, for which the permeability was related to the fabric's thickness and the widths of the SYDs. The width of the SYDs will be treated as being constant over the whole fabric. A loop over the elements will be performed such that a permeability will be assigned to each element, which is based on the thickness of the fabric at the element's position and the current infusion time, i.e. the situation during the associated infusion experiment. During this loop, volumes will be assigned to the elements as well. These volumes are the porous spaces between the fibres and can be determined with the time and position dependent measured thickness of the fabric and equation (5.3) and (5.2), for which the latter concerns the fibre volume fraction.

From the second cycle with $k \geq 2$, the previously determined element fill factors will be corrected, since their volumes have been changed, due to the time dependent cavity height. For this, an algorithm needs to be developed to do this properly. After all element fill factors and averaged element viscosities have been updated, the system matrix will be assembled and solved for the nodal pressures. With the determined element fluxes, the developed filling scheme in section 4.3.1 may be applied to process the transport of the flows. Subsequent time steps will be taken (realised by increasing the integer k) to obtain a time related fill progression, which will be recorded by storing the fill properties for each time step. Finally, the simulated fill progression can be compared with the fill progressions that were obtained from the experiments.

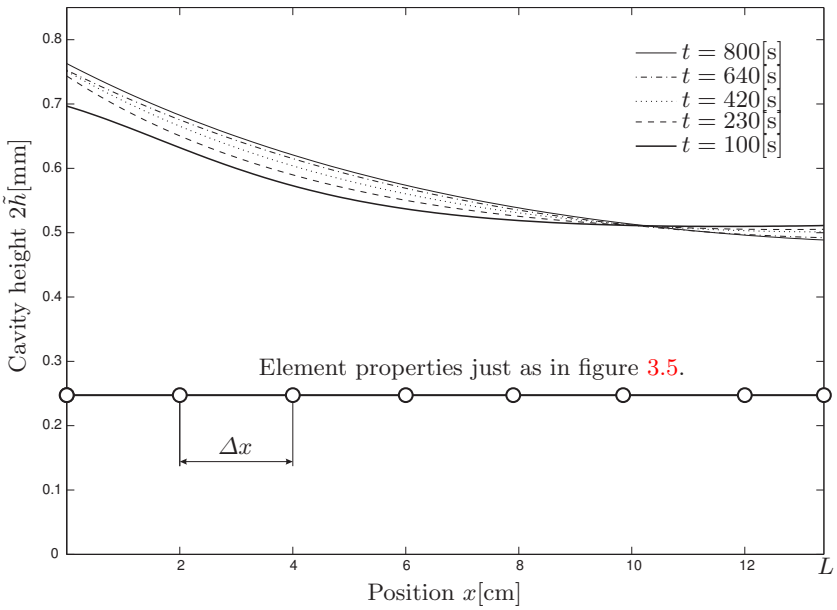

Fig. 6.9. Typical cavity height evolution $2\tilde{h}(x,t)$ (H.1) during the infusion experiment, which could be represented by serially connected 1D elements. The Cartesian coordinate x corresponds with the coordinate definition in figure 5.1(b).

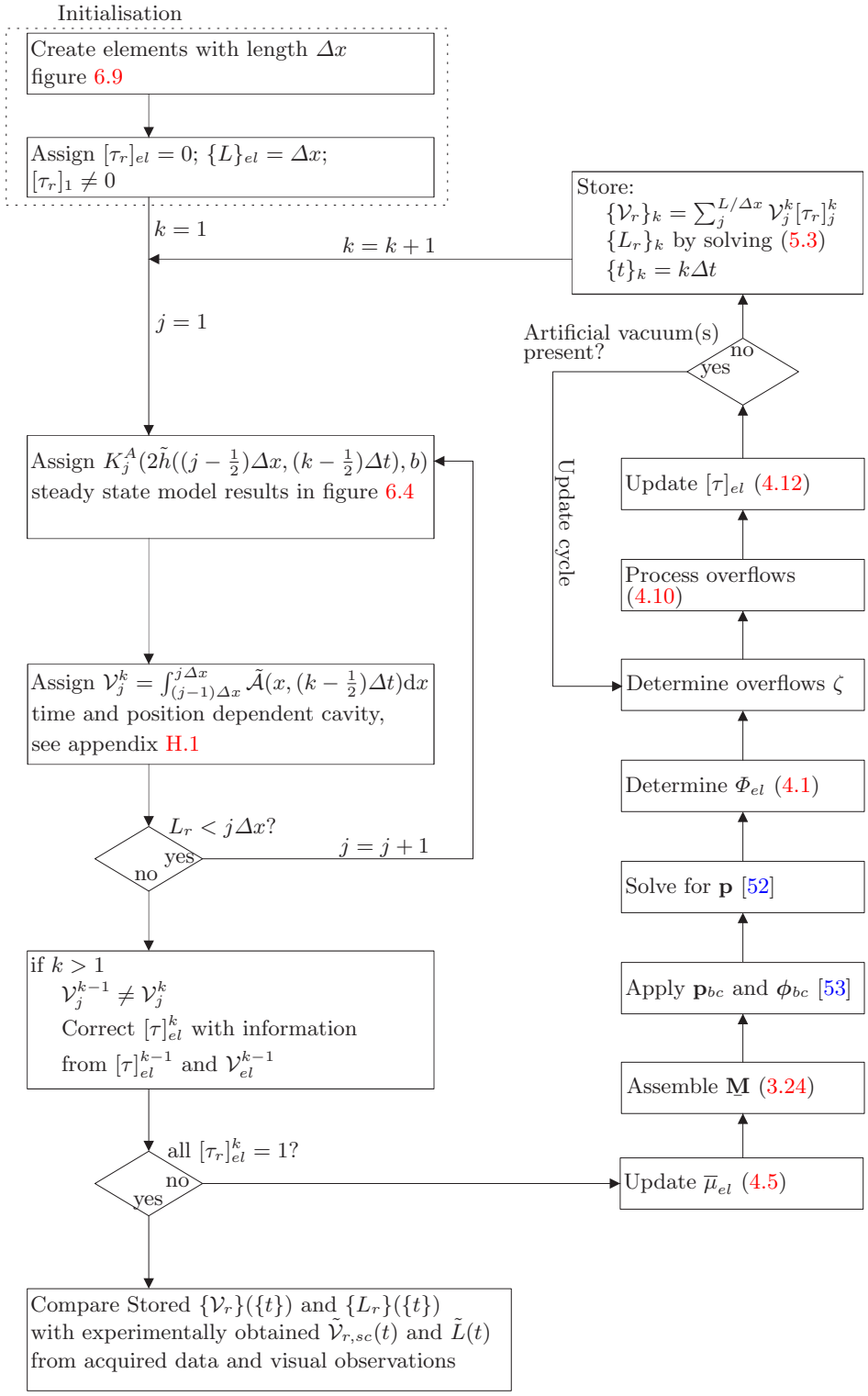

Fig. 6.10. Modified flow chart in which steady state model results and the developed filling scheme are processed to obtain a time related fill progression, to be compared with the experiment results finally. The integer j refers to the element number, while the integer k refers to a time step number.

7

Conclusions

7.1 Steady State Model Configuration

To interpret the conclusions, it is useful to consider figure 7.1 for the definition of directions and SYD dimensions.

Effect of SYD dimensions on the (isotropy of the) effective permeability of NCFs

- The effective permeability in both the 0° and 90° direction depends linearly on the SYD length l, SYD width b and the fabric's thickness $2h$, within the investigated range. This is remarkable, since solutions for simple channel flow give a non-linear dependency of the permeability on the smallest dimension of the cross-sectional flow area.
- The effective permeability prediction in the 90° direction is mostly and significantly influenced by the SYD length l. The dependency of the SYD length l on the effective permeability prediction in the 0° direction is low. As a result, the anisotropy of the permeability is highly dependent on the SYD length l.
- The SYD width b influences both the effective permeability prediction in the 0° and 90° direction a lot. Increasing the SYD width b by 50% results in a twice as big permeability in both the 0° and 90° direction. As a result, the dependency of the SYD width b on the anisotropy of the permeability is low.
- The dependency of the fabric's thickness $2h$ (twice the SYD height h) on the anisotropy and the effective permeability in both the 0° and 90° direction is low.

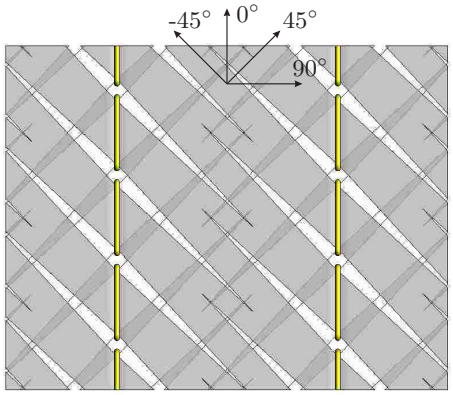

(a) Piece of NCF. The fabric's thickness is the sum of two stacked SYD heights h and is transversely directed.

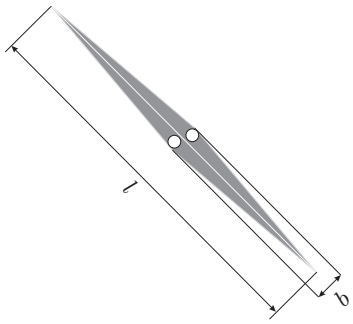

(b) SYD

Fig. 7.1. Definition of the fabric's orientation and the dimensions of the SYD. The 0° direction indicates the machine direction of the fabric.

Effect of added details

- The abovementioned dependencies of l, b and $2h$ on the anisotropy and the effective permeability in both the 0° and 90° direction, are independent of the presence of the added details.
- Depending on their permeability, adding the external channels only, could lead to an increase of the effective permeability in the 0° direction. Also, depending on the permeability, only adding the regions that describe the penetrating stitch yarns in the SYDs could lead to a decrease of the effective permeability in the 0° direction. However, adding both details and processing the channel dimensions that were obtained from the microscopy, ultimately gives a permeability prediction in the 0° direction that is $\approx 10\%$ lower, compared to the configuration without the added details.
- The added details barely affect the effective permeability prediction the 90° direction of the fabric.
- The added details affect the anisotropy of the permeability by $\approx 8\%$ (more isotropic).

7.2 Experiments vs. Steady State Model

- The difference in the predicted anisotropy of the permeability and the nearly isotropic permeability that followed from the infusion experiments, suggest that flow at micro level is significant. Since the SYD lengths mostly influence the anisotropy of the permeability, it is expected that micro flows near the SYD intersection points are the most important.
- Since the dimensions of the SYDs and the permeability of the added details influence the effective permeability and the isotropy of the permeability, it is recommended to perform analyses with statistically distributed dimensions of the SYDs and the external channels. The results may also give an explanation for the difference between the predicted anisotropy and the nearly isotropic determined permeability from the infusion experiments.

7.3 Transient Model Configuration

- The simulated filling process and its associated developing pressure field give a better understanding of the flow behaviour at meso level.
- It was found that the order of accuracy reads $\mathcal{O}(\Delta t)$ and that the filled volume at a particular time could be over- or underestimated, depending on the curvature of $\Phi_{el}(t)$ and the size of Δt.
- Unlike flow front tracking methods, the filling scheme here processes both resin and air transport through the domain. Therefore, inclusion of air at meso level can be simulated. Subsequently, the movement of trapped air can be simulated. Air also moves through micro channels in reality but this was not accounted for, since the model is based on the meso level. However, it is expected that air at micro level is important due to its low viscosity.
- The developed filling scheme shows non-uniform filling for a particular configuration of the element properties and connections.
- Inclusion behaviour (which appears for non-uniform filling) in the fill simulations is an important phenomenon, which is the main cause for the difference between the transient obtained fill progression and the fill progression that was predicted by using the effective permeability prediction from the steady state model configuration.

Appendices

A

Derivation of SYD intersection points

In figure A.1, points P and Q are assigned according to definition 2 in section 2.2. The following distances can be extracted from the figure:

$$\Delta x = Q_x - P_x \tag{A.1}$$

$$\Delta y = Q_y - P_y \tag{A.2}$$

$$\Delta y_r = \frac{\Delta x}{\tan|\theta_P^u|} \tag{A.3}$$

where the subscripts x and y indicate the x- and y-component of the particular point respectively.

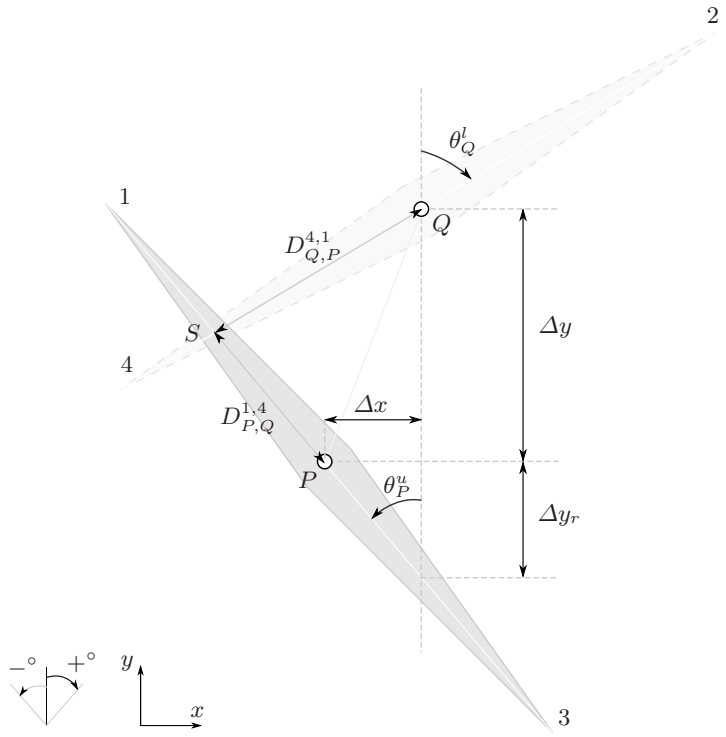

Fig. A.1. Intersecting SYD arms with their roots in different points, i.e. point P and Q. The SYD in the upper ply has a darker hatched surface and the SYD in the lower ply a lighter hatched surface.

A local coordinate system will be defined with its origin in point Q. The new positions of the stitch yarn penetration points P and Q will be:

$$P'(\hat{x}', \hat{y}') = P'(P_x - Q_x, P_y - Q_y)$$
$$Q'(\hat{x}', \hat{y}') = Q'(0, 0)$$

To derive the intersection point, the center lines of the SYDs will be described by a linear relation with a slope a and an offset c:

$$y = ax + c, \tag{A.4}$$

in which the expressions for a reads:

$$a_Q = \frac{\cos|\theta_Q^l|}{\sin\theta_Q^l}$$
$$a_P = \frac{\cos|\theta_P^u|}{\sin\theta_P^u}$$

The angles that will be subjected to the sine function, will not be the absolute values in order to correctly represent the center lines with a positive or negative slope. The offset c_Q is just zero, because the origin of the local coordinate system has been placed in point Q. Offset c_P becomes simply:

$$c_P = -(\Delta y + \Delta y_r)$$

The intersection point S lies on the same y-coordinate of both lines, such that:

$$\frac{\cos|\theta_Q^l|}{\sin\theta_Q^l}x = \frac{\cos|\theta_P^u|}{\sin\theta_P^u}x - (\Delta y + \Delta y_r)$$

Substitution of (A.1) till (A.3), using $Q_x = Q_y = 0$ and solving for x gives the x-coordinate of the intersection point S:

$$x = S_x = \frac{-\frac{P'_x}{\tan|\theta_P^u|} - P'_y}{\left(\frac{\cos|\theta_P^u|}{\sin\theta_P^u} - \frac{\cos|\theta_Q^l|}{\sin\theta_Q^l}\right)}$$

Using relation (A.4) for point Q and substituting the x-coordinate of the intersection point gives:

$$y = S_y = \frac{\cos|\theta_Q^l|}{\sin\theta_Q^l}S_x$$

Now the intersection distances can easily be calculated as:

$$D_{P,Q}^{e,f} = \sqrt{(P'_x - S_x)^2 + (P'_y - S_y)^2}$$
$$D_{Q,P}^{f,e} = \sqrt{(S_x)^2 + (S_y)^2},$$

where e and f refer to an arm of a SYD in point P in the upper ply and point Q in the lower ply respectively, see figure 2.7.

B

ANSYS CFX-5

During this research and in NORDLUND [4], the CFD software ANSYS CFX-5 [47] was used. Some steps leading to the solution of the flow problem will be shown. The used approach involves discretising the spatial domain into finite control volumes using a mesh. A domain can be meshed by using meshing software, e.g. CFX-MESH. The mesh consists of pieces that are formed into hexahedral, tetrahedral, wedge or pyramid shaped elements. These elements and their finite element shape functions N_j are summarised in appendix B.1 and are tri-linear, in terms of parametric coordinates. They can be used to relate the solution field variables at the nodes (where these are stored) to the interior of the element, e.g. at the integrations points k_{ip}. This variation of quantities is needed, because some terms in the equations require solution or solution gradients to be evaluated at the integration points k_{ip} of an element. It can be seen in figure B.1, that the integration points are located at the centre in each surface segment of a 3D element. The surface segments surround the finite volume.

The governing equations are conservation of mass (1.8), momentum (1.10) and a passive scalar expressed in Cartesian coordinates. The passive scalar equation is:

$$\frac{\partial}{\partial t}\rho\phi + \boldsymbol{\nabla}\cdot\rho\mathbf{u}\phi = \boldsymbol{\nabla}\cdot\Gamma\boldsymbol{\nabla}\phi,$$

in which ϕ could represent temperature, enthalpy, mass fraction, turbulence related variables, etcetera and Γ is the diffusivity. This equation will not be mentioned any more, but it has been shown in order to see the possibilities of the software.

The governing equations (1.8) and (1.10) will be integrated over each control volume using the mesh. Applying Gauss' divergence theorem to convert some volume integrals into surface integrals and assuming that the control volume does not deform in time, results in:

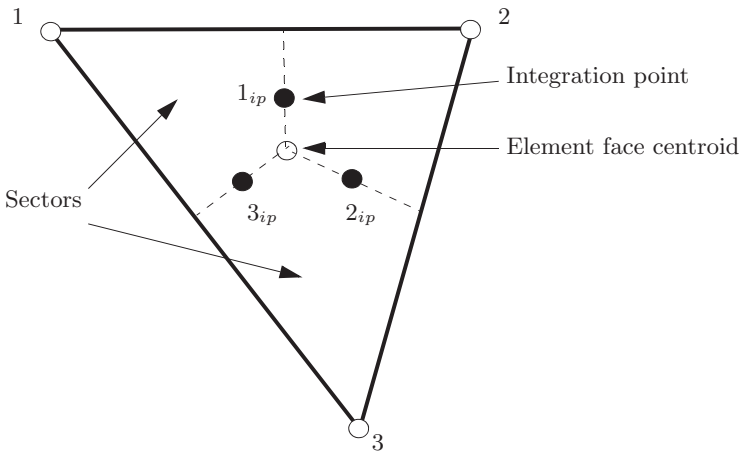

Fig. B.1. Surface segment of a 3D element. Integration points k_{ip} are located at the centre in each surface segment of a 3D element

$$\frac{\mathrm{d}}{\mathrm{d}t}\int_V \rho \mathrm{d}\mathcal{V} + \int_S \rho \mathbf{u}\cdot \mathrm{d}\mathbf{n} = 0 \tag{B.1}$$

$$\frac{\mathrm{d}}{\mathrm{d}t}\int_V \rho \mathbf{u}\mathrm{d}\mathcal{V} + \int_S \rho \mathbf{u}\mathbf{u}\cdot \mathrm{d}\mathbf{n} = \int_V \rho \mathbf{f}\mathrm{d}\mathcal{V} - \int_S p\mathrm{d}\mathbf{n} + \int_S \underline{\boldsymbol{\tau}}\cdot \mathrm{d}\mathbf{n}, \tag{B.2}$$

where $_V$ and $_S$ denote volume and surface regions of integration, and d$\mathbf{n}$ is the differential Cartesian component of the outward normal surface vector.

The first term on the left hand side of equations (B.1) and (B.2) is the transient term. This term will be split into two parts, see the ANSYS CFX-SOLVER theory book [47]. Then it can be discretised using a first or second order Backward Euler scheme. More details will not be mentioned because only steady state solutions were obtained, in which the time dependent terms have no bearing on the accuracy. The reason why in many numerical schemes the time dependent terms are kept in steady state problems, is to prevent instability in the numerical solution process.

The discrete form of the equations (B.1) and (B.2) by using a first order Backward Euler scheme, are respectively:

$$\mathcal{V}\left(\frac{\rho-\rho^o}{\Delta t}\right) + \sum_{ip}(\rho \mathbf{u}\cdot \Delta \mathbf{n})_{ip} = 0 \tag{B.3}$$

$$\mathcal{V}\left(\frac{\rho\mathbf{u}-\rho^o\mathbf{u}^o}{\Delta t}\right) + \sum_{ip}(\rho\mathbf{u}\mathbf{u}\cdot \Delta \mathbf{n})_{ip} = \overline{\rho\mathbf{f}}\mathcal{V} - \sum_{ip}(p\Delta \mathbf{n})_{ip} + \sum_{ip}(\underline{\boldsymbol{\tau}}\cdot \Delta \mathbf{n})_{ip}, \tag{B.4}$$

where the subscript ip denotes an integration point, $\Delta\mathbf{n}$ is the discrete outward surface vector, the superscript o indicates the old time level and Δt is the time step. As mentioned before, in steady state the time step has no effect on the solution's accuracy but it determines how convergence proceeds. The over bar in the right hand side of equation (B.4) indicates averaging the adjacent values to the integration point.

The second term on the left hand side of equations (B.1), (B.2), (B.3) and (B.4) is the advection term. To relate the velocity gradients to the nodal values of the finite volumes, a difference scheme will be used. This scheme can be adjusted by a blending term, to obtain:

- First Order Upwind Differencing Scheme
- Numerical Advection Correction Scheme (Specified blend)
- High Resolution Scheme (HRS)

A Central Difference Scheme is suitable as well but uses the tri-linear shape functions to relate velocity gradients to the nodal values. It is second order accurate, but for some reasons only appropriate for Large Eddy Simulations (LES).

Body force terms, i.e. the first term on the right hand side of (B.2) and (B.4) will be an averaged term by using a Volume-Weighted, harmonic or arithmetic method. The second term on the right hand side is the pressure gradient term and its value will be evaluated by using the shape functions. The last term on the right hand side of equation (B.2) and (B.4) is called the diffusion term. To relate gradients of vector $\mathbf{u}$ at the integration point to the nodal values, the FE approach is used, i.e. using the shape functions and their derivatives, see the expression with derivatives for $\underline{\boldsymbol{\tau}}$ in (1.12).

An additional momentum-like equation will be added to each integration point in order to obtain pressure-velocity coupling. This equation does not introduce a time step dependent steady state solution. But to control the rate of convergence in a steady state solution, time steps can be controlled. Time steps can be manually controlled by using the "Local Time step Factor" or by specifying a "Physical Time step" according to an estimate for advection dominating flows:

$$\Delta t = \frac{L}{2U}, \tag{B.5}$$

where L is a characteristic length of the domain and U the mean velocity in the domain. Since for complex domains these parameters are hard to determine, there is an "Auto Time-scale" option as well. A similar relation like (B.5) will be used to relate a characteristic length to a characteristic velocity. The characteristic length will be determined according to a specified method:

- Conservative

$$L_{sc} \equiv \min(L_V, L_{ext})$$

- Aggressive

$$L_{sc} \equiv \max(L_V, L_{ext}),$$

where L_V and L_{ext} are defined as:

$$\begin{aligned} L_V &\equiv \mathcal{V}^{\frac{1}{3}} \\ L_{ext} &\equiv \max(L_x, L_y, L_z), \end{aligned} \tag{B.6}$$

in which $\mathcal{V}$ is the total domain volume and L_x, L_y and L_z are the extends of the domain in Cartesian directions. Three velocity types are defined as:

$$\begin{aligned} U_{bc} &\equiv \max|\overline{\mathbf{u}}_{bc}| \\ U_{nd} &\equiv |\overline{\mathbf{u}}_{nd}| \\ U_{\Delta p} &\equiv \sqrt{\frac{p_{bc,max} - p_{bc,min}}{\overline{\rho}_{nd}}}, \end{aligned}$$

where U_{bc} is the arithmetic average of the velocity on a boundary, U_{nd} is the arithmetic average of the nodal velocities, $p_{bc,max}$ and $p_{bc,min}$ are the maximum and minimum pressure values on an open boundary and $\overline{\rho}_{nd}$ is the arithmetic average nodal density. Subsequently the time step Δt can be determined by:

$$\Delta t = \min(\Delta t_u, \Delta t_{\Delta p}),$$

in which Δt_u and $\Delta t_{\Delta p}$ are:

$$\begin{aligned} \Delta t_u &\equiv 0.3 \frac{L_{sc}}{\max(U_{bc}, U_{nd})} \\ \Delta t_{\Delta p} &\equiv 0.3 \frac{L_{sc}}{U_{\Delta p}} \end{aligned}$$

Finally the non-linear equations are linearised (coefficient iteration) and assembled into a solution matrix. Multigrid will be used to find a solution iteratively. The Algebraic Multigrid method Additive Correction is used to prevent the need to mesh the geometry using a series of different mesh spacings.

B.1 ANSYS CFX-5 shape functions

Different types of elements that can be used in ANSYS CFX-5. Their shape functions N_j are tri-linear, in terms of parametric coordinates.

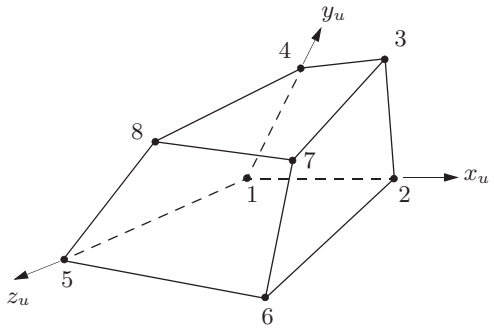

$$
\begin{aligned}
N_1 &= (1-x_u)(1-y_u)(1-z_u)\\
N_2 &= x_u(1-y_u)(1-z_u)\\
N_3 &= x_u y_u(1-z_u)\\
N_4 &= (1-x_u)y_u(1-z_u)\\
N_5 &= (1-x_u)(1-y_u)z_u\\
N_6 &= x_u(1-y_u)z_u\\
N_7 &= x_u y_u z_u\\
N_8 &= (1-x_u)y_u z_u
\end{aligned}
$$

(a) Hexahedral element.

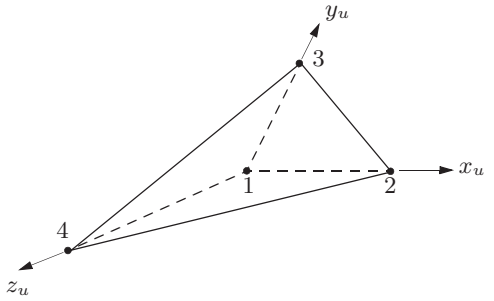

$$
\begin{aligned}
N_1 &= 1-x_u-y_u-z_u\\
N_2 &= x_u\\
N_3 &= y_u\\
N_4 &= z_u
\end{aligned}
$$

(b) Tetrahedral element.

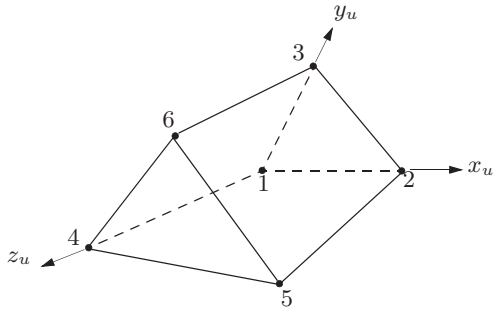

$$
\begin{aligned}
N_1 &= (1-x_u-y_u)(1-z_u)\\
N_2 &= x_u(1-z_u)\\
N_3 &= y_u(1-z_u)\\
N_4 &= (1-x_u-y_u)z_u\\
N_5 &= x_u z_u\\
N_6 &= y_u z_u
\end{aligned}
$$

(c) Wedge element.

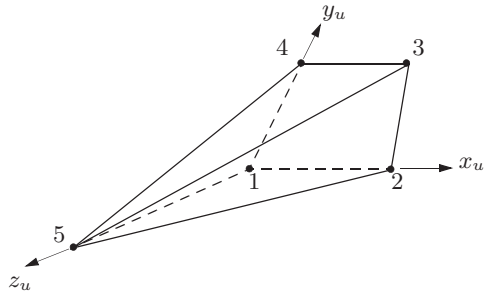

$$
\begin{aligned}
N_1 &= (1-x_u)(1-y_u)(1-z_u)\\
N_2 &= x_u(1-y_u)(1-z_u)\\
N_3 &= x_u y_u(1-z_u)\\
N_4 &= (1-x_u)y_u(1-z_u)\\
N_5 &= z_u
\end{aligned}
$$

(d) Pyramid element.

Fig. B.2. Element types with their shape functions, as they are used in ANSYS CFX-5.

C

Domain Obstacles

Objects in a flow channel generally influence the flow behaviour. It has been shown by Hu and Liu [36] and Nordlund and Lundström [37] that solid cylinders, representing the stitch yarns in flow channels, influence the permeability of these channels significantly. To draw an independent conclusion of this behaviour and to get used to the ANSYS CFX software, one of the domains used by Hu and Liu [36] has been reproduced, see figure C.1(e).

The flow channel has a rectangular cross-section, characterised by width W and height H. A solid cylinder is positioned perpendicularly to the flow in the center of the channel. Inlet boundary conditions are applied at surface 3 and opening boundary conditions are applied at surface 4. These conditions form a specified pressure difference such that Re << 1, to guarantee slow viscous flow. Surfaces 1, 6 and 7 contain no-slip boundary conditions, representing a wall. Because of the presence of two symmetry planes, a quarter of the domain has been modelled in order to reduce the number of elements and consequently computational time. Triangular elements were used to mesh the surfaces and tetrahedral elements to mesh the volume, see figure C.1(f). The domain around the solid cylinder was refined by using some layers of prismatic elements, over the length of the original elements that were located there. The solution was obtained by assuming a laminar flow, a steady state situation and an incompressible fluid. Automatic time-stepping and the HRS difference scheme for the advection term were used, see section B. Meshes were varied in order to obtain the number of elements to solve the problem with sufficient accuracy.

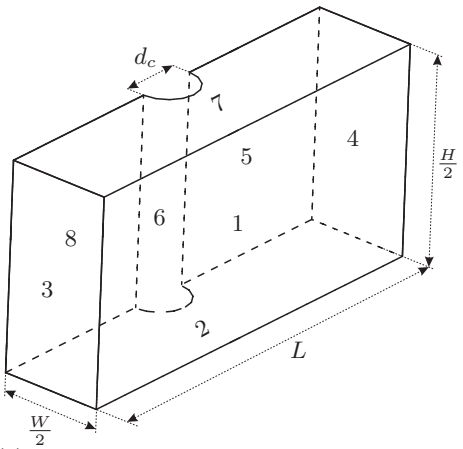

(e) Quarter of a flow domain with a solid cylinder within. Surfaces 2, 5 and 8 contain symmetry boundary conditions.

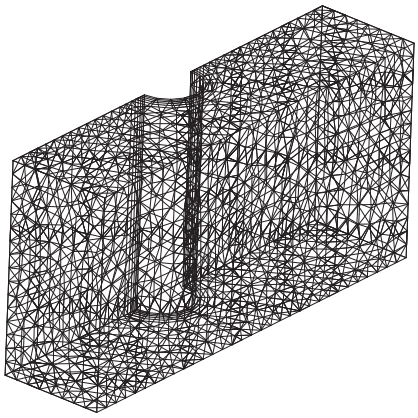

(f) Typical mesh that was used in ANSYS CFX-5.

Fig. C.1. Properties of the flow domain that has been used to determine the influence of a solid cylinder on the permeability.

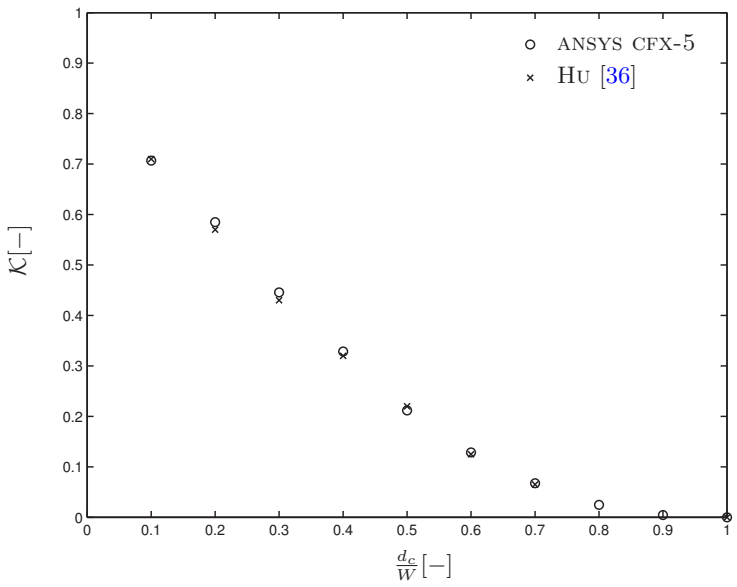

Fig. C.2. Influence of the possessed space by the cylinder in the flow domain, on the permeability.

The domain in figure C.1(e) has also been modelled without the object to obtain the dimensionless permeability $\mathcal{K}$, as defined in (3.30). The permeability has been determined with (1.1). The results are shown in figure C.2 and show good agreement with the result obtained by Hu [36]. Hereby, it has been shown that the permeability can be influenced significantly by the stitch yarn. The influence is dependent on how much width of the domain will be taken by the stitch yarn. As the stitch yarn captures more space in the domain, the change of its influence on the permeability will decrease slightly.

D

Solution Accuracy for External Channels

Accuracy analyses were done to obtain reliable model configurations in ANSYS CFX. For all analyses, the surfaces were meshed by using triangular and quadrilateral elements (see appendix B.1). The volume mesh contains wedge elements (also referred to as triangular prisms). The solution was obtained by assuming a laminar flow, a steady state situation and an incompressible fluid. Automatic time-stepping and the HRS difference scheme for the advection term were used, see appendix B.

D.1 Extruded Layers

To mesh the domain in figure 3.7(a), the `extruded 2D` mesh option has been used in CFX-MESH. A mesh with one layer of thickness could be used for 2D problems in which the flow runs parallel to the cross-sectional area of the external channel (figure 3.7(a)). For this problem, the flow runs perpendicular to this cross-sectional area. To impose the boundary conditions correctly and to find an accurate approximation to the solution, more layers in the thickness direction are needed. It is expected that velocity gradients are only present over the cross-sectional area of the channel and not in the direction of the channel's length. Therefore, it is expected that extruding the 2D mesh to a minimum number of layers, would be sufficient. Simulations have been carried out with different numbers of extruded layers, after which the permeability K^A has been determined according to (1.3). The pressure values were determined, such that $1{\cdot}10^{-5} < \mathrm{Re} < 1{\cdot}10^{-4}$ (gives reliable results according to appendix D.3). Note that Reynolds numbers (1.2) in ANSYS CFX are calculated by using the length L_V as defined in (B.6). Since the domain has a very large aspect ratio, L_V is an overestimation and so is the Reynolds number in this case.

The results of simulations with different number of extruded layers are shown in figure D.1. The cross-sectional geometry was constant for all analyses. To mesh the geometry, 8265 elements per extruded layer were used. Each layer had a constant length in the extrusion direction. As recommended in [47], This length taken, this length was equal to the characteristic length of the largest element in the 2D surface mesh. From D.1, it may be concluded that extruding the 2D mesh to three layers is sufficient. This mesh is shown in figure 3.7(b).

D.2 Mesh Size

For the same cross-sectional geometry, the number of elements in the 2D mesh were varied. These elements were extruded to three layers of equal extrusion length (appendix D.1). Flow simulations were carried out in order to see the influence of the mesh size on the permeability. The same settings in ANSYS CFX were used as in the simulations from which figure D.1 was generated. Figure D.2 shows the results. For this domain, approximately $3.7 \cdot 10^4$ elements per extruded layer are sufficient to obtain an accurate approximation to the solution. The associated number of elements that fit in the maximum channel height, will be used in other configurations of the cross-sectional area (parametric study).

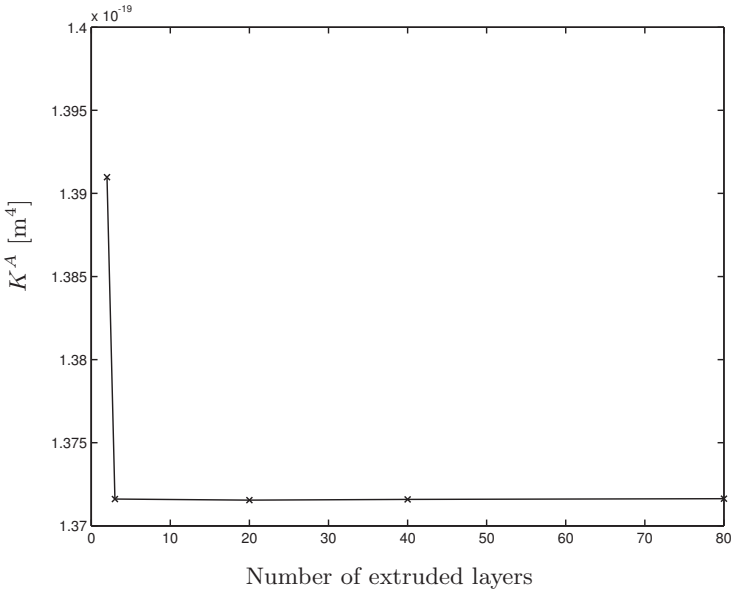

Fig. D.1. The influence of the number of extruded layers on the permeability. The extruded layers originate from the 2D surface mesh of the channel's cross-section. The analyses were done for $g = 2 \cdot 10^{-3}$ [m], $2f = 0.0159 \cdot 10^{-3}$ [m], $1 \cdot 10^{-5} < \mathrm{Re} < 1 \cdot 10^{-4}$ and 8265 elements per layer were used.

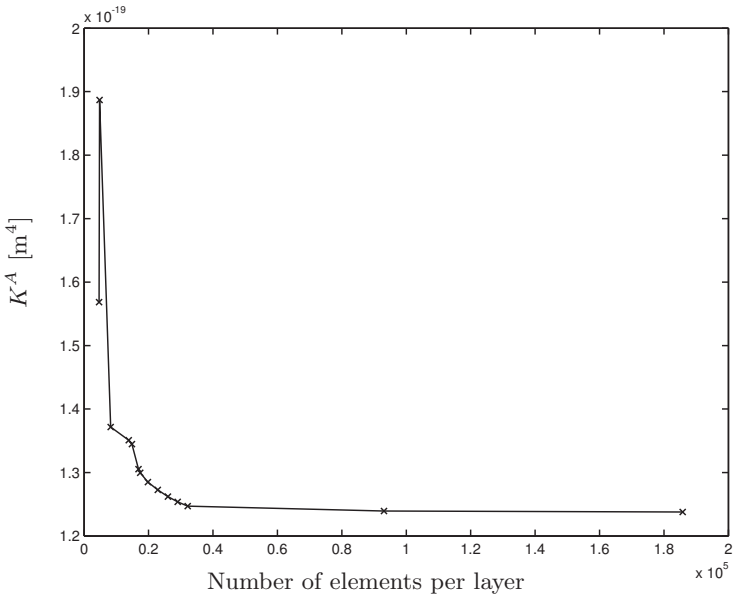

Fig. D.2. Determined permeability at different number of elements per extruded layer. Each analysis considered a domain with three extruded layers. The analyses were done for $g = 2 \cdot 10^{-3}$ [m], $2f = 0.0159 \cdot 10^{-3}$ [m] and $1 \cdot 10^{-5} < \mathrm{Re} < 1 \cdot 10^{-4}$.

D.3 Reynolds Number Dependence

For a particular number of elements, the influence of the Reynolds number on the resulting permeability was investigated. The 2D mesh was extruded to three layers of equal extrusion length and the same cross-sectional area as appendix D.1 was used. Figure D.3 shows the results. The different Reynolds numbers were realised by modifying the pressure difference over the length (the extrusion direction) of the domain. From Re > 1, the resulting flow solution becomes unrealistic and unreliable. This is caused by the presence of the non-linear velocity term in the Navier-Stokes equations (B.4). Generating flow solutions for this domain, should be done with Re $<< 1$.

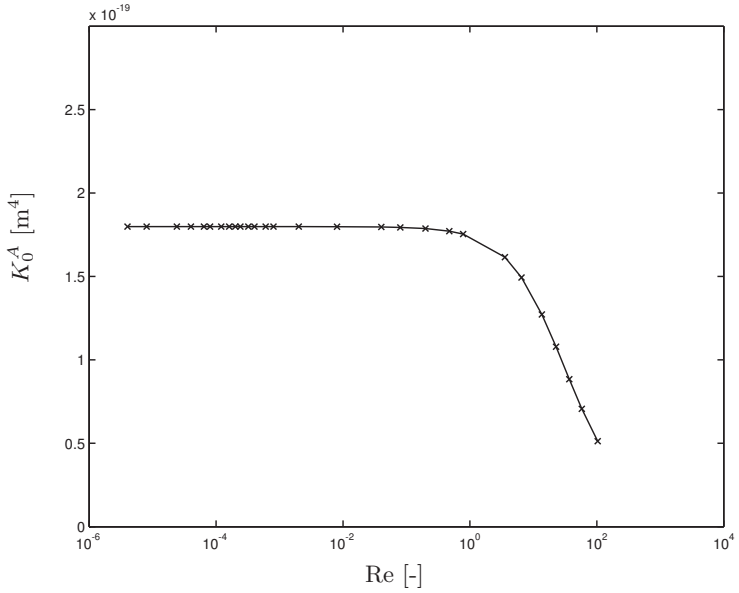

Fig. D.3. The permeability has been determined for different pressure boundary conditions, such that the Reynolds number was varied. The analyses were done for $g = 2 \cdot 10^{-3}$ [m] and $2f = 0.0159 \cdot 10^{-3}$ [m]. Three extruded layers were used with 14580 elements per layer.

D.4 Results External Channels

See section 3.4.1 for a detailed explanation. The fit coefficients to describe the response surfaces in figure 3.8 with, are listed in table D.1. The fit is a two-dimensional polynomial of the sixth order:

$$\tilde{K}^A_{(0)}(g, 2f) = \sum_{j=0}^{6} \sum_{k=0}^{6-j} a_{jk\,(0)} g^j (2f)^k \tag{D.1}$$

Table D.1. Fit coefficients a_{jk}, which were used in equation (3.31) and (D.1) to obtain the plots in figure 3.8. The permeabilities K^A have the dimension [m^4]. The dimensions g and f have the dimension [m].

	K^A	K_0^A		K^A	K_0^A
a_{00}	3.0624e-020	-2.2498e-019	a_{04}	-5.3401e-001	-1.0012e000
a_{10}	-9.2445e-018	6.2475e-016	a_{50}	-4.7661e-004	-8.7824e-004
a_{01}	-6.0595e-015	3.3342e-014	a_{41}	3.1647e-003	-1.4475e-002
a_{20}	-5.6169e-013	1.0333e-013	a_{32}	1.6851e000	5.3631e-001
a_{11}	2.2668e-011	-9.2077e-011	a_{23}	-1.2288e001	2.1095e001
a_{12}	3.9268e-010	-1.7774e-009	a_{14}	-1.46505e003	1.0049e003
a_{30}	-3.1308e-010	-1.563e-009	a_{05}	9.9349e003	9.0743e003
a_{21}	9.7493e-008	6.2498e-008	a_{60}	8.2095e-002	1.5132e-001
a_{12}	-3.832e-006	3.9141e-006	a_{51}	1.6208e000	3.6787e000
a_{03}	2.2912e-007	5.5679e-005	a_{42}	-1.0670e002	7.748e001
a_{40}	9.3177e-007	1.8845e-006	a_{33}	-1.2725e004	-7.0349e003
a_{31}	-6.689e-005	-8.957e-006	a_{24}	3.16453e005	-3.0669e004
a_{22}	-1.5146e-003	-1.7945e-003	a_{15}	4.454363e006	-4.8858e006
a_{13}	1.4485e-001	-6.8337e-002	a_{06}	-5.1446e007	-3.3467e008

E

Solution Accuracy for SYD Domain Obstacles

E.1 Reynolds Number Dependence

The Reynolds number (1.2) was defined in section 1.3. The Reynolds number is important for the analysis of the domain in figure 2.9. Since the fluid could flow to one or more openings in the domain, inertia effects play an important role. If the flow is characterised by a high Reynolds number, non-linear terms in the Navier-Stokes equations (1.10) and its discretised form in (B.4) are significant and the fluid could show the behaviour as in figure E.1(a), in which since streamlines pass multiple regions with different permeabilities. In this case, the method described in section 3.4.2 is not applicable.

To find a valid range for the Reynolds number, simulations have been carried out for different pressure gradients. During the simulations, a sufficiently fine mesh was used (see appendix E.2). Triangular elements were used to mesh the surfaces and tetrahedral elements to mesh the volume. The solution was obtained by assuming a laminar flow, a steady state situation and an incompressible fluid. Automatic time-stepping and the HRS difference scheme for the advection term were used

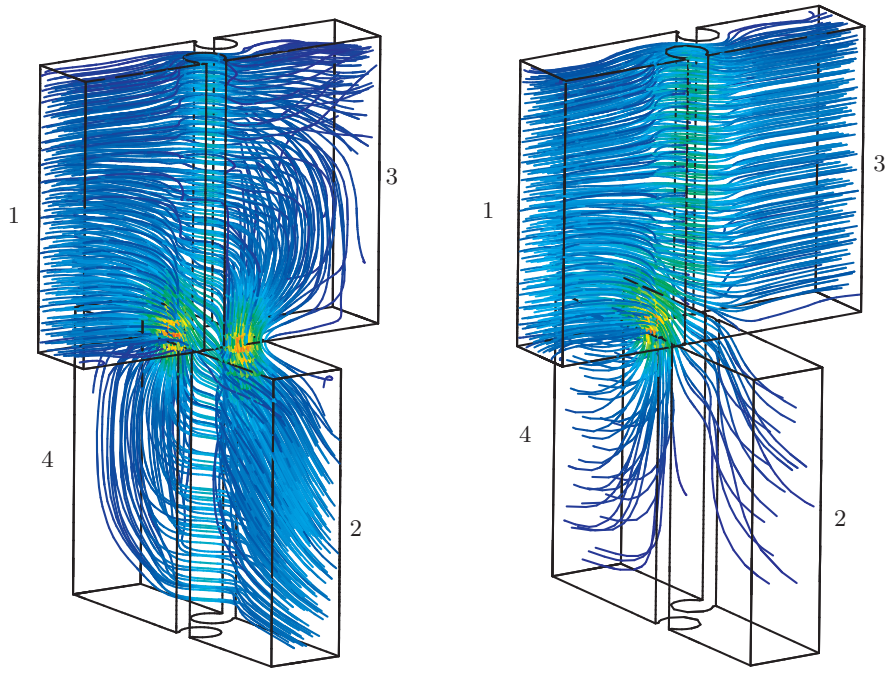

(a) Re >> 1, inertia effects are significant.

(b) Re << 1, inertia effects are negligible.

Fig. E.1. Plotted streamlines in the modelled domain around the stitch yarns for two different conditions. As can be seen, inertia effects are very important in justifying the method's validity.

(see appendix B). However, the advection term (non-linear term in (B.4)) is negligible at low Reynold numbers, but can not be turned off in ANSYS CFX-5. Note that the Reynolds number will be determined by using the characteristic length L_{vol}, according to the definition in (B.6) in appendix B.

Figure E.2 shows the results of the determined permeabilities for different flow paths. This figure shows that at Reynolds numbers greater than $1 \cdot 10^{-1}$, result in varying and unrealistically determined permeabilities (situation as in figure E.1(a) occur). The results should be constant, since permeability is a geometrical property. Reynolds numbers smaller than $1 \cdot 10^{-1}$ give more or less the same permeabilities and are reliable. Further simulations will be performed at Reynolds numbers smaller than $1 \cdot 10^{-1}$.

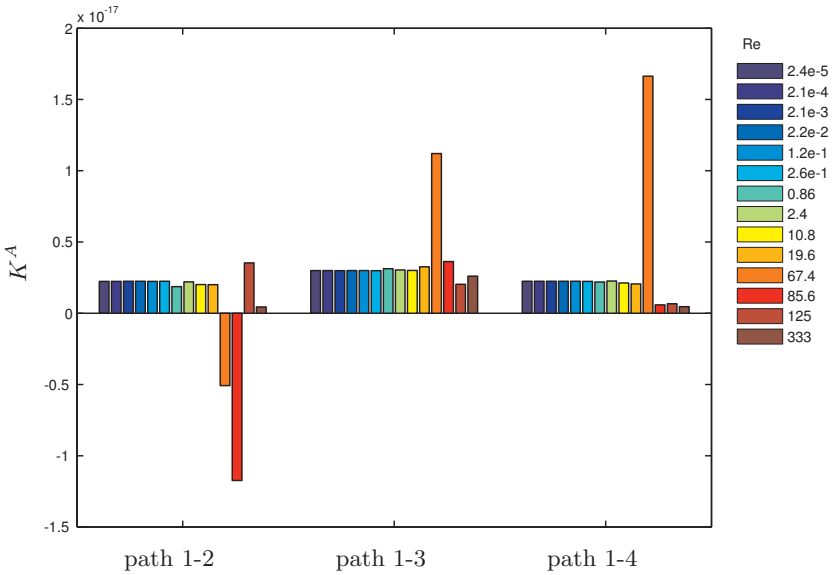

Fig. E.2. Higher Reynolds numbers and thus more significance of the inertia, result in inconsistent and unrealistic permeabilities.

E.2 Mesh Size

In general, more elements in a FE method to describe a particular domain, result in a better approximation to the solution. Evaluating a solution variable like the mass flux Φ_m at different mesh sizes shows the converging behaviour in figure E.3. In these simulations, a relative high pressure was applied at opening 1 and lower identical pressures at openings 2, 3 and 4 in figure 2.9. Figure 3.9(a) shows a typical mesh that was used during the parametric study. The domain around the stitch yarns was refined by using some layers of prismatic elements, over the length of the original elements that were located there. This can be done with the `inflation` command in CFX-MESH as recommended in the documentation [47]. The domains (figure 2.9) that were used to do a parametric study on, will be meshed by the number of elements in figure E.3 for which the mass fluxes do not seem to vary any more ($\approx 5 \cdot 10^5$ elements).

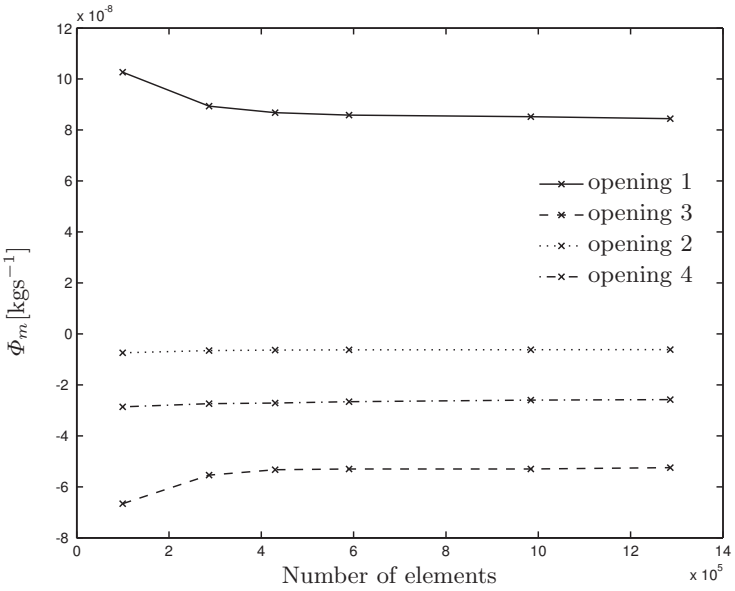

Fig. E.3. Convergence of the mass flux by increasing the amount of elements, which describe the domain as in figure 3.9(a).

E.3 Validation of Independent Load Cases Approach

To check the described method to determine the permeabilities for its reliability, four load cases were applied at the opening boundaries in 2.9:

$$\mathbf{p} = \begin{Bmatrix} p_1 \\ p_2 \\ p_3 \\ p_4 \end{Bmatrix} = \begin{Bmatrix} 1 \\ 0 \\ 0 \\ 0 \end{Bmatrix} [\mathrm{Nm}^{-2}] \tag{E.1}$$

$$= \begin{Bmatrix} 0 \\ 1 \\ 0 \\ 0 \end{Bmatrix} [\mathrm{Nm}^{-2}] \tag{E.2}$$

$$= \begin{Bmatrix} 0 \\ 0 \\ 1 \\ 0 \end{Bmatrix} [\mathrm{Nm}^{-2}] \tag{E.3}$$

$$= \begin{Bmatrix} 0 \\ 0 \\ 0 \\ 1 \end{Bmatrix} [\mathrm{Nm}^{-2}] \tag{E.4}$$

The permeabilities were determined, as described in section 3.4.2. The results in figure E.4 show determined permeabilities that are constant for the different load cases, which shows the good reliability of this method.

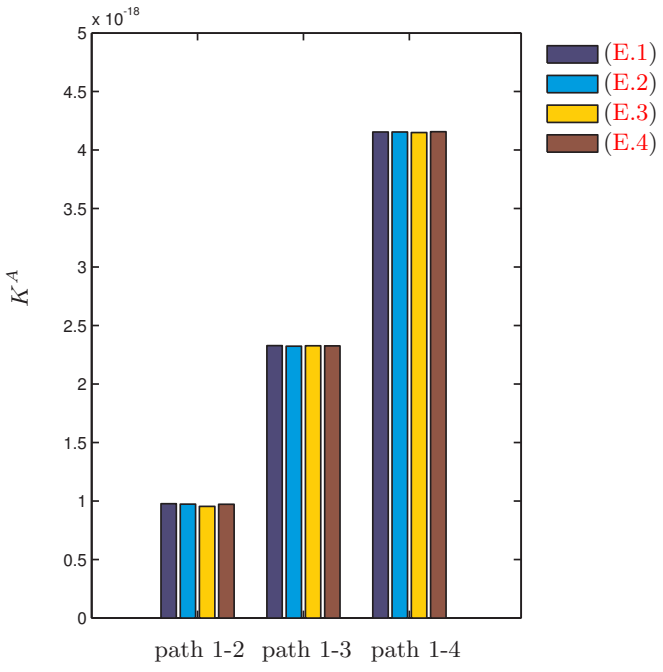

Fig. E.4. Four different load cases and the resulting permeabilities. The paths indicate the flow paths between the openings or nodes in figure 2.9 or 3.9(b) respectively.

E.4 Results SYD Domain Objects

See section 3.4.2 for a detailed explanation. The plots in the following figures were obtained by a third order polynomial fit in the form of equation (3.37) and (3.38):

$$\tilde{K}^A_{\substack{12\\13\\14}}(h,b) = \sum_{j=0}^{3}\sum_{k=0}^{3-j} a_{jk}{}_{\substack{12\\13\\14}} h^j b^k \tag{E.5}$$

$$\tilde{K}^A_{\substack{0\\12\\13}}(h,b) = \sum_{j=0}^{3}\sum_{k=0}^{3-j} a_{jk}{}_{\substack{0\\12\\13}} h^j b^k, \tag{E.6}$$

for which the coefficients were solved. These are listed in table E.1. In the figures, h and b refer to the height and the width of the SYD respectively. Logarithmic plots have been depicted as well to see the behaviour of K^A and K^A_0 at very low values.

Table E.1. Fit coefficients as they were used in equations (3.37) and (3.38) or (E.5) and (E.6) to obtain the plots in figures E.5 till E.7. The permeabilities K^A have the dimension [m^4]. The dimensions h and b have the dimension [m].

	K^A_{12}	$K^A_{0\,12}$	K^A_{13}	$K^A_{0\,13}$	K^A_{14}
a_{00}	1.2406e-018	-7.8072e-017	2.4355e-017	-5.0164e-017	-1.4674e-017
a_{10}	5.2556e-014	4.6276e-014	9.3278e-014	1.2078e-013	6.2578e-014
a_{01}	-4.5143e-014	1.3618e-012	-4.8873e-013	7.9329e-013	2.4007e-013
a_{20}	3.8023e-011	6.4353e-012	-3.7155e-011	-9.0097e-011	3.5359e-011
a_{11}	-1.1001e-009	-8.2124e-010	-1.6669e-009	-1.587e-009	-1.0934e-009
a_{02}	6.3064e-010	-7.6928e-009	3.5067e-009	-3.98e-009	-1.0833e-009
a_{30}	-2.3749e-008	-4.8859e-008	-1.141e-007	-1.467e-007	-2.614e-008
a_{21}	-1.234e-007	2.5907e-007	9.7003e-007	1.7868e-006	-1.0169e-007
a_{12}	4.9942e-006	4.2398e-006	6.1128e-006	5.0254e-006	4.8128e-006
a_{03}	-2.5155e-006	1.3499e-005	-8.439e-006	6.1225e-006	8.717e-007

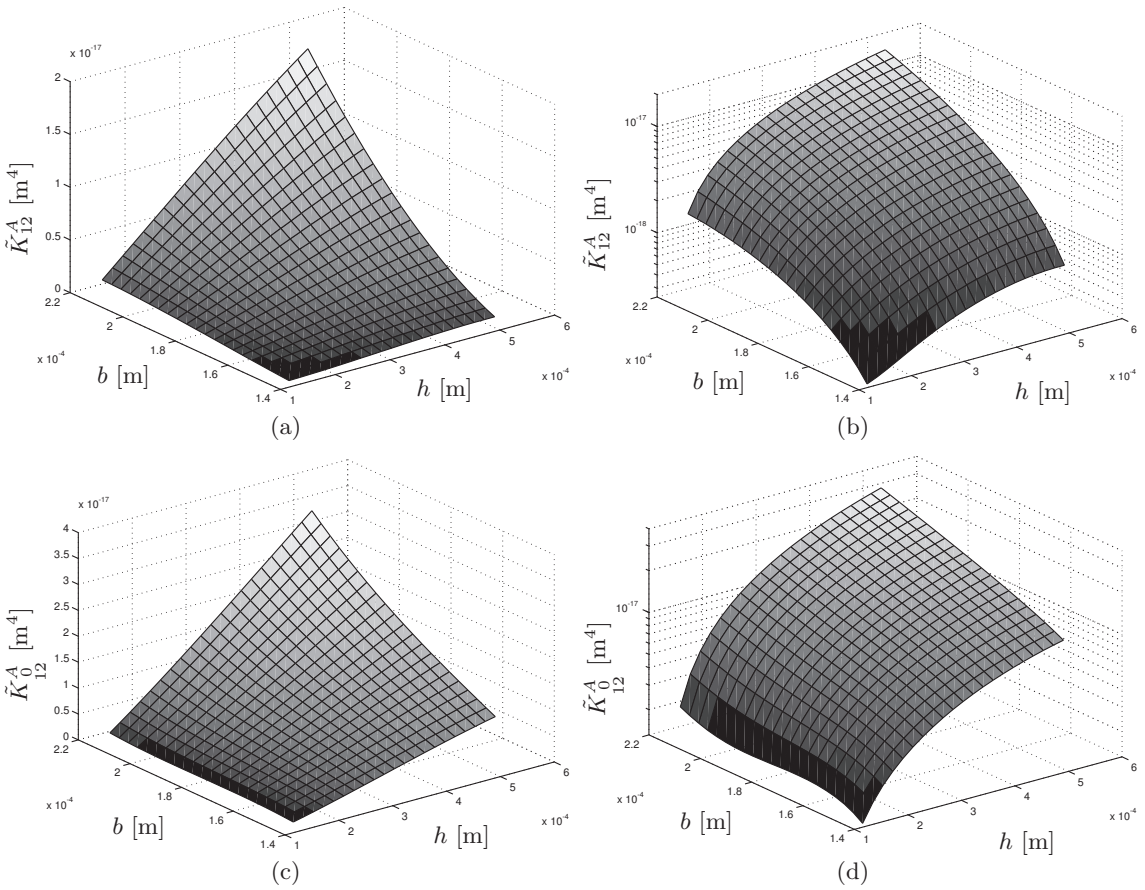

Fig. E.5. See table E.1 for the plot data.

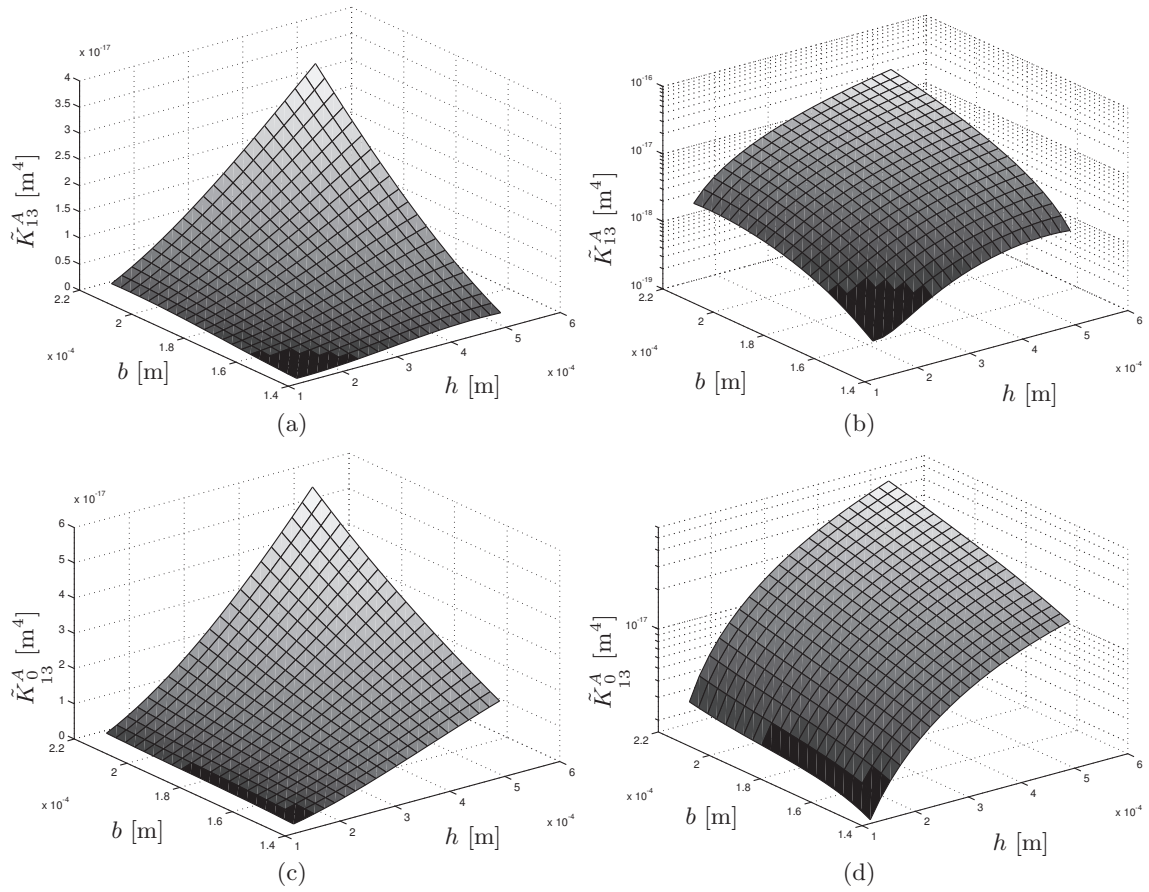

Fig. E.6. See table E.1 for the plot data.

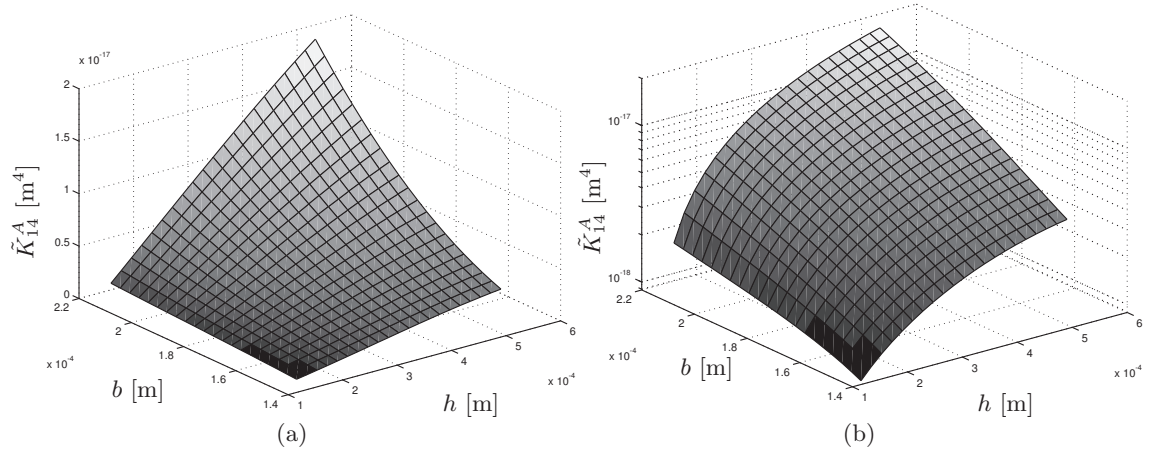

Fig. E.7. See table E.1 for the plot data.

F

Steady State Configuration of the Network Flow Model

F.1 Unit Cell Sensitivity

The effect of the number of unit cells on the effective permeability has been investigated. One unit cell is characterised by the repetitive geometry between two subsequent stitch yarn penetration points in the 0° direction (B) and two subsequent stitch yarn penetration points in the 90° direction (A) of the fabric. The number of unit cells is characterised by the number of stitch distances $\#A$ and $\#B$ and a certain amount of configurations of a piece of fabric was modelled. For each configuration, the effective permeability in the 0° and 90° direction was determined. The results are represented in figure F.1 and were obtained by using the parameters that are listed on page 38. Here, the number of stitch distances $\#A$ and $\#B$ has been varied.

Figure F.1 shows that for an increasing number of unit cells, the determined permeabilities K_E^0 and K_E^{90} converge to a particular value. These results were obtained by using SYD lengths $l = 10$[mm]. Similar behaviour was observed for other SYD lengths. Assembling more repetitive local properties (like permeability, flow area, lengths and pressure differences), leads to a more representative global behaviour of those properties. Some effects that are related to the number of unit cells are:

- As can be seen in figure 2.7, SYDs in one unit cell intersect with SYDs from another unit cell. This explains the steep behaviour in the range where a small number of unit cells were used. When there is one unit cell, there are just less connections, compared to a configuration with two or more unit cells.
- Above reasoning suggests a lower permeability prediction, when less unit cells are used. This can be observed in figure F.1, but does not seem to happen for the K_E^0 prediction for a varying

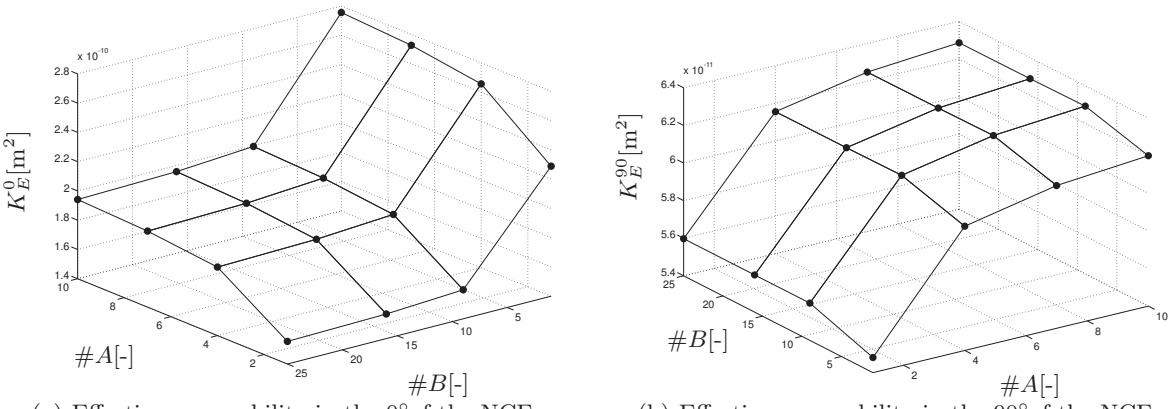

(a) Effective permeability in the 0°of the NCF.

(b) Effective permeability in the 90°of the NCF.

Fig. F.1. Effect of the number of unit cells (stitch distances) in the 0°($\#B$) and the 90°direction ($\#A$) of the NCF, on the effective permeability of the fabric. Settings of parameters are listed on page 38 ($l = 10$[mm]), but the number of stitch distances $\#A$ and $\#B$ has been varied.

number of stitch distances B. The term $\overline{L}$ is overestimated, since this variable is determined by using the average distance between the regions with nodes with a high and nodes with a low pressure boundary condition. See figure F.2(a) for the presence of those nodes in the upper and lower dashed boxes. The overestimation of $\overline{L}$ was used in the permeability (4.2) and the flow area (4.3) determination. Combining those equations yields the presence of a squared overestimated $\overline{L}$ contribution in (4.2) and results in the overestimation of K_E^0 for a small number of unit cells in the 90°direction ($\#B$).

- Nodal nett fluxes along the sides of the domain are smaller than comparable regions in the domain's interior (figure F.3(b)), due to the absence of periodic boundary conditions. Using more unit cells results in a smaller boundary effect on the effective permeability.
- Determination of the effective cross-sectional flow area $\mathcal{A}_E$ (4.3) that was based on the volume of inter bundle channels, becomes more representative when more unit cells are used. The cross-sectional flow area will vary along the pressure gradient direction, but in a repetitive sense (unit cells). These variations show less influence as the effective cross-sectional flow area $\mathcal{A}_E$ increases, since the variations remain the same.
- Above reasoning can be applied to the effective permeability. The local permeability varies along the pressure gradient direction, but in a repetitive sense with a constant variation.

Further permeability determinations will be done for an element network with a size of $10A \times 25B$.

F.2 Example

This example shows the results that were produced by the numerical program. Post-processing the results gives graphical representations of the solutions and makes interpretation of these results easier. The following properties of the modelled piece of NCF were used:

- Piece of fabric characterised by a number of stitch distances $10A$ and $25B$ ($A = 5.71$[mm], $B = 2.20$[mm]).
- Modelling a bi-axial NCF, which means a lower and an upper ply with their associated SYDs.
- Permeability of SYDs ($1{\cdot}10^{-17} > K^A_{SYD} > 1{\cdot}10^{-18}$) determined with the results from Mortensen [38], see section 3.3.
- Permeability of the region in the SYD with the stitch yarn obstruction, determined with the results from section 3.4.2 ($d_c = 0.071$[mm], $K^A_{ist} \approx 1 \cdot 10^{-18}$ [m^4]).
- Permeability of the external channels determined with the results from section 3.4.1, combined with the results of the microscopy analyses in appendix H.5 ($K^A_{est} = 7.85 \cdot 10^{-19}$ [m^4]).
- Permeability of the inter ply elements set to be highly porous compared to the other elements, since there is no relation for their permeabilities yet.
- Constant SYD dimensions $l = l^u = l^l = 10$[mm], $h = 0.4$[mm] and $b = b^u = b^l = 0.142$[mm].

Figure F.2(a) shows the result of the pre-processing stage, which was done by the sequence of five processes in the upper left corner of figure 4.2. A SYD intersection search was done, elements were created and element permeabilities K^A_{el} were assigned, which are shown in figure F.2(a). To determine the permeability in the 0°direction of the NCF (K^0_E), pressure boundary conditions have to be applied to nodes within the dashed boxes. To determine the permeability in the 90°direction of the NCF (K^{90}_E), pressure boundary conditions have to be applied to nodes within the dotted boxes. The results in the subsequent figures for this example were obtained by using the first option.

Solving the system of equations for the unknown nodal pressures gives the nodal pressure distribution in figure F.3(a). The global pressure field varies linearly over this piece of NCF. The pressure differences vary at the local scale (at the element level), since these elements have different permeabilities as was shown in figure F.2(a).

Figure F.3(b) shows the nodal nett fluxes. These were known for the nodes without pressure boundary conditions, i.e. equal to zero due to the incompressibility assumption. The nodes with pressure boundary conditions can be seen as the connection between the flow domain and the external environment. The nodes with the high pressure boundary conditions have nodal nett fluxes that are greater than zero and the nodes with the low pressure boundary conditions have nodal nett fluxes

that are less than zero. The sum of all positive and negative nett fluxes equal zero, again due to the incompressibility assumption. The permeability of this piece of NCF may now be determined with equation (4.2).

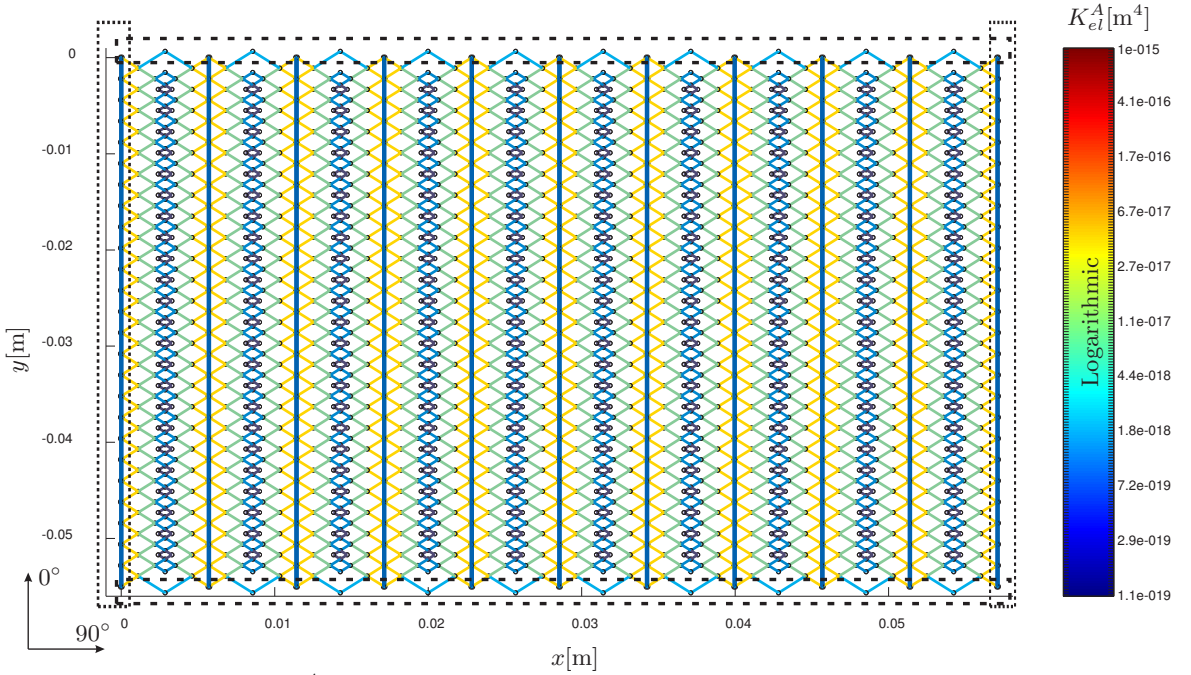

(a) element permeabilities K_{el}^{A}. Pressure boundary conditions may be applied to the nodes within the dashed and dotted boxes to determine the permeability K_E^0 or K_E^{90} respectively.

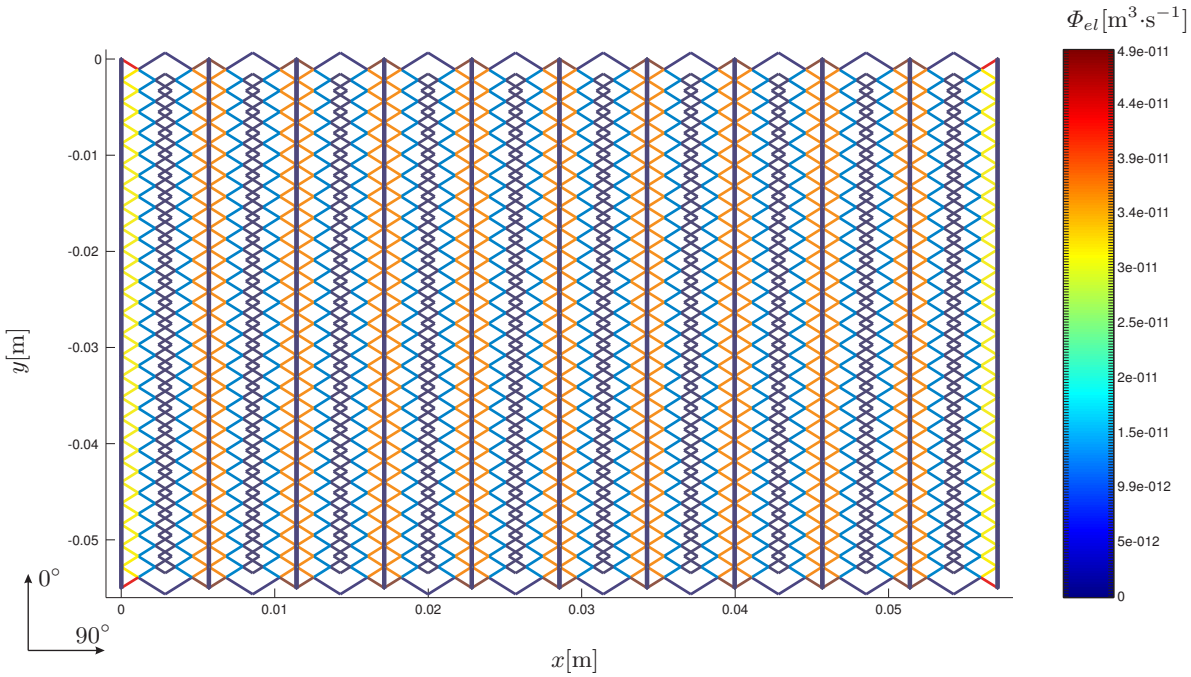

(b) element fluxes Φ_{el}.

Fig. F.2. An example of a piece of NCF with the parameter settings listed on page 38. Solving the assembled system results in a pressure distribution as in figure 4.3(a), which can be used to determine the element fluxes Φ_{el}.

Element fluxes Φ_{el} may be calculated as well. Using the solved pressure field in equation (4.1) gives the result in figure F.2(b). As was expected from the element permeability distribution in figure F.2(a), element flows differ and are dominating in elements that represent the widest part of the SYDs. Also, these elements show some boundary effects along the left and right sides of the flow domain (figure F.3(a) shows these effects as well). These effects disappear, when periodic boundary conditions are applied along these sides. This means that the nodes on the left side are actually the same nodes on the right side, such that there are no boundaries on these sides (imagine a piece of paper, shaped into a cylinder-like geometry). The program is not able to process this type of boundary conditions yet, but could be incorporated quite easily. However, these boundary effects are expected to influence the permeability determination minimally, certainly when a considerable amount of unit cells are modelled (appendix F.1).

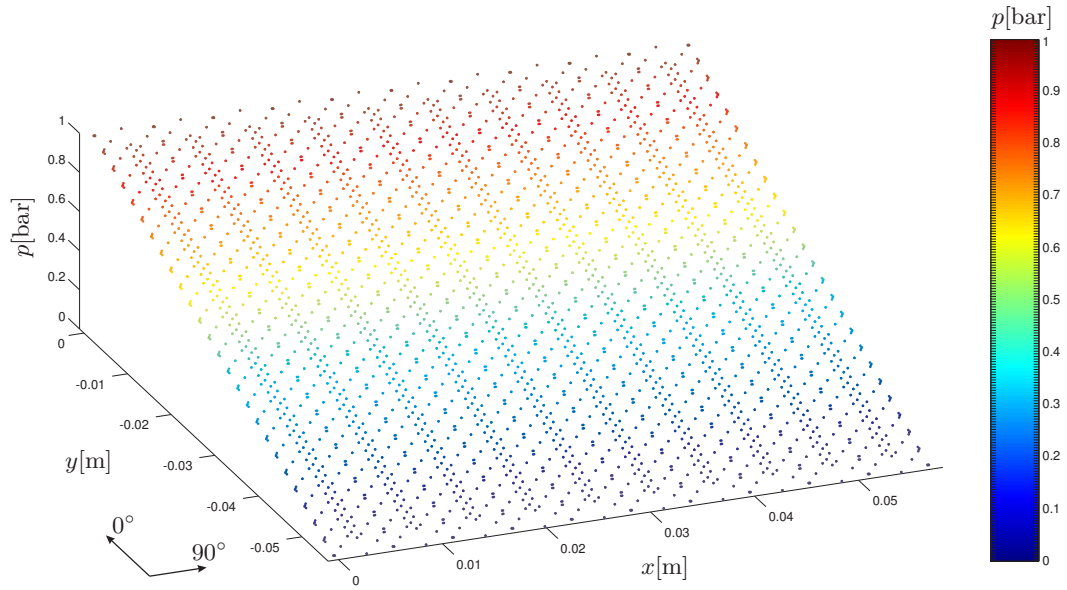

(a) Nodal pressures.

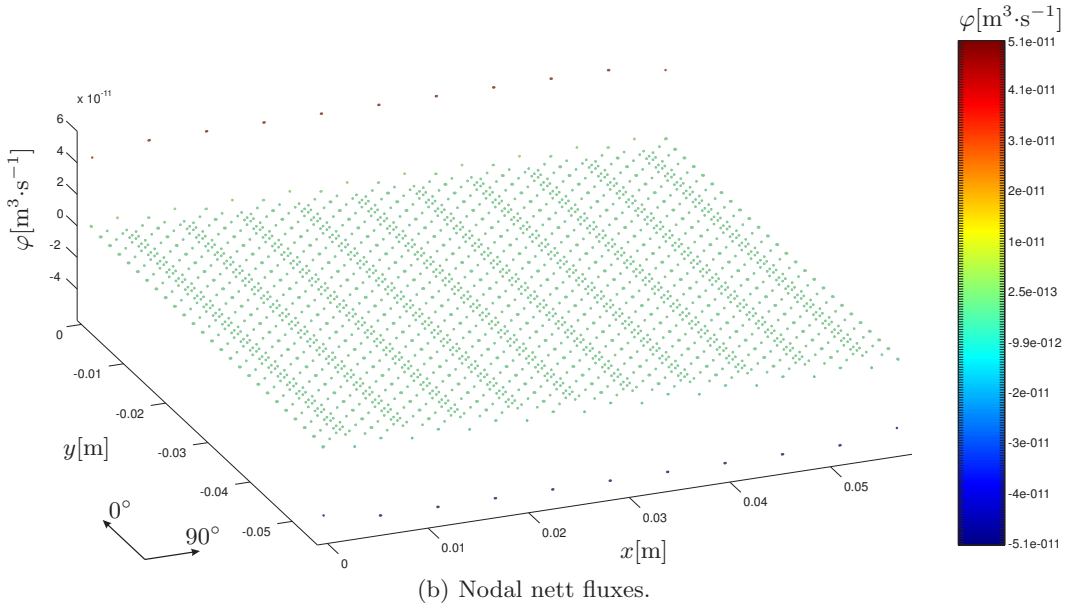

(b) Nodal nett fluxes.

Fig. F.3. Nodal solutions from the network in figure F.2(a).

G

Transient Configuration of the Network Flow Model

G.1 Flow Front Position Derivation

Consider the tube with a constant permeability K and cross-sectional area $\mathcal{A}$ in figure G.1. The boundary values p_h and p_l are constant. Making use of Darcy's law separately in both the resin and air filled parts of the tube, and using the continuity equation (1.8) with the incompressibility condition $\partial\rho/\partial t = 0$, results in the following expression:

$$\begin{aligned} \Phi_r &= \Phi_a \\ \frac{(p_{if} - p_h)}{\mu_r \mathcal{V}_r} &= \frac{(p_l - p_{if})}{\mu_a \mathcal{V}_a} \end{aligned}$$

with p_{if} the pressure on the (resin-air) interface. Expressing this relation for the pressure at the interface and making use of $\mathcal{V}_a = \mathcal{V}_{el} - \mathcal{V}_r$, gives:

$$p_{if} = \frac{p_h \mu_a (\mathcal{V}_{el} - \mathcal{V}_r) + p_l \mu_r \mathcal{V}_r}{\mu_a (\mathcal{V}_{el} - \mathcal{V}_r) + \mu_r \mathcal{V}_r} \tag{G.1}$$

Evaluation of Darcy's law (1.3) only for the resin filled part of the tube gives:

$$\frac{\mathrm{d}\mathcal{V}_r}{\mathrm{d}t} = -\frac{\mathcal{A}K^A}{\mu_r}\frac{(p_{if} - p_h)}{\mathcal{V}_r}$$

Rearranging gives:

$$\mathrm{d}t = \frac{\mathcal{V}_r \mu_r}{\mathcal{A}K^A(p_h - p_{if})}\mathrm{d}\mathcal{V}_r \tag{G.2}$$

Substitution of (G.1) in (G.2), followed by integration gives:

$$t(\mathcal{V}_r) = t_r = \frac{\mu_a \mathcal{V}_r \mathcal{V}_{el} + \frac{1}{2}\mathcal{V}_r^2(\mu_r - \mu_a)}{\mathcal{A}K^A(p_h - p_l)},$$

in which t_r is the time, which was needed to obtain the substances' (resin-air) interface at $\mathcal{V} = \mathcal{V}_r$ (see figure G.1). Solving for $\mathcal{V}_r$ gives two roots for which the following is a physical realistic one:

$$\mathcal{V}_r(t_r) = \frac{\sqrt{\mu_a^2 \mathcal{V}_{el}^2 + 2\mathcal{A}K^A(p_h - p_l)(\mu_r - \mu_a)t_r} - \mu_a \mathcal{V}_{el}}{\mu_r - \mu_a}, \tag{G.3}$$

or expressed for the permeability:

$$K^A(\mathcal{V}_r, t_r) = \frac{\mu_a \mathcal{V}_r \mathcal{V}_{el} + \frac{1}{2}\mathcal{V}_r^2(\mu_r - \mu_a)}{\mathcal{A}(p_h - p_l)t_r} \tag{G.4}$$

For this formulation, the amount of filled volume $\mathcal{V}_r$ was related to the position of the resin-air interface. Using this formulation has the restriction that the cross-sectional area $\mathcal{A}$ is constant along the pressure gradient direction. This area will vary over an NCF's unit cell (for which its dimensions are characterised by stitch distances A and B), but it has been assumed that any effects due to this variable area are allowed to be neglected when a sufficient amount of serially connected unit cells are modelled.

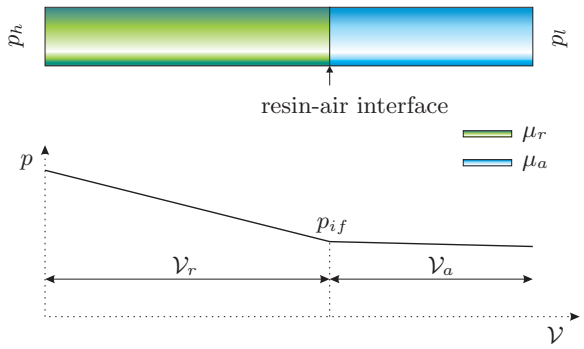

Fig. G.1. A tube with volume $\mathcal{V}_{el}$ with a constant permeability K and cross-sectional area $\mathcal{A}$, and a variable viscosity μ and pressure gradient $\mathrm{d}p/\mathrm{d}\mathcal{V}$ over its length. Two substances are present, characterised by their viscosities μ_r and μ_a.

G.2 Flow Intersection Points

This section explains the chosen strategy for the filling scheme, especially based on the flow intersection points (nodes). An optional strategy that was not used, could focus on the elements that contain more than one substance only (flow front tracking). Such a strategy was not applied, because a more detailed approach was needed to include the effect of local element permeabilities and volumes, on the element flows. These flows may differ from flow behaviour with a uniform effective permeability (obtained from a steady state solution).

The used strategy considers the flows of any substance in each element, for every time step. Consider the element network in figure G.2, in which a negative pressure gradient from the left to the right has been assumed. The arrows indicate the flow directions. Figure G.2(a) shows an initial situation, in which elements 1 and 4 are the *kick off* elements and are filled with resin (they may also be partly filled with resin initially). They will be supplied with resin during the fill simulation.

After determining a time step Δt (appendix G.3), successive connected elements could be filled in one single time step. The bounded area (dashed line) in figure G.2(b) shows this progression. Within a number of update cycles (see figure 4.2), the resin in elements 5, 6 and 3 was supplied by element 4 only. As mentioned above, the filling scheme considers the flow of the substance with viscosity μ_a (air) as well. This means that during the time step Δt, air was transported from element 2 to element 3. Since the assumption on page 42 (concerning the position of the substances in an element), air was transported through element 3 to the downstream elements, which have not been drawn.

Figure G.2(c) shows a similar situation as in figure G.2(b), in which element 1 supplied resin to elements 2 and 3. Element 6 donated some air to element 3, which was transported to downstream elements, again due to the assumption of the substances' position in an element. If this assumption had not been made, a situation as in the bounded area in figure G.2(d) arises after several time steps. To control these situations, a lot of bookkeeping per element will be needed due to a variable number of pieces with a particular substance within an element. This number would be time step dependent and leads to a heavily loaded computational memory.

The use of *artificial vacuums* in the filling scheme is some kind of a controlling mechanism. Overflows ζ have to be processed in elements' *artificial vacuums*. The program will check the size of donations and the *artificial vacuums* of each element. The program gives a warning if this condition has not been met. In this way, loss or production of substances due to complex situations and improper programming, will be detected. However, these warnings did not appear, while these checks were being executed during all fill simulations.

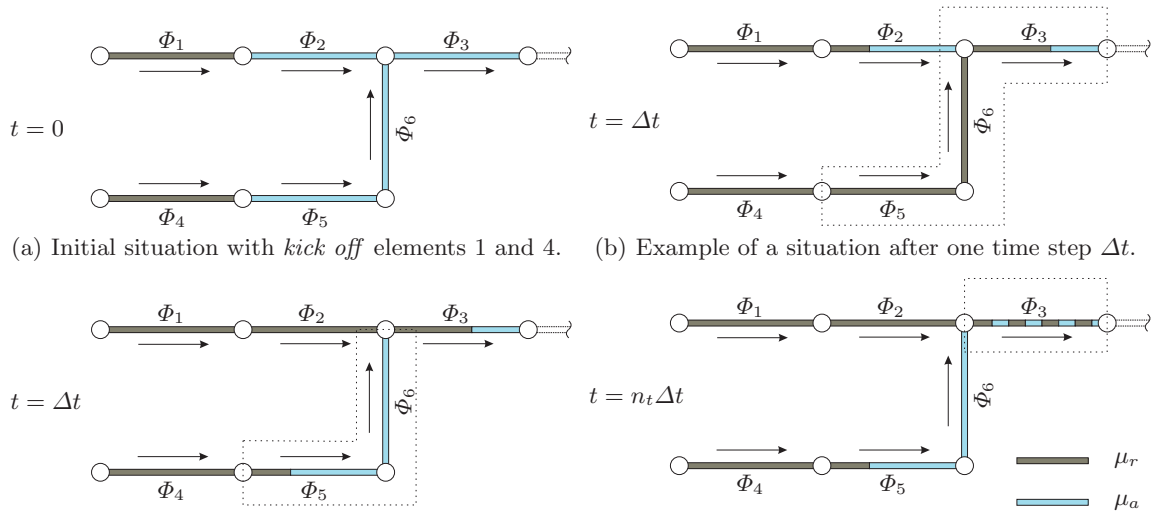

(a) Initial situation with *kick off* elements 1 and 4.

(b) Example of a situation after one time step Δt.

(c) Another example of a situation after one time step Δt.

(d) Situation that occurs, when not using the assumption on page 42, considering the substances' position in an element.

Fig. G.2. Different phenomena to account for during the fill simulation. The arrows indicate the flow direction.

G.3 Time Step Control

During a fill simulation (transient solution), a time step Δt is needed to determine and process overflows (see figure 4.2). An appropriate constant time step could be chosen, which could be used throughout the whole simulation. Since the nature of this problem results in a network of connected elements with very different volumes and permeabilities (differences up to four orders of magnitude), and the non-linear movement of substances' interfaces (see equation (4.15)), led to the development of a time step controlling scheme.

The time step determines the amount of pressure field solutions during a fill simulation. The more the updates of the pressure field, the more accurate a transient solution should be. The time step controlling scheme is based on the movement of the substances' interface. This movement is related to the number of time steps ψ, for which the interface travels along one element. For example, $\psi = 2$ indicates that an element has to be filled within two time steps and $\psi = 0.5$ indicates that two elements have to be filled within one time step.

The time step controlling scheme consists of several steps, which are numbered from 1 till 6. It is recommended to read these steps with help of figure G.3. This figure contains the indices j, k, m and n, which are related to sets $\mathcal{T}, \mathcal{U}, \mathcal{W}$ and $\mathcal{X}$ respectively. These sets contain several elements, which are related to some criteria, as will be mentioned in the steps below. These steps have to be executed during each time step determination, according to the following sequence:

1. Create a set $\mathcal{T}$, containing elements j for which:

$$\tau_r > 1 - \frac{1}{\psi} \tag{G.5}$$

These elements j can be seen as *donating* elements. The criterion ψ can be related to one of the following cases:

- $\psi > 1$: Select filled and partly filled elements. This criterion is related to the minimum number of time steps, for which an element may be filled.
- $\psi < 1$: Select all elements. This criterion is related to the number of successively connected elements with the same size, to be filled in one time step. Because successively connected elements are occasionally identical, this criterion could not guarantee that ψ^{-1} number of successively connected elements are filled in one time step. However, the minimum time step determination in step 6 ensures that the number of successively connected elements to be filled will be $\leq \psi^{-1}$. In this way, inaccuracy has an upper bound related to ψ^{-1}.

2. For each element j in set $\mathcal{T}$, select the connected elements on the low pressure side, which satisfies:

$$\tau_r < 1 \tag{G.6}$$

   Store these elements k in another set $\mathcal{U}$. These elements can be seen as *receiving* elements.
3. Filter for unique elements k in set $\mathcal{U}$, such that duplicates disappear. Per unique element k, a set $\mathcal{W}_k$ contains its *donating* elements m for which the criterion (G.5) has to be satisfied. Actually this process is a rearrangement. This relation will not be checked again during the algorithm, because the filter process uses set $\mathcal{T}$, in which elements j (which are actually *donating* elements) were already selected by criterion (G.5).
4. For each element k in set $\mathcal{U}$, collect the other *receiving* elements n. These *receiving* elements n are connected to the high pressure side of element k or to the low pressure side of its donating elements in its set $\mathcal{W}_k$. Store these elements n in a set $\mathcal{X}_k$, including the evaluated element k from set $\mathcal{U}$.
5. Determine time step according to:

$$\Delta t_k = \frac{\mathcal{V}_k^{\#} \frac{\sum_n \Phi_n}{\Phi_k} + \sum_m t_m \Phi_m}{\sum_m \Phi_m}, \tag{G.7}$$

   in which t_m is the time, which is needed to fill element m first, before resin arrives at element k (see appendix G.3.1 for the derivation of (G.7)). This has to be accounted for, because the accuracy criterion is based on the position of the substances' interface. This reasoning and the assumption of the position of the substance with μ_r (positioned at the high pressure side of an element, see section 4.3.1) explains the focus on the resin transport only. The term $\mathcal{V}_k^{\#}$ represents the volume of element k, which has to be filled within one time step:

$$\mathcal{V}_k^{\#} = \frac{\mathcal{V}_k}{\psi}$$

6. For each element k from set $\mathcal{U}$, a time step was determined. The time step to be applied, will be the minimum time step that was obtained:

$$\Delta t = \min \Delta t_k \tag{G.8}$$

G.3.1 Time Step Derivation

Consider the network of randomly filled elements in figure G.3. The pressure gradient is indicated by the arrow. This implies that the substances in elements $1, 2$ and 3 will flow to the elements $4, 5$ and 6.

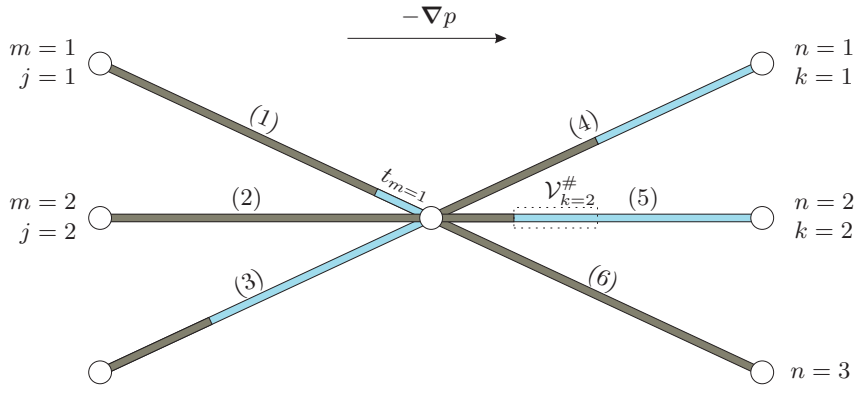

Fig. G.3. Random situation of filled and partly filled elements, having equal volumes and permeabilities. The pressure gradient is indicated by the arrow. The indices j, k, m and n correspond to elements in the sets $\mathcal{T}$,$\mathcal{U}$,$\mathcal{W}$ and $\mathcal{X}$ respectively, based on criteria as described in the numbered steps on page 109. Each element contains indices, which means that the particular element appears in the corresponding set. The bounded area (dashed line) indicates the volume that has to be filled for element 5 during one time step when $\psi = 4$.

To determine a new time step during the fill simulation, the steps in the enumeration on page 109 will be taken. Consider for example the second element ($k = 2$) in set $\mathcal{U}$, which is element 5 (figure G.3). The bounded area (dashed line) indicates the volume of element 5, which has to be filled during one time step Δt ($\psi = 4$). Elements $1, 2$ and 3 are *donating* elements of element 5. Since the movement of the substances' interface is the most important motion during the transient solution (accuracy), the amount of substance with viscosity μ_r (resin) that will be delivered to element 5, needs to be calculated. Since $\psi = 4$, it is unlikely that element 3 will deliver resin to element 5 within the next time step. Therefore, this element was already excluded during step 1 on page 109 by criterion (G.5).

The total amount of resin, which will flow from elements 1 and 2 to elements $4, 5$ and 6, will be:

$$\sum_{m=1}^{2} (\Delta t_k - t_m)\Phi_m = \sum_{n=1}^{3} \mathcal{V}_{r}^{n}, \tag{G.9}$$

which follows from the assumption of a constant volume flow within Δt_k, see equation (4.7). The right hand side term represents the total amount of resin that will be delivered, divided over elements $4, 5$ and 6. The term Δt_k represents the time step with its determination based on element element k, which is $k = 2$ in this example. The term t_m is the time after which resin will flow from element m to elements n.

Actually, air from element 3 will be transported to elements $4, 5$ and 6 as well. This element was not included in equation (G.9), since the assumption of the position of the substance with μ_a, positioned at the low pressure side of all elements (see section 4.3.1), was accounted for. This means that the air from element 3 will be transported to elements (which were not drawn) at the low pressure side of elements $4, 5$ and 6, during one or more update cycles.

The total amount of resin that will be delivered to elements $4, 5$ and 6 will be divided, based on their flow rates Φ_n. This means that the delivered amount of resin to element 5 becomes:

$$\mathcal{V}_{r}^{k=2} = \frac{\Phi_{k=2}}{\sum_{n=1}^{3} \Phi_n} \sum_{n=1}^{3} \mathcal{V}_{r}^{n} = \mathcal{V}_{k=2}^{\#}$$

Substitution in equation (G.9) gives:

$$\sum_{m=1}^{2} (\Delta t_k - t_m)\Phi_m = \mathcal{V}_{k=2}^{\#} \frac{\sum_{n=1}^{3} \Phi_n}{\Phi_{k=2}}$$

Solving for Δt_k and generalising gives:

$$\Delta t_k = \frac{\mathcal{V}_k^{\#} \frac{\sum_n \Phi_n}{\Phi_k} + \sum_m t_m \Phi_m}{\sum_m \Phi_m}$$

H

Experiments

H.1 Deformation Mechanisms

During an infusion experiment, the pressure difference between the atmospheric pressure and the lower pressure inside the cavity, leads to a distributed load on the glass plates' surfaces. The stiffnesses of the glass plates result in significant tilt and deflection, compared to the initial cavity height $2h$. A particular cavity height is associated with a particular fibre volume fraction V_f. Since permeability depends heavily on the fibre volume fraction, it is necessary to quantify these deformation mechanisms.

Before the infusion experiment starts, the lower glass plate serves as a height reference for height measurements that will be done during the infusion experiments. As is shown in figure 5.1(c), the lower glass plate bends upwards during an infusion experiment. The deflection Δy_{lp} has been measured at the centre position of the lower glass plate and was more or less constant throughout the whole infusion

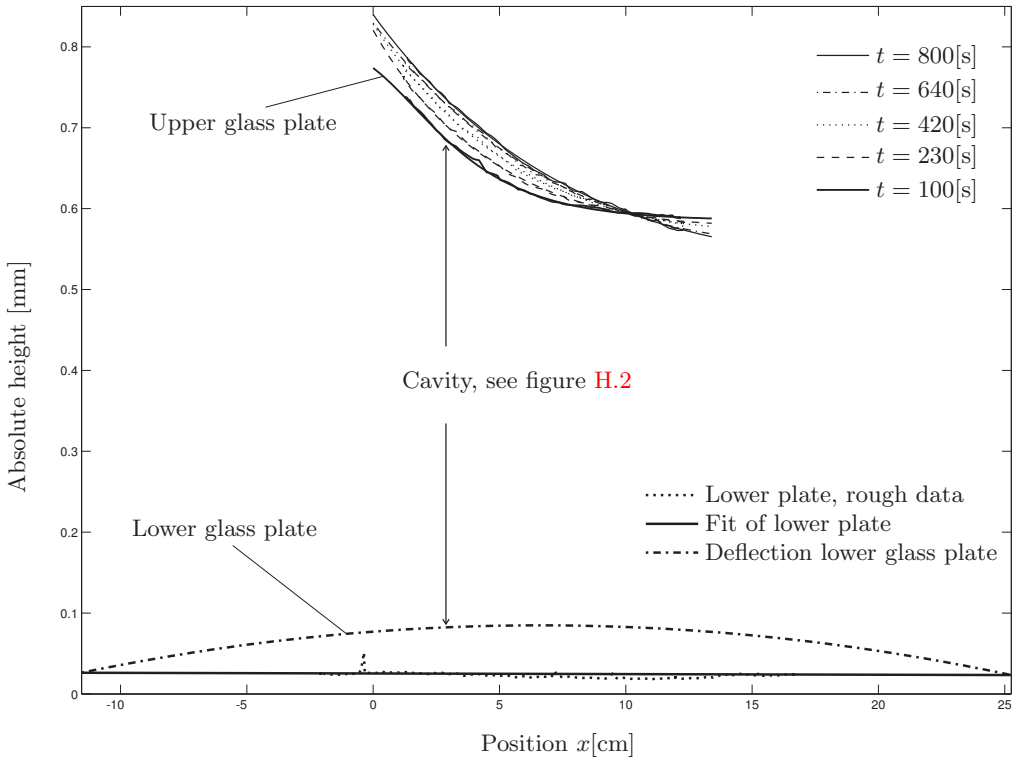

Fig. H.1. Typical cavity shape evolution, during the infusion experiment. The Cartesian coordinate x corresponds with the coordinate definition in figure 5.1(b). Both rough and fitted height measurements of the upper glass plate have been plotted, which represent the lower side of the upper glass plate. This means that the thicknesses of the upper glass plate and the transparent foil have been processed.

experiment (Δy_{lp}=60·10^{-6}[m]). Since this glass plate has been clamped on the aluminium frame, it has been assumed that this plate remains its height reference at the edges (clamping points). Between these points, the height reference will be corrected by assuming a parabolic deflection over the length L_{lp} with a maximum deflection Δy_{lp} at the centre (see the "Deflection lower glass plate" graph in figure H.1). The height of the lower glass plate could then be described by:

$$\tilde{H}_{lp}(x) = a_1 x^2 + a_2 x + a_3$$

The smaller upper glass plate is positioned on top of the fabric. Just as the lower glass plate, this upper glass plate bends as well, due to a resulting distributed load. Since this glass plate is free to move, tilting is the most significant mechanism, as is shown in figures 5.1(c). Figure H.1 shows the typical cavity shape during an infusion experiment, at several infusion times t. On top, the absolute upper glass plate heights are displayed. Fits through these data points are generally obtained by polynomial functions, in the form of:

$$\tilde{H}_{up}(x,t) = a_4 x^2 + a_5 x + a_6$$

Figure H.2 shows the cavity height $2\tilde{h}$ at several infusion times t, which was extracted from the data in figure H.1, i.e. :

$$2\tilde{h}(x,t) = \tilde{H}_{up}(x,t) - \tilde{H}_{lp}(x) \tag{H.1}$$

The permeability calculation method, as explained in section 5.2, determines the permeability at several flow front positions L_r to extract its position dependency that is a result of the varying cavity height and its associating varying fibre volume fraction. At this point $x = L_r$, the permeability of the already saturated region of the fabric is needed, which is in front of the flow front, i.e. $x \leq L_r - \Delta x$ (see figure 5.2). Since the cavity height is time dependent, the permeability within $x \leq L_r - \Delta x$ is time dependent as well. However, it is hard to process this time dependency in the permeability determination method.

Since there is an initial (minimum at $t = 100$[s]) cavity height $2\tilde{h}(x, t = 100)$ and a final (maximum at $t = 800$[s]) cavity height $2\tilde{h}(x, t = 800)$, something can be said about the maximum and the minimum permeability respectively. The permeability determinations will be done for these extreme cavity heights, such that an initial (at $t = T1$) and final cavity (at $t = T2$) related permeability can be obtained.

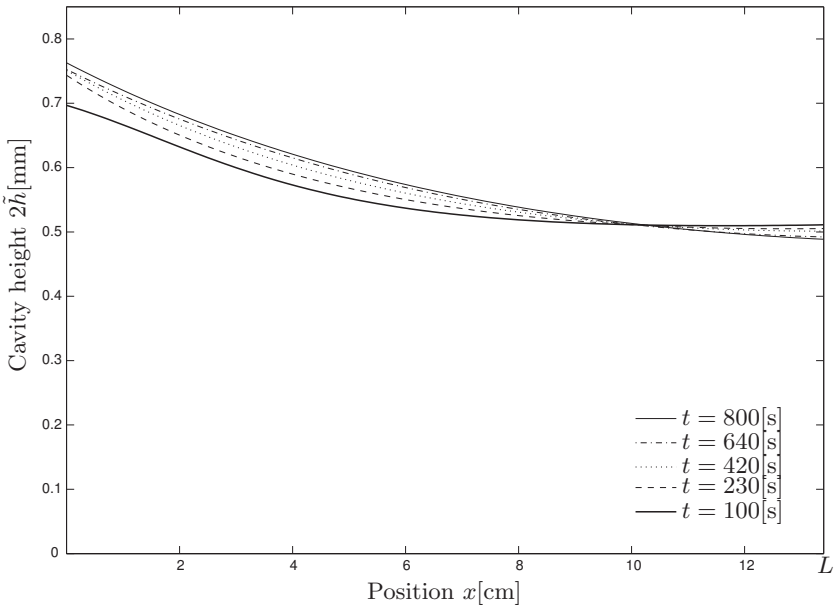

Fig. H.2. Typical cavity height evolution $2\tilde{h}(x,t)$ (H.1), during the infusion experiment. The Cartesian coordinate x corresponds with the coordinate definition in figure 5.1(b).

H.2 Volume Flow Complication

In the last stage of performing experiments, accumulation of the infusion liquid was observed near the entrance region, where the gauze was positioned (see figures 5.1(b) and H.3). This behaviour was observed in the measurement data that was extracted from the load cell. The measured decrease of mass of the bucket was translated to an increase of liquid volume, being infused in the fabric.

Figure 5.3(b) shows the cross-sectional area $\tilde{\mathcal{A}}(x)$, derived with (5.2) with $2\tilde{h}(x)$ from figure 5.3(a). Integration over the total length of the fabric gives the amount of volume $\tilde{\mathcal{V}}(x = L)$ (figure 5.3(c)), which could be filled by the liquid. Comparing this result with figure 5.4(a), gives volumes that do not correspond. The overestimation of the infused liquid is assumed to be a result of the accumulating liquid, as indicated in figure H.3.

Fits through data points obtained by the load cell's data, are applied in the form of:

$$\tilde{\mathcal{V}}_r(t) = a_7 t^{a_8} + a_9, \tag{H.2}$$

for which the graph in figure 5.4(a) was a result. The time t_e of arriving of the flow front at the end of the fabric was known from visual observations (section 5.3.2). Since the fibreless volume $\tilde{\mathcal{V}}(x = L)$ of the fabric is known as well, equation (H.2) was scaled like:

$$\tilde{\mathcal{V}}_{sc}^{r}(t) = a_{10}\tilde{\mathcal{V}}_r(t), \tag{H.3}$$

such that:

$$\tilde{\mathcal{V}}_r(t_e) = \tilde{\mathcal{V}}(x = L)$$

This manipulation conserves the curves shape, which is important for the permeability determination. It is assumed that this shape should more or less be the same when accumulation of the liquid did not occur, since:

- the permeability of the accumulation region (near the gauze) is much greater than the fabric's permeability and,
- the assumption that the increase of accumulation was constant during the infusion experiment.

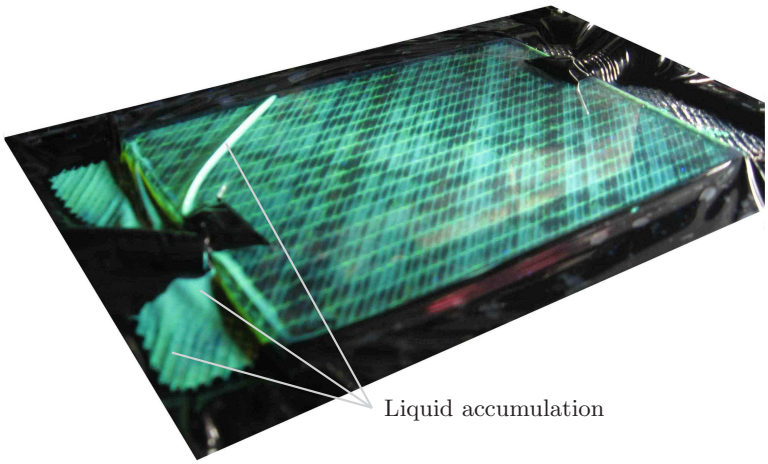

Fig. H.3. Liquid accumulation near the entrance region results in an overestimation of the volume flow.

H.3 Viscosity Measurements

The liquid to be used during the infusion experiments, has to fulfil some criteria. It has to be an incompressible, Newtonian and homogeneous liquid without any particles or different phases. It also has to be viscous, such that a high pressure gradient is needed to infuse the fabric, while still having a controlled infusion process (not too fast). The high pressure gradient was needed to obtain an accurate pressure measurement at the pump side, since the sensor exports a signal (voltage) that is logarithmically related to the pressure as shown in appendix H.4, which considers the calibration. The mixture of VAN GILSE SCHENKSTROOP (some kind of maple syrup) and water with the volume ratio 6:1 fulfills these criteria. Viscosity measurements were executed with a BROOKFIELD DIGITAL VISCOMETER, MODEL DV-E, by using spindle number (code) 21. The results of these measurements are depicted in table H.1 and figure H.4.

The measurements were done at different shear rates, to verify the liquid's Newtonianity. From table H.1, it can be seen that there is a small amount of shear thinning, i.e. as the shear rate increases, the viscosity decreases. However, the change in viscosity at different shear rates is not significant. Since the infusion processes during the experiments exhibit different shear rates, changing from fast to slow as the infusion time increases, an averaged viscosity for each temperature measurement was determined. These values are plotted as circles in figure H.4. The solid line represents a linear fit that relates viscosity and temperature. This result will be processed in the permeability determination in section 5.3.

Table H.1. Viscosity measurement values in [mPa·s], for different temperatures and shear rates.

RPM [-]	10	12	20	30	50	60	
Shear rate [s^{-1}]	0,93	1,12	1,86	2,79	4,65	5,58	
Temperature T [°C]							Averaged
18,5	1210	1200	1190	1187			$1,20 \cdot 10^3$
20,1	1035	1025	1018	1012			$1,02 \cdot 10^3$
21			953	942	929		$9,41 \cdot 10^3$
22		900	883	872	856		$8,78 \cdot 10^2$
23		813	793	787	780	775	$7,90 \cdot 10^2$
24			715	708	705	702,5	$7,08 \cdot 10^2$
25			665	660	656	652,5	$6,58 \cdot 10^2$

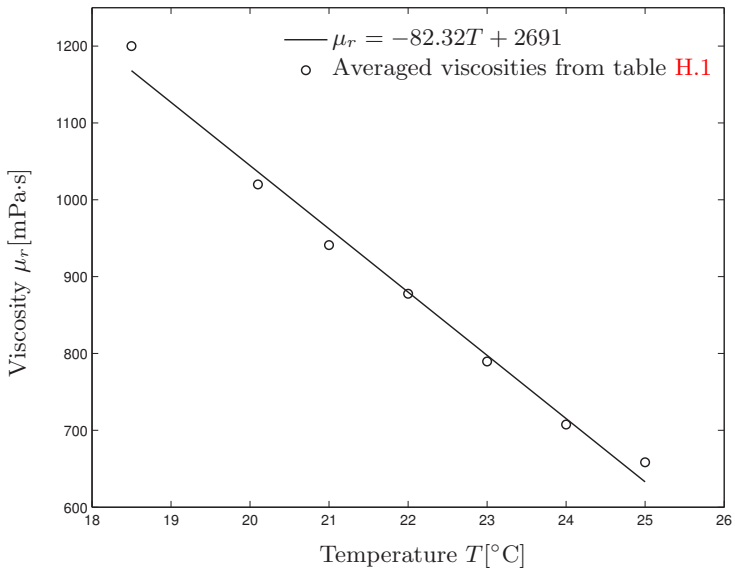

Fig. H.4. Temperature dependent viscosity for VAN GILSE SCHENKSTROOP and water with the mixture volume ratio 6:1.

H.4 Calibration Pressure Sensor

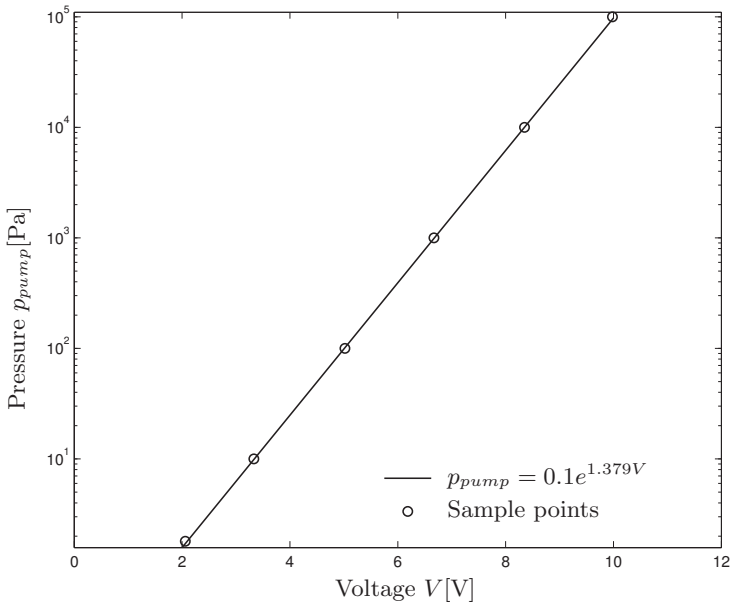

Fig. H.5. Calibration data of the pressure sensor, attached to a LEYBOLD THERMOVAC TM20 acquisition box.

H.5 External Channel Dimensions

In order to validate the network flow model (chapter 4), the dimension of the external channel's cross-section need to be known. One experiment was done by using a resin, such that the geometry of the infused fabric became a solid after the resin had cured. A sample was cut out and subsequently embedded to do some preparations, in order to make the observation surface appropriate for light microscopy.

Three positions at the sample's cross-sectional area, contained the cross-section of stitch yarns that run from one to another stitch yarn penetration point. One of these is shown in figure H.6. On top

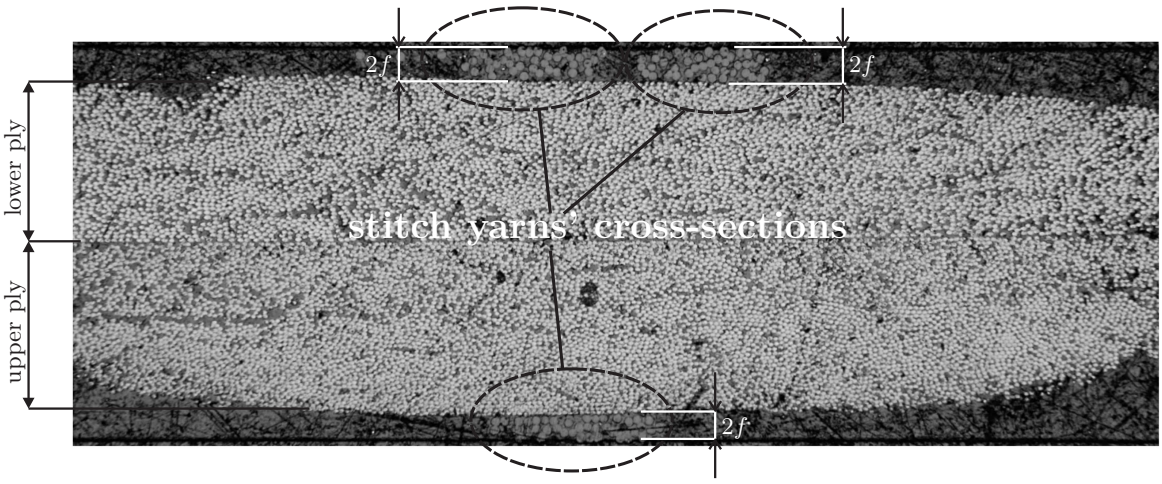

Fig. H.6. One of the three images, which were used to determine the external channels' heights $2f$.

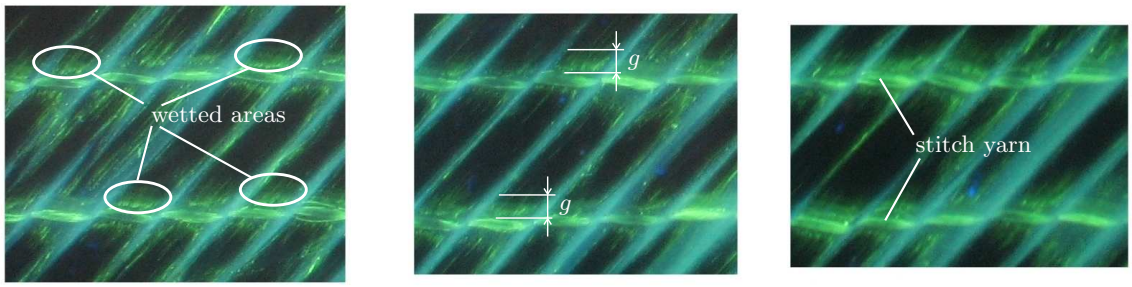

Fig. H.7. On the left: encircled wetted area, identified as external channels with their widths g.

of the fabric, two stitch yarns' cross-sections are identified. The stitch yarn contains several filaments and can be seen clearly. At the bottom of the fabric, one stitch yarn's cross-section is identified. This number of stitch yarns' cross-sections is a characteristic of this chain warp knit stitch pattern, see figure 2.4(c).

As is the case in figure H.6 and the other images that were made, the stitch yarns lie on the fabric's surfaces and are not pushed inside the fabric. It is likely that during the infusion process, the stitch yarns were slightly pushed inside the fabric due to compression of the fabric. This compression is a result of the high atmospheric pressure outside and the low pressure inside the cavity. During the curing process, the difference between the pressure in the cavity and the atmospheric pressure could have been decreased. As a result, compression decreases as well and it is likely that the stitch yarns position themselves at the fabric's surface again. It is assumed that during the infusion process, the height of the elliptical cross-section of the stitch yarn will be equal to the characteristic dimension $2f$ in figure 2.8.

From the microscopy image in figure H.6, nothing can be said about the width g (defined in figure 2.8) of the external channels. However, during an infusion experiment, close ups of the infused regions of the fabric were made and are depicted in figure H.7. The close ups were made at different positions of the fabric. The infusion liquid was visualised by adding a small amount of fluorescent, which becomes visible under infra-red light. Next to the stitch yarns, areas are filled with the liquid. This means that during the infusion process, the stitch yarns were pushed slightly inside the fabric, which resulted in the external channels. These wetted areas next to the stitch yarns, will be used to estimate the external channels' widths.

Finally, an estimation of these channels' dimensions can be made. For the measurements in figure H.6, an image with a calibration grid was used. This image was made with the same camera and microscope settings. No calibration grid was used for the measurements in figure H.7, since this image was unexpectedly useful. The calibration was done by using the stitch distance A. The results are:

$$\begin{aligned} \overline{g} &= 0.6013[\text{mm}] \\ \overline{2f} &= 0.0458[\text{mm}] \end{aligned} \tag{H.4}$$

These values are the averaged of a set of measurements that were carried out at different positions in figure H.6 and H.7 by using Optimas, which is image analysis software. It is likely that the external channel dimensions will vary over the infused fabric. For now, any idea of the order of these dimensions of these channels is sufficient to serve as an input for the network flow model.

H.6 Flow Front Propagations

Figure H.8 shows the typical flow front propagations in the 0° and 90° direction of the fabric that were observed during the experiments. As can be seen, there is a straight front without dry spots or any race tracking along the sides of the fabric. This observation justifies the assumptions that were made, based on the flow front's behaviour.

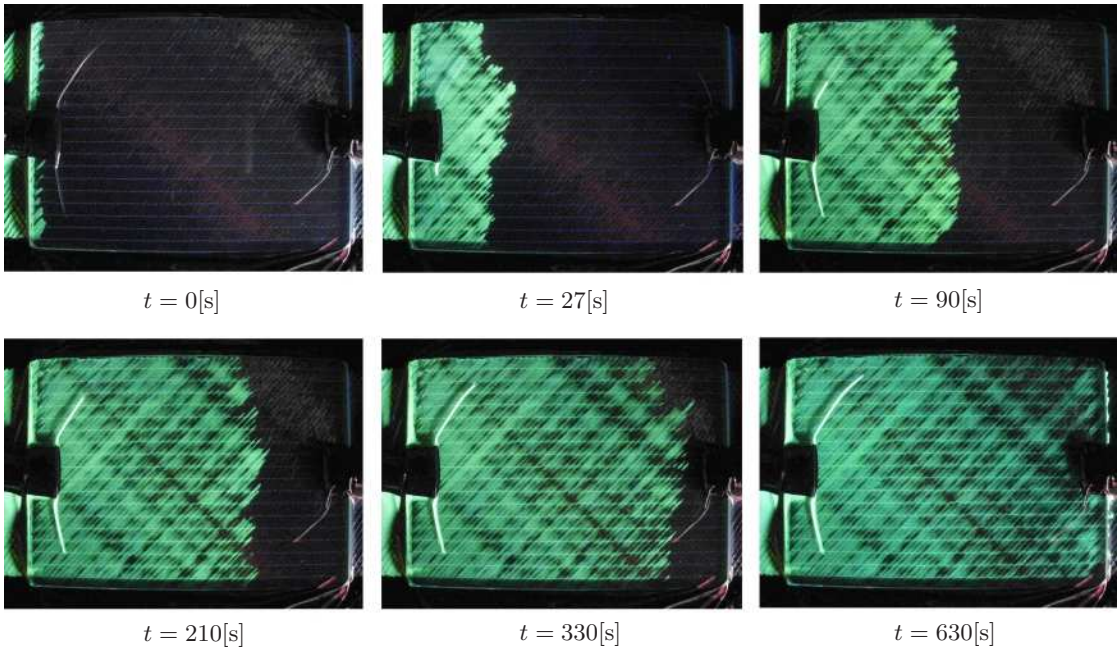

(a) Infusion experiment in the 0° direction.

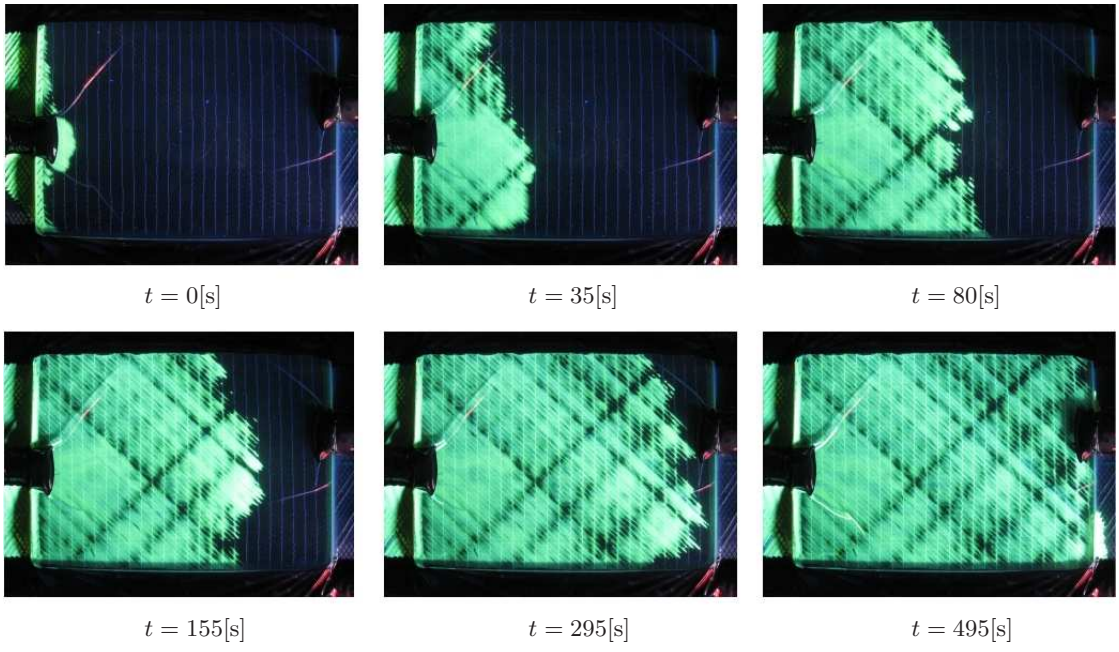

(b) Infusion experiment in the 90° direction.

Fig. H.8. Flow front propagation during the infusion experiment.

Nomenclature

Dimensions

[°]	degree
[m]	meter
[N]	Newton
[s]	second
[V]	voltage
[Ω]	Ohm

Scalars

a	fit coefficient	[case dep.]
A	needle spacing	[m]
$\mathcal{A}$	area	[m^2]
b	SYD width	[m]
B	stitch distance	[m]
c	constant	[case dep.]
$\mathcal{C}$	compactness	[-]
d	stitch yarn diameter	[m]
D	intersection distance	[m]
e	half length of major axis of an ellipse	[m]
E	error	[-]
f	half length of minor axis of an ellipse	[m]
$\mathcal{F}$	Darcy-Weisbach friction factor	[-]
g	width of the external channel	[m]
$\mathcal{G}$	gravity	[ms^{-2}]
h	SYD height	[m]
H	height	[m]
j	integer	[-]
K	permeability	[m^2]
K^A	area included permeability	[m^4]
$\mathcal{K}$	dimensionless permeability	[-]
l	SYD length	[m]
L	length	[m]
$\mathcal{L}$	packing coefficient	[-]
n	number of nodes	[-]
n_d	number of degrees of freedom	[-]
n_t	number of time steps	[-]

N	total quantity	[-]
p	pressure	[$\mathrm{Nm^{-2}}$]
P	point	[-]
$\mathcal{P}$	perimeter	[m]
Q	point	[-]
r	radius	[m]
R	hydraulic resistance	[$\mathrm{Nsm^{-5}}$]
$\mathcal{R}$	electric resistance	[Ω]
S	point	[-]
$\mathcal{S}$	surface	[$\mathrm{m^2}$]
t	time	[s]
T	temperature	[°C]
$T1$	initial cavity time	[s]
$T2$	final cavity time	[s]
$\mathcal{T}$	set with elements j	
u	first velocity component of $\mathbf{u}$	[$\mathrm{ms^{-1}}$]
U	mean velocity	[$\mathrm{ms^{-1}}$]
$\mathcal{U}$	set with elements m	
V	electrical voltage	[V]
$\mathcal{V}$	volume	[$\mathrm{m^3}$]
V_f	fibre volume fraction	[-]
W	width	[m]
$\mathcal{W}$	set with elements k	
x	first Cartesian component of $\mathbf{x}$	[m]
$\mathcal{X}$	set with elements n	
y	second Cartesian component of $\mathbf{x}$	[m]
z	third Cartesian component of $\mathbf{x}$	[m]
Z	Kozeny constant	[-]

Scalars Greek

α	geometrical correction factor	[-]
γ	change of any variable ψ	[%]
Γ	diffusivity	[]
δ	donation volume fraction	[-]
ζ	overflowing volume	[$\mathrm{m^3}$]
θ	fibre direction, relative to machine direction	[°]
μ	dynamic viscosity	[$\mathrm{Nsm^{-2}}$]=[Pa·s]
κ	change of the permeability	[%]
λ	anisotropy	[-]
Λ	change of anisotropy	[%]
ρ	volumetric density	[$\mathrm{Ns^2m^{-4}}$]
ρ_A	areal density	[$\mathrm{Ns^2m^{-3}}$]
ρ_L	linear density	[$\mathrm{Ns^2m^{-2}}$]
τ	fill factor volume fraction	[-]
Φ	volumetric flow rate	[$\mathrm{m^3s^{-1}}$]
Φ_m	mass flow rate	[$\mathrm{Nsm^{-1}}$]
ϕ	passive scalar	[anything]
φ	nodal flux	[$\mathrm{m^3s^{-1}}$]
ψ	number of time steps in which an interface moves along an element	[-]
ω	weighting function	

Vectors

$\mathbf{F}$	force	[N]
$\mathbf{g}$	gravitational acceleration	[ms^{-2}]
$\mathbf{n}$	normal	[-]
$\mathbf{N}$	shape function	[m]
$\mathbf{p}$	nodal pressures	[Nm^{-2}]
$\mathbf{u}$	velocity	[ms^{-1}]
$\mathbf{v}$	superficial velocity	[ms^{-1}]
$\mathbf{x}$	Cartesian coordinates	[m]

Vectors Greek

$\mathbf{\Phi}$	volumetric flow rate	[m^{3}s^{-1}]
$\boldsymbol{\varphi}$	nodal fluxes	[m^{3}s^{-1}]

2nd order tensors

$\underline{\mathbf{I}}$	identity tensor	[-]
$\underline{\mathbf{K}}$	permeability tensor	[m^2]
$\underline{\boldsymbol{\tau}}$	viscous stress tensor	[Nm^{-2}]

2D Matrices

$\underline{\mathbf{M}}$	element system matrix	[N^{-1}s^{-1}m^5]

Arrays

$[\delta]$	donation	[-]
$[\tau]$	fill factor	[-]

Named dimensionless groups

Re	Reynolds number

Subscripts

$_0$	initial/nominal indicator
$_{11}$,$_{22}$,$_{33}$	principle directions

a	air
B	body
bc	boundary condition
c	compacted
C	control
e	end, final
E	effective
el	element or fabric
est	refers to externally stitch yarn related channels
f	fibre
h	high
H	hydraulic
ist	refers to internally stitch yarn related channels
ip	integration point
if	interface
j	subsequent index number
k	subsequent index number
l	low
lp	lower plate
m	subsequent index number
n	subsequent index number
max	maximum
min	minimum
nd	node
p	parallel
P	at point P
Q	at point Q
r	resin
s	serial
S	surface
sc	scaled
u	indicates normalised coordinate
up	upper plate
v	artificial vacuum
V	volume
x	in x-direction
y	in y-direction

Subscripts Greek

α	penetration points grid indicator in x-direction
β	penetration points grid indicator in y-direction

Superscripts

0	in the machine (stitch) direction
90	perpendicular to the machine (stitch) direction
$*$	considering the variable in a new state
$\#$	indicating a part of the associated quantity
E	SYD arm indicator for point P
F	SYD arm indicator for point Q

^{l}	lower
^{o}	old time level
^{u}	upper

Accents

$\tilde{}$	approximated
$'$	transformed
$\hat{}$	penetration point indicator

Mathematical

$\cdot$	contraction
$\sim$	proportional to
$=$	equal to
$\equiv$	defined as
$\perp$	perpendicular to
$\|\|$	parallel to
$\overline{\quad}$	mean value
$^{-1}$	inverse
∂	partial derivative operator
Δ	difference
$\boldsymbol{\nabla}$	gradient operator
∇^2	Laplace operator: $\boldsymbol{\nabla} \cdot \boldsymbol{\nabla}$
$\sum$	summation
$\sqrt{}$	square root
cos	cosine
d	derivative operator
$\int$	integration
e-017	equivalent to $\cdot 10^{-17}$
ln	natural logarithm
log	logarithm
max	maximum
min	minimum
$\mathcal{O}$	order of magnitude
sin	sine
tan	tangent
#	number of

Abbreviations

1D	one dimensional
2D	two dimensional
3D	three dimensional
CAD	Computer Aided Design
CFD	Computational Fluid Dynamics
CFRP	Continuous Fibre Reinforced Polymers
FE	Finite Elements
HRS	High Resolution Scheme

ISD	In Stitch Direction
LCM	Liquid Composite Moulding
LES	Large Eddy Simulation
NCF	Non Crimp (stitched) Fabric
NLR	National Aerospace Laboratory
PDE	Partial Differential Equation
PSD	Perpendicular to Stitch Direction
RTM	Resin Transfer Moulding
UT	University of Twente
VARTM	Vacuum Assisted Resin Transfer Moulding
VOF	Volume of Fluid

Bibliography

[1] R. ten Thije. *Finite Element Simulations of Laminated Composite Forming Processes*. PhD thesis, University of Twente, September 2007. ISBN-13: 978-90-365-2546-6.

[2] E.A.D. Lamers. *Shape distortions in fabric reinforced composite products due to processing induced fibre reorientation*. PhD thesis, University of Twente, April 2004. ISBN 90-365-2043-6.

[3] R. Loendersloot. *The Structure–Permeability Relation of Textile Reinforcements*. PhD thesis, University of Twente, 2006. ISBN 90-365-23337-0.

[4] M. Nordlund. *Permeability Modelling and Particle Deposition Mechanisms Related to Advanced Composites Manufacturing*. PhD thesis, Luleå University of Technology, October 2006.

[5] H. Darcy. *Les fontaines publiques de la Ville de Dyon*. Dalmont, Paris, 1856.

[6] Malcolm and Bolton. *A guide to soil mechanics*. Cambridge : M.D. & K. Bolton, 1991.

[7] S.P. Neuman. Theoretical derivation of darcy's law. *Acta Mechanica*, 25:153–170, 1977.

[8] J.G. Williams, C.E.M. Morris, and B.C. Ennis. Liquid flow through aligned fiber beds. *Polymer Engineering and Science*, 14(6):413–419, 1974.

[9] B.R. Gebart. Permeability of uni–directional reinforcements for RTM. *Journal of Composite Materials*, 26(8):1100–1133, 1992.

[10] R.C. Lam and J.L. Kardos. The permeability and compressibility of aligned and cross-plied carbon fibre beds during processing of composites. In *Proceedings of Annual Technical Conference – ANTEC*, pages 1408–1412, 1989.

[11] G.L. Batch, Y.-T Chen, and C.W. Macosko. Capillary impregnation of aligned fibrous beds: Experiments and model. *Journal of Reinforced Plastics and Composites*, 15:1027–1051, 1996.

[12] J.D. Muzzy, Y. Zhang, and J. Bradly. Flow of thermoplastics through fibre assemblies. In *Proceedings of FPCM-5, Plymouth*, pages 71–78, 1999.

[13] T.G. Gutowski, Z. Cai, S. Bauer, D. Boucher, J. Kingery, and S. Wineman. Consolidation experiments for laminate composites. *Journal of Composite Materials*, 21:650–669, 1987.

[14] H.C. Brinkman. A calculation of the viscous force exerted by a flowing fluid on a dense swarm of particles. *Applied Scientific Research A*, 1:27–34, 1947.

[15] K.M. Pillai and S.G. Advani. Numerical and analytical study to estimate the effect of two length scales upon the permeability of a fibrous porous medium. *Transport in Porous Media*, 21(1):1–17, October 1995.

[16] S. Ranganathan, F.R. Phelan Jr., and S.G. Advani. A generalized model for the transverse fluid permeability in unidirectional fibrous media. *Polymer Composites*, 17(2):222–230, April 1996.

[17] B.M. Yu and L.J. Lee. A simplified in-plane permeability model for textile fabrics. *Polymer Composites*, 21(5):660–685, October 2000.

[18] N.D. Ngo and K.K. Tamma. Microscale permeability predictions of porous fibrous media. *International Journal of Heat and Mass Transfer*, 44:3135–3145, 2001.

[19] Z. Cai and A.L. Berdichevsky. Estimation of the resin flow permeability of fiber tow preforms using the self-consistent method. *Polymer Composites*, 15(3):240–246, June 1994.

[20] C. Lekakou and M.G. Bader. Mathematical modelling of macro- and micro-infiltration in resin transfer moulding (rtm). *Composites Part A*, 29A:2937, 1998.

[21] M. Nordlund and T.S. Lundström. Effect of multi-scale porosity in local permeability modelling of non-crimp fabrics. *Submitted to Transport in Porous Media*, 2006.

[22] J. Wenström. Report on ncf processing behaviour and quality with standard carbon yarns. Technical Report FALCOM G4RD-CT-00694 - WP2.1-1, Devold AMT, 2003.

[23] T. Truong Chi, M. Vettori, S.V. Lomov, and I. Verpoest. Carbon composites based on multiaxial multiply stitched preforms. part IV: - Mechanical properties of composites and damage observation. *Composites Part A*, 36(9):1207–1221, 2005.

[24] J. Wiggers, A.C. Long, P.Harrison, and C.D. Rudd. The effects of stitch architecture on the shear compliance of non-crimp fabrics. In *Proceedings of sixth ESAFORM Conference on Material Forming*, pages 851–854, 2003.

[25] R.H.W. ten Thije, R. Loendersloot, and R. Akkerman. Material characterization for finite element simulation of draping with non–crimp fabrics. In *Proceedings of ESAFORM, Salerno, Italy*, pages 859–862, 2003.

[26] A.P. Mouritz, K.H. Leong, and I. Herszberg. A review of the effect of stitching on the in-plane mechanical properties of fibre-reinforced polymer composites. *Composites Part A*, 28(12):979–991, 1997.

[27] C. Weimer and P. Mitschang. Aspects of the stitch formation process on the quality of sewn multi-textile-preforms. *Composites Part A*, 32(10):1477–1484, 2001.

[28] S.V. Lomov, E.B. Belov, T. Bischoff, S.B. Ghosh, T. Truong Chi, and I. Verpoest. Carbon composites based on multiaxial multiply stitched preforms. part I: Geometry of the preform. *Composites Part A*, 33:1171–1183, 2002.

[29] C. Lekakou, S. Edwards, G. Bell, and S.C. Amico. Computer modeling for the prediction of the in-plane permeability of non-crimp stitch bonded fabrics. *Composites Part A*, 37:820–825, 2006.

[30] M. Schneider, K. Edelmann, and U. Tiltmann. Quality analysis of reinforcement structures for composites by digital image processing. In *Proceedings of SAMPE Europe, Paris*, volume 25, pages 267–272, 2004.

[31] T.S. Lundström. The permeability of non-crimp stitched fabrics. *Composites Part A*, 31:1345–1353, February 2000.

[32] M. Nordlund and T.S. Lundström. The effect of geometrical features of non-crimp fabrics on the permeability. In *Proceedings of ECCM-11 Conference, Rhodos, Greece*, 2004. [CD-Edition].

[33] M. Nordlund, T.S. Lundström, V. Frishfelds, and A. Jakovics. Permeability network model for non-crimp fabrics. *Composites Part A*, 37(6):826–835, 2006.

[34] R. Loendersloot, S.V. Lomov, R. Akkerman, and I. Verpoest. Carbon composite based on multiaxial multiply stitched preforms. part V: Geometry of sheared biaxial fabrics. *Composites Part A*, 37:103–113, 2006.

[35] R. Loendersloot, R.H.W. ten Thije, R. Akkerman, and S.V. Lomov. Permeability prediction of non-crimp fabrics based on a geometric model. In *Proceedings of ECCM-11 Conference, Rhodos, Greece*, 2004. [CD-Edition].

[36] Jinlian Hu, Yi Liu, and Xueming Shao. Effect of stitches on the permeability of interbundle channels in stitched fabrics. *Textile Research Journal*, 73:691–699, August 2003.

[37] M. Nordlund and T.S. Lundström. Numerical study of the local permeability of noncrimp fabrics. *Journal of Composite Materials*, 39(10), 2005.

[38] Niels Asger Mortensen, Fridolin Okkels, and Henrik Bruus. Reexamination of hagen-poiseuille flow: Shape dependence of the hydraulic resistance in microchannels. *Physical Review E*, 71 (057301), May 2005.

[39] Frank M. White. *Fluid Mechanics*. McGraw-Hill, fourth edition, 1999.

[40] Robert W. Fox, Alan T. McDonald, and Philip J.Pritchard. *Introduction to Fluid Mechanics*. John Wiley & Sons Inc., 6 edition, 2004. ISBN 0-471-20231-2.

[41] S.V. Lomov, G. Huysmans, Y. Luo, R. Parnas, and A. Prodromou. Textile composites models: integrating strategies. *Composites Part A*, 32(10):1379–1394, 2001.

[42] S.V. Lomov, G. Huysmans, and I. Verpoest. Hierarchy of textile structures and architecture of fabric geometric models. *Textile Research Journal*, 71(6):534–543, 2001.

[43] S.V. Lomov and I. Verpoest. Modelling of the internal structure and deformability of textile reinforcements: Wisetex software. In *Proceedings of ECCM-10, Brugge*, 2002. [CD-edition].

[44] E.B. Belov, S.V. Lomov, I. Verpoest, T. Peters, D. Roose, R.S. Parnas, K. Hoes, and H. Sol. Modelling of permeability of textile reinforcements: lattice boltzmann method. *Composites Science and Technology*, 64:1069–1080, 2004.

[45] M.A.A. Spaid and Jr. F.R. Phelan. Lattice boltzmann methods for modeling microscale flow in fibrous porous media. *Physics of fluids*, 9(9):2468–2474, 1997.
[46] M. Nordlund and T.S. Lundström. Numerical calculations of the permeability of non-crimp fabrics. In *Proceedings of ICCM-14 Conference, San Diego, USA*, pages –, 2003. [CD-Edition].
[47] *ANSYS CFX-Solver, Release 10.0: Theory*. ANSYS Europe Ltd., 2005.
[48] R. Loendersloot and R. Akkerman. A permeability prediction for non-crimp fabrics. In *Proceedings of FPCM-8, Douai, France*, pages 73–81, 2006.
[49] R. Loendersloot, R. Akkerman, and S.V. Lomov. A permeability prediction for (un)sheared non-crimp fabrics. In *Proceedings of FPCM-7, Newark Delaware*, pages 367–372, 2004.
[50] R. Loendersloot and R. Akkerman. A permeability prediction for non-crimp fabrics. In *Proceedings of ESAFORM-9, Glasgow*, pages 803–806, 2006.
[51] M.J. Fagan. *Finite Element Analysis – Theory and Practice*. Addison Wesley Longman Limited, 2 edition, 1996. ISBN 0-582-02247-9.
[52] MathWorks Inc. *Matlab 7.1 Release 14 Documentation*, 2005.
[53] R.D. Cook, D.S. Malkus, M.E. Plesha, and R.J. Witt. *Concepts and Applications of Finite Element Analysis*. John Wiley & Sons, Inc., fourth edition, 2002. ISBN 0-471-35605-9.
[54] A. Koorevaar. Fast, accurate, reliable 3d - reactive rtm simulation. 2002. ISCM 2002.
[55] J.A. Luoma and V.R. Voller. An explicit scheme for tracking the filling front during polymer mold filling. *Applied Mathematical Modelling*, 24:575–590, 2000.
[56] R.V. Mohan, N.D. Ngo, and K.K. Tamma. On a pure finite-element-based methodology for resin transfer mold filling simulations. *Polymer Engineering and Science*, 39(1):26–43, January 1999.
[57] R. Akkerman, R.H.W. ten Thije, and R. Loendersloot. Appendix II - permeability, drapeability and compressibility - three interrelated properties. Technical Report FALCOM G4RD-CT-00694 - WP4.3-1 - App II, University Twente, 2003.

Nawoord

In het najaar van 2004 begon ik met de pre-master van werktuigbouwkunde aan Universiteit Twente. Voor de toelating werd om een motivatie brief gevraagd. Één van de alinea's luidde:

> "Mijn afstudeeropdracht voor de opleiding HBO-werktuigbouwkunde heb ik uitgevoerd aan de Universiteit Twente. De opdracht had te maken met onderzoek naar een productieproces van composiet producten. Van diverse vezelpakketten moesten de in-plane permeabiliteiten bepaald worden. Tijdens deze opdracht realiseerde ik me dat er nog veel valt te onderzoeken en te optimaliseren aan het productieproces van composieten. Het is voor mij een uitdaging om meer kennis op te doen van composieten en hun productieprocessen. Ik zie veel toekomst in dit kennisgebied en zal vol enthousiasme aan deze opleiding beginnen en eindigen."

Deze master afstudeeropdracht is uitgevoerd bij de vakgroep "Productie Technologie", waar ik voor de HBO ook mijn afstudeeropdracht heb uitgevoerd. Kennelijk zit ik op het pad dat ik vier jaar geleden al in gedachten had. Ik ben aan mijn afstudeeropdracht begonnen met de drang werk af te leveren waar ik zelf trots op mag zijn. Dit heeft de nodige energie en concentratie gevergd maar ik kan u vertellen dat, dat doel zeker is verwezenlijkt. Het mocht echter enige tijd op zich laten wachten. De negen maanden die normaal staan voor een WB afstudeeropdracht, wordt voor bijna iedere student officieus verlengd tot een jaar. In mijn geval was de duur nog langer. Ik heb echter erg mooie dingen mogen meemaken dankzij het vertrouwen van mijn hoogleraar Remko Akkerman. Dankzij hem heb ik mijn zegje kunnen doen op conferenties als de "Tenth Engineering Mechanics Symposium", de "Sixth SAMPE Benelux Student Seminar" en in juli 2008 staat de "Ninth International Conference on Flow Processes in Composite Materials" op mij te wachten. Remko, bedankt voor de begeleiding die je me tijdens deze opdracht heb gegeven en voor de inspirerende discussies die we hadden en de daaruit voortvloeiende ideeën.

Laurent Warnet is tijdens mijn HBO afstudeeropdracht en tijdens deze master afstudeeropdracht een zeer inspirerend persoon geweest (ook op gebied van mountainbiken(MTB-en)). Laurent, bedankt voor de hulp die je me tijdens de fasen met het experimentele werk in de labs hebt gegeven en alle andere tips daarnaast. Je ervaring op experimenteel gebied is ongekend.

Met Wouter Grouve en Réne ten Thije heb ik regelmatig discussies gehad over leuke problemen die ik tijdens mijn afstudeeropdracht tegen kwam, vooral op het gebied van permeabiliteit. Het definiëren en voorleggen van problemen is een stap die mij vaak de helft van de weg naar de oplossing toe heeft opgeleverd. Jongens, bedankt voor het aanhoren en het meedenken. Ashok, omdat je Nederlands al best goed is en je ook vind dat we tegen jou in het Nederlands moeten praten, schrijf ik het volgende bedankje ook in het Nederlands. Ik heb erg veel geleerd van je correcties op al die versies van het afstudeerverslag. Bedankt voor de verduidelijkingen betreft de Engelse grammatica en het daarmee gepaarde geduld. Discussies met mensen uit de OPM afstudeerzaal waren ook altijd interessant en erg gezellig. Heren (en enkele dames), jullie (Lieuwe, Rolf, Hugo, Krijn, Max, Pieter, Maarten, Nico, Marlous, etc.) zijn er teveel om op te noemen maar ik moet jullie allen bedanken voor de leuke tijd, vooral tijdens de koffiepauzes. Hierbij noem ik Jacob Reiding nog apart, wegens een deal die we maakte over een vernoeming in het nawoord, in ruil voor een "home made" Wheatstone brug. Jacob, bedankt voor het meedenken tijdens de experimenten. Betreft de Wheatstone brug, deze heb ik helaas niet kunnen gebruiken, maar het was een leuk klein projectje, nietwaar?

Mijn familie, in het bijzonder mijn ouders wil ik bedanken voor het vertrouwen dat zij in mij hadden. Ma en pa, zonder jullie was de weg naar vandaag de dag een stuk moeilijker geweest, bedankt! Janine, ik mag heel erg boffen met een meisje als jij. Gelukkig had jij ook nog vertrouwen in me, ondanks je verbazing over de afstudeerduur bij WB-ers. Binnenkort ben je hopelijk niet meer de enige kostwinner ;). Martijn, jij ook bedankt voor het opzetje van de website. Ziet er erg gelikt uit! Joop en Dicky, ook bedankt voor de aanmoedigingen!

Ook wil ik mijn oud-flatgenoten bedanken voor de geweldige tijd die ik heb gehad aan de Witbreuksweg (dat mis ik nog steeds een beetje). Er waren altijd leuke discussies en gezamenlijk koffie drinken was toen nog normaal (dit lijkt te verdwijnen bij de nieuwe generatie flatbewoners). David en Ronald, technische vraagstukjes (wiskundige of Matlab-achtige) waren af en toe het onderwerp van gesprek en waren/zijn erg vermakelijk. Maar ook buiten dit nerd-gedoe, hebben wij ons uitstekend vermaakt. Mark maakt hier ook deel van uit, daarbij was het erg leuk om wat experimenteel werk als toekijkende te ervaren op het BMT lab (om problemen met Charlie te voorkomen in de nachtelijke uurtjes). Dat is een keer wat anders dan WB-opstellingen.

Één van mijn bezigheden om de studie zo nu en dan te ontvluchten was het MTB-en. Wouter, bedankt voor het gezelschap die tijd en bedankt voor het motiveren van zo'n slome fietser als ik. Het parcourtje op het Hulsbeek kunnen we nu wel dromen. De tripjes naar het Hermanspad in Duitsland waren erg gaaf. Ik moet toegeven dat het fietsritme is verwaterd in de laatste fase van mijn afstuderen. Wouter en Wouter, ik ga mijn best doen weer wat tijd te maken om te fietsen.

Laat ik niet verder gaan, anders gaat dit allemaal erg lijken op een nawoord van een proefschrift, daar mag ik nog even mee wachten... Voor iedereen die ik niet genoemd heb, voel je niet benadeeld, ik ben je ongetwijfeld vergeten.

Sebastiaan Haanappel
17 juni 2008